ORNL-TM-3416

Contract No. W-7405-eng-26

METALS AND CERAMICS DIVISION

FUELS AND MATERIALS DEVELOPMENT PROGRAM QUARTERLY PROGRESS REPORT FOR PERIOD ENDING MARCH 31, 1971

P. Patriarca

JULY 1971

OAK RIDGE NATIONAL LABORATORY
Oak Ridge, Tennessee
operated by
UNION CARBIDE CORPORATION
for the
U.S. ATOMIC ENERGY COMMISSION

DISTRIBUTION OF THIS DOCUMENT IS UNLIMITED

DISCLAIMER

FOREWORD

This quarterly progress report describes research and development on nuclear fuels and materials at the Oak Ridge National Laboratory for the U.S. Atomic Energy Commission. This work is either sponsored by or of particular interest to the Fuels and Materials Branch of the Division of Reactor Development and Technology.

Progress on these programs is reported for the three major divisions of the work — Fast Reactor Technology, Space Power Technology, and General Reactor Technology — under the appropriate AEC activity titles listed below.

Chapter Number	AEC Activity Title	189a Number	AEC Activity Number
	PART I. FAST REACTOR TECHNOLOGY		
1	FBR OXIDE FUELS DEVELOPMENT	10090	04 40 02 01 1
2	DEVELOPMENT OF ADVANCED FBR FUELS	10092	04 40 02 01 1
3	FBR CLAD AND STRUCTURAL ALLOY DEVELOPMENT MECH PROP OF ALLOYS IN REACTOR	10026 10097	04 40 02 01 1 04 40 02 03 1
4	FAB DEV OF FBR CLADDING	10202	04 40 02 04 1
5	WELDING DEV — FBR SS COMPONENTS	10219	04 40 02 04 1
6	PROPERTIES OF FERRITIC STEEL WELDS	10241	04 40 02 05 1
7	NDT TECHNIQUES FOR FBR	10106	04 40 02 04 1
8	SODIUM CORROSION STUDIES	10096	04 40 02 02 1
9	SODIUM REMOVAL AND CAUSTIC EFFECTS	10248	04 40 02 02 1
10	DEV OF FBR NEUTRON-ABSORBER MATERIALS	10242	04 40 02 02 1
	PART II. SPACE POWER TECHNOLOGY		
11	DEVELOPMENT OF NITRIDE FUELS	10213	04 40 02 01 1
12	CLADDING MATERIALS FOR SPACE ISOTOPIC HEAT SOURCES*	10507	04 30 05 04 1
13	PHYSICAL AND MECHANICAL METALLURGY OF REFRACTORY ALLOYS	10110	04 40 02 05 1

---

*Sponsored by Division of Space Nuclear Systems.

Chapter Number			
14	TUNGSTEN METALLURGY	10104	04 40 02 04 1
15	FAST-NEUTRON IRRADIATION EFFECTS ON ELECTRICAL INSULATORS*	10068	04 30 02 02 1

PART III. GENERAL REACTOR TECHNOLOGY

16	FUEL ELEMENT FABRICATION DEVELOPMENT	10107	04 40 02 04 1
17	TRANSURANIUM ELEMENT PROCESSING — TARGET FABRICATION†	85	05 05 05 00 0
	HIGH FLUX ISOTOPE REACTOR†	88	05 05 05 00 0
	RADIATION DAMAGE†	103	05 06 01 03 0
18	JOINING RESEARCH ON NUCLEAR MATERIALS	10103	04 40 02 04 1
19	NONDESTRUCTIVE TESTING	10220	04 40 02 04 1
20	ADVANCED MATERIALS FOR STEAM GENERATORS	10217	04 40 02 02 1

---

*Sponsored by Division of Space Nuclear Systems.

†Sponsored by Division of Research.

CONTENTS

PART I. FAST REACTOR TECHNOLOGY

FUELS

CLADDING AND OTHER STRUCTURAL MATERIALS

PART II. SPACE POWER TECHNOLOGY

FUELS

CLADDING AND OTHER STRUCTURAL MATERIALS

PART III. GENERAL REACTOR TECHNOLOGY

FUELS

CLADDING AND OTHER STRUCTURAL MATERIALS

SUMMARY

PART I. FAST REACTOR TECHNOLOGY

FUELS

1. DEVELOPMENT OF FBR OXIDE FUELS

Sol-gel-derived $(U,Pu)O_2$ powder for pellets and sol-gel microspheres were prepared for cold dissolution studies at WADCO. A theoretical analysis of the reduction of $(U,Pu)O_2$ in flowing H_2 shows that the reduction process is kinetically controlled and is limited by the rate at which H_2O can be removed from the furnace. We are presently manufacturing 11 replacement fuel pins for a 37-pin EBR-II unencapsulated subassembly. We are also fabricating fuel pins containing $(U,Pu)O_2$ pellets prepared by WADCO from mechanically mixed powders. These pins will be used to study fuel-cladding mechanical interaction during power cycling.

To date, 10 metallographic sections have been removed from various axial locations along the fuel column of pin S-1-E which was irradiated in the EBR-II to a peak burnup of 6% FIMA, a peak linear heat rate of 14 kW/ft, and a peak calculated cladding inner surface temperature of 570°C. No significant fuel-cladding chemical interaction has been observed in any of these sections. Although the electron microprobe analyses are incomplete, we have observed a distinct accumulation of Cs on the inner surface of the cladding in the fuel cracks and occasionally in localized spots on the central void surface. There has been no indication of Cs or other fission product intergranular penetration into the cladding. This is further evidence that there has been no significant fuel-cladding chemical interaction even in low-density fuel regions. This is in agreement with our previous observations from thermal flux irradiation tests, but contradicts a recent suggestion that low-density particulate fuels are more susceptible to fuel-cladding chemical interactions. Our observation is they are less susceptible to fuel-cladding chemical interaction than other fuels on the basis of the data at hand.

Three capsules in this same series that are now at nominally 6 at. % burnup are scheduled for continued irradiation in subassembly X119. We have been advised by the EBR-II Project that, because of other higher priority tests, subassembly X119 will not be inserted into the reactor before run 49. The availability of space for the start of the irradiation of Series II unencapsulated subassembly X112, which is being shared with the Babcock and Wilcox Company, cannot be determined at this time. We completed the conceptual design of a third EBR-II test series, an experiment which is designed to take advantage of the higher flux levels available following the recent EBR-II power increase to 62.5 MW. The fuel pins will be $(U,Pu)O_2$ using natural U and will be large in diameter to obtain prototypic heat rates and temperatures. The fission yields will be typical of those obtained under fast reactor conditions, as opposed to all high heat rate $(U,Pu)O_2$ fuel pins previously irradiated in the EBR-II. This will allow the examination of fuel-cladding chemical interactions with the higher O potentials expected from proportionally greater Pu fissioning in the fuel.

To examine the usefulness of the FMØDEL fuel performance code in predicting irradiation behavior of LMFBR fuel pins, comparisons have been made between the calculations and measurements on General Electric F2 series of EBR-II irradiation experiments. The comparison was based on cladding diametral expansion, fuel radial porosity distributions and diameters of central void, columnar, and equiaxed grain regions. Overall agreement between predicted and measured fuel pin behavior is acceptable.

2. DEVELOPMENT OF ADVANCED FBR FUELS

Approximately 500 pellets of (U,Pu)N to be irradiated in EBR-II have been fabricated during this quarter. Characterization of the fuel is about half completed. Machining of the fuel pellets will commence shortly. Nearly 200 pellets of UN were fabricated for use in sodium bonding technique development and for blanket pellets in the EBR-II irradiation pins.

Comminution of (U,Pu)N by ball milling in hexane has been found to result in carbon contamination of the nitride but the presence of oxygen contaminant in the nitride powder results in carbothermic reduction during sintering and a loss of some of the carbon contaminant. A marked improvement in sintering of (U,Pu)N was observed for ball-milled powders.

The Dumas method for nitrogen determination in nitrides has been developed to easily measure nitrogen in UN and U_2N_3 phases and should be easily applicable to (U,Pu)N. We have observed that the dissolution vessel geometry is very important when dissolving samples of (U,Pu)N for the coulometric determination of the heavy metal. A reflux condenser is required in order to maintain high accuracy in the analysis.

A tentative phase diagram for the Pu-Cr-N system has been determined in the range 790 to 1705°C. No ternary compound has been observed in the composition fields examined.

Many of the components for the EBR-II capsule assemblies have been received and capsule fabrication is proceeding. Sodium bonding and NDT techniques for the (U,Pu)N irradiation pins are proceeding well.

CLADDING AND OTHER STRUCTURAL MATERIALS

3. MECHANICAL PROPERTIES OF ALLOYS IN REACTOR ENVIRONMENTS AND DEVELOPMENT OF LMFBR CLADDING AND STRUCTURAL MATERIALS

Examination of annealed type 304 stainless steel irradiated at 590°C to fast fluences of 1.8, 2.3, and 3.5×10^{22} neutrons/cm^2 has shown that the rate of nucleation of voids decreases sharply with increasing fluence, but that void growth continues. Thus, at high fluences swelling should become proportional to the fluence raised to the power of 1.5 compared with a power of 5 at low fluences. Type 304 stainless steel was irradiated to a fluence of 2.5 × 10^{22} neutrons/cm^2 at 450°C in three metallurgical conditions: (1) annealed, (2) cold-worked 10%, and (3) cold-worked 10% and annealed 24 hr at 480°C and 100 hr at 700°C (recovered). The cold-worked specimen swelled less than the annealed one because of a large decrease in void concentration. The recovered specimen swelled more than the annealed one because of an increase in void sizes.

Tensile tests on standard and Ti-modified types 316 stainless steel in the irradiated and unirradiated conditions showed the properties to be sensitive to metallurgical condition (annealed and 20% cold-worked), aging, and irradiation. Samples of standard and Ti-modified stainless steel irradiated at 450 to 800°C to a peak fluence of 2.7 × 10^{22} neutrons/cm^2 have been removed from EBR-II and partially characterized. The Ti-modified steel consistently shows smaller density changes than those of the standard alloy.

Subassembly X034A has been removed from EBR-II. Gas gaps between the outside tube and the specimen holders were used to obtain temperatures above ambient. Dimensional changes due to swelling of the components caused some shifts in the irradiation temperature.

All materials prepared previously for transmission electron microscopy were prepared from small pieces that could be handled in the laboratory. However, the radiation levels of tantalum made it necessary to develop techniques for preparing samples in the hot cells. Samples of recrystallized Ta irradiated in EBR-II at 425, 585, 790, and 1000°C to fluences of 2.5 to 4.4 × 10^{22} neutrons/cm^2 have been thinned and examined. The sample irradiated at 425°C contained small loops but no voids. The samples irradiated at the other three temperatures contained voids.

High-purity aluminum, 50% cold-worked 1100 grade, 50% cold-worked 8001 grade, "O" temper 6061 grade, and T-6 temper 6061 grade were irradiated in HFIR at 140 to 200°C at neutron fluences of 0.4 to 1.6 × 10^{22} neutrons/cm^2. Voids were found in the high-purity aluminum over much of the temperature range, but voids were not observable in the other alloys. Silicon precipitates arising from the transmutation of aluminum were present in most materials. Creep-rupture tests on 8001 showed that irradiation increased the rupture life, decreased the creep rate, and decreased the fracture strain.

4. FABRICATION DEVELOPMENT OF FBR CLADDING

This study to examine the relationships between defect size and the stress-rupture properties is continuing. A technical report describing our results with cold-worked type 316 stainless steel is in the process of being published.

Our work on the planetary swaging of type 316 stainless steel has been completed and a report has been written.

5. WELDING DEVELOPMENT FOR FBR STAINLESS STEEL COMPONENTS

The mechanical properties, both creep-rupture and tensile, of submerged-arc welds in stainless steel are being determined. There is a general decrease in rupture elongation as rupture time increases. However there are unexplainable differences in rupture strengths for several welds, and we are trying to determine the reason. The results of a preliminary evaluation of the tensile data are presented.

A comprehensive evaluation of shielded metal-arc welds is also under way. This involves mechanical properties, heat treatment effects, and corrosion studies. Heat treatments lowered the rupture lives by about one order of magnitude. The results of a metallographic examination of welds exposed to a wide variety of heat treatments are reported. Factors influencing sigma-phase formation are receiving particular attention. Strauss tests on a number of as-welded and welded-and-heat treated samples have been performed.

6. PROPERTIES OF FERRITIC STEEL WELDS

Studies have been conducted on welds in low-carbon low-alloy steels. At 565°C (1050°F), there is a factor of two difference in the ultimate tensile strength between the low-carbon (0.003%) and high-carbon (0.11%) steels studied. Subjecting the welds to a postweld heat treatment of 700°C (1300°F) for 1 hr resulted in a strength difference of only 40% (50,000 psi vs 69,000 psi). All welds had excellent reduction-in-area values (in excess of 80%) after the postweld heat treatment. Evidence of a deleterious effect of low strain rate on the ductility of the weld metal is shown. Hardness data indicate that the strength of the as-welded heat-affected zone of the low-carbon steel is low. Thermal excursions due to the multipass weld techniques are indeed beneficial and perhaps final passes for reasons of heat treatment may be required.

Stabilized low-alloy steel slabs 1-in. thick have been received and are being rolled to 1/2- and 1/4-in. thicknesses for subsequent weldability studies.

7. NONDESTRUCTIVE TESTING TECHNIQUES FOR LMFBR

In the development of the eddy-current instrument for identification of flaws, we completed construction on the two-frequency oscillator and power amplifier module and designed and constructed eleven tuned amplifiers covering a frequency range from 1 KHz to 2 MHz. Difficulty has been encountered in ultrasonically identifying the reference flaws in the stainless steel welds when using the Delta configuration.

Two new designs of coil systems are being studied for the eddy-current measurement of cold work in fuel element cladding. Bifilar-wound coils exhibit greater sensitivity to changes in permeability but have more drift than a side-by-side coil array. Other benefits of the side-by-side configuration include ease of fabrication and decreased problems with thermal expansion.

8. SODIUM CORROSION STUDIES

In tests designed to evaluate the effect of Cr and Mo on the diffusion coefficients of O in V at 600°C, we simultaneously exposed specimens of O doped alloyed and unalloyed V to Na. The initial results indicate that a surface reaction may control the rate of oxygen transfer between the specimens, thus making it impossible to determine diffusion coefficients.

We studied the oxidation kinetics of V—20% Ti at 1000°C as a function of O_2 pressure, surface area and surface preparation. Oxidation occurs in two stages: an initial linear stage followed by a stage in which the rate decreases with time.

9. SODIUM REMOVAL AND CAUSTIC EFFECTS

We have begun dissecting the ALCO/BLH steam generator to determine the causes of cracking in the lower tube sheet. Extensive sodium-containing deposits were apparent in the argon gas space above the sodium, and attack typical of hydroxide corrosion was found beneath these deposits.

We have terminated our studies of the effects of sodium leaks on the oxidation of stainless steel in nitrogen plus oxygen mixtures. The effectiveness of various sodium removal techniques was evaluated by exposing several different alloys to a short duration sodium soak, stripping the specimens of residual sodium, and reexposing the alloys in sodium. Reexposure to sodium caused attack in proportion to the quantity of impurities left by the stripping process.

10. DEVELOPMENT OF FBR NEUTRON-ABSORBER MATERIALS

X-ray scattering from irradiated crystals of boron carbide show a composite of sharp and diffuse reflections. The lattice parameters calculated from the sharp maxima show an increase in the $\underline{a}$ and the $\underline{c}$ hexagonal indices; however, the lattice parameters calculated from the diffuse maxima show an increase in $\underline{a}$ and a decrease in $\underline{c}$. Further chemical analyses of the boron carbide powder in ORR capsules indicate that boron as elemental boron or as B_2O_3 was responsible for the higher gas release observed in some of the capsules. A problem exists in obtaining reliable burnup analyses for the irradiated boron carbide powders. Analysis of $^{10}B/^{11}B$ ratio indicate that the burnup is about three times as high as that indicated by lithium analysis. There are difficulties in obtaining a representative sample for the $^{10}B/^{11}B$ analysis since the present technique involves an extremely small sample from a powder where the burnup gradient could be relatively high.

PART II. SPACE POWER TECHNOLOGY

FUELS

11. DEVELOPMENT OF URANIUM MONONITRIDE FUELS

Two capsules containing T-111 clad UN fuel elements have been installed in the ORR and are now operating satisfactorily at 1000°C cladding temperature. During startup operation the capsules experienced short-lived temperature perturbations reflecting shifting of the NaK container with respect to the primary vessel. Thermal analysis also revealed a slightly off-center condition of the NaK container with respect to the primary vessel. This caused a lower effective thermal resistance between the fuel elements and the ORR coolant, thus necessitating operation of the fuel elements at a higher heat rating than anticipated to achieve the desired cladding temperature.

A third capsule containing T-111 and Nb—1% Zr clad UO_2 fuel elements is being assembled. A plan for testing of refractory metal clad UN fuel in EBR-II has been prepared and issued as an informal 189a proposal.

CLADDING AND OTHER STRUCTURAL MATERIALS

12. CLADDING MATERIALS FOR SPACE ISOTOPIC HEAT SOURCES

We are continuing to qualify Pt-Rh-W alloys for use as isotopic heat source cladding materials. Fabrication procedures have been developed for the production of small quantities of sheet and rod. The recrystallization temperature of Pt—26% Rh—8% W cold worked 35% was found to be about 1050°C. Grain growth was slow below 1400°C. The Pt—26% Rh—8% W alloy was found to be much stronger than Pt—30% Rh at all temperatures and equivalent to TZM at 1316•C. Air oxidation of Pt-Rh-W alloys to 1200°C is only a factor of 3 higher than pure Pt. Compatibility of Pt-Rh-W alloys with T-111 at simulated reentry temperatures indicate an improvement of about 100°F is possible over the Pt—30% Rh/T-111 capsule combination. No indication of interaction was evident upon aging 1000 hr at 900°C. The compatibility of CVD tungsten as a diffusion barrier in contact with Pt—26% Rh—8% W was found to be excellent even at simulated reentry temperatures as high as 1600°C. Long time tests at lower temperatures are in progress. Gas tungsten-arc welds on 20-mil sheet were found to be ductile and without cracks in the as-welded condition and after bending 90°.

13. PHYSICAL AND MECHANICAL METALLURGY OF REFRACTORY ALLOYS

The pressure-temperature-composition relationships in the nitrogen/T-111 system have been determined in the range of 1200—1600°C. Nitrogen partial pressures were about two orders of magnitude higher than those reported for unalloyed tantalum. Creep tests of T-111 at 1400°C in low partial pressures of nitrogen, such as those expected from UN fuels, resulted in moderate strengthening. No emissivity differences were detected in tests run in nitrogen or vacuum indicating that a nitride film does not form on the T-111 surface.

The effect of oxygen on the tensile properties of T-111 were determined to help elucidate the magnitude of the problem for plutonium-238 oxide fueled space isotope heat sources. Oxidized samples given a 15-min, 1700°C reentry-type heat treatment exhibited moderate reductions in ductility and increases in strength up to about 200 ppm. Surprisingly, both strength and ductility were nearly independent of oxygen content from 200 to 2800 ppm. In contrast, as-oxidized specimens containing only 800 ppm oxygen fractured in an extremely brittle manner even at temperatures as high as 1316°C.

The stress-rupture behavior of longitudinal GTA welds in Ta—10% W were compared to unwelded control specimens, transverse GTA welds and transverse EB welds. The creep behavior of the niobium alloy SU-31 was also determined.

Scanning electron microprobe analysis of fractures in TZM welds revealed modest amounts of oxygen in hot-cracked areas but none in cold-cracked areas. Repairs to a damaged molybdenum corrosion loop were made by welding on T-111 components using Mo–46% Re filler.

Samples of Mo-Zr and Mo-Nb alloys have been obtained and characterized in preparation for determining the lattice thermal conductivity of molybdenum. Electrical resistivity measurements on Mo-ThO_2 cermet isotope fuel simulants showed the product produced by chemically vapor depositing the molybdenum to be a 40% better conductor than one produced by blending molybdenum and thoria powders.

14. TUNGSTEN METALLURGY

Experiments on the chemical vapor deposition (CVD) of tungsten with a dispersion of fine particles were not successful in obtaining the desired volume fraction of particles. Studies on CVD of small diameter W–25% Re thermocouple sheath tubes showed that the deposition conditions producing the highest quality tubes resulted in slow deposition rates and low metal recovery.

In our creep testing program we are emphasizing determination of the low strain creep behavior of CVD tungsten for test times greater than 1000 hr. Six ultrahigh-vacuum creep machines with optical strain measurement capability have been installed and are undergoing operational checkout. In another phase of our creep testing program, the creep strength of tungsten at 1800°C was lower in a partial pressure of CH_4 than in vacuum.

We have completed the design of a high-temperature tungsten irradiation experiment for EBR-II and have submitted a request for Approval-in-Principle. Determination of the high-temperature electrical resistivity and Seebeck coefficient of tungsten and tungsten alloy control specimens is under way. We are also rechecking the low-temperature physical properties of tungsten alloys to allow accurate application of the alloying method of component separation.

15. FAST-NEUTRON IRRADIATION EFFECTS ON ELECTRICAL INSULATORS

A final topical report will be published in June 1971 entitled "Effects of Fast Neutrons on Polycrystalline Alumina and Other Electrical Insulators at Temperatures from 60 to 1230°C," by G. W. Keilholtz, R. E. Moore, and H. E. Robertson.

PART III. GENERAL REACTOR TECHNOLOGY

FUELS

16. DEVELOPMENT OF FUEL ELEMENT FABRICATION

The irradiation experiment, PM capsule No. 1, is operating satisfactorily in the HFIR. This experiment is designed to evaluate several parameters that are believed to influence the performance of both ATR and HFIR fuel elements at high fission densities.

CLADDING AND OTHER STRUCTURAL MATERIALS

17. IRRADIATION DAMAGE TO ALUMINUM AND ALUMINUM ALLOYS

Nothing to report.

18. JOINING RESEARCH ON NUCLEAR MATERIALS

Tensile tests at 650°C have been completed on the Incoloy 800 welds made with both experimental and commercially obtained filler metals. Two of the commercially produced alloys were submitted by International Nickel Company for evaluation. They compared favorably with the recommended filler metal (Inconel filler metal 82) for joining Incoloy 800.

An investigation of a microfissured electron-beam weld which joined an Inconel 600 tube to an Inconel-82-clad carbon steel tubesheet was conducted. The microfissure occurred in the overlay (the heat-affected zone of the weldment) at a location in which a stress concentration occurred due to the weld bead geometry. The microfissure was attributed to liquation of a Nb-rich phase during welding.

The Schaeffler Diagram, which is often employed for predicting the amount of ferrite in autenitic stainless steel welds, does not consider the large effect of heat input. Further, high Mn contents tend to provide erroneous ferrite predictions. Alloys with 5% Mn which are predicted to be all austenite were found to contain from 3 to 8% ferrite.

19. NONDESTRUCTIVE TESTING

We have written new computer programs for determining both magnitude and phase of impedance for a reflection coil above single and multiple layers of conductors. Standards for conductivity measurements are being prepared. In our studies for measuring the thickness of one material clad on another, we developed the criteria for design of coils for maximum sensitivity to clad thickness with an attendant minimum response to changes in coil-to-specimen spacing.

A dual gate system has been developed for performing frequency analysis on different portions of an ultrasonic pulse. This improves the capability to measure accurately the size of irregular flaws. The optical equipment for viewing ultrasound is being moved to a new facility and modified to allow studies of Bragg diffraction and volume holography as well as schlieren techniques. EDM notches were made in a tube and subsequently used successfully as an ultrasonic reference standard after the tube had been filled with powder and swaged into a rod.

We are converting our x-ray scattering and fluorescent studies to the use of a high intensity x-ray source and mechanical scanning system to permit dynamic measurements. Crystal monochromaters are being investigated to minimize the total amount of radiation on the specimen. Optical magnification of the radiographic image is being studied to minimize the relative effect of jitter in the video system for radiographic interpretation. A conceptual design has been completed for installation of a ^{252}Cf source in the laboratory.

20. ADVANCED MATERIALS FOR STEAM GENERATORS

In assessing the effect of surface finish on the corrosion of steam generator alloys, specimens in the ground condition and others with the effects of grinding removed by electropolishing were exposed in steam for 14,000 hr at 650 and 595°C (1200 and 1100°F). Electropolishing substantially increased the amount of corrosion of Incoloy 800 in this period, moderately increased it for Inconel 600, but slightly decreased the amounts in the cases of Inconel 625 and Hastelloy X. Whereas the amount of corrosion on electropolished Incoloy 800 was comparatively large for this period of exposure, the total attack in 20 years still would be impressively low because its corrosion rate decreases significantly with time.

Steam exposures consisting of cycling between 480°C (900°F) and the steam-saturation temperature (280°C or 540°F), and containing NaCl and O as contaminants, produced stress-corrosion cracking in weldments of Hastelloy X welded with itself as the filler metal. This was unexpected since some of the stainless steel specimens thought to be more crack-prone had not begun to fail.

PART I. FAST REACTOR TECHNOLOGY

FUELS

1. DEVELOPMENT OF FBR OXIDE FUELS

P. Patriarca   A. L. Lotts   C. M. Cox

The purpose of this program is to advance the technology of $(U,Pu)O_2$ as a fuel for the liquid-metal-cooled fast breeder reactor (LMFBR). The oxide fuels studied in this program are derived from coprecipitation, mechanical blending, and sol-gel processes and are fabricated by cold pressing and sintering and Sphere-Pac. We emphasize determination of the properties and performance of oxide fuels derived from the sol-gel process and fabricated by Sphere-Pac techniques, but we also compare these fuels with those fabricated by other processes. The main objectives of the program are (1) to establish the performance characteristics and limitations of $(U,Pu)O_2$ fuel fabricated by the different processes, (2) to obtain a fundamental understanding of the mechanisms that are involved in the behavior of fuel elements under irradiation, (3) to develop fabrication techniques that provide both economy and a product with optimized performance, and (4) to develop analytical methods sufficiently accurate to optimize experimental design and to predict the response of fuel elements to LMFBR service conditions.

Fuel Fabrication and Characterization

J. D. Sease

The purpose of our fuel fabrication work is to provide suitable fabrication processes for sol-gel-derived materials and to fabricate irradiation test specimens and capsules for a variety of irradiation tests in incorporating fuels derived from various processes.

Characterization (R. A. Bradley and W. H. Pechin)

The development of sol-gel fuel fabrication requires characterization of both the chemical composition and physical properties of the material to control the process and to interpret meaningfully the irradiation behavior. In many cases the analytical technique itself must be developed or modified to meet the requirements of mixed oxide fuels. In this section we report both the development or improvement of analytical techniques and the results of analyses on mixed oxide fuels.

Moisture Analysis. — We reported previously that the results of moisture analysis on $(U,Pu)O_2$ pellets were highly variable when the moisture analyzer was exposed to air while loading the sample, but much less variable when the analyzer was protected from the air with a plastic glove bag while loading the sample.[1]

We fabricated an air lock to prevent exposure of the moisture analyzer to the air while loading samples. The air lock, shown in Fig. 1.1 consists of a 3/4-in. ball valve with adaptors to provide an O-ring seal with the furnace tube and a sample loading chamber which can be evacuated and back-filled with an inert gas.

Two pellets have been analyzed for moisture content with the use of this loading chamber. The pellet to be analyzed was placed in a Pt boat in the air lock, the ball valve was closed, and the air lock was evacuated and back-filled with He twice. This is comparable to the evacuation given loaded fuel rods prior to making the closure weld.

The blank on the moisture analyzer after subtracting the electronic blank was nil. The moisture contents of the two pellets heated to 900°C were 3.5 and 4.0 ppm. It appears that the air lock is successful in reducing the blank and in decreasing the variation in the results of moisture analyses. In the future we will compare the results obtained by evacuating and back-filling the air lock with those obtained by purging the air lock with dry N.

Preparation of Sol-Gel $(U,Pu)O_2$ for Cold Dissolution Studies at WADCO

(R. A. Bradley)

Approximately 1 kg of sol-gel $(U,Pu)O_2$ powder for pellets and 200 g of microspheres are required for cold dissolution studies at WADCO.[2] The powder for pellets is to be in three batches with Pu/(U + Pu) ratios of 0.15, 0.20, and 0.25. Each batch is to be divided into three subbatches for calcining at 500, 600, and 700°C. The calcination

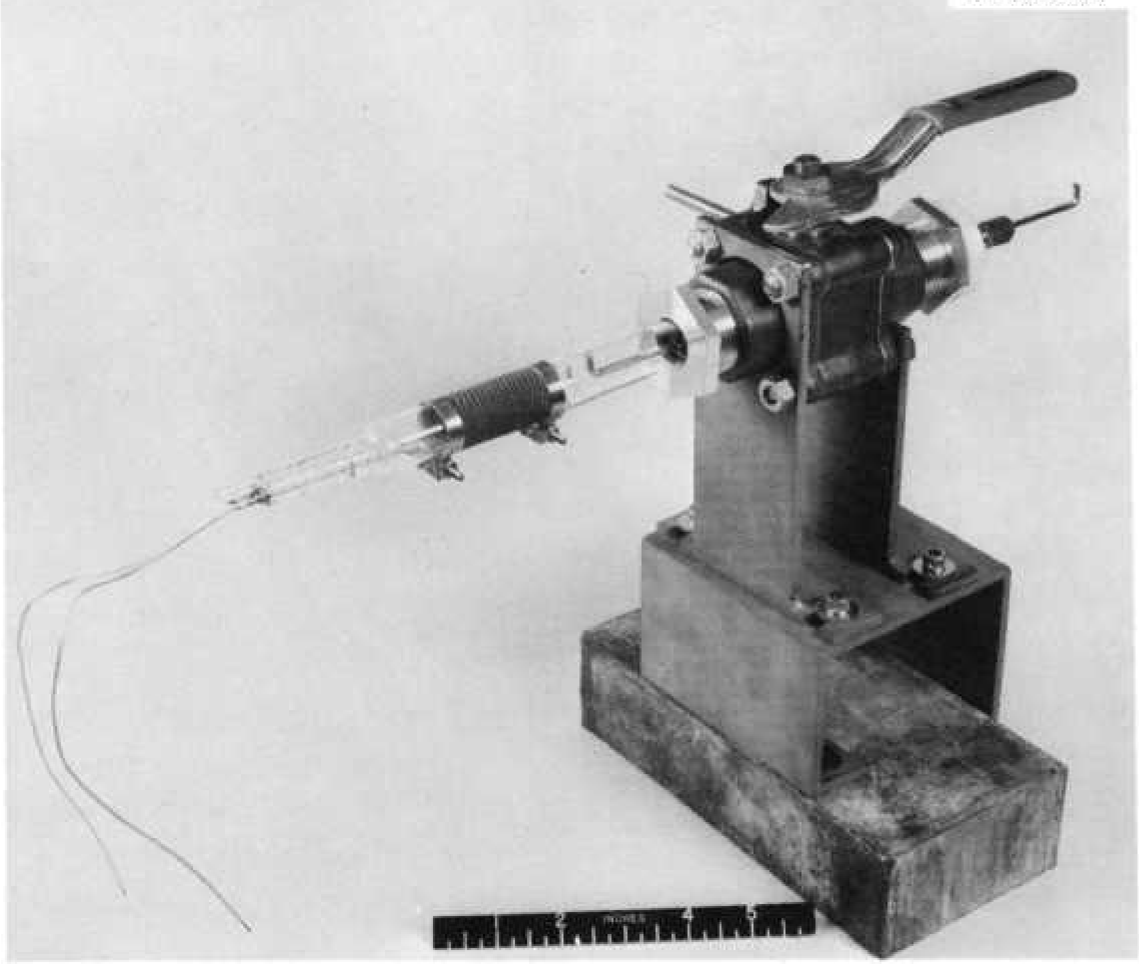

Y-105944

Fig. 1.1. Sample Loading Chamber for Moisture Analyzer.

conditions (atmosphere, time at temperature, etc) are to be such that the powder calcined at 600°C can be fabricated into 91% dense pellets. The powder may be ball-milled or preslugged and granulated to achieve this density.

All three batches have been blended and dried, and ground to —325 mesh powder. One subbatch was calcined at 600°C by an oxidation-reduction technique. A test sinter of this material showed it could be fabricated into pellets in the density range of 93 to 96% of theoretical; therefore, we are calcining the remainder of the powder in a similar manner.

The microspheres were prepared by the Chemical Technology Division. We adjusted the oxygen-to-metal ratio to 1.987 ± 0.006 by heat treating at 1350°C for 24 hr in Ar—8% H_2.

Kinetic Analysis of the Synthesis of $(U,Pu)O_{2-x}$ From Stoichiometric Oxide (T. B. Lindemer and R. A. Bradley)

Uranium-plutonium dioxide fuel for LMFBR applications is required to have an oxygen-to-metal ratio of ∿1.97. For some of our irradiation experiments oxygen-to-metal ratios as low as 1.94 are required. It is not always easy to achieve these oxygen-to-metal ratios; therefore, we have been investigating the reduction of mixed oxide to the hypostoichiometric state.

We performed a theoretical analysis of the reduction of $(U,Pu)O_2$ in flowing H_2. The analysis showed that the reduction process is kinetically controlled and is limited by the rate at which H_2O can be removed from the furnace. Using Markin's[3] thermodynamic data, an equation was developed to predict the time required for reduction to any oxygen-to-metal ratio. The details of this analysis have been described elsewhere.[4]

Series II Unencapsulated Fuel Pins for Irradiation in the Experimental Breeder Reactor II (R. A. Bradley, J. H. Erwin, E. J. Manthos, W. J. Leonard, and M. K. Preston)

We have fabricated and shipped to the reactor site 20 unencapsulated fuel pins, 19 of which are scheduled for incorporation in a 37-pin, EBR-II subassembly to be shared with Babcock and Wilcox Company.[5] The pins contain sol-gel Sphere-Pac fuel and pellets in type 316 stainless steel cladding. The fabrication of the pins was described previously.[6,7]

We are now manufacturing 11 replacement pins for this subassembly. The requirements for these pins and the insertion schedule were reported previously.[5] The clad tubes, bottom end plugs, Ni shield rods, and spring retainer seats for 23 fuel pins have been machined and inspected. The Inconel-X retainer springs are on hand but not inspected. All hardware items for weld development, Xe tagging qualification, and for archive fuel pins have been machined, inspected, and cleaned.

Fabrication and test procedures are being revised to incorporate minor design changes in the fuel pin and to upgrade our quality assurance program.

Fuel Reprocessing Fuel Pins (R. A. Bradley)

We previously fabricated 12 encapsulated fuel pins for irradiation in the Engineering Test Reactor (ETR). The irradiated fuel pins will be used by the Chemical Technology Division for fuel reprocessing studies. The fabrication and characterization of the fuel and the assembly of the fuel pins were reported previously.[8]

During this report period we assembled all of the data on the fuel and fuel pin and submitted it for documentation as MET-FCT-DP-1.

Mechanical Interaction Test Fuel Pin (R. A. Bradley)

We are fabricating the fuel pins for a series of irradiation experiments to study fuel-cladding mechanical interaction during power cycling.[9,10] The first two capsules (MINT-1 and MINT-2) will each contain about 9.6 in. of $(U_{0.75},Pu_{0.25})O_2$ pellets prepared by WADCO[11] from mechanically mixed powders with the densities and dimensions given in Table 1.1.

The fabrication and characterization of the fuel for the MINT-1 capsule were described previously.[12] We loaded the fuel into the fuel pin, made the closure weld, and inspected the weld by radiography, He leak check, and dye penetrant. The weld was satisfactory. A summary of the fuel dimensions and density for MINT-1 is given below.

Fuel length (in.)	9.59
Fuel weight (g)	44.827
Fuel diameter	0.1949
Average pellet density (% of theoretical)	89.3
Average planar smear density (% of theoretical)	85.3
Fuel column smear density (% of theoretical)	83.3

The pellets for MINT-2 have been received from WADCO and the data summary provided by WADCO indicates that the pellets conform to RDT E-13-6* chemistry requirements with the exception of gas content and the following elements which were not measured due to the small size of the batch: S, Ta, W, and rare earths. Processing experience indicates that the elements not determined should create no problems; however, we have submitted a sample for analysis by spark source mass spectrometry. We heat treated the pellets to reduce the gas release value to meet the specification of 0.5 cm^3/g. After heat treatment the oxygen-to-metal ratio of the fuel was 1.966 ± 0.012, the gas release was 0.04 ± 0.01 cm^3/g, and the H_2O content was $\sim$5 ppm. These pellets are presently being dimensionally inspected.

Relocation of Alpha Facility (R. A. Bradley and J. D. Sease)

The Fuel Cycle Alpha Facility (FCAF) was constructed to replace the Interim Alpha Facility, Building 3019, which has been operated by the Metals and Ceramics and Chemical Technology Divisions since 1964. A description of the FCAF and the operations to be performed therein was given previously.[13]

All of the glove boxes were moved from the Interim Alpha Facility, Building 3019, to the FCAF and connected to the glove box exhaust system. The utilities (purge gas, furnace gas, cooling H_2O, etc) have been connected to most of the glove boxes. The nuclear safety review has been approved by the Criticality Committee and the Operating Procedures and Hazards Analysis have been approved by the Radioactive Operations Committee. Except for a few pieces of equipment, the lab is now back in full operation.

---

*RDT Standard for Fast Flux Test Facility Driver Fuel Pin Fuel Pellet, October 1970, USAEC-DRDT.

Fuel Pins for the Gulf General Atomic F-1 Experiment in EBR-II

(R. A. Bradley)

In previous months we fabricated eight fuel pins containing $(U,Pu)O_2$ pellets for the GCBR F-1 irradiation experiment in collaboration with Gulf General Atomic.[14] We have been requested to prepare the fuel for five additional pins that will be used in replacement capsules. The fuel requirements will be the same as in the first eight capsules except for the items listed in Table 1.2.

We are presently preparing the sol-gel UO_2-PuO_2 powder for use in pellet fabrication. Five of the required six batches have been blended and dried to shards.

Table 1.1 Fuel Requirements for MINT-1 and MINT-2

Capsule Identification	Pellet Density (% of Theoretical Density)	Pellet Diameter (in.)	End Configuration
MINT-1	89.5 ± 1.0	0.194 ± 0.0005	∿0.002 in dish
MINT-2	92.0 ± 1.0	$0.198 \pm ^{0.0000}_{0.0005}$	flat

Table 1.2 Requirements for GCBR F-1 Replacement Fuel Pins

Number of Pins	Fuel Form[a]	Oxygen-to-Metal Ratio	Smear Density (% of Theoretical)	Pellet Density (% of Theoretical)
1	Annular Pellets	1.96	85.0	99.2
2	Annular Pellets	1.96	85.0	99.2
3	Solid Pellets	1.98	85.0	88.6

[a] All dished both ends

Fission Product Behavior in Oxide Fuels (J. M. Leitnaker)

Fission products in mixed oxides may cause several important effects. One of these is that they may interact directly with the cladding material. A second effect is that these fission products affect the O potential of the fuel and, as a secondary result of this effect, that the O will react with the cladding material. A third effect is that the volume of the fission products may cause the fuel to swell.

We are beginning to investigate these effects. Initially, we are studying the U-Eu-O system, which represents one end of the rare-earth fission products, which themselves represent one-fourth of all fission products and about half of the so-called oxide formers. We intend to base extrapolation calculations of rare-earth fission product behavior in oxide fuel on the results of such studies.

During the past report period essentially all the effort has been on completion and calibration of the new furnace system and spring assembly. The vacuum system was completed and leak checked. The new furnace was installed and the furnace tube plumbed so that samples could hang freely. A controller system was modified so that control at 1000°C is within the limits of our measurement, ±2°C.

The most difficult part of the equipment "shakedown" was calibration of the spring. Enough thermal expansion takes place in the apparatus so that relative changes must be measured. Several points have been fixed on the water jacket which thermostats the spring from which measurements can be made.

A zero point on the water jacket can be read to within a standard deviation of 0.017 mm. Calibration of the spring reveals this deviation corresponds to 0.15 mg. Precision of reading has improved with practice.

Calibration of the system in Ar and He has revealed a difference in buoyancy effect in the two gases. At room temperature this difference is easily determined. At high temperature the determination of a difference is much more difficult. The spring lengthens, relative to the tube, as the temperature of the furnace increases. This difference is referred to as Δ. In Ar the effect is linear with temperature and probably indicates some heat transfer through the system to the spring despite the thermostating of both. Also, the precision is excellent; the average deviation of the Δ points from a straight line is less than 0.01 mm. In He the precision is not nearly so good; we believe this lack of precision arises because of the high heat transfer properties of He relative to Ar.

These data indicate that every point must have corrections arising from both a gas buoyancy effect and from a heat transfer effect. The heat transfer in Ar and the buoyancy effect are nearly the same as in CO_2. Thus, in equilibrating in CO/CO_2 mixtures, only a slight correction need be made for the molecular weight difference of the gases. Hydrogen is similar to He in its thermal conductivity as well as in molecular weight; similar problems may be expected in H_2 as in He.

These calibrations indicate substantial numerical corrections need to be made to the data reported previously.[15] Rather than compute these corrections we will rerun the sample. As noted previously,[15] the measurement was only qualitative because of the temperature uncertainties as well as the lack of calibration. We have started measurements on a sample of $(U,Eu)O_2$ in CO/CO_2 mixtures. We will probably run the sample in H_2 as well, but will then recalibrate the system in He.

Thermal Expansion of Rare Earth Oxide-UO_2 Solid Solutions (L. A. Harris)

The objective of the x-ray studies is to obtain the lattice parameters for a series of mixed oxides of U and Eu as a function of temperature and O pressure. Thus, quantitative data can be secured on which to base the extrapolation of all fission product behavior. The method of investigation involves the use of a high-temperature x-ray diffractometer attachment, and CO/CO_2 gas mixtures.

The work carried out over the past report period involved the examination of solid solution mixtures of UO_2 containing 0, 20, and 40 mole % Eu. In addition, two samples of UO_2 with Ce [$(U_{0.8},Ce_{0.2})O_{2\pm x}$, $(U_{0.6},Ce_{0.4})O_{2\pm x}$] were examined.

An O analyzer has been obtained and placed at the out-flow end of our system. Thus the O content of the gas mixture from the cylinder may be compared with the O content of the gas leaving the high-temperature x-ray diffractometer attachment. In this way any leaks in the system can be observed.

The $(U_{0.8},Ce_{0.2})O_{2\pm x}$ and $(U_{0.6},Ce_{0.4})O_{2\pm x}$ samples were heated in a CO/CO_2 gas mixture of 10/1. The results from these experiments are listed in Table 1.3. A plot of these data shows that the expansion for both samples is linear; however, their slopes differ. Further experiments are planned to check these results. However, one possible explanation may be the fact that CeO_2 is an anion defect fluorite structure whereas UO_2 usually tends to have excess anions; thus, it is conceivable that some of the Ce^{+4} ions are going to Ce^{+3} while some U^{+4} ions go to U^{+5}, the net effect could be a slight increase in the lattice parameters for the Ce-rich solid solution.

The results of the experiments carried out on $(U_{0.8},Eu_{0.2})O_{2\pm x}$ and $(U_{0.6},Eu_{0.4})O_{2\pm x}$ are listed in Table 1.3. A plot of the data for the $(U_{0.6},Eu_{0.4})O_{2\pm x}$ sample heated in several different CO/CO_2 gas mixtures parallel each other with small displacements to larger lattice dimensions associated with the more reducing gas mixtures. These results can possibly be explained on the basis of U^{+5} ions going to U^{+4} as the gas mixtures become more reducing.

It should be noted that the plots of lattice parameters versus temperature for the $(U_{0.6},Eu_{0.4})O_{2\pm x}$ sample (Fig. 1.2) do not appear linear. These findings are in contradiction to data reported previously.[16] Previous data indicated a linear relationship between lattice parameters and temperature. The present data have been corrected for possible sample holder distortion by use of ThO_2 as an internal standard while previous data were not. Further, data illustrated in Fig. 1.2 were on samples which were heated to 1000°C for several hours before obtaining data. The previous method consisted of first taking the diffraction pattern at room temperature and then obtaining data at successively higher temperatures. A kinetic effect may be indicated which will be investigated during the coming report period. Future experiments are to be carried out in which the sample will be held at a given temperature,

Table 1.3 Lattice Parameters for Rare Earth Oxide-UO_2 Solid Solutions

Composition	Temperature (°C)	A_o(A)	CO/CO_2
$(U_{0.8},Ce_{0.2})O_{2\pm x}$	964	5.530	10/1
	760	5.514	
	512	5.494	
	300	5.478	
	Room	5.456	
$(U_{0.6},Ce_{0.4})O_{2\pm x}$	966	5.542	10/1
	766	5.520	
	512	5.493	
	400	5.479	
	Room	5.444	
$(U_{0.8},Eu_{0.2})O_{2\pm x}$	1030	5.502	1/10
	734	5.482	
	516	5.456	
	308	5.442	
	Room	5.427	
$(U_{0.6},Eu_{0.4})O_{2\pm x}$	980	5.480	1/10
	718	5.459	
	504	5.441	
	318	5.430	
	Room	5.412	
$(U_{0.6},Eu_{0.4})O_{2\pm x}$	976	5.478	1/100
	700	5.455	
	500	5.440	
	324	5.429	
	Room	5.412	

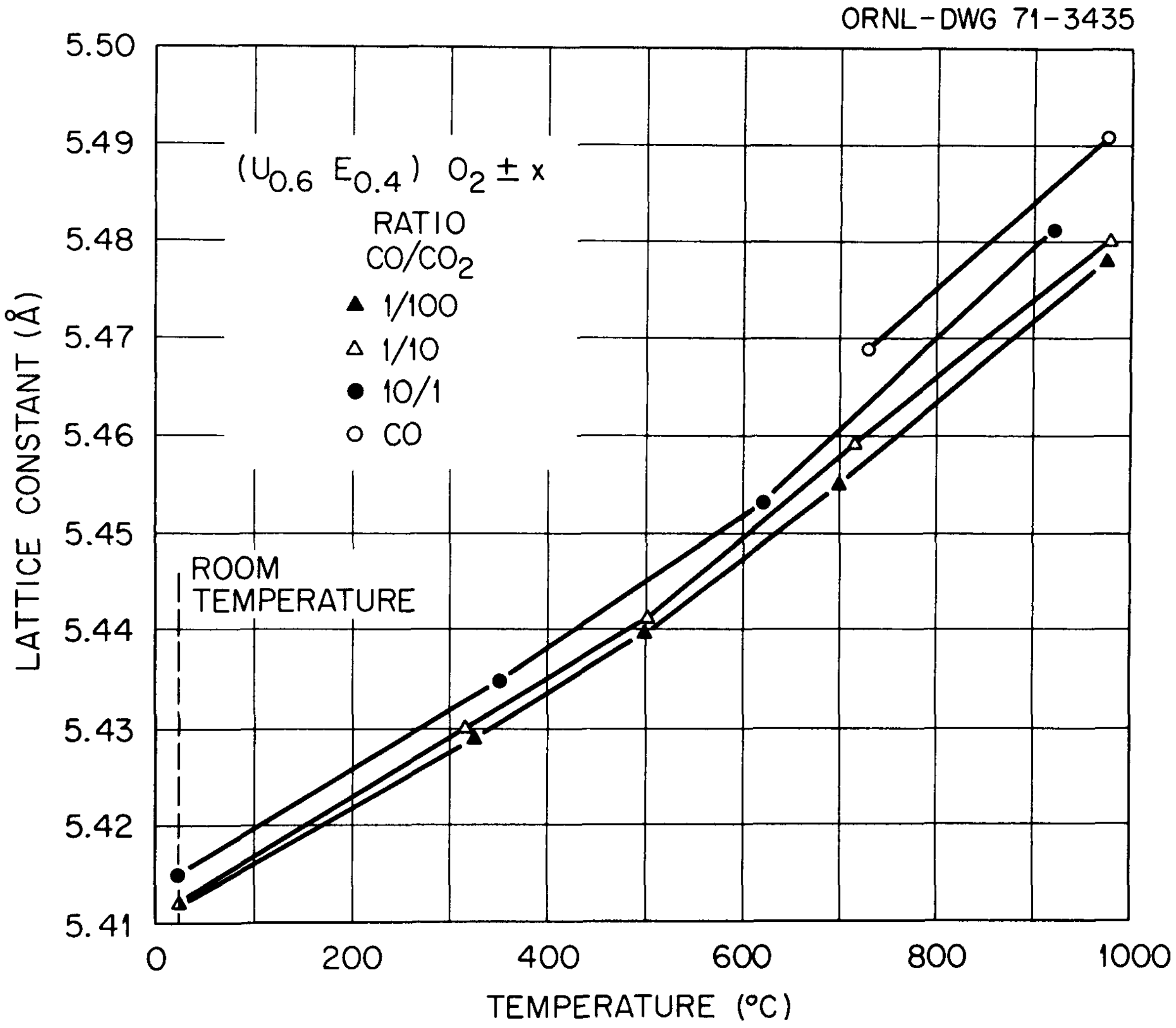

Fig. 1.2. Lattice Parameters of $(U_{0.6},Eu_{0.4})O_{2\pm x}$ as a Function of Temperature and CO-CO_2 Ratio.

while the CO/CO_2 gas mixture is varied in order to determine how real are the variations of lattice parameters with O pressure.

Additional experiments were performed with UO_2; however, the results of these experiments were inconclusive and require further work.

It is important to note that these results indicate that a simple linear expansion cannot be used for $(U,Pu)O_2$ fuel, but that it varies nonlinearly with temperature as fission products build up. The magnitude of this nonlinearity has not yet been ascertained.

Irradiation Testing of $(U,Pu)O_2$ Fuels

C. M. Cox T. N. Washburn

The performance characteristics of mixed $(U,Pu)O_2$ fuels are being evaluated in a variety of irradiation tests for potential application in an LMFBR. We are now concentrating on comparative tests of fuel fabricated as pellets or as microspheres loaded by the Sphere-Pac technique. The program includes thermal-flux experiments, which permit use of instrumented capsules and continuously controlled heat rates, and fast flux experiments, in which the fission rate distribution and radiation effects on the cladding are more typical of those for operating conditions anticipated in an LMFBR.

Fast Flux Irradiation Tests (A. R. Olsen, J. L Miller, Jr. and D. R. Cuneo)

The fast flux irradiation tests in the EBR-II are designed to approximate conditions to be encountered in a commercial-scale LMFBR. The objective of these tests is to establish the effects of fuel fabrication form (Sphere-Pac or pellet), void distribution, and stoichiometry on the swelling of the fuel, mechanical and chemical interactions of fuel and cladding, release of fission gas, and distribution of fission products in a $(U,Pu)O_2$ fuel operating at typical heat rates to design levels of burnup.

The five Series I encapsulated tests all contain Sphere-Pac fuels. Two of the capsules, S-1-A and S-1-E, were returned to ORNL after the initial period of irradiation in subassembly X050 which was discharged from the EBR-II at the end of run 42 on May 18, 1970. The other three capsules are scheduled for continued irradiation in subassembly X119.

As reported previously[17,18] only the pin from capsule S-1-E was scheduled for destructive examination. The pin from S-1-A was being held for a transient test. However, because of the current concern about fuel-cladding chemical interactions and particularly the effect of fuel density on these reactions, the pin from S-1-A will now be destructively examined also. Since the calculated peak cladding inner surface temperature for this type 304 stainless steel-clad pin is 570°C and such reactions have been reported for temperature in excess of ∿520°C, this pin is of particular interest. The examination of pin S-1-A is scheduled to start next report period.

To date, ten sections have been removed from various axial locations along the fuel column of pin S-1-E. The calculated operating conditions for these sections are given in Table 1.4. Composite transverse macrophotographs of Sections A and B from the bottom and center of the feed column were published in the previous report of this series.[17] Section D from the top of the fuel column was taken in an area shown to be of lower density than the rest of the fuel bed.[18] As can be seen in Fig. 1.3, there were no fine microspheres in this region. The absence of such fine microspheres would reduce the bed density to 62 to 67% of theoretical.[19] The calculated inner cladding surface temperature at this location is 570°C. No significant fuel-cladding chemical interaction was observed in this low density region even at this temperature. The region of Section D with the greatest degree of metallographically observed reaction is shown in Fig. 1.4 along with a similar section from the fuel-cladding interface region from Section B at the peak fission rate region of the fuel. In both cases there was no observed intergranular penetration of the cladding.

Section K, adjacent to Section D, was prepared for microprobe analysis by polishing in a nonaqueous medium. Although the microprobe analyses are incomplete, some preliminary observations are available. There was a distinct accumulation of Cs on the inner surface of the cladding, in the fuel cracks, and occasionally in localized spots on

Table 1.4 Calculated Operating Conditions for Sections Removed from Series I Pin S-1-E

Section Identification	Purpose for Removing Section	Heat Rate[a] (kW/ft)	Surface Cladding Temperature Inner (°C)	Outer (°C)
A	Transverse Metallography	11.1	490	451
B	Transverse Metallography	13.5	550	510
C	Burnup Analysis	13.4	555	510
D	Transverse Metallography	10.3	570	530
E	Longitudinal Metallography	10.2	570	540
F	Longitudinal Metallography	Insulator	470	470
G	Transverse Metallography	13.3	560	510
H	Burnup Analysis	10.6	570	530
J	Microprobe Analysis	13.3	560	510
K	Microprobe Analysis	10.3	570	530

[a] Heat rate calculated from EBR-II fission rates for localized section.

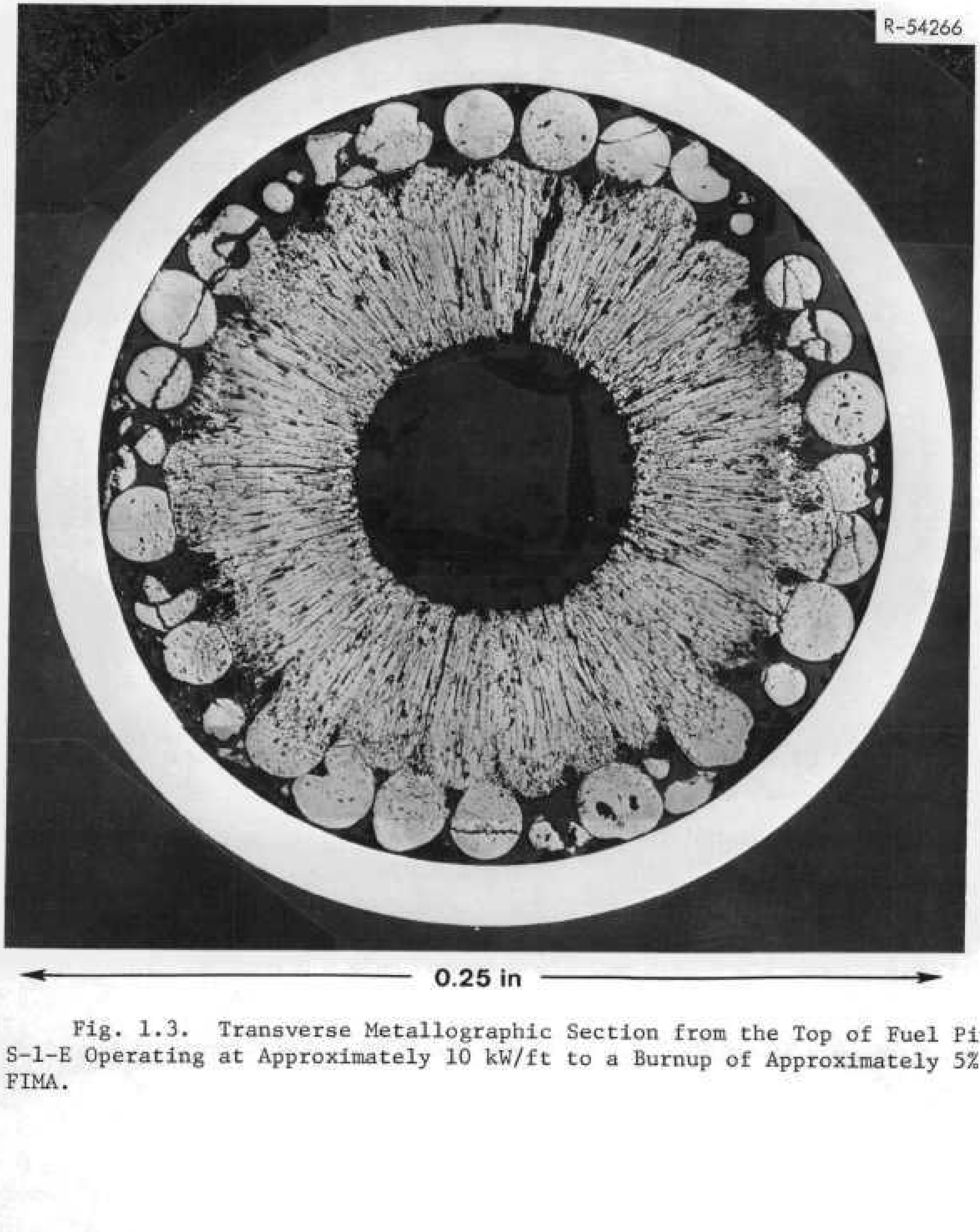

Fig. 1.3. Transverse Metallographic Section from the Top of Fuel Pin S-1-E Operating at Approximately 10 kW/ft to a Burnup of Approximately 5% FIMA.

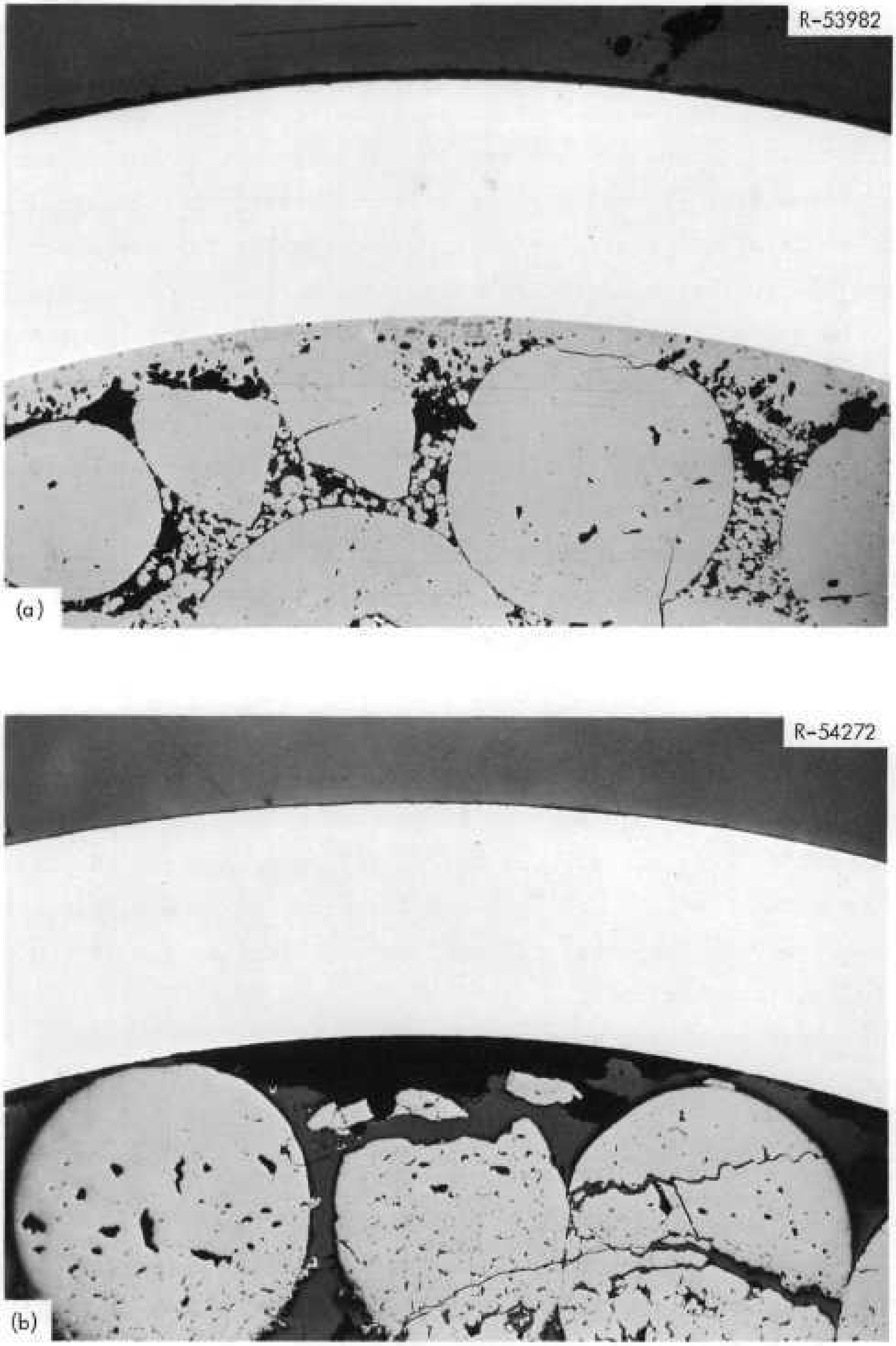

Fig. 1.4. (U,Pu)O_2 Fuel-Cladding Interfaces From two Sections of EBR-II, Series I Pin S-1-E. (a) Peak heat rate region with 316 stainless steel cladding inner surface temperature of 550°C and (b) top of fuel with cladding inner surface temperature of 570°C.

the central void surface. There was no indication of Cs or other fission product intergranular penetration into the cladding. This is further evidence that there was no significant fuel-cladding chemical interaction even in this low density fuel region, in agreement with our previous observations from thermal flux irradiation tests;[20] but contradicts a recent suggestion[21] that low-density, particulate fuels are more susceptible to fuel-cladding chemical interactions.

The Series II unencapsulated pin tests were described previously.[22] These tests will be irradiated in subassembly X112 together with similar fuel pins fabricated by the Babcock and Wilcox Company. The ORNL pins were shipped to the EBR-II site in December. Nineteen of the ORNL pins for Series II have been examined by the EBR-II Project and approved for inclusion in subassembly X112. A total of 20 pins was shipped to Idaho, but one, OP-4, was found to have a small localized area with lack of required penetration in one of the closure welds. Thus the spare pin OS-13 will be placed in subassembly X112, position 22. Since both pins were originally scheduled for burnup of 5% FIMA, the substitution only changes the order of irradiation and not the total plan. Pin OP-4 was returned to ORNL and we will attempt to salvage it using the existing weld repair procedure. Babcock and Wilcox shipped their 18 pins to Idaho on January 18, 1971. On March 23 we were informed that all pins on hand have been inspected and approved and fabrication of the subassembly will be initiated in April.

We have completed revisions to the Series II data package following review by the EBR-II Project. These revisions have been sent to the experiment manager at EBR-II and have been incorporated in the data package which is being reviewed for publication.

Because of other higher priority tests, subassembly X119 will not be inserted into the reactor before run 49. The availability of space for the start of the irradiation of the Series II subassembly X112 cannot be determined at this time.

Fuel Cladding Compatibility Under Prototypic Fast Flux Irradiation Conditions (C. M. Cox)

We have completed conceptual design of a third EBR-II test series based on the nominal test matrix shown in Table 1.5. This test is designed to take advantage of the higher flux levels available following the recent EBR-II power increase to 62.5 MW. The fuel pins will be $(U_{0.75},Pu_{0.25})O_{2-x}$ using natural U so that the fission yields will be typical of those obtained under fast reactor conditions, as opposed to all high heat rate $(U,Pu)O_2$ pins previously irradiated in EBR-II. This will allow us to examine fuel-cladding chemical interactions with the higher O potentials expected from Pu as opposed to U fission products and thus run a more conservative test than has been done heretofore. The basic feasibility of the experiment was established by preliminary discussions[23] with the EBR-II Project, and a request for Approval-in-Principle was submitted to RDT.

Uninstrumented Thermal Flux Irradiation Tests (A. R. Olsen and D. R. Cuneo)

A series of uninstrumented capsules is being irradiated in the X-basket facilities of the ETR. Each capsule contains four test pins arranged in tandem. The initial objective of these tests was to investigate at extended burnup the effects of fabrication form on release of fission gas, migration of fission products, and swelling of the fuel. The capsules now being irradiated are to provide short-cooled irradiated fuel for LMFBR reprocessing studies. The current status of these tests is given in Table 1.6.

Capsules 43-113 and 43-117 completed their scheduled irradiation during the past report period. Neutron radiographs are being obtained at the TREAT facilities before the capsules are returned to ORNL.

Instrumented Tests in the ETR (T. N. Washburn and R. A. Buhl)

The ETR instrumented tests are designed to determine the performance of mixed oxide fuel under simulated LMFBR design operating conditions.

The first two capsules (43-120 and 43-121) are being irradiated to investigate fuel swelling and fuel-cladding chemical interactions of

Table 1.5

EBR-II Series III $(^{238}U_{0.75}, Pu_{0.25})O_2$ Fuel Pins

Nominal Test Matrix

Fuel Form[a]	Burnup Level 1 Smear Density (%)	Burnup Level 1 Peak Clad Temp (°C)	Burnup Level 1 O/M	Burnup Level 2 Smear Density (%)	Burnup Level 2 Peak Clad Temp (°C)	Burnup Level 2 O/M
P	80	650	1.93	80	600	1.93
P	80	650	1.98	80	600	1.98
P	90	650	1.93	90	600	1.93
P	90	650	1.98	90	600	1.98
P	80	600	1.93			
P	80	600	1.98			
P	80	650	1.93			
P	80	650	1.98			
P	90	600	1.93			
P	90	600	1.98			
P	90	650	1.93			
P	90	650	1.98			
AP	85	650	1.98	85	650	1.93
S	85	650	1.98	85	650	1.93
P	85	650	1.98	85	650	1.93
AP	85	650	1.93			
S	85	650	1.93			
AP	85	650	1.98			
S	85	650	1.98			

[a] P = solid pellets; AP = annular pellets; S = Sphere-Pac.

Table 1.6 Noninstrumented Thermal Flux Tests of $(U,Pu)O_2$ Fuels

Experiment Number	Fuel		Number of Rods	Peak Burnup (% FIMA)[a]	Peak Linear Heat Rate (W/cm)	Peak Cladding Inner Surface Temperature (°C)	Status March 1971
	Form	Composition					
43-99	Sphere-Pac	$(^{235}U_{0.80},Pu_{0.20})O_{2.00}$	2	1.5[b]	1640[b]	1000	Examined
43-100	Sphere-Pac	$(^{235}U_{0.80},Pu_{0.20})O_{2.00}$	2	1.4[b]	1470[b]	900	Examined
43-103	Sphere-Pac Pellet	$UO_{2.02}(20\%\ ^{235}U)$ $UO_{2.00}(20\%\ ^{235}U)$	3 1	5	690	530	Examined
43-112	Sphere-Pac	$(^{238}U_{0.85},Pu_{0.15})O_{1.97}$ $UO_{2.02}(20\%\ ^{235}U)$	3 1	0.7	500	360	Examined
43-113	Sphere-Pac	$(^{238}U_{0.85},Pu_{0.15})O_{1.97}$ $UO_{2.02}(20\%\ ^{235}U)$	3 1	10[c]	500[c]	380[c]	Being examined
43-115	Sphere-Pac	$(^{238}U_{0.85},Pu_{0.15})O_{1.97}$ $UO_{2.02}(20\%\ ^{235}U)$	3 1	6.5	600	460	Examined
43-116	Sphere-Pac	$(^{238}U_{0.85},Pu_{0.15})O_{1.97}$	4	1.5[c]	600[c]	460[c]	Processed
43-117	FTR Pellets	$(^{238}U_{0.75},Pu_{0.25})O_{1.98}$	4	1.5[c]	430[c]	360[c]	Being examined
43-118	FTR Pellets	$(^{238}U_{0.75},Pu_{0.25})O_{1.98}$	4	4.0[c]	430[c]	360[c]	In-reactor
43-119	FTR Pellets	$(^{238}U_{0.75},Pu_{0.25})O_{1.98}$	4	8.0[c]	430[c]	360[c]	In-reactor
43-123	FTR Pellets	$(^{238}U_{0.75},Pu_{0.25})O_{1.98}$	4	4.0	350[c]	310[c]	In preparation

[a] FIMA is fissions per initial actinide metal atom

[b] Rods failed in reactor from overpowering

[c] These are target design values

Sphere-Pac and pellet $(U,Pu)O_2$ fuels. These capsules have been irradiated for ∿179 EFPD to a peak burnup of ∿3.6% FIMA (as of March 14, 1971). Each capsule contains four fuel pins with two thermocouples at the axial midplane of each fuel pin. The peak cladding inside surface temperature is 540°C with the reactor at 175 MW.

All temperature data received from ETR have been keypunched, and the data are presently being plotted as described in previous reports.

Burnup and depletion analyses have been initiated to determine the precise time in which a step in flux will be required. The only step available due to restrictions involved with the Pb tube will be from a flux of 0.9×10 neutrons cm^{-2} sec^{-1} to 1.3×10^{14} neutrons cm^{-2} sec^{-1} which represents a 44.5% increase in power.

The second set of tests on this series will consist of three instrumented capsules, each designed to measure fission gas pressure during testing and each containing one fuel pin with a 20-in.-long column of fuel. One capsule will contain FTR type pellets of the highest permissible density (94% of theoretical), the second will contain FTR pellets of the lowest permissible density (88% of theoretical), and the third will contain a packed bed of Sphere-Pac U-Fines fuel. In the latter fuel, all the Pu is contained in the coarse fraction (∿400-μm diam) microspheres of composition $(U_{0.73},Pu_{0.27})O_2$, and a fine fraction (<44-μm diam) of depleted UO_2 is infiltrated into the coarse bed.

The FTR pellets are presented en route from WADCO. After receiving the pellets they will be subjected to a complete characterization.

Tests of Thermal Performance (R. B. Fitts)

These irradiation tests are designed[24] to monitor the thermal performance of fuel pins as they operate in the Oak Ridge Research Reactor Poolside Facility. The temperature of the fuel pin cladding and fuel center and the rates of heat generation are continuously recorded. These data are used to evaluate the thermal characteristics of the fuel and fuel pins and the effects of irradiation conditions upon the temperatures and structural changes within the operating fuels.

Data from the third capsule in this series, capsule SG-3,[25,26] wherein Sphere-Pac[27] and pellet[26] fuel forms were compared, have indicated[28] a higher gap conductance and better thermal performance for the Sphere-Pac than for the pellet fuel. The difference between the fuels was small and therefore statistical analysis of the data is being implemented to assess the significance of these measured differences.

Tests of Mechanical Interaction of Fuel and Cladding (R. B. Fitts, R. L. Senn,* and R. A. Bradley)

The intent of our program is to measure in-reactor the axial extension of both the fuel column and cladding and also the fuel pin internal gas pressure during operation of prototypic LMFBR fuel pins under carefully controlled conditions. These include programmed power cycles and an occasional overpower cycle. The irradiation capsules are designed so that the fuel pin operates in the ORR Poolside irradiation facility at LMFBR prototypic power and temperature conditions. The irradiation tests will last one to two years and will give burnup levels of 5 to 9%.

As described previously,[29] the first in-reactor power cycling capsule (MINT-1) will contain a prototype Fast Test Reactor (FTR) fuel pin. All of the parts of the fuel pin and capsule have been procured and assembly is in progress.

The MINT-1 transducer instrumentation[30] (two position transducers and one pressure transducer) in the in-test calibration device has been bench tested and the instruments calibrated. The final bench test assembly incorporated equipment for programmed activation of the electromagnet which lifts the measuring train for operation of the calibration system. This programmed operation will minimize the impact loading on the system which resulted from simple on-off operation of the electromagnet and which had caused the premature failure of the calibration system in earlier tests.

The thermocouples which will measure the temperature in the NaK annulus surrounding the fuel pin cladding have been successfully brazed[30] to the inside of the primary containment wall of the capsule.

---

*Reactor Division

The fuel pin has been loaded with fuel and sealed.[31] It is now ready for final assembly into the capsule.

The fuel for the MINT-1 capsule was obtained from Hanford Engineering Development Laboratory and has been examined for characterization purposes by metallography and electron microscopy. The metallography samples revealed two second-phase structures in the fuel. The most massive form of second-phase had a metallic appearance immediately after polishing but turned gray on exposure to the air and the other was simply a "gray phase" more uniformly distributed in the fuel.

Electron microprobe analysis of the large, metallic inclusions showed that they contained a high concentration of Fe. In addition, small areas of high Fe concentration (not gray) were located in other regions of the pellet. Such inclusions may result from Fe pickup during fuel fabrication. Chemical analysis of a whole pellet by wet chemistry, mass spectroscopy, and emission spectroscopy shows that the total Fe content of the fuel is <200 ppm.

Electron microprobe analysis of the smaller "gray phase" shows that these are associated with areas of high Pu concentration although all areas of high Pu concentration are not gray. Rounded structured areas of high Pu concentration are seen throughout the fuel pellet. These Pu concentrations are to be expected in mechanically blended fuel.

These second-phase concentrations are not considered serious enough to cause difficulty in the fuel or fuel pin during the MINT-1 test.

Analysis of Fuel Element Performance

C. M. Cox

The objectives of this work are a fundamental understanding the behavior of LMFBR fuel elements and the development of analytical models to describe their performance and probability of their failure under various operating conditions. Special emphasis is given to modeling fuel-cladding mechanical interactions and to characterizing irradiated $(U,Pu)O_2$ fuels. This work is an integral part of the irradiation testing program, providing design methods and evaluation of the tests.

Comparison of Predicted and Actual Fuel Pin Performance (F. J. Homan)

To examine the usefulness of the FMØDEL fuel performance code in predicting the irradiation behavior of $(U,Pu)O_2$ LMFBR fuel pins, we have compared the performance calculated by FMØDEL with performance measured in-test and by postirradiation examination.[32] Comparisons were made in three areas (1) cladding diametral expansion, (2) fuel radial porosity distributions, and (3) diameters of central void, columnar, and equiaxed grain regions.

For comparisons between the predicted and measured cladding diametral expansions, central void diameters, and diameters of the columnar and equiaxed grain regions, pins from the General Electric F2 series of irradiation experiments in EBR-II (Ref. 33) were used. The radial porosity distribution comparison was made on a low burnup pin irradiated in the ETR.[34]

Overall agreement between predicted and measured fuel pin behavior is acceptable. A summary of the diametral expansion comparisons is shown in Fig. 1.5. Each point plotted represents one axial position on the pin specified. A summary of the fuel restructuring comparisons is shown in Fig. 1.6. The comparisons shown here represent pins ranging in fuel density from 83.8 to 98.2% of theoretical, and peak linear heat rates ranging from 9.7 to 17.4 kW/ft. Agreement between the calculated and predicted fuel radial porosity distributions is shown in Fig. 1.7. It appears that the predicted distribution agrees well with the data, except at the center of the pin where restructuring is underpredicted.

Sensitivity of Fuel Temperatures to Porosity Distribution (W. J. Lackey and F. J. Homan)

Recently we reported measurements of the variation in percent porosity with radial position for an irradiated fuel pin.[35] Knowledge of the radial porosity distribution is necessary in order to calculate fuel temperatures, creep rate, and other fuel properties. Below,

ORNL-DWG 71-3349

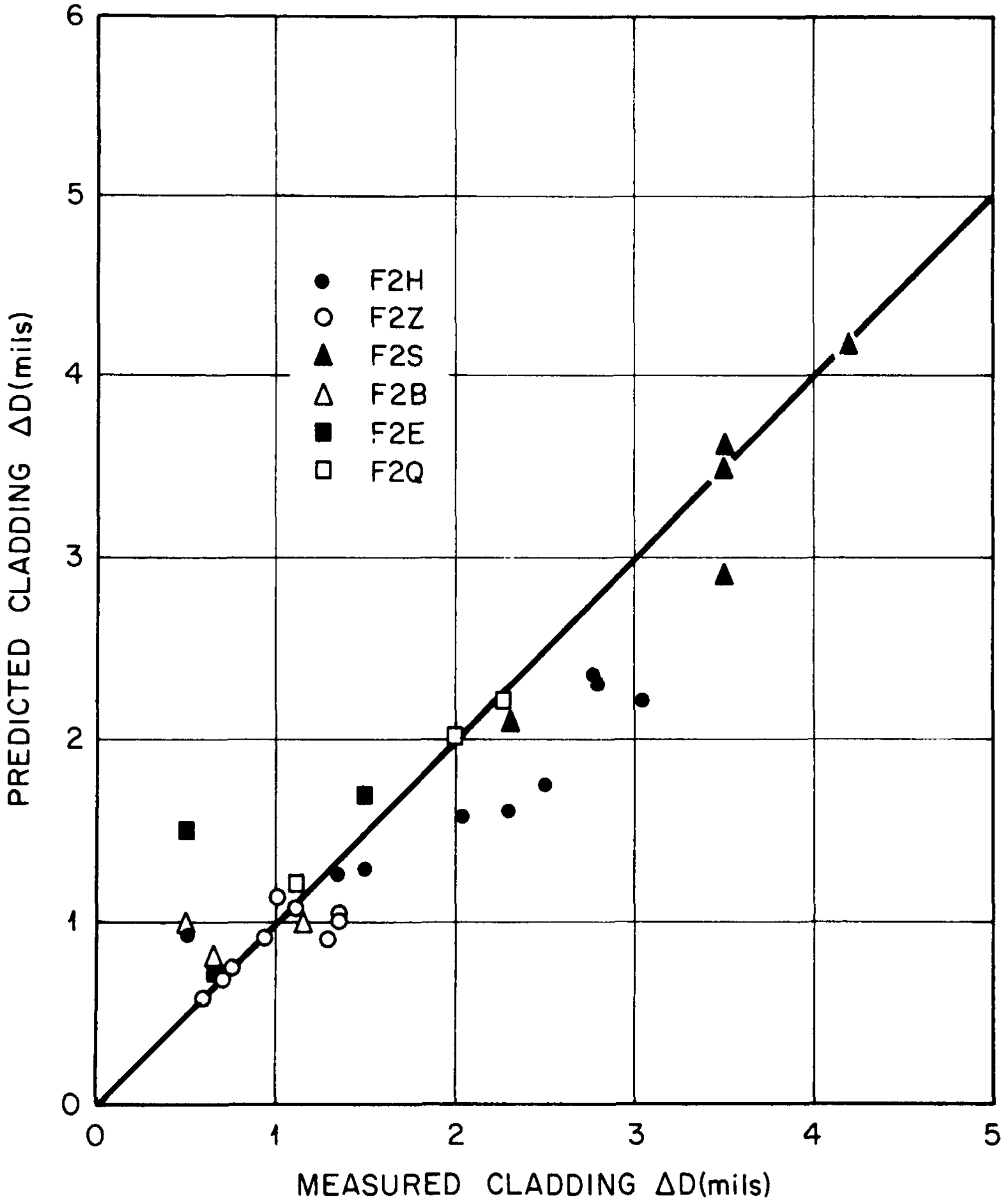

Fig. 1.5. Summary of Comparison Between Predicted and Measured Cladding Diametral Expansions.

ORNL-DWG 71-3034

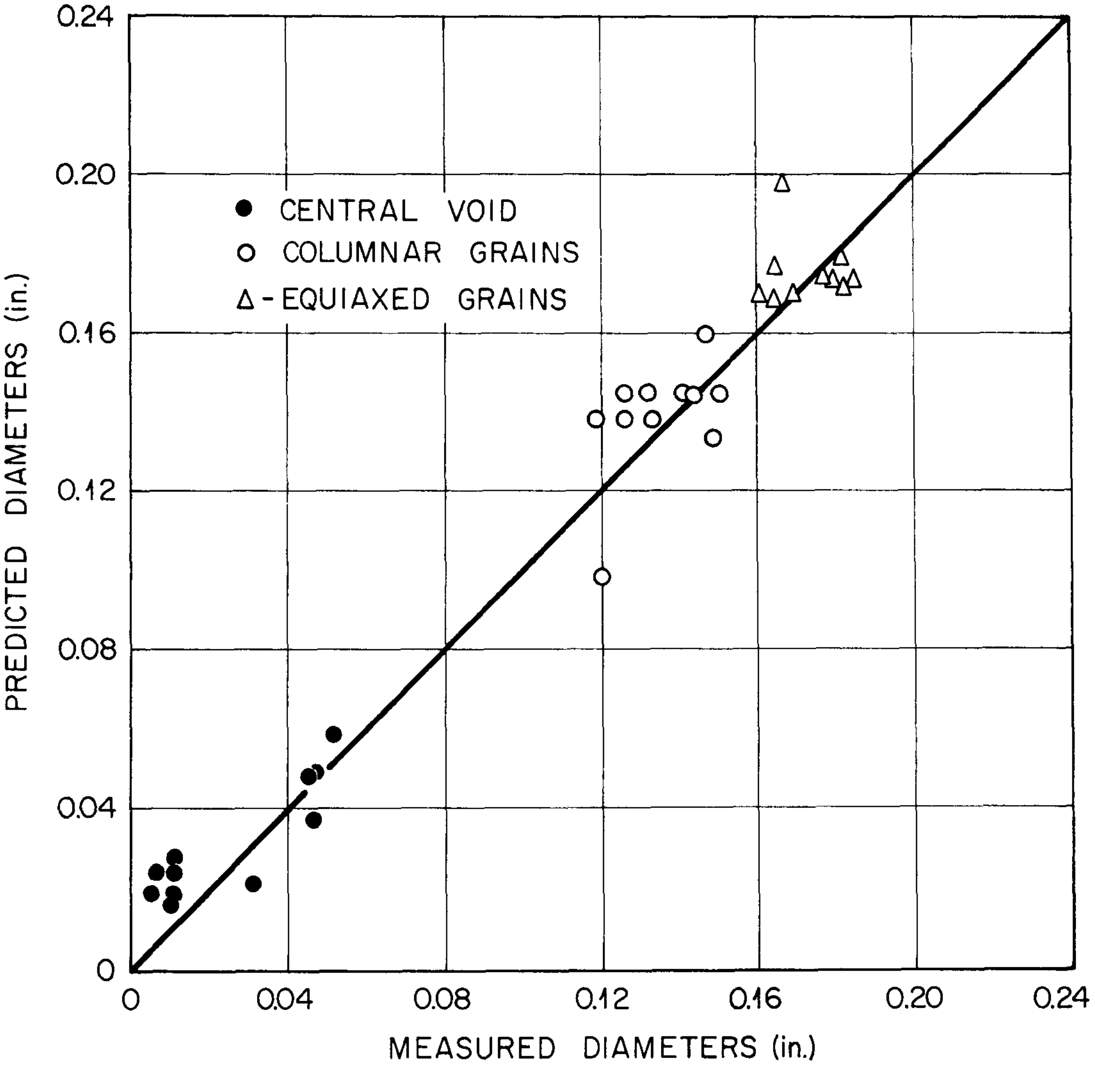

Fig. 1.6. Summary of Comparisons Between Predicted Diameters for Central Void, Columnar and Equiaxed Grain Regions.

ORNL-DWG 71-914

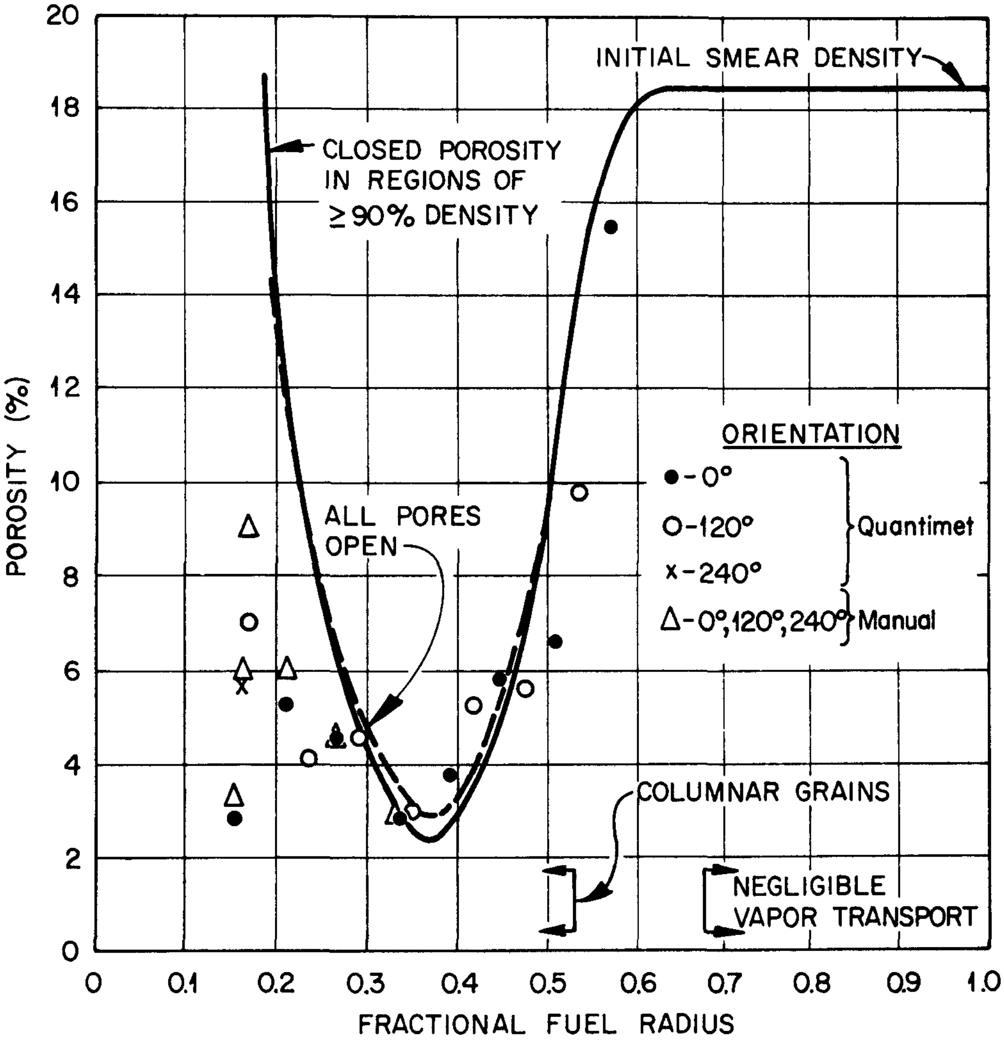

Fig. 1.7. Comparison of the Calculated and Measured Radial Variation in Porosity for $(U_{0.85},Pu_{0.15})O_2$ Irradiated at 13.6 kW/ft to 0.7% FIMA.

we have examined the sensitivity of fuel temperatures to the radial porosity distribution. Since a current LMFBR design criterion is that there be only a small probability that central fuel temperatures reach the melting point, it is extremely important to be able to reliably predict fuel temperatures.

In order to determine the sensitivity of fuel temperatures to the shape of the radial porosity distribution, temperatures have been calculated for the continuous and three-zone step function porosity distributions shown in Fig. 1.8. The parabolic region of the continuous porosity distribution is a least-squares fit to experimentally measured porosity values for a transverse section (43-112-3C) of a $(U_{0.85},Pu_{0.15})O_{2.00}$ Sphere-Pac fuel pin.[35] This pin was irradiated in the ETR at a linear heat rate of 13.6 kW/ft to a burnup of 0.7% FIMA. The three-zone step function porosity distribution is more or less arbitrary with the restriction that the total amount of porosity in each zone be the same for both the continuous and step function distributions.

Temperatures calculated using versions of the PRØFIL (Ref. 36) code appropriately modified to accept the specified porosity distributions are plotted in Fig. 1.8. For all practical purposes the two temperature profiles are identical, the maximum difference being 18°C.

These results should not be interpreted as evidence that a model for predicting porosity distributions in fuel pins is not needed since, in general, one does not know the porosity distribution and thus cannot construct a sufficiently accurate three-zone step function. It should also be recognized that even though the three-zone step function appears adequate for predicting temperature profiles for those cases where the porosity distribution is known, it may not be possible to accurately predict other aspects of fuel behavior which are dependent on porosity; e.g., creep, by using a three-zone model.

To demonstrate that generally it is not possible to construct a sufficiently accurate three-zone step function without some prior knowledge of the actual porosity distribution, we have calculated the temperature profile for the fuel pin discussed above using our best estimate of the porosity distribution prior to experimental

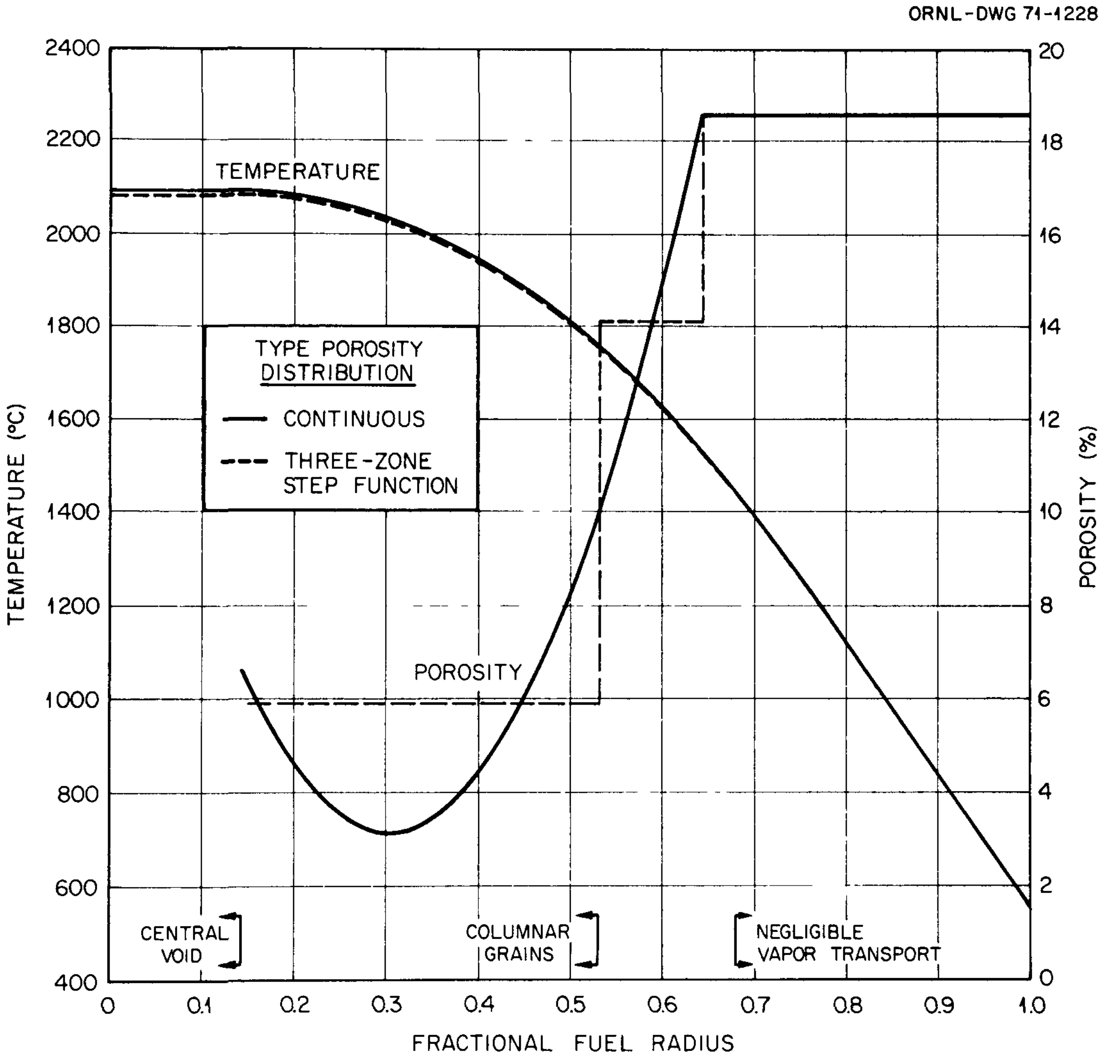

Fig. 1.8. Similarity of Fuel Temperatures Calculated From a Continuous and Three-Zone Step Function Porosity Distribution.

determination of the porosity. This model assumes that the portion of the fuel which is hotter than 1750°C restructures to a density of 97% of theoretical, between 1450 and 1750°C the fuel is 92% dense, and below 1450°C no densification occurs. Temperatures calculated with the PR0FIL code using these assumed porosities are compared in Fig. 1.9 with the previously discussed temperature profile calculated from the continuous porosity distribution. For the high temperature region there is a significant difference (200°C) in the calculated temperatures which demonstrates the necessity of accurate knowledge of the porosity distribution.

Microscopy of $(U,Pu)O_2$ Fuels (W. J. Lackey)

In-reactor grain growth of $(U,Pu)O_2$ is being studied because of its potential influence on fuel creep, fission gas release, and swelling which, in turn, are expected to influence fuel pin performance. Previously we reported[37] the variation in grain size with radial position for two Sphere-Pac $(U_{0.85},Pu_{0.15})O_2$ fuel pins irradiated in the ETR to burnups of 0.5 and 0.7% FIMA. We now report similar measurements for the Sphere-Pac pin shown in Fig. 1.10, which contained fuel from the same batch as the previous two pins, which was irradiated to a burnup of 4.2% FIMA.

Grain size for the unrestructured region of the higher burnup fuel pin (43-115-4B) is plotted as a function of radial position in Fig. 1.11. Previous data for one of the low burnup pins which operated at practically the same linear heat rating are shown for comparison. For any given radius and at the region of transition from equiaxed to columnar grains, the equiaxed grains are larger in the high burnup pin. We had previously considered the possibility that a stable or limiting grain size for any given temperature would be reached early in life, but this is clearly not true. In a similar manner to that previously used for the low burnup pin,[37] we will calculate the temperature profile and fit the data for the higher burnup pin to an equation which relates grain size to time and temperature. Such an analysis should lead to an expression which can be used to reliably predict grain size as a function of irradiation time and temperature.

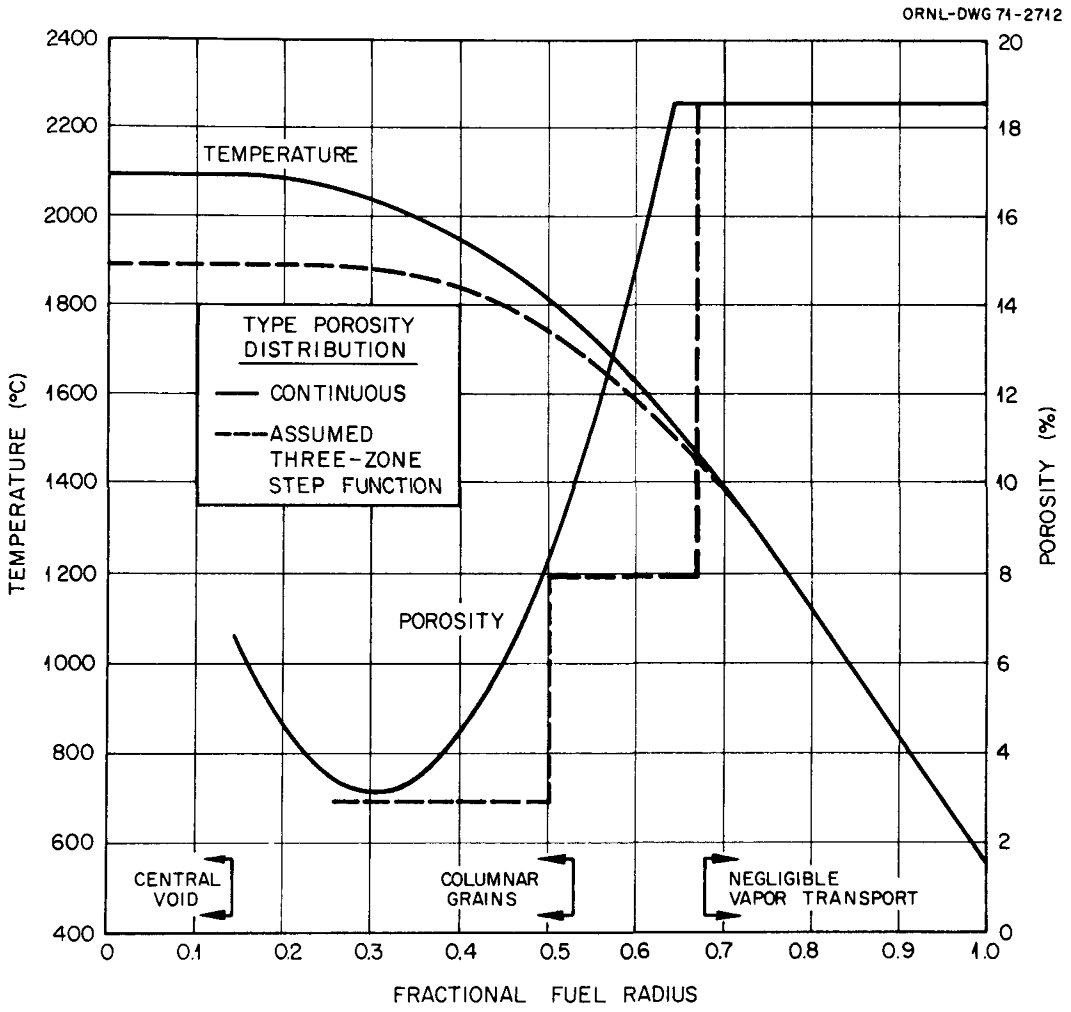

Fig. 1.9. Difference in Fuel Temperatures Calculated From a Continuous and Assumed Three-Zone Step Function.

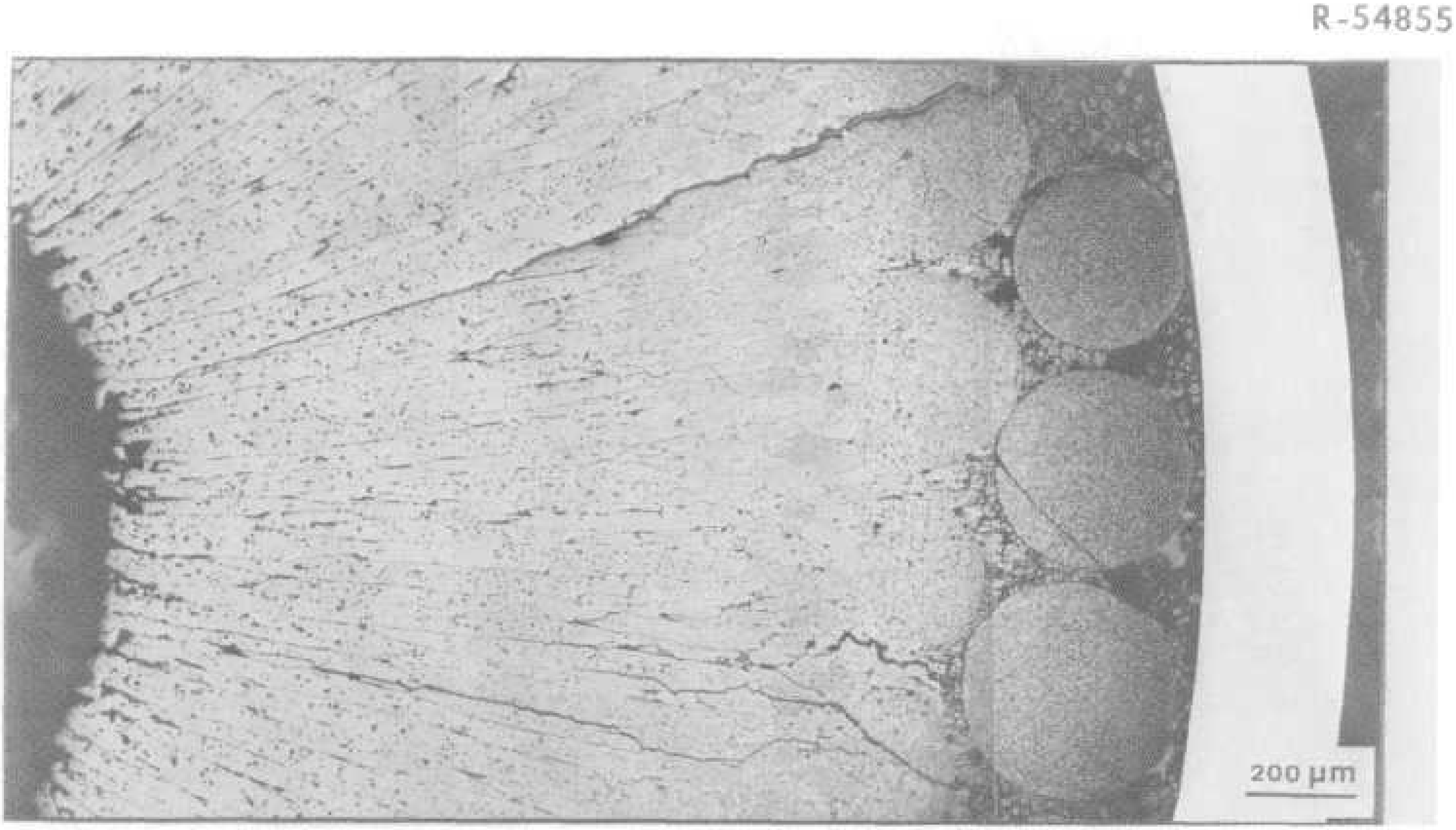

Fig. 1.10. $(U_{0.85},Pu_{0.15})O_{2.00}$ Fuel Pin (43-115-4B) After Irradiation at a Linear Heat Rate of 14.0 kW/ft to a Burnup of 4.2% FIMA. Etched with cerium nitrate-bearing fuel etchant.

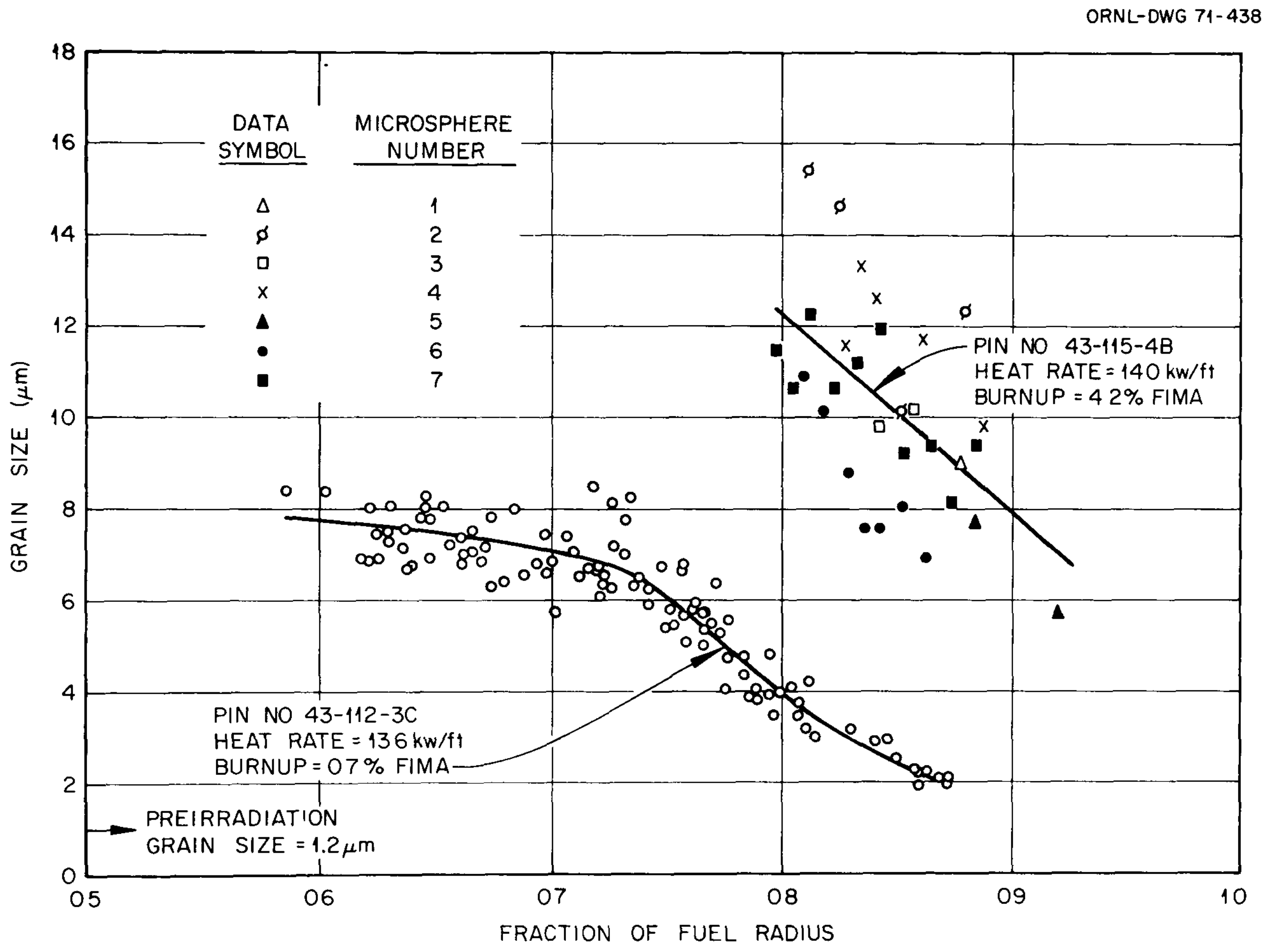

Fig. 1.11. Comparison of In-Reactor Equiaxed Grain Growth for two $(U_{0.85},Pu_{0.15})O_2$ Fuel Pins Which Operated at a Linear Heat Rate of about 14 kW/ft to Burnups of 0.7 and 4.2% FIMA.

An interesting and likely important outgrowth of this study was the observation that within the equiaxed grain region of the higher burnup pin there were subgrains on the order of 1 to 3 μm in size. Subgrains have been observed in the columnar grain region of $(U,Pu)O_2$ by Michels and Latimer[38] and recently by us and in equiaxed grains of irradiated UO_2 (Ref. 39) and $(U,Pu)O_2$ (Ref. 40). In the current study the subgrains were generally hexagonal and as shown in Fig. 1.12 were observable in high magnification light micrographs because the subgrain boundaries were decorated with either inclusions or voids. The possibility exists that the subgrain boundaries will influence fuel creep, fission gas release, and swelling in a similar manner to that expected for normal grain boundaries. That is, Nabarro-Herring creep may depend on the subgrain size and subgrain boundaries may interact with fission gas bubbles thus influencing gas release and fuel swelling.

In conjunction with the in-reactor grain growth study, we are measuring the out-of-reactor grain growth occurring in archive fuel subjected to a series of statistically designed time-temperature treatments. All of the thermal treatments have been completed and the resulting specimens have been metallographically polished and replicated. The replicas are being examined by electron microscopy primarily for the purpose of accurately measuring grain size. Optical microscopy of the out-of-reactor grain growth specimens which were subjected to the most severe thermal treatments (1550°C for 9 and 45 hr) showed, in addition to grain growth, extensive agglomeration of porosity; i.e, the number of pores decreased and the pore size increased. Although no quantitative measurements have been made, it appears that the density of the microspheres actually decreased during the 1550°C treatments. Decreases in density are unusual, but have been observed for UO_2 (Ref. 41), ThO_2 (Ref. 42), and $(U,Pu)O_2$ (Ref. 43) isothermally annealed out-of-reactor and perhaps during irradiation of $(U,Pu)O_2$ (Ref. 44). Thus, this mechanism of swelling may be a contributing factor to fuel swelling in the unrestructured region of ceramic fuel pins.

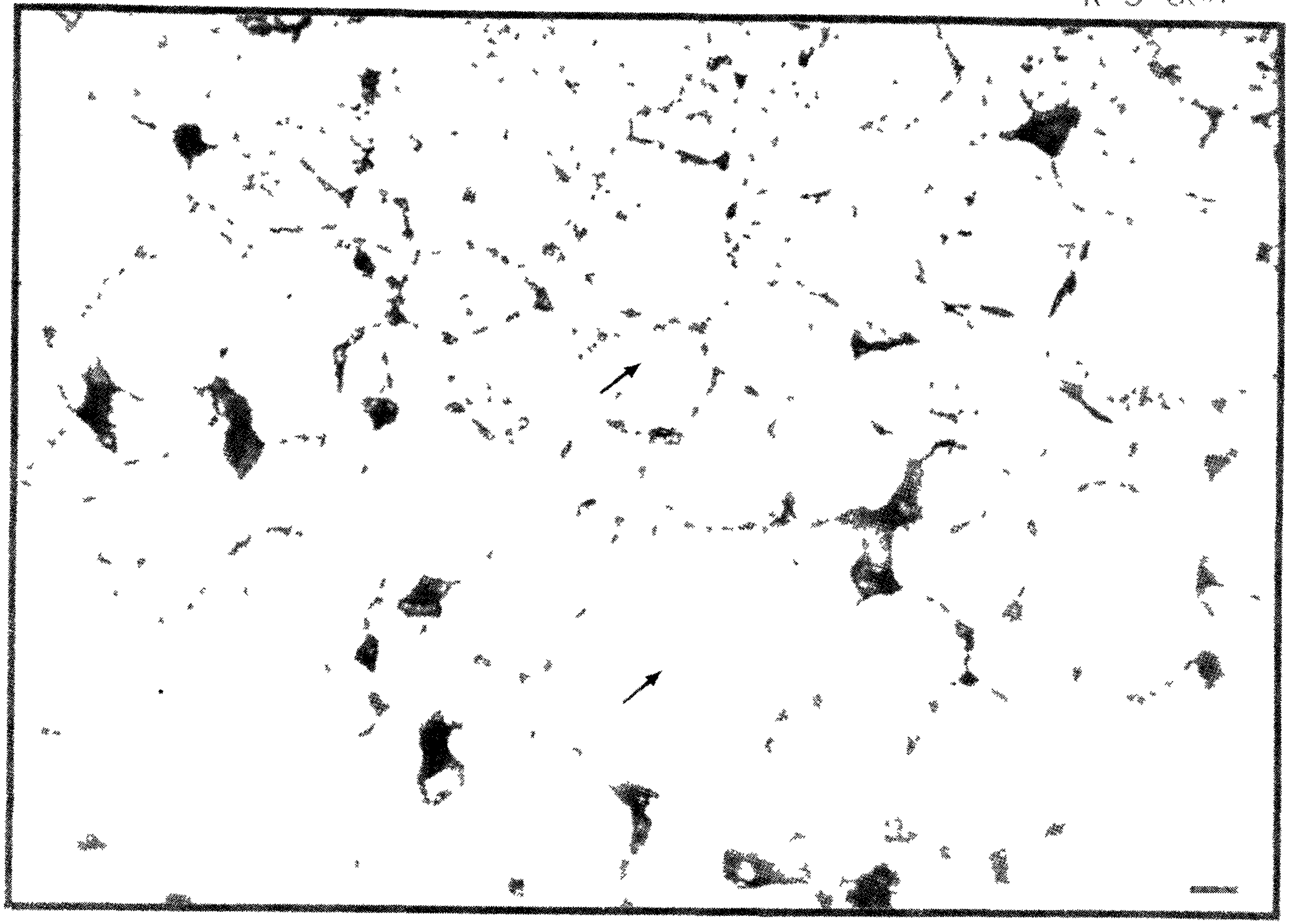

R-54300

Fig. 1.12. Subgrains Within Equiaxed $(U_{0.85},Pu_{0.15})O_{2.00}$ Grains.

Electron Microprobe Analysis of Irradiated (U,Pu)O_2 (J. L Miller, Jr. W. J. Lackey)

Electron microprobe analysis has been used to study the distribution of Pu and U and to identify a gray phase in a transverse section of a Sphere-Pac ($U_{0.85}$,$Pu_{0.15}$)$O_{2.00}$ fuel pin (43-112-3C)[45-47] irradiated in the ETR at a linear heat rate of 13.6 kW/ft to a burnup of 0.7% FIMA. The present study verified the results and extended a preliminary microprobe analysis of this pin.[46]

Briefly, the microstructure of the pin analyzed was typical. There was a central void, columnar grains, equiaxed grains, and an unrestructured region consisting of the original microspheres. As shown in Fig. 1.13, fuel had been deposited onto the hot side of the microspheres at the region of transition from columnar to equiaxed grains by vapor transport down the temperature gradient.

A radial scan was made for Pu and U in the columnar grain region. The Pu/(U + Pu) ratios calculated from the strip-chart record are plotted in Fig. 1.14 for the region of the columnar grains near the central void. For this region there was an increase in Pu content on approaching the central void. The largest increase occurred within 100 μm of the central void, but there was a detectable gradient in the Pu content as far as 260 μm from the central void. Over the remainder of the columnar grain region there were no detectable gradients in the Pu content. More quantitative determinations of the Pu/(U + Pu) ratio than those obtainable from the strip-chart records were obtained by making 100-sec point counts. These data revealed, in general agreement with the radial scan, that the Pu/(U + Pu) ratio was 20% about 20 μm from the central void, while the ratio was 16.4% at 300 μm.

An alpha-autoradiograph of this pin (Fig. 1.15), made with cellulose nitrate, only very faintly revealed the concentration of Pu near the central void. Thus, since the initial fuel composition was 15% Pu and the microprobe analyses showed the Pu content adjacent to the central void to be 20%, the detection limit of the alpha-autoradiographic technique is ∿5% Pu/(U + Pu).

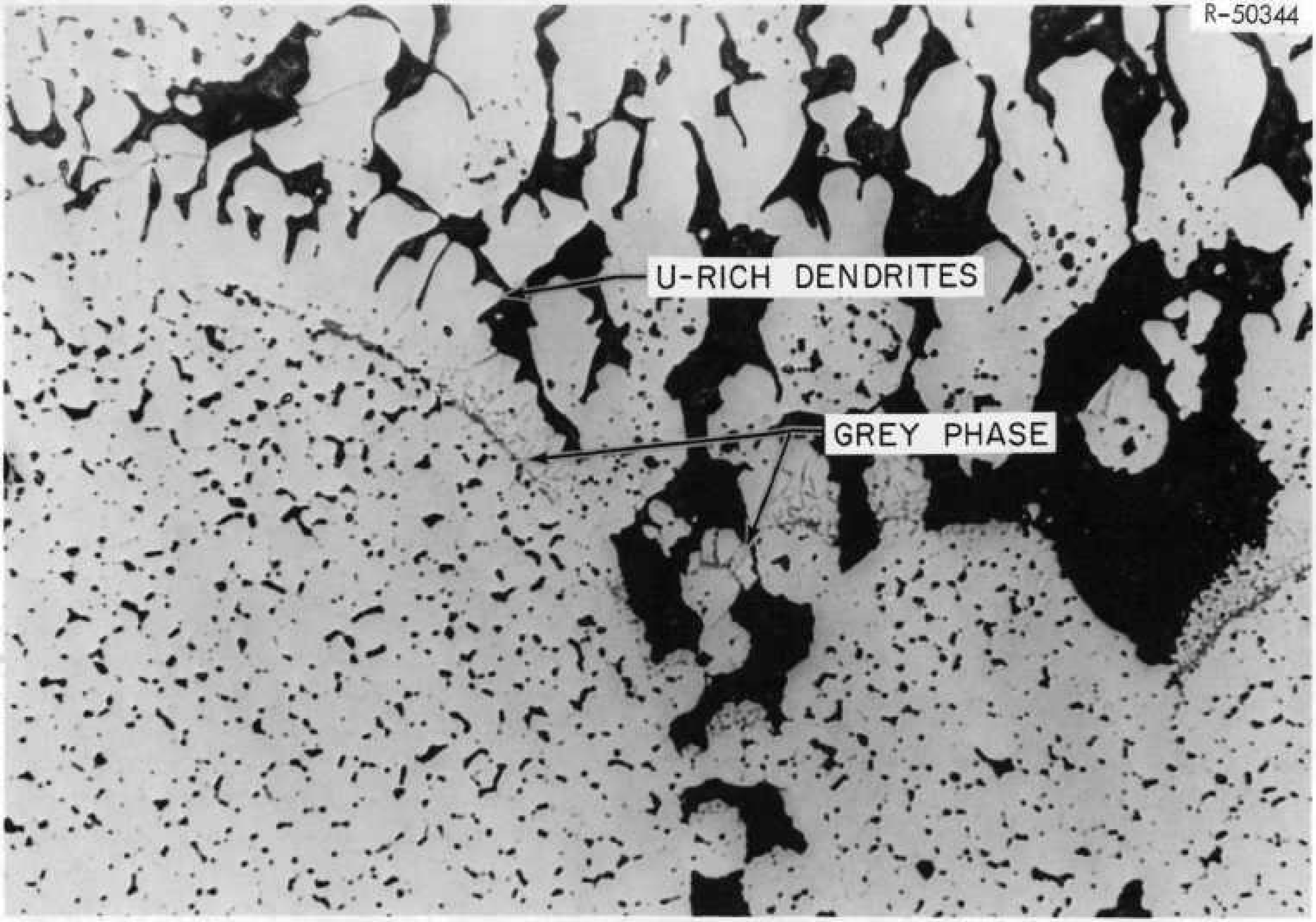

Fig. 1.13. Fuel Dendrites and an Al-Bearing Gray Phase Deposited on the Hot Side of $(U_{0.85},Pu_{0.15})O_{2.00}$ Microspheres Located at the Region of Transition From Columnar to Equiaxed Grains. As polished, 500×.

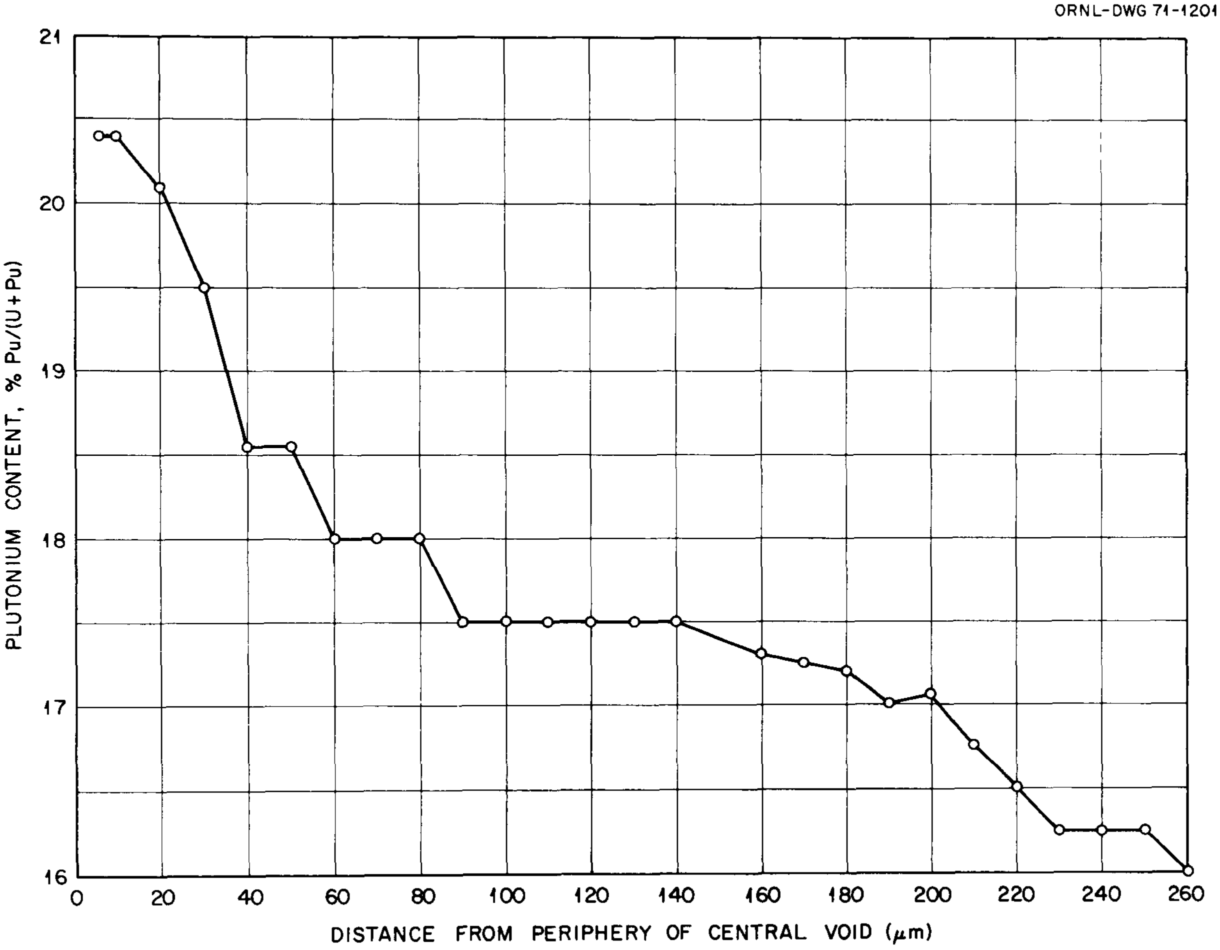

Fig. 1.14. Variation in Pu Content with Radial Position for $(U_{0.85},Pu_{0.15})O_{2.00}$ After Irradiation at a Linear Heat Rate of 13.6 kW/ft to 0.7% FIMA.

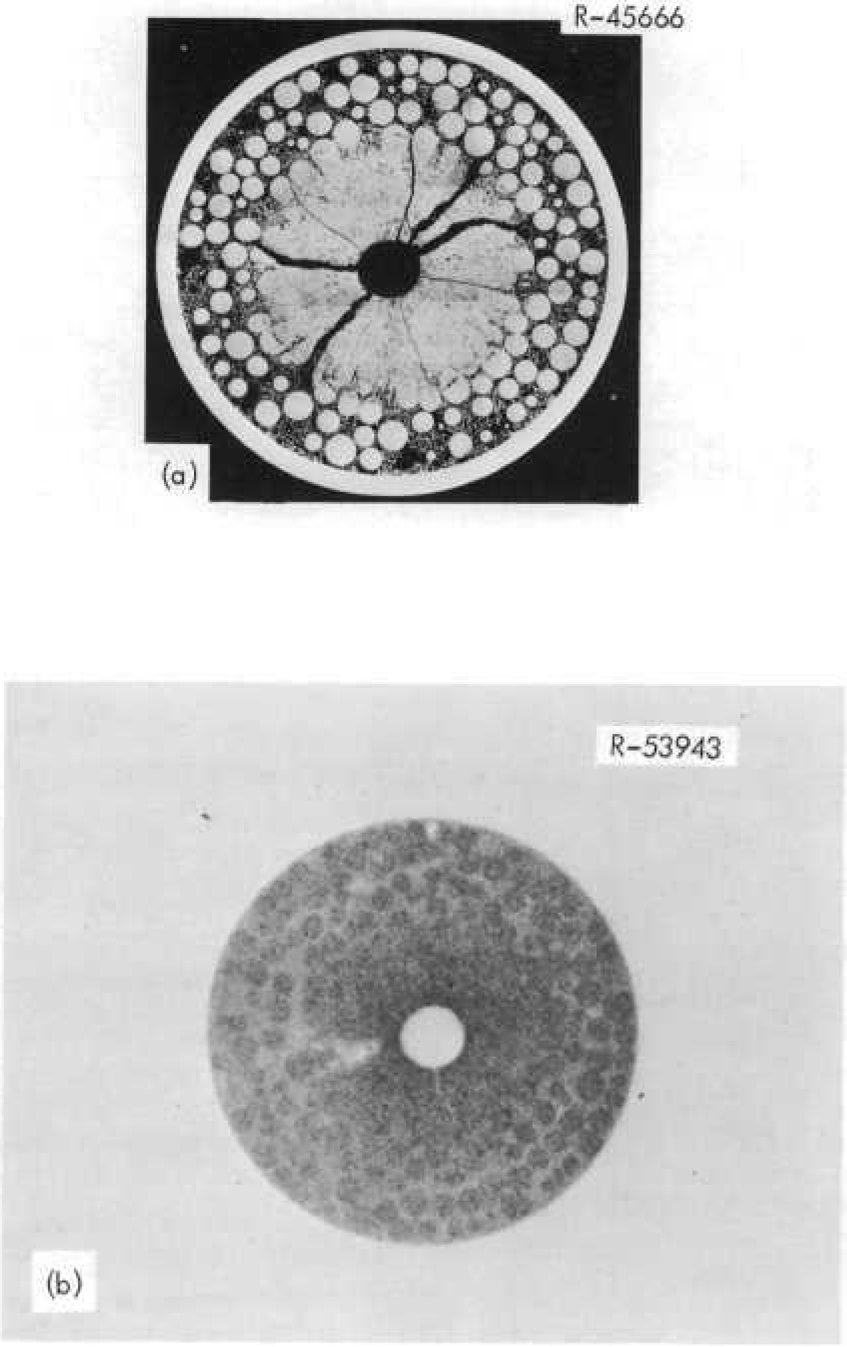

Fig. 1.15. Macrograph and Alpha-Autoradiograph of $(U_{0.85},Pu_{0.15})O_{2.00}$ Fuel Pin 43-112-3C. (a) Macrograph and (b) alpha-autoradiograph.

Attention was given to determining the composition of the dendritic fuel material deposited on the hot side of microspheres located at the transition from colunnar to equiaxed grains. Although insufficient data were obtained to accurately define the Pu content of the vapor-deposited material, it was demonstrated that the deposited material was rich in U compared to both the coarse microspheres onto which the fuel had deposited and to the adjacent columnar grains. This confirms our previous data[47] and is an important observation from a mechanistic viewpoint in that it shows that, at least for some radial positions in this fuel pin, actinide redistribution occurred via a vapor transport mechanism. The approximate composition of the deposited material was 12% Pu/(U + Pu); the deposited material may have a Pu content as low as 8%. Since the as-fabricated fuel was virtually stoichiometric, the formation of U-rich deposits is in agreement with both mass spectrometric data[48] and thermodynamic calculations[49] which show the vapor formed by such fuel to be rich in U compared to the starting fuel composition.

As shown in Fig. 1.16, Al was found in a gray nonmetallic phase ∿1 μm thick located between the dendritic fuel deposits and the micro spheres. The gray phase is presumed to Al_2O_3. Although the specimen had been metallographically prepared using alumina, the Al Kα x-ray intensity was far too strong to be a result of residual grinding and polishing compound. Emission spectrographic analyses showed the as-fabricated fuel contained 19 ppm Al. This low concentration could be consistent with the above observation since the thermal gradient apparently caused the Al to concentrate.

Fission Product Migration in $(U,Pu)O_2$ Nuclear Fuels (P. T. Carlson and J. L Miller, Jr.)

The purpose of this investigation is to develop, both from theoretical and experimental viewpoints, an understanding of the redistribution of solid fission products in mixed oxide fuels subjected to large temperature gradients. Experiments have been initiated to study the radial migration of selected fission products in irradiated $(U,Pu)O_2$ fuels. Of current interest is a section of fuel pin S-1-E, a Sphere-Pac

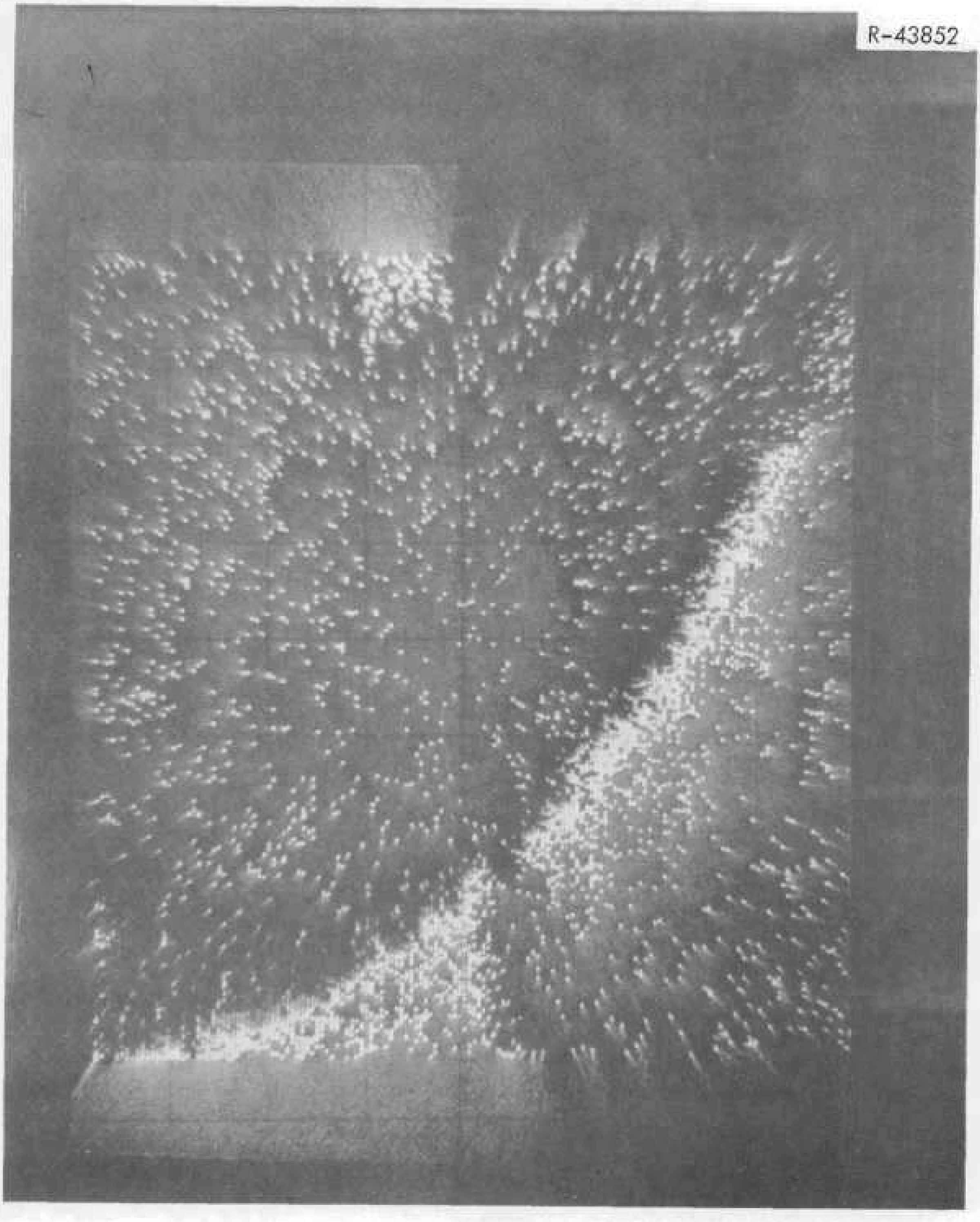

Fig. 1.16. CRT Display of Al Kα X-Rays Emitted by a Nonmetallic Gray Phase Deposited on the Surface of a Coarse Microsphere. A similar region of the specimen is shown in Fig. 1.13.

pin of 316 stainless steel clad mixed oxide material, which has been irradiated in the EBR-II.

The application of the laser vaporization apparatus for microsampling mixed oxide fuel pin cross sections, as described in previous reports,[50,51] has been suspended in favor of a more direct and rapid means of ascertaining the concentration of metallic fission products. Attention is currently focused on the use of the electron probe microanalyzer for the investigation of metallic inclusions located in the matrices of $(U,Pu)O_2$ fuel pins. The microprobe has the advantage of a relatively small sampling area (1- to 2-μm diam) compared with the size crater (200- to 300-μm diam) formed by the laser vaporization technique. The smaller probe spot size will permit more selective examination of the mixed oxide pins. Furthermore, the x-ray intensities obtained from microprobe analysis can be converted to units of weight percent when proper standards are available.

The electron microprobe is presently being employed on sample S-1-E-J for the examination of the numerous metallic inclusions found in the oxide matrix. The inclusions range in size from 5- to 10-μm diam and, therefore, lend themselves nicely to microprobe analysis. The radial distribution of the fission products Mo, Ru, Tc, Rh, and Pd in the metallic inclusions are to be determined, with primary attention focused on the behavior of the elements Mo, Ru, and Tc.

The behavior of the fission product Mo in mixed oxide fuels has recently been discussed by Lawrence *et al.*,[52] with particular emphasis on the effect of its presence on the oxygen-to-metal ratio within the fuel. In their investigation of $(U,Pu)O_2$ pellet fuel clad in 304 stainless steel, it was found that under the influence of reactor condition thermal gradients, the Mo migrated toward the cooler region of the fuel. This effect was also observed by O'Boyle *et al.*[53] in their study of vibratorily compacted fuels. The combined effect of the O migration and subsequent oxidation of the Mo is thought to establish a concentration gradient of Mo, which results in the diffusion of Mo toward the cladding. In contrast, the fission products Ru and Tc have been shown[53] to preferentially migrate toward the hotter portions of the fuel under reactor conditions. In addition, it was determined that the elements Mo, Ru, and Tc together comprise approximately 90 wt % of each metallic inclusion with the remaining 10 wt % consisting of Rh and Pd.

The importance of studying thermal diffusion of fission products, such as Mo, Ru, and Tc, is apparent when we consider that estimates of the contribution of a particular fission product to the swelling of the fuel pin depend intimately on reliable information concerning the location of that fission product.

Irradiation Data on Mixed Oxide Fuel Pins (W. H. Bridges)

A compilation of the data on fuel pins irradiated in a fast environment is being made in support of our development of modeling codes. As of January 1, about 800 pins had or were being tested in EBR-II. Complete postirradiation data are available on only a small percentage. The data collected on the various pins are being analyzed and prepared for insertion into the FM0DEL fuel pin modeling code.

Testing of Off-Site Computer Codes (W. H. Bridges)

During the quarter we have received two computer codes from the Argonne Code Center. One is a thermal-hydraulic code for a subassembly and the other is a fuel swelling modeling code.

The C0BRA-II computer code[54] calculates the steady-state flow and enthalpy in the subchannels of pin-type nuclear fuel elements. The model calculation includes the effects of turbulent and diversion crossflow mixing, subcooled voids, mechanical distortions, and fuel element design. The code was run under F0RTRAN IV, level H control, and except for roundoff errors the results of the included sample input data were exactly as published.[54] Consideration is currently being given to the necessary input data for the analysis of LMFBR-type elements.

The computer code BUBL-1 (Ref. 55) is being checked out for possible use within the framework of our FM0DEL fuel pin modeling code.[56] BUBL-1 predicts fuel swelling and fission gas release based on movement of the fission gas bubbles by a surface diffusion mechanism under a thermal gradient. Interactions of the bubbles with dislocations and grain boundaries act as temporary trapping sites prior to release. The fission gas events are followed using a Monte Carlo technique in which the individual bubbles are followed through their time history from nucleation to release.

While the code is written in F0RTRAN IV, it was designed for a CDC-6600 computer. Some amount of revision to the main program and the subroutines was necessary to even check out the code with sample problem included. The first part of the illustrative problem was finally run and agreed with the author's result. The second part, however, which involved higher temperatures and longer times exceeded the numerical capacity of the IBM 360 (approx 10^{75}). This does not result in an overflow in the CDC machine which handles numbers to about 10^{300}. Methods for solving the problem are currently being tried.

References

1. R. A. Bradley and W. H. Pechin, LMFBR Fuel Cycle Studies Progr. Rept. November 1970, No. 21, ORNL-TM-3250, pp. 64–67.

2. R. E. Lerch, Application of Aqueous Technology to LMFBR Separations Processes. Program Plan for Task T-2: Fuel Dissolution Characteristics, WHAN-FR-33 (December 1970).

3. T. L. Markin, "Thermodynamic Data for Uranium and Uranium-Plutonium Oxides Applied to Fuel Preparation Problems," Chem. Eng. Progr. Symp. Ser. 80, 43 (1967).

4. T. B. Lindemer and R. A. Bradley, Kinetic Models for the Synthesis of $(U,Pu)_2$-y by Hydrogen-Reduction and Carbothermic Techniques, ORNL-TM-3358, in press.

5. A. R. Olsen, Fuels and Materials Development Program Quart. Progr. Rept. September 30, 1969, ORNL-4480, pp. 29–33.

6. R. A. Bradley, W. J. Leonard, T. B. Lindemer, R. B. Pratt, and W. H. Pechin, Fuels and Materials Development Program Quart. Progr. Rept. June 30, 1970, ORNL-4600, pp. 7–10.

7. R. A. Bradley, W. J. Leonard, T. B. Lindemer, and W. H. Pechin, Fuels and Materials Development Program Quart. Progr. Rept. September 30, 1970, ORNL-4630, pp. 13–15.

8. R. A. Bradley, "Fuel Reprocessing Fuel Pins," Fuels and Materials Development Program Quart. Progr. Rept. December 31, 1970, ORNL-TM-3300, in press.

9. R. B. Fitts, V. A. DeCarlo, and J. G. Morgan, Fuels and Materials Development Program Quart. Progr. Rept. March 31, 1970, ORNL-4560, pp. 63–66.

10. R. B. Fitts, R. L. Senn, and R. A. Bradley, "Tests of Mechanical Interaction of Fuel and Cladding," pp. 25–26, this report.

11. Formerly Battelle Memorial Institute, Pacific Northwest Laboratory.

12. R. A. Bradley, "Mechanical Interaction Test Fuel Pin," Fuels and Materials Development Program Quart. Progr. Rept. December 31, 1970, ORNL-TM-3300, in press.

13. R. A. Bradley and J. D. Sease, "Relocation of Alpha Facility," Fuels and Materials Development Program Quart. Progr. Rept. December 31, 1970, ORNL-TM-3300, in press.

14. P. W. Flynn, High-Temperature Fast-Flux Irradiation Experiment for Mixed-Oxide Fuel Rods, GA-10264 (October 15, 1970).

15. J. M. Leitnaker, *Fuels and Materials Development Program Quart. Progr. Rept. September 30, 1970*, ORNL-4630, p. 25.

16. Personal communication, L. A. Harris.

17. A. R. Olsen, *Fuels and Materials Development Program Quart. Progr. Rept. September 30, 1970*, ORNL-4630, pp. 27—29.

18. A. R. Olsen, "Fast Flux Irradiation Tests," *Fuels and Materials Development Program Quart. Progr. Rept. December 31, 1970*, ORNL-3300, in press.

19. R. B. Fitts, A. R. Olsen, and J. Komatsu, *Fuels and Materials Development Program Quart. Progr. Rept. March 31, 1968*, ORNL-2217, pp. 135—140.

20. A. R. Olsen, "Intermediate Burnup Irradiation Tests of Sphere-Pac Sol-Gel Fuels," *Trans. Am. Nucl. Soc.* **13**(1), 32—33 (June 1970).

21. C. E. Cronthomel and C. E. Johnson, *Reactor Development Program Progr. Rept. August 1970*, ANL-7737, pp. 113—114.

22. A. R. Olsen, *Fuels and Materials Development Program Quart. Progr. Rept. September 30, 1969*, ORNL-4480, pp. 29—33.

23. Telephone conversation, C. M. Cox and J. H. Kittel, February 23, 1971.

24. R. B. Fitts and V. A. DeCarlo, *Fuels and Materials Development Program Quart. Progr. Rept. June 30, 1968*, ORNL-4330, pp. 20—23.

25. R. B. Fitts, D. R. Cuneo, V. A. DeCarlo, and K. R. Thoms, *Fuels and Materials Development Program Quart. Progr. Rept. September 30, 1969*, ORNL-4480, pp. 26—27.

26. R. A. Bradley, *Fuels and Materials Development Program Quart. Progr. Rept. September 30, 1969*, ORNL-4480, pp. 6—8.

27. F. G. Kitts, R. B. Fitts, and A. R. Olsen, "Sol-Gel Urania-Plutonia Microsphere Preparation and Fabrication into Fuel Rods," pp. 195—210 in *Intern. Symp. Plutonium Fuel Technol., Scottsdale Arizona, 1967*, *Nucl. Met.* *13*, American Institute of Mining, Metallurgical, and Petroleum Engineers, New York (1968).

28. R. B. Fitts, E. L. Long, Jr., and J. R. Miller, "Thermal Performance Tests," *Fuels and Materials Development Program Quart. Progr. Rept. December 31, 1970*, ORNL-TM-3300, in press.

29. R. B. Fitts, R. L. Senn, J. G. Morgan, and J. D. Jenkins, *Fuels and Materials Development Program Quart. Progr. Rept. June 30, 1970*, ORNL-4600, pp. 58—63.

30. R. B. Fitts and R. L. Senn, "Fuel-Cladding Mechanical Interaction Tests," *Fuels and Materials Development Program Quart. Progr. Rept. December 31, 1970*, ORNL-TM-3300, in press.

31. R. A. Bradley, "Mechanical Interaction Test Fuel Pin," pp. 7—8, this report.

32. F. J. Homan, C. M. Cox, and W. J. Lackey, *Comparisons Between Predicted and Measured Fuel Pin Performance*, ORNL-TM-3386 (in press). Paper to be published in *Proceedings of The American Nuclear Society Conference on Fast Reactor Fuel Element Technology, New Orleans, Louisiana, April 13—15, 1971*.

33. R. C. Nelson *et al.*, *Performance of Plutonium-Uranium Mixed-Oxide Fuel Pins Irradiated in a Fast Reactor (EBR II) to 50,000 MWd/Te*, GEAP-13549, General Electric Company, Breeder Reactor Development Operation (1969).

34. W. J. Lackey and T. M. Kegley, Jr., *LMFBR Fuel Cycle Studies Progr. Rept. October 1970*, No. 20, ORNL-TM-3217, pp. 79—82.

35. W. J. Lackey and T. M. Kegley, Jr., "Microscopy of $(U,Pu)O_2$ Fuels," *Fuels and Materials Development Program Quart. Progr. Rept. December 31, 1970*, ORNL-TM-3300, in press.

36. C. M. Cox and F. J. Homan, *PRØFIL — A One-Dimensional FØRTRAN IV Program for Computing Steady-State Temperature Distributions in Cylindrical Ceramic Fuels*, ORNL-TM-2443, Addendum (August 1969).

37. W. J. Lackey, *Fuels and Materials Development Program Quart. Progr. Rept. September 30, 1970*, ORNL-4630, pp. 47—54.

38. L. C. Michels and T. W. Latimer, "Studies of Fuel Swelling," *Reactor Development Program Progr. Rept. February 1970*, ANL-7669, pp. 112—113.

39. Thomas R. Padden, *Microstructural Changes Associated with Irradiation Burnup of Uranium Dioxide*, WAPD-T-1501 (August 1962).

40. W. E. Baily, C. N. Spalaris, D. W. Sandusky, and E. L. Zebroski, "Effect of Temperature and Burnup on Fission Gas Release in Mixed Oxide Fuel," pp. 195—210 in *International Symposium on Ceramic Nuclear Fuels*, The American Ceramic Society, Inc., Columbus, Ohio (1969).

41. Nayla A. L. Mansour and J. White, "Causes of Residual Porosity in Sintered Uranium Dioxide," *Powder Met.*, No. 12, 108 (1963).

42. K. H. McCorkle and C. S. Morgan, *Metals and Ceramics Division Annual Progr. Rept. June 30, 1970*, ORNL-4570, p. 26.

43. J.D.L. Harrison, E. Foster, and L. E. Russel, "The Sintering Behavior of Mixed UO_2 and PuO_2 Powders," pp. 140–165 in *Powder Metallurgy in The Nuclear Age*, Plansee Proc. 1961, F. Benesovsky, Ed. (Springer-Verlag), Vienna, 1962.

44. Personal communication between W. J. Lackey and R. B. Fitts, January 1971.

45. W. J. Lackey, *Fuels and Materials Development Program Quart. Progr. Rept. September 30, 1970*, ORNL-4630, pp. 47–54.

46. W. J. Lackey, *Fuels and Materials Development Program Quart. Progr. Rept. March 31, 1970*, ORNL-4560, pp. 71–74.

47. W. J. Lackey and J. L Miller, Jr., *Fuels and Materials Development Program Quart. Progr. Rept. June 30, 1970*, ORNL-4600, pp. 69–71.

48. A. D. Tevebaugh and P. E. Blackburn, *Reactor Development Program Progr. Rept. July 1970*, ANL-7726, pp. 142–144.

49. W. J. Lackey, A. R. Olsen, and D. K. Bates, "Actinide Redistribution in Irradiated $(U,Pu)O_2$," *Fuels and Materials Development Program Progr. Rept. December 31, 1970*, ORNL-TM-3300, in press.

50. P. T. Carlson, *LMFBR Fuel Cycle Studies Progr. Rept. December 1971*, No. 22, ORNL-TM-3281, pp. 73–75.

51. P. T. Carlson, *LMFBR Fuel Cycle Studies Progr. Rept. January 1971*, No. 23, ORNL-TM-3312, pp. 103–104.

52. L. A. Lawrence and J. A. Christensen, "Molybdenum Distribution in Irradiated Oxide Fuels," *J. Nucl. Mater.* **37**, 248–250 (1970).

53. D. R. O'Boyle, F. L. Brown, and J. E. Sanecki, "Solid Fission Product Behavior in Uranium-Plutonium Oxide Fuel Irradiated in a Fast Neutron Flux," *J. Nucl. Mater.* **29**, 27–42 (1969).

54. D. S. Rowe, C0BRA-II: *A Digital Computer Program for Thermal-Hydraulic Subchannel Analysis of Rod Bundle Nuclear Fuel Elements*, BNWL-1229 (February 1970).

55. H. R. Warner, *BUBL-1 — A Statistical Fuel Swelling and Fission Gas Release Model*, WAPD-TM-942 (September 1970).

56. F. J. Homan, *LMFBR Fuel Cycle Studies Progr. Rept. January 1971*, No. 23, ORNL-TM-3312, pp. 86–88.

2. DEVELOPMENT OF ADVANCED FBR FUELS

P. Patriarca J. L. Scott

The carbides and nitrides of U and Pu, which have thermal conductivities about five times that of $(U,Pu)O_2$, have the potential for significantly reducing power costs for the liquid-metal-cooled fast breeder reactor (LMFBR). These reductions arise from higher specific power, higher linear heat ratings, shorter doubling times, and reduced capital costs. Improved nuclear safety is also possible through their use.

The main question regarding the use of carbides or nitrides is whether they will perform satisfactorily under LMFBR core conditions to burnups above 100,000 MWd/metric ton. The goal of our program is to answer this question for $(U,Pu)N$; other laboratories have been assigned to evaluate $(U,Pu)C$. The ORNL program consists of irradiation tests in a thermal reactor, the Engineering Test Reactor (ETR), and in a fast reactor, the Experimental Breeder Reactor-II (EBR-II). It includes fuel fabrication and characterization of the fuel, design, fabrication, and characterization of the fuel pins, and examination of the fuel pins after irradiation. Finally, a small study is included to define quality standards of fuel and cladding to avoid compatibility problems during irradiation.

Synthesis, Fabrication, and Characterization of Advanced FBR Fuels

V. J. Tennery

<u>Synthesis and Fabrication of Mixed Nitrides</u> (E. S. Bomar)

We have fabricated 500 pellets of $(U,Pu)N$ during this quarter. These pellets will be used for the loading of seven pins for irradiation in the EBR-II. We prepared the pellets using our standard procedure[1] except for minor process modifications. The method was essentially the same as that used to make pellets for ETR irradiation pins. Dry grinding was used because we encountered difficulty with carbon contamination of the nitride powder during milling in hexane (see subsequent section entitled "Ball Milling and Sintering of Nitrides," pp.57–60.

Nitride powder was synthesized in approximately 100-g batches from arc-melted alloy containing 16.5% Pu and 83.5% U enriched to 93% in the ^{235}U isotope. Conversion was effected by successive exposure to H_2 and N_2 gases over a range of temperatures yielding a powder consisting of essentially the mononitride phase. Two powder batches were combined together prior to grinding. After cold pressing, groups of 30 pellets were sintered in each of two tungsten containers for 6 hr at 2250°C in a N atmosphere at 630 torr. Pellet length varied because we used a volumetric measurement of the powder for die loading. Since the fuel stack height rather than individual pellet height is the significant dimension for loading the irradiation pin, we selected a volumetric die loading procedure rather than quantitatively weighing the powder required for each pellet. This greatly simplified the pellet fabrication. Representative results for control pellets from six groups of sintered pellets appear in Table 2.1.

The first group of pellets was sintered at 2200°C in N_2 at 630 torr for 5 hr. The density of four control pellets ranged from 85 to 88% of theoretical. We resintered the first group a second time for 6 hr at 2250°C which increased the density to 90–91% of theoretical. Subsequent groups of pellets were all sintered for 6 hr at 2250°C.

One control pellet from each group of 60 pellets was first used for measurement of density with a Hg pycnometer,[2] then a small sample was removed for x-ray diffraction, and the remainder of the pellet was submitted for metallographic examination. A second pellet was subdivided for O, C, N, U, and Pu determinations. The results of these examinations are also given in Table 2.1.

The densities calculated from volumes obtained with the Hg pycnometer were consistently higher than those calculated from measurements with a micrometer.

Metallographic examination of a representative pellet from each 60-pellet group disclosed a dense structure having fine, uniform porosity. The microstructures were essentially single phase except for the infrequent occurrence of very fine particles of a second phase near

Table 2.1. $(U_{0.86}Pu_{0.16})N$ for EBR-II Irradiation Pins

Furnace Run No.	Sample No.	Powder Batches[1]	Green Pellets Density[2,3] (% Theo)	Sintered Pellets Density[2] (% Theo)	Hg Pyc Density[4] (% Theo)	% by Weight O	C	N	U[5]	Pu[5]	Lattice Parameter (A)
				After first sintering (5 hr at 2200°C)							
1	509	ES-1-3 ES-2-3	61.0	84.8	—	—	—	—	—	—	
	510		62.1	85.8	—	—	—	—	—	—	
	511		62.2	86.6	—	—	—	—	—	—	
	512		—	88.4	—	—	—	—	—	—	
				After second sintering (6 hr at 2250°C)							
2	509			90.2	91.0						4.89052
	510			90.4	—	0.043	0.034	5.42	79.26	15.24	
	511			90.7	—						
	512			91.3	—				Mass balance 99.997		

Table 2.1. (Continued)

Furnace Run No.	Sample No.	Powder Batches[1]	Green Pellets Density[2,3] (% Theo)	Sintered Pellets Density[2] (% Theo)	Sintered Pellets Hg Pyc Density[4] (% Theo)	% by Weight O	% by Weight C	% by Weight N	% by Weight U[5]	% by Weight Pu[5]	Lattice Parameter (A)
3	569	ES-3-3 ES-4-3	60.3	89.6	89.9						4.89070
	570		59.8	88.8	—	0.041	0.043	5.40	79.23	15.30	
	571		60.9	88.3	—				Mass balance 100.014		
	572		59.9	89.8	—						
	599		—	90.5	—						
	600		—	90.7	—						
4	629	ES-5-3 ES-6-4	53.4	90.2	91.6						4.89105
	630		54.5	90.0	—	0.044	0.055	5.40	79.24	15.32	
	631		54.2	90.8	—				Mass balance 100.06		
	632		53.9	89.5	—						
5	689	ES-7-4 ES-8-4	59.1	88.6	91.8						4.89074
	690		60.0	88.9	—	0.045					
	691		58.6	88.2	—						
	692		59.8	88.1	—						

Table 2.1. (Continued)

Furnace Run No.	Sample No.	Powder Batches[1]	Green Pellets Density[2,3] (% Theo)	Sintered Pellets							Lattice Parameter[6] (A)
				Density (% Theo)	Hg Pcy Density[4] (% Theo)	% by Weight					
						O	C	N	U[5]	Pu[5]	
6	749	ES-9-4 ES-10-4	58.1	89.8	92.4						4.89054
	750		58.1	91.0	——	0.0384					
	751		56.4	89.7	——						
	752		57.2	90.4	——						
7	808	ES-11-5 ES-12-5	56.9	90.4	——						4.89052
	809		56.8	90.2	——	0.0496					
	810		57.8	91.1	——						
	811		57.2	91.0	——						

---

[1] Two 100 g batches of powder combined and blended. Portions weighing 6.5 g were then ground for 20 min. in small steel mills.

[2] Calculated from micrometer measurements and weight.

[3] Density of 14.32 g/cm^3 used for theoretical density.

[4] Volume measured by displacement of Hg at 15 psi using a precision piston.

[5] Average atomic weight in this alloy: U = 235.16, Pu = 239.14.

[6] Measurements made 28 days after pellet was sintered.

the surface of some pellets. These particles had the appearance of oxide. Their location is such that they will be removed when the pellets are ground to final size.

Synthesis and Fabrication of Uranium Nitride (V. J. Tennery and R. A. Potter)

We have fabricated about 1 kg of UN powder into UN pellets to provide the UN insulator pellets required for the EBR-II irradiation pins and three EBR-II type pins fueled with UN. The latter are required for the development of the Na bonding and NDT techniques prior to handling the Pu-bearing fuel. The UN pins contain high density pellets with a column height of about 14.5 in. The machining of the UN cylinders to be used as insulator material in the seven EBR-II pins will commence shortly. We have produced about 200 pellets of sintered UN during this quarter.

Ball Milling and Sintering of Nitrides (E. S. Bomar and V. J. Tennery)

During the last report period[3] we described our initial experiments with ball milling using hexane as a suspension medium. The sinterability of UN and (U,Pu)N was improved by this treatment, but an unexpected increase in C content was found in the milled powder and the sintered pellets. The O and C contents resulting from several different treatments for both powders and pellets are given in Table 2.2. A pellet made from $(U_{0.82},Pu_{0.18})N$ powder sintered to 92% of theoretical in 5 hr at 1800°C under a reduced N pressure. The microstructure was free of any metallic phases.

A second 200-g charge of UN was milled in Fisher ACS grade hexane which had been handled only in glass containers. An earlier procedure involved storing the hexane in polyethylene bottles in the glove boxes. We observed a slow attack on the polyethylene by the hexane. We determined the amount of C contributed by the previously used polyethylene bottle. An increase in C content of the UN resulted when we used hexane stored in glass or polyethylene. Therefore, after ball milling the UN for 32 hr the principal source of C was the hexane itself. Analysis by gas chromatography of hexane exposed to polyethylene for 24 hr showed a polyethylene content of 250 mg/l. At this concentration a

Table 2.2. Ball Milling of Nitrides in Hexane

Nitride	Condition	Powder		Sintered Pellets			
		O(PPM)	C(PPM)	Sintering Conditions	O(PPM)	C(PPM)	Density
UN	As synthesized	500	—				
	Milled 1 hr	1350	—	1800°C for 300 min. in	1400		
	2 1/2 hr	—	—	N_2 plus Ar mixture[1]	1400	—	89.4
	16 hr	—	—		1100	—	92.6
	17 hr	1700	—		880	—	94.2
						1800	97.5
$(U_{0.82}Pu_{0.18})N$	As synthesized	922	402				
	Milled 1 hr	—	—	Same	—	—	Capped
	4 hr	—	—		—	—	95.7
	16 hr	1512	3000		—	—	93.0
	32 hr	1435	4650		1051	5000	96.4[2]
	32 hr powder retreated with H_2 and N_2	—	—	Same	—	—	91.8[3]
$(U_{0.82}Pu_{0.18})N$	Reference sample[4]	1435	4650				
	First oxidized sample[5]	2445[6]	4650[7]	2200°C for 100 min. in N_2 at 630 torr	427	2650	94.0
	Second	3605	4650		389	1795	95.1
	Third	6585	4650		655	1755	95.9
	Fourth	10468	4650		400	1750	97.0

[1] Heated under vacuum to 1400°C. Back filled with N_2 to 10^{-2} torr then added Ar to 630 torr.
[2] Metal found at intergranular locations in microstructure.
[3] No free metal in microstructure.
[4] Milled 32 hr; powder then resynthesized.
[5] Oxidized in glove box atmosphere.
[6] Presumes weight increase during controlled exposure to glove-box atmosphere resulted from O pick-up only.
[7] C content assumed constant during oxidation in glove-box atmosphere.

maximum of 62 mg of polyethylene would be added to the 200-g charge of nitride. Since the increase in C during milling amounted to about 900 mg, the observed polyethylene content accounts for only 1/18 of the total C increase observed in the milled nitride powder.

We also checked the possibility of a mechanical carryover of hexane to the powder compact due to insufficient drying. This determination was made by maintaining a pressed pellet of mixed nitride overnight under vacuum then analyzing the powder from the pellet for both O and C. The C content of the powder was not significantly reduced but unexpectedly the O level dropped from 1386 to 580 ppm. This result indicated that some of the O in the nitride was held very loosely in the powder.

Since BMI had not experienced difficulty with C pickup while using Mallinckrodt's Nanograde hexane, we obtained a quantity of this particular grade of hexane and ground a third 200-g charge of UN in it for 32 hr. A pellet sintered from this nitride contained 2480 ppm of C, which is substantially greater than the 300–600 ppm normally found in our sintered nitride pellets made by using dry grinding procedures. We conclude, therefore, that some reaction must take place between the nitride and the Nanograde hexane as well during the grinding process.

Low C contents could result for sintered nitrides if circumstances were such that O was available in the nitride and during high-temperature sintering the C reacted with the O and the CO and CO_2 formed were carried away from the furnace charge during sintering. We tested this premise by exposing a portion of ball milled $(U_{0.82},Pu_{0.18})N$ powder to a glove box atmosphere of Ar. Pickup of impurity, presumed to be O, was followed by periodic weighing. Powder samples were removed at intervals and fabricated into a pellet. The increase in O content was inferred from changes in weight of the powder during exposure to the glove box atmosphere. The results for four pellets prepared in this manner are given in Table 2.2. The O content of the starting powders ranged up to 10,500 ppm while the C content was 4650 ppm. Analysis of the sintered pellets showed that the O content dropped to 400–650 ppm and the C was reduced to 2650–1750 ppm. The residual C showed an inverse dependence on the initial O content but the relation was not linear. This is probably because a large fraction of the available O was removed during evacuation prior to sintering and thus was not available for carbothermic reduction during the sintering procedure.

In the nitride powders produced by our process a significant fraction of the O is apparently only bound in the nitride very loosely. These results indicate, however, that as the O concentration changes during sintering toward a value of 400–600 ppm, the C content is also reduced indicating that carbothermic reduction is occurring in these materials.

New Facilities (V. J. Tennery)

Several new facilities are being prepared for operation in our inert-atmosphere Pu facility. The general purposes and status of these are briefly described below.

Helium Purifier and Recirculator for Plutonium Glove Box Atmosphere (E. S. Bomar)

Several auxiliary components must be designed and fabricated before the purifier can be put into service including the storage and distribution of a liquid N supply line and control for makeup He, glove box header overpressure protection system, and the hardware to regulate the pressure at the off-gas side of individual boxes when the system is in the closed loop mode of operation. Design work is being done by the General Engineering and Construction Division.

Mercury Pycnometer Facility (J. P. DeLuca)

The Hg pycnometer was installed this quarter. Delivery of the pycnometer was made February 18, 1971. The device was installed in the glove box, checked out, and found to operate satisfactorily. The accuracy of the instrument is such that fuel sample volumes can be determined to better than ±0.001 cm^3. The unit is now being used routinely to characterize (U,Pu)N pellets.

Description of Mercury Pycnometer. — A schematic diagram of the Hg pycnometer is shown in Fig. 2.1. The sample chamber is approximately 1 cm in diam × 1 cm high. The ultraprecision syringe can displace 2.5 cm^3 of Hg and the Hg pressure can be read from 0–1400 torr by means

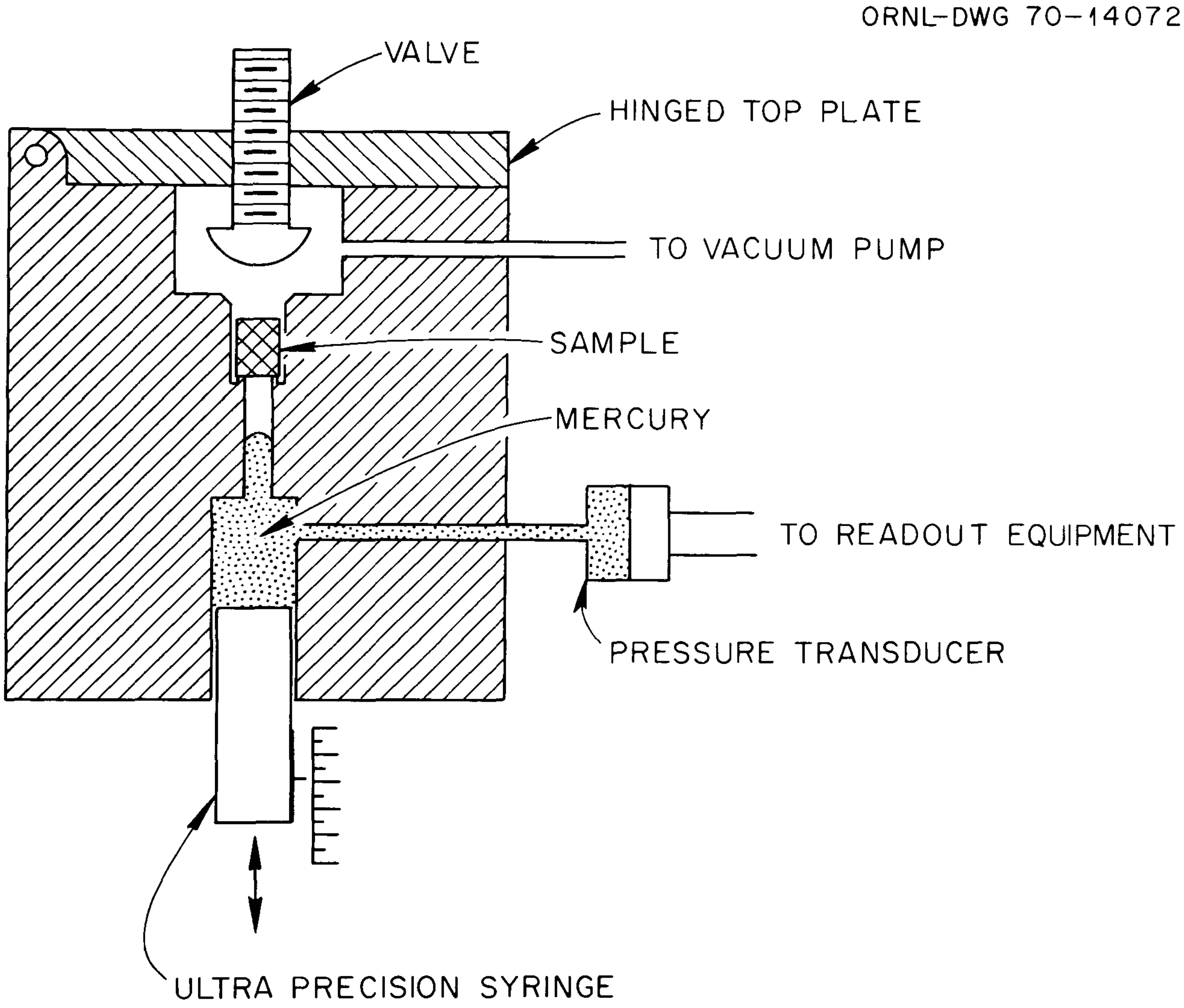

Fig. 2.1. Schematic Diagram of Mercury Pycnometer

of a stainless steel diaphragm transducer. The electronic readout and control system consists of the vacuum readout of the sample chamber, the Hg pressure readout, and the remote drive system for the syringe. The system also includes a Hg vapor detector to continuously monitor the off-gas stream. A Hg filter system was installed and it has been observed that the Hg vapor content of the box gas, which is usually 150–250 wppb Hg, can be effectively filtered to below 10 wppb before it is dumped to the off-gas system.

An analytical balance is also located in the glove box. Thus, a complete density determination can be made within the one glove box. The operation of the pycnometer is very straightforward and it takes approximately 5 min. to make one determination.

Oscillatory Grinder (V. J. Tennery)

The ability to grind ceramic powders to increase their sintering activity is basic to the development of experimental fuels for irradiation experiments. The experimental difficulties are increased for (U,Pu)N powders because of the extreme tendency of these materials to become contaminated with O. The high hardness of these materials also leads to contamination by the grinding medium itself unless the grinding method and medium are chosen very carefully.

The use of hexane for wet ball milling of nitride powders does not at present look promising because of the C contamination which occurs apparently due to the presence of the organic liquid. We intend to also evaluate dry oscillatory grinding for (U,Pu)N. A grinder has been purchased and is on hand. An inert atmosphere glove box has been ordered. The vendor presently is in the midst of a strike and the original delivery date of March 30, 1971 has been indefinitely postponed.

Characterization of Nitride Fuels

V. J. Tennery

X-Ray Diffraction Studies of Uranium-Plutonium Nitrides (V. J. Tennery)

We are in the process of completing the x-ray self-damage study of (U,Pu)N and will terminate this work as of June 30, 1971. Our measurements will consist of data for (U,Pu)N solid solutions for a period of about 1.3 years from the date of the last high temperature anneal for the samples.

Development of the Dumas Technique for the Determination of Nitrogen in (U,Pu)N (V. J. Tennery and J. L. Botts*)

The Kjeldahl method is the standard technique used in the FFTF program for N analysis of the oxide and nitride fuels. However, this technique characteristically gives significantly lower results when sesquinitride phases are present. Lindemer and Bradley,[4] have observed that the use of N_2-H_2 gas mixtures for reducing mixed oxides can result in the solution of N into the fluorite lattice of the oxide and the subsequent precipitation of a M_2N_3-type phase. Consequently, the dissolution step in the Kjeldahl analysis may result in low N values since the M_2N_3 phase is very difficult to dissolve in acids. When a mononitride phase is present the dissolution procedure used prior to the Kjeldahl determination is of utmost importance if N losses are to be avoided prior to the distillation and titration steps of the analysis.

We have compared the N values determined for a sample of $(U_{0.8},Pu_{0.2})N$ using HCl + HF and H_3PO_4 for dissolution of the samples. The use of Cu selenate in the dissolution was also investigated. The results obtained for a number of N determinations of (U,Pu)N are given in Table 2.3. The use of H_3PO_4 is superior to other acids for dissolution of nitride samples. Copper selenate was found to be unsatisfactory. The Dumas method for N determinations has been found to be satisfactory for both mononitrides and sesquinitride phases.

Our experiences with the Kjeldahl method have been unsatisfactory for nitride samples containing the M_2N_3 sesquinitride type of phase. The principal problem as mentioned previously is in the inability to achieve complete dissolution in acids and the tendency to lose some of the N from the sample as gaseous N rather than complexing it in the dissolution liquid. To overcome these difficulties we have assembled a Dumas N analysis facility and have evaluated it by analyzing several UN samples including UN and U_2N_3. The method involves the oxidation of a sample with the subsequent release of N, followed by the quantitative

---

*Analytical Chemistry Division

Table 2.3. Comparison of Dissolution Methods for Sample of $(U_{0.8}Pu_{0.2})N$

Dissolution Acid	Analyzed Nitrogen[a] Content, wt %	Total Nonmetal[b] Content, wt %
H_3PO_4	5.44, 5.45, 5.46	5.53
HCl + HF	5.14, 5.15, 5.01	5.24

[a] Triplicate aliquots were analyzed as shown.

[b] Oxygen plus carbon content of sample was 0.093 wt %.

collection and measurement of the N gas. This method is capable of analyzing the N in U_2N_3 phases as easily as mononitride phases since it is not dependent upon a dissolution step.

Typical N results obtained on sintered UN (sample A), UN powder (sample B), and UN_x (sample C) as well as the other major elements are given in Table 2.4. From these data it is obvious that sesquinitride-type phases can be analyzed readily for N using the Dumas technique.

Study of Coulometric Methods for the Determination of Actinide Metals in (U,Pu)N (V. J. Tennery and J. L. Botts*)

During this report period we made a study of the dependence of the determined U value in UN as a function of the type of vessel used for sample dissolution. The samples were analyzed coulometrically in three different laboratories at ORNL in order to determine if significant variations in the determinations occurred from this source.

The UN used for the investigation was the sintered sample A material in Table 2.4. The three kinds of dissolution containers studied were reflux condenser, Erlenmeyer flask, and simple beaker. Twenty samples of UN, sample A, were dissolved under carefully controlled conditions with the only variable being the dissolution vessel. The samples were then titrated electronically by the standard method and the results are given in Table 2.5. It is clear from these results that only the reflux condenser type of dissolution vessel is suitable for nitrides if a negative actinide metal bias is to be avoided in the analysis. The susceptibility to a negative bias of the N determination and the results just presented can lead to inaccurate determinations of both actinide metal and N in these materials with a resultant metal/nonmetal ratio near unity which is not indicative of the true composition of the sample.

Compatibility of Mixed Nitrides and Carbides with LMFBR Cladding Alloys (J. M. Leitnaker)

Our approach to compatibility in high-performance fuel systems is to characterize interactions that can occur between the fuel and cladding material. A basic understanding of these reactions may point to methods

---

*Analytical Chemistry Division

Table 2.4. Chemical Analysis Results for UN and UN_x Phases

	Dumas			Kjeldahl[b]			Content, wt %				
Sample	Determinations	% N	% S[a]	Determinations	% N	% S	U[c]	O	C	Percent Mass Balance[d]	Mole Ratio[d] N + O + C/U
A	36	5.47	0.35	19	5.49	0.90	94.48	0.029	0.04	100.02	0.997
B	17	5.46	0.34				94.44	0.049	0.04	99.99	0.999
C	17	8.40	0.32				91.55	0.028	0.03	100.01	1.571

[a] % S = relative standard deviation; $\% S = \frac{s \times 100}{\bar{x}}$ where s = standard deviation of a set and $\bar{x}$ = mean of the set.

[b] Phosphoric acid dissolution was used.

[c] Uranium was determined gravimetrically.

[d] The Dumas nitrogen results were used for this calculation.

Table 2.5. Effect of Dissolution Vessel Geometry Upon Coulometric Uranium Determination in UN, Sample A

Sample No.	Vessel	Wt % Uranium[a]			% Deviation from Theo[b]		
		Lab A	B	C	Lab A	B	C
1–7	Reflux	94.42	94.37	94.41	–0.05	–0.11	–0.06
8–15	Flask	94.35	94.36	94.34	–0.13	–0.12	–0.14
16–20	Beaker	94.03	94.02	94.03	–0.46	–0.48	–0.46

[a] The results are an average of three determinations from each dissolution; i.e., an average of 21, 24, and 15 determinations, respectively. The relative standard deviation for each set of results was % S $\leq$ 0.07%.

[b] U content of $^{238}U^{14}N$ = 94.47%.

for tailoring the fuel so that the reactions cannot occur and perhaps to methods for hindering these reaction kinetics.

Pu-Cr-N System (J. P. DeLuca)

The investigation of the Pu-Cr-N system has continued this quarter with the heat treating of two additional mixtures of Pu, Cr, and N. Enough information has been acquired to date to allow us to present the ternary phase diagram of the Pu-Cr-N system between 800 and 1700°C at 1 atm total pressure.

The results of the first five samples were discussed previously[5] and a tentative phase diagram of the Pu-Cr-N system was prepared. The experiments performed this quarter further verify the ternary phase diagram of the Pu-Cr-N system. The two experiments to be described were attempts to produce a ternary Pu-Cr-N compound. Such a compound has as yet not been reported, although Spear *et al.*[6] have reported and Benz *et al.*[7] have indexed a ternary U-Cr-N compound. Benz reported the stoichiometry of the ternary compound U_2CrN_3 (note: $N/M = 1$). He also reported the existence of Th_2CrN_3.

Sample Pu-Cr-N-11 was hot pressed. The starting material for this experiment was obtained from one of the pellets of sample Pu-Cr-N-7. The pellets were crushed and placed in the graphite die within a Ta liner and end pieces. The pressure was held at approximately 5300 psi and the temperature was 1130 ± 20°C. The sample was hot pressed for 6 hr and 15 min. Because there was no provision to hold a static N_2 pressure over the sample, N_2 gas was purged into the box at a rate such that if good mixing occurred the sample would have seen a partial pressure of N_2 of 2.1 torr. After the heat treatment the sample was rapidly cooled by dropping it out of the hot zone of the furnace.

From visual examination of the sample it was observed that the PuN-Cr_2N compact had not reacted with the Ta liner and the compact had sintered well. Other samples run at similar temperatures but with no mechanical pressure did not sinter appreciably.

X-ray analysis of this sample showed that there were two condensed phases present, Cr_2N and PuN. Also, the lattice parameter of PuN for this sample was determined to be 4.9059 A ± 0.0001 A very nearly that of single phase PuN, 4.9049 A,[8] indicating no reaction between Cr_2N and PuN. This agrees with the Pu-Cr-N diagram in Fig. 2.1. This sample lies on a constant Pu/Cr ratio line in the shaded field of PuN and Cr_2N. This has been true of all samples examined in this system. PuN does not react with the Cr compounds and the resulting Cr compounds could always be predicted from examination of the Cr-N binary system.

In a second attempt to produce a ternary compound, PuH_3 was used. The single phase CrN was produced by heating Cr powder at 900°C in 1 atm NH_3. The PuH_3 was prepared by heating Pu metal under 1 atm of H_2 at 250°C. A pelletized sample of 78.8 a/o Cr composed of PuH_3 and CrN was heated for 148 hr under 1 atm N_2.

The pellets did not sinter and x-ray analysis clearly showed that there were only two phases present, PuN and CrN, thus confirming the single earlier result that there is a conode between CrN and PuN.

As a result of these last two experiments, it appears that Fig. 2.2 is an accurate representation of the Pu-Cr-N ternary phase diagram within the temperature range from 790 to 1705°C and a N_2 pressure range of 2×10^{-7} to 760 torr.

In this three-component system if one assumes that Pu has a negligible effect on the equilibrium N_2 pressure of the Cr nitride, then one can tabulate, for any given temperature, the N pressure across the two-phase fields and the N_2 pressure required to have three condensed phases in equilibrium in the Pu-Cr-N system. These pressures and temperatures are shown in Table 2.6.

Irradiation Testing of Mixed Nitrides

T. N. Washburn

Thermal Flux Tests (T. N. Washburn)

The initial series of irradiation tests are two capsules of four pins each, noninstrumented, and conducted in the ETR. These tests are of the "screening" type to evaluate the performance of nitride fuel synthesized from metal. The peak linear heat rating is 30 kW/ft to burnups to 30,000 and 60,000 MWd/metric ton. The fuel is cold-pressed

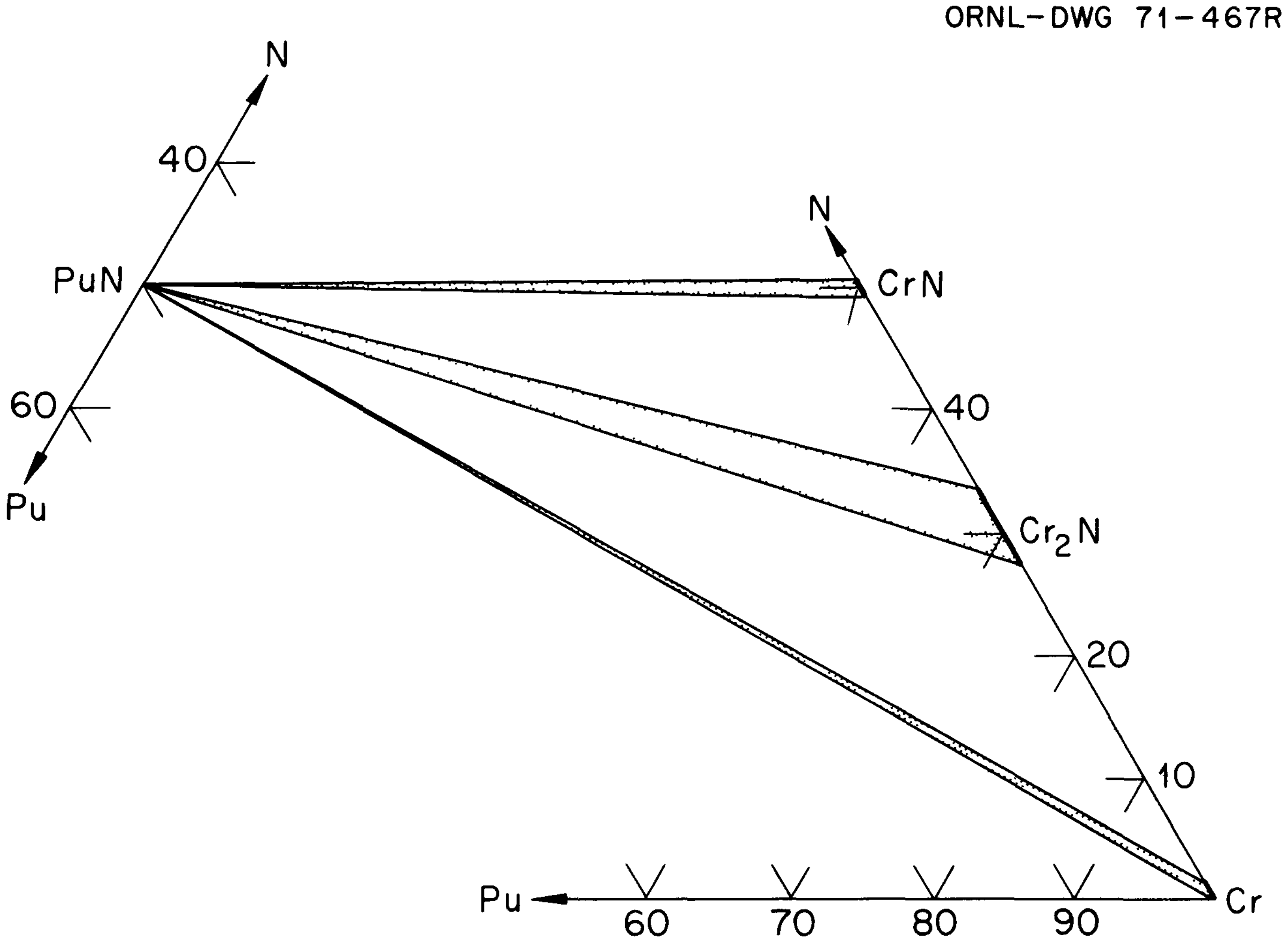

Fig. 2.2. Partial Pu-Cr-N Phase Diagram from 790 to 1705°C.

Table 2.6. Temperature, Pressure, and Phase Relations in the Pu-Cr-N System

Phases in Equilibrium	$\text{Log}_{10}\ P_{N_2}$ (atm)			
	800°C	1000°C	1200°C	1400°C
$(Cr)_N$-PuN	$-10.5 < \log P < -5.1$	$-7.9 < \log P < -3.4$	$-5.9 < \log P < -2.2$	$-4.8 < \log P < -1.3$
$(Cr)_N$-Cr_2N-PuN	-5.1		-2.2	-1.3
Cr_2N-PuN	$-5.1 < \log P < -1.9$	$-3.4 < \log P < 0.15$	$-2.2 < \log P < 1.1$	$-1.3 < \log P < 2.1$
Cr_2N-CrN-PuN	-1.9	-0.15	1.1	2.1
CrN-PuN	$-1.9 < \log P$	$-0.15 < \log P$	$1.1 < \log P$	$2.1 < \log P$

pellets with densities from 86 to 81% of theoretical, and the fuel pins have a 0.010-in. radial gap between the fuel pellet and cladding ID. This gap is filled with NaK-19 to enhance heat transfer.

Capsules 43-N1 and 43-N2 were neutron radiographed at TREAT prior to insertion into the ETR during cycle 110 shutdown. The reactor went to full power on December 9, 1970; as of March 20, 1971, the capsules have operated for approximately 65 EFPD at a burnup of approximately 1.7% FIMA.

Fast Flux Test (E. J. Manthos, M. K. Preston, and J. H. Erwin)

Seven unencapsulated fuel pins, five for testing and two for spares, are being fabricated for testing in an EBR-II E-19 subassembly. The 19 pin subassembly will be shared with Battelle Memorial Institute, Columbus Laboratories (BCL) in a cooperative effort. A description of the ORNL fuel pins is shown in Table 2.7.

Table 2.7 Series I — Unencapsulated Fuel Pins For Irradiation Testing in EBR-II

Fuel		Fuel Pin	
Composition	$(U_{0.18},Pu_{0.82})N$	Smear density, % T.D.	78
Enrichment, % ^{235}U	93	Na bond thickness, in.	0.010
Pellet diameter, in.	0.260	Fuel column length, in.	13.5
Pellet density, % T.D.	~90	Overall length, in.	40
Cladding		Operating Conditions	
Material	316 SS	Linear heat rating, W/ft	30
OD, in.	0.310	Specific power, kW/gm	220
Wall thickness, in.	0.015	Peak cladding temp, °C	~650
Condition, % cold work	20	Fuel centerline temp, °C	~1050

The same cladding tubing and end fitting rod stock will be used by BCL and ORNL. The tubing has been received and was fabricated by Carpenter Technology Corporation from vacuum melted stock to FFTF specification A-0086. Overinspection of the tubing was performed by WADCO for both BCL and ORNL.

The end fitting and stock was fabricating by ORNL from the same vacuum melted stock that the cladding tubing was made. The finished rod stock was inspected by ORNL and is also being characterized by ORNL. One hundred and sixty feet of the rod was shipped to BCL and 100 ft retained by ORNL.

The fabrication and quality assurance plan MET-FCT-FQ-7 has been written. The final engineering drawing M-11310-EN-008 was accepted and issued. The fabrication procedure for the fuel pins was written and is being reviewed. In addition, numerous other procedures have been revised and/or addenda have been written to describe operations referred to in the fabrication procedure.

An ultrasonic transducer probe and penetrator were purchased and used to Na bond some dummy stainless steel pellets in simulated fuel pins. The method appears promising and consists of the following: Solid Na encased in a stainless tube open at both ends is added to the top of the pellet column and the fuel pin is backfilled with He and sealed. The fuel pin is loaded into a stainless steel support tube which is positioned on the ultrasonic probe. They are then vibrated ultrasonically for about 30 min at a temperature of 400–500°C. The support tube and fuel pin are then withdrawn and preferentially slowly cooled (30 min) in water from the bottom to the top. We plan to Na bond dummy fuel pins loaded with depleted UN pellets to determine the conditions which yield the best bond.

Fabrication of the fuel pin interior components and end fittings has commenced and should be completed late in April. All of the hardware necessary for weld qualification, Na bond tests, Xe tagging test, archive rods, and the EBR-II pins is being fabricated. Machining of the cladding tubing should be completed at about the same time also. All of the data forms necessary for the inspections of the fuel pin components have been prepared.

Other hardware items such as the x-ray radiography shape correction form, weld diameter gages, end plug placement tools, and welding heat sinks have been fabricated.

All of the depleted UN pellets to be used in the development of the final Na bond technique have been fabricated and machined. Two more batches will be completed in April. Grinding to final diameters of the U-PuN pellets should commence late in April or early in May. All of the UN insulator pellets to be used in the EBR-II pins have been made and machined.

References

1. E. S. Bomar and V. J. Tennery, Fuels and Materials Development Program Quart. Progr. Rept. March 31, 1970, ORNL-4560, pp. 40–45.
2. J. P. DeLuca, Fuels and Materials Development Program Quart. Progr. Rept. December 31, 1970, ORNL-TM-3300, pp. 75–77.
3. E. S. Bomar and V. J. Tennery, Fuels and Materials Development Program Quart. Progr. Rept. December 31, 1970, ORNL-TM-3300, pp. 69–73.
4. T. B. Lindemer and R. A. Bradley, Metals and Ceramics Division, Oak Ridge National Laboratory, private communication.
5. J. P. DeLuca, Fuels and Materials Development Program Quart. Progr. Rept. December 31, 1970, ORNL-TM-3300, pp. 81–86.
6. K. E. Spear and J. M. Leitnaker, "Phase Investigations in the U-Cr-N System," to be published.
7. R. Benz and W. H. Zachariasen, "Crystal Structure of Th_2-CrN_3, Th_2MnN_3, U_2CrN_3, and U_2MnN_3," J. Nucl. Mater. **37**, 109–113 (1970).
8. V. J. Tennery and E. S. Bomar, "Lattice Parameter of (U,Pu)N Solid Solutions," J. Amer. Ceram. Soc., **54**(5), 1971.

3. MECHANICAL PROPERTIES OF ALLOYS IN REACTOR ENVIRONMENTS AND DEVELOPMENT OF LMFBR CLADDING AND STRUCTURAL MATERIALS

J. R. Weir, Jr. and H. E. McCoy, Jr.

The main emphasis of this program is on austenitic stainless steels. Included in our work are types 304 and 316 stainless steel and Ti-modified types 304 and 316 stainless steel. Types 318, 19-9-DL, and 12R72HV stainless steel have also been included in recent experiments inserted into the Experimental Breeder Reactor-II (EBR-II). The irradiation effects are determined by measurements of swelling and mechanical properties after irradiation. Experiments are run in three reactors: the EBR-II, the Oak Ridge Research Reactor (ORR), and the High-Flux Isotope Reactor (HFIR). Comparative results should reveal any effects of flux and reactor spectrum. Specimens of each material are irradiated in a variety of conditions so that the effects of irradiation temperature, fluence, and metallurgical condition can be evaluated.

Several specimens of Ta from the General Electric Nuclear Systems Programs experiments were examined by transmission electron microscopy. The activity level of these samples required that we develop techniques for thinning specimens in the hot cell.

Some work on Al-base alloys is also described in this section, although it is supported by the Division of Research. This work is important for several reasons: (1) since several reactors now in operation use Al as a structural material, any limits on their period of operation must be determined; (2) irradiation damage to Al alloys parallels in many ways that observed in austenitic stainless steels; and (3) since the fluence required to initiate swelling in pure Al is relatively low, fluences that produce large amounts of swelling can be obtained in short periods of time. This last characteristic makes it possible to observe the variation of swelling with fluence over a wide range of variables.

Austenitic Stainless Steels

Swelling of Type 304 Stainless Steel (E. E. Bloom, J. O. Stiegler)

Immersion density measurements on type 304 stainless steel irradiated at about 590°C to fluences in the range of 2.0 to 3.5 X 10^{22} neutrons/cm^2 (> 0.1 MeV) suggested that the density decrease for this irradiation temperature was a much stronger function of the fast neutron fluence than at lower irradiation temperatures.[1] To further investigate this possibility we have examined by transmission electron microscopy specimens of type 304 stainless steel irradiated at 590°C to 1.8 X 10^{22}, 2.3 X 10^{22}, and 3.5 X 10^{22} neutrons/cm^2. The specimens were from the same heat of material and were irradiated in the annealed condition.

The size distributions and concentrations of voids are shown in Fig. 3.1. At a fluence of 1.75 X 10^{22} neutrons/cm^2 there were 8 X 10^{13} voids per cubic centimeter with diameters in the range of 75 to 460 A. Increasing the fluence to 2.25 X 10^{22} neutrons/cm^2 produced an increase in both void concentration and mean and maximum void diameters. A further increase in fluence to 3.5 x 10^{22} neutrons/cm^2 produced only a small increase in void concentration, but shifted the size distribution curve to larger sizes. In the highest fluence specimen no voids smaller than about 180 A were observed. Thus, it appears that at irradiation temperatures close to the upper limit for void formation (such as 590°C) the nucleation rate decreases sharply at fluences of about 3 to 4 X 10^{22} neutrons/cm^2, but that void growth continues. The volume changes calculated from transmission electron microscopy were 0.036%, 0.11%, and 0.31% in order of increasing fluence. The immersion density measurement on the bulk specimen irradiated to 3.5 X 10^{22} neutrons/cm^2 gave a density decrease of 0.34%, in good agreement with the value calculated from electron micrographs.

Thus, it appears that over this range of fluence the density change is approximately proportional to $(\phi t)^5$. For these three specimen the mean and maximum void diameters increased as $(\phi t)^{0.5}$. Since void nucleation appears to have ceased, the swelling should become proportional to $(\phi t)^{1.5}$ for fluences greater than about 4 X 10^{22} (> 0.1 MeV). Figure 3.2 shows the available swelling data for type 304 stainless steel

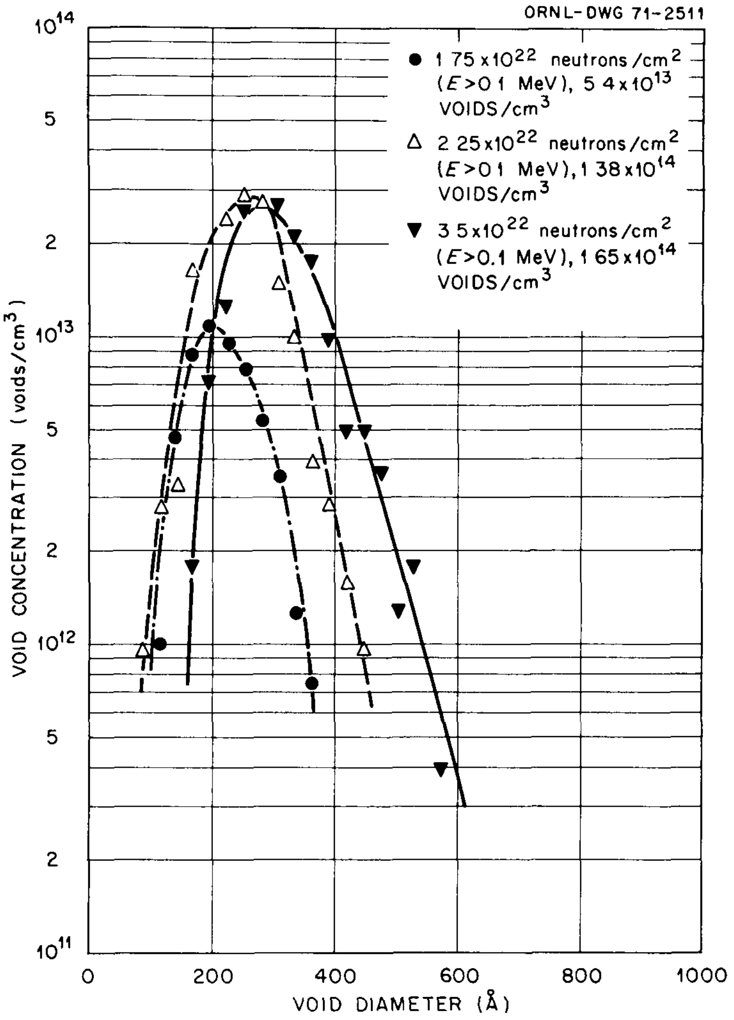

Fig. 3.1. Effect of Fast Neutron Fluence on the Void Size Distribution in Type 304 Stainless Steel Irradiated at 590°C.

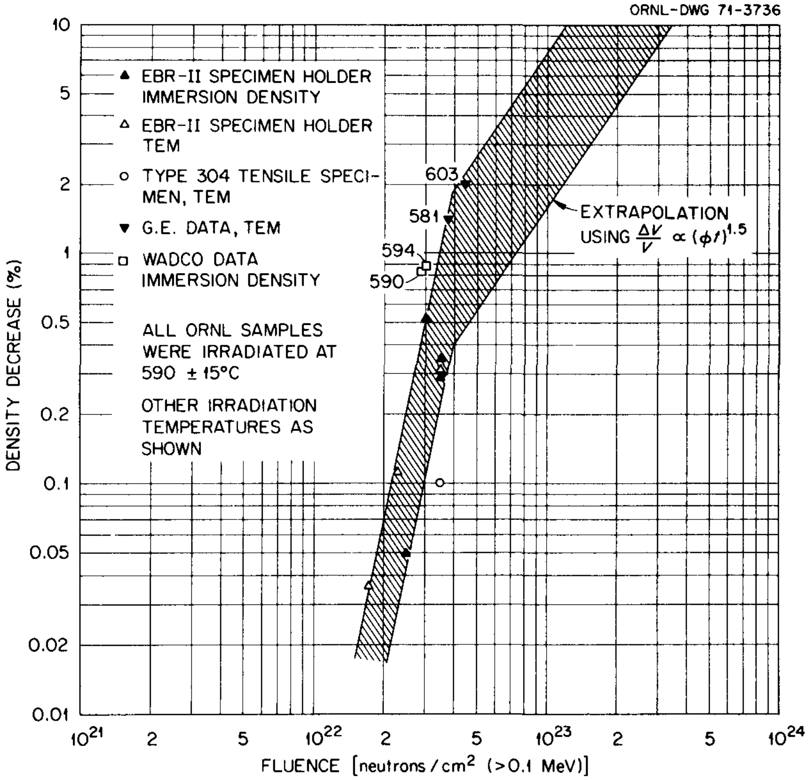

Fig. 3.2. Swelling of Annealed Type 304 Stainless Steel at 590°C.

irradiated at about 590°C and an extroplation of these data using the transmission electron microscopy observation that nucleation has ceased and the void diameters are increasing as $(\phi t)^{0.5}$.

The Effect of Thermo-Mechanical Treatments on Void Formation in Irrairradiated Stainless Steel (J. O. Stiegler, E. E. Bloom)

Although swelling resulting from the formation of voids is commonly observed in metals irradiated at temperatures between about 0.3 and 0.5 of their absolute melting temperatures, there are indications that purity and structure are important factors governing the kinetics of nucleation and growth of the voids. For example, among the (fcc) metals, voids appear to form more easily as purity increases,[2,3] but even in specimens of comparable purity gross differences may exist in the sizes and concentrations of voids.[4] Even in alloys as complex as the austenitic stainless steels, small changes in composition alter the appearance of the voids. Voids in type 347 stainless steel are more numerous and smaller than those in type 304 stainless steel,[5] and the addition of 0.2 wt % Ti to type 304 stainless steel appreciably reduces the concentration of voids in specimens irradiated at 450°C (ref. 6).

In principle, structural imperfections such as dislocations and grain boundaries (which act as sinks for vacancies and interstitials) and He atoms ought to influence the formation of voids. Although this possibility has been less extensively studied, preliminary results indicate a strong effect. Farrell and Houston[7] studied the distribution of voids in cold-worked Fe that had partially recrystallized during irradiation. Voids were both more numerous and larger in recrystallized regions than in non-recrystallized areas that contained a fine cell substructure. Bullough, Eyre, and Perrin,[8] in a theoretical analysis of the kinetics of void growth, concluded that cold working should have a beneficial effect on swelling, at least at low fluences, by suppressing the concentration of vacancies and thus the rate of void growth. They pointed out that at high fluences the kinetics of void growth followed a $(\mathrm{time})^{1.5}$ law in annealed materials and a $(\mathrm{time})^{4}$ law in cold-worked ones; therefore, a point could be reached at which cold-worked materials would swell more than annealed ones. This treatment neglected the nucleation of voids and assumed equal concentrations of voids in annealed and cold-worked materials.

We began an experiment to examine the effect of dislocation density on the formation of voids in type 304 stainless steel. Two specimens were deformed 10% by swaging at room temperature before irradiation; one was irradiated in the cold-worked condition and the other was annealed first 24 hr at 482°C and then 100 hr at 700°C to produce a recovered microstructure. This is a common strengthening treatment for this alloy. The specimens were mounted in an annealed type 304 stainless steel holder and irradiated in a row 2 position of the EBR-II at 450±15°C at a flux of 1.4×10^{15} neutrons/cm^{+2} sec^{+1} to a fluence of 2.5×10^{22} neutrons/cm^2 (> 0.1 MeV). This irradiation is estimated on the average to displace each atom 28 times. After irradiation, density changes of the specimens and the holder were measured by an immersion technique, and the concentrations and sizes of voids were determined by transmission electron microscopy.

Micrographs illustrating typical void distributions in the annealed, recovered, and cold-worked specimens are shown in Fig. 3.3. The void concentration was about an order of magnitude lower in the cold-worked specimen than in the recovered and annealed specimens, (2.1×10^{14} vs 1.9 and 2.0×10^{15} voids/cm^3, respectively).

Void sizes differed significantly among the three conditions. On the average voids were smallest in the cold-worked specimen and largest in the recovered one. Histograms of the void size distributions are shown in Fig. 3.4, and statistics describing the void population and swelling are given in Table 3.1. Void size and concentration parameters for annealed type 304 stainless steel calculated from the empirical equation developed by Brager et al.,[9] also given in Table 3.1, are within a few percent of the experimentally determined values. Extremely good agreement exists between calculated and measured density changes for the annealed material. The differences for the cold-worked and recovered materials may be a result of densification during irradiation from precipitation of carbides and σ phase. The density changes derived from electron microscopy are probably a better description

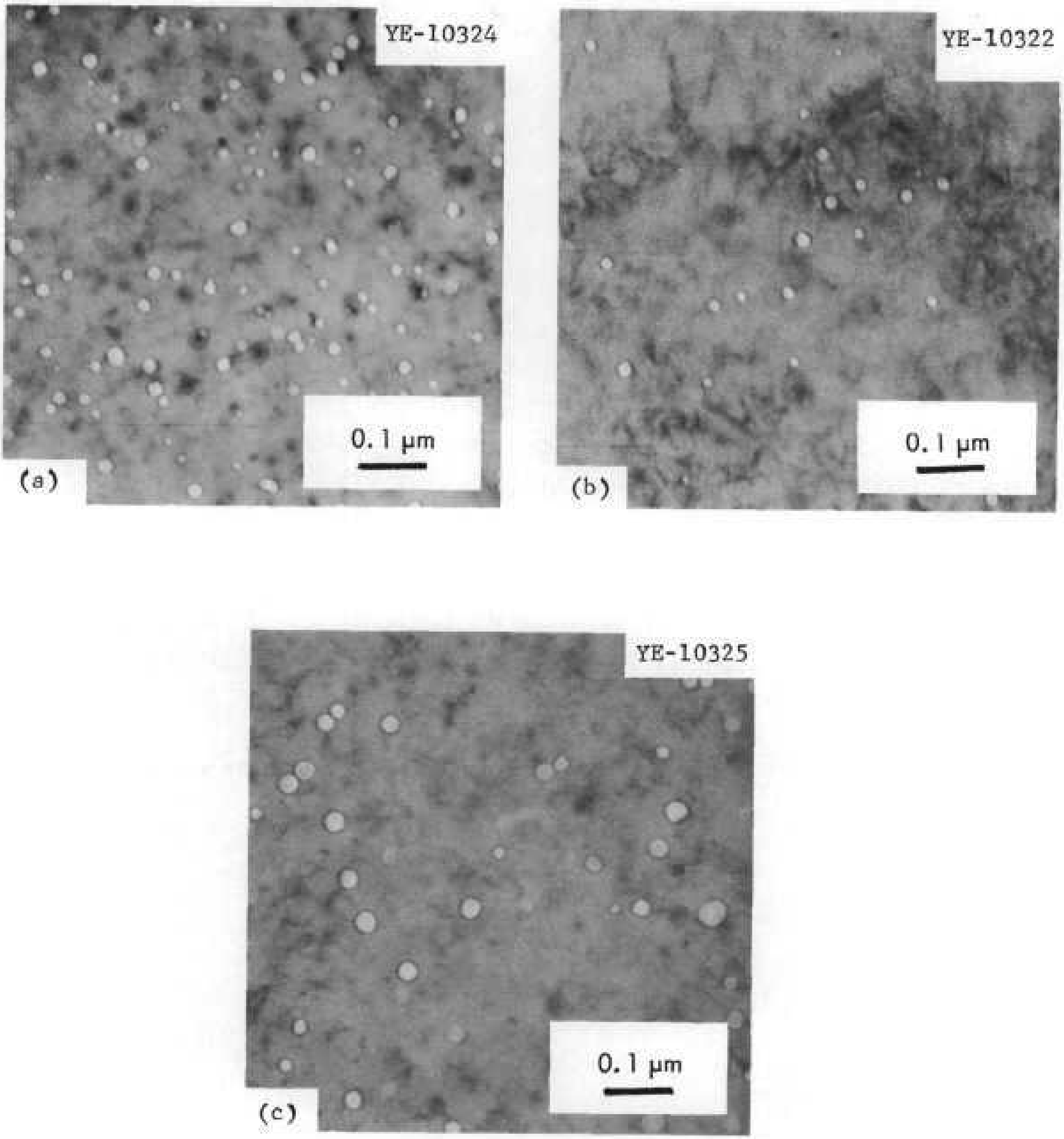

Fig. 3.3. Transmission Electron Micrographs Illustrating the Void Populations in Type 304 Stainless Steel Irradiated in EBR-II to a Fluence of 2.5×10^{22} neutrons/cm^2 (> 0.1 MeV) at 450°C. (a) annealed and fully recrystallized before irradiation, (b) cold worked 10% by swaging before irradiation, and (c) cold worked 10% by swaging, then annealed 24 hr at 482°C and 100 hr at 700°C before irradiation.

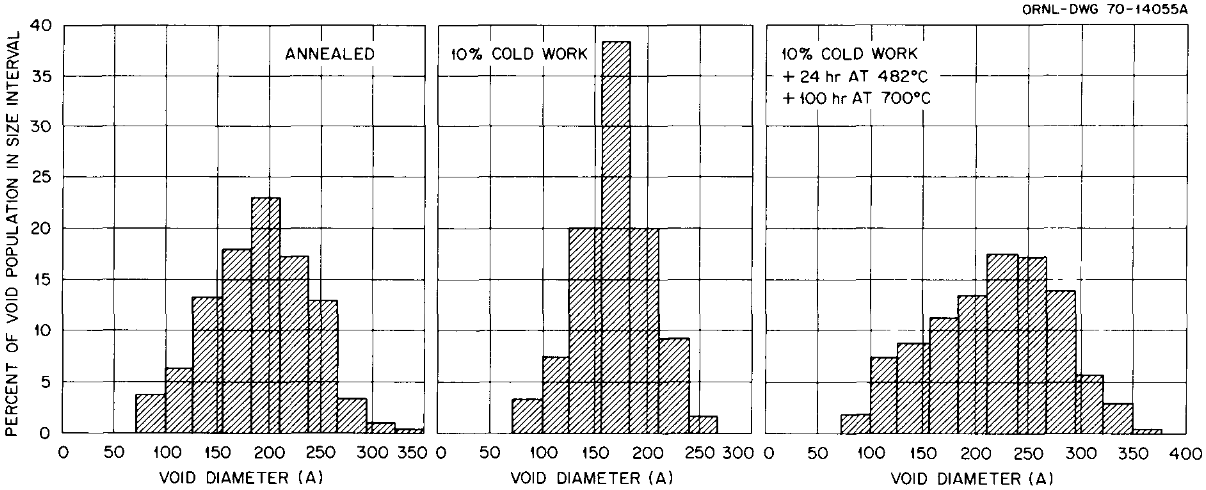

Fig. 3.4. Void Size Distributions for the Specimens Shown in Fig. 3.3.

Table 3.1. Concentration and Size of Voids and Swelling in Irradiated Type 304 Stainless Steel

Material Condition	Concentrations of Voids (voids/cm^3)	Average Diameter of Voids (A)	Calculated Void Volume (%)	Measured Density Change (%)
Annealed				
Measured	2.0×10^{15}	193	0.89	-0.88
Calculated[a]	1.88×10^{15}	189	0.88	-
Cold Worked 10%	2.1×10^{14}	170	0.06	+0.08
Cold Worked 10%, Annealed 24 hr at 480°C and 100 hr at 700°C	1.9×10^{15}	220	1.28	-0.62

[a] H. R. Brager et al., Irradiation Produced Defects in Austenitic Stainless Steel, WHAN-FR-16 (December 1970).

of swelling due to void formation during irradiation than are those based on immersion density. The net density change is, of course, given by the immersion measurement.

In summary, the cold-worked specimen swelled appreciably less than the annealed one because of a large decrease in void concentration; void sizes were only slightly smaller. On the other hand, the recovered specimen swelled more than the annealed one because of an increase in void sizes; concentrations were not affected.

Although the voids tended to be distributed in patches in the cold-worked specimen, the general microstructure of the specimen was too complex to reveal any relationship between the voids and deformation features. The structure consisted basically of a relatively uniform distribution of dislocations interspersed among platelets of ϵ phase. The dislocation density was too high to measure.

The recovery treatment reduced the density of dislocation to about 10^{10} cm/cm^3 and resulted in precipitation of small carbides (about 100 A in diameter) on the dislocations. Some sheets or platelets of what was probably a recovered form of the ϵ phase were also present.

After irradiation, the platelets were decorated by $M_{23}C_6$ precipitates. Areas adjacent to the ε platelets were denuded of voids, but within about 1000 A of the platelets the void population assumed its general form.

It is clear from this work that under at least some irradiation conditions cold working is an effective means of retarding swelling, but that the presence of high sink densities is no guarantee that swelling will be reduced. Indeed, it may be enhanced. Electron microscopy reveals some possible reasons why very high dislocation densities retard swelling and moderately high densities enhance it. A dislocation density of 10^{10} cm/cm^3 has no influence on void nucleation but apparently does increase the rates of void growth. During irradiation, voids absorb both vacancies and interstitials, and their rate of growth depends on differences in the rates at which point defects arrive. It is generally accepted that voids are able to grow because dislocations preferentially remove interstitials from the system due to the stronger elastic interaction between interstitial atoms and dislocations than between vacancies and dislocations.[8,10,11] In effect, a dislocation line has a greater capture volume for interstitials than for vacancies. When the density of dislocation is extremely high, as in the cold-worked material, the dislocations act as efficient sinks for both vacancies and interstitials and thus depress the concentrations of both. When the density of dislocations is lower as in the recovered material, the dislocations still act as efficient sinks for the interstitial atoms but not for vacancies because of the higher mobility and volume for capturing interstitials. As a result, voids experience a greater net concentration of vacancies and thus grow at a faster rate than in materials that are free of dislocations.

The greatly reduced swelling in the cold-worked material could arise because the high density of dislocations reduces the concentrations of both interstitials and vacancies. This should increase the critical void nucleus size and also reduce the driving force for void growth. The main difference between the cold-worked and annealed specimens, however, was in the void concentrations; void sizes were only slightly affected. Nucleation of voids is known to be stimulated strongly by the He produced in these materials by transmutation reactions.[12,14] In fact, in stainless steel specimens irradiated at temperatures above about 500°C, voids are usually located on dislocations and precipitate particles,[15] both of which are known to be preferred sites for precipitation of He bubbles. The high density of dislocations may suppress nucleation of voids by trapping He atoms, either individually or in groups too small to stabilize nucleation of voids under the available vacancy supersaturation. If this latter mechanism is responsible for the reduced concentration of voids in the cold-worked specimen, the beneficial effect of cold work may be lost at higher fluences where the continuously increasing concentration of He may allow growth of subcritical nuclei into voids. The larger number of trapping sites in the cold-worked material may increase the concentration of voids to a value higher than that in annealed materials.

The physical basis for the suggestion that at high fluences swelling in cold worked materials may exceed that in annealed ones is different from that offered earlier by Bullough _et al_.[8] They suggested that cold working would alter growth rates and kinetics but not the process of nucleation. At low fluences, the reduction in swelling is largely caused by a reduced concentration of voids. This may be reversed at high fluences if He is responsible for nucleation of voids.

Cold working has been shown to reduce swelling substantially in stainless steel irradiated to a fluence of 2.5×10^{22} neutrons/cm^2 at 450°C. There is reason to use caution in extrapolating this conclusion to irradiations to higher fluences. Furthermore, the cold-worked microstructure will be effective in reducing swelling only at irradiation temperatures below which significant recovery occurs. If recovery does occur during the early stages of irradiation, for example, swelling may be increased.

Mechanical Properties of Standard and Titanium-Modified Types 316 Stainless Steel (E. E. Bloom, D. Fahr)

The effects of fast neutron irradiation and thermal aging on the tensile and creep-rupture properties of standard and Ti-modified types 316 stainless steel are being investigated. Specimens have been irradiated in the annealed and cold worked conditions at temperatures of 450 to 850°C and to fast neutron fluences up to 2.7 X 10^{22} neutrons/cm^2 (> 0.1 MeV). Annealed and cold worked specimens have been aged at temperatures of 350 to 750°C to times of 4000 hr and are being tested to determine the effects of annealing on the mechanical properties.

Yield stress as a function of test temperature for annealed and 20% cold worked type 316 stainless steel is shown in Fig. 3.5. In the annealed condition aging for 4000 hr at temperatures up to 550°C caused no change in yield stress while aging at 650°C increased the yield stress from 19,000 to 27,000 psi. This strengthening is apparently caused by carbide precipitates formed in the matrix during aging at 650°C (ref. 16). As shown in Table 3.2 specimens aged at 650°C and tested at 550 and 650°C exhibited the increased yield stress while specimens aged at 550°C and tested at 550 and 650°C did not. Irradiation at temperatures below about 700°C resulted in an increased yield stress as compared to the annealed condition. At the lower irradiation temperatures (below 600°C) the strengthening is due to the radiation produced voids and dislocation loops;[17,18] while at the higher temperatures (above 600°C) precipitation of carbides and possibly sigma phase may be controlling. Thermal aging and neutron irradiation caused a decrease in the yield stress of the 20% cold worked material at all temperatures in the range 450 to 700°C.

Table 3.2. Effect of Aging and Test Temperature on the Yield Stress of Type 316 Stainless Steel

Aging Treatment	Test Temperature °C	Yield Stress psi
4000 hr at 550°C	550	18,600
4000 hr at 550°C	650	17,800
4000 hr at 650°C	550	29,000
4000 hr at 650°C	650	26,900

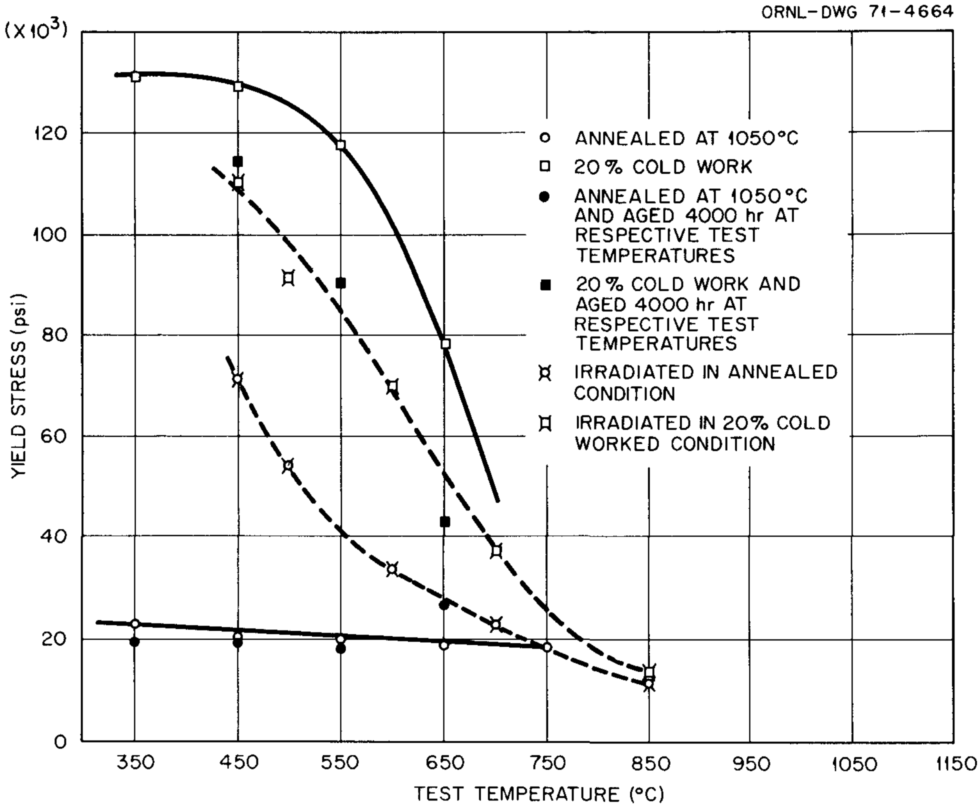

Fig. 3.5. Effect of Irradiation and Thermal Aging on the Yield Strength of Annealed and 20% Cold Worked Type 316 Stainless Steel. Specimens were irradiated at temperatures near the test temperature to fluences in the range 1.2 to 2.3 × 10^{22} neutrons/cm^2 (> 0.1 MeV).

The effects of irradiation and thermal aging on the ductility are quite complicated (Fig. 3.6). In the annealed condition the alloy exhibits a ductility minimum at 650°C. Aging at 650°C increases the total elongation and removes the minimum. Similar behavior was observed in a different heat of type 316 stainless steel used in previous studies.[19] The ductility of specimens irradiated in the annealed condition is lower than that of the control specimens and decreases with increasing temperature. Previous results[18, 20] for type 304 stainless steel have indicated that specimens irradiated and tested at 450°C have reduced uniform strains due to reduced ability of the material to work harden (due to the presence of voids and dislocation loops), and thus necking occurs early in the deformation. At high irradiation and test temperatures the stress-strain behavior is unaffected, but ductility is reduced by premature fracture at grain boundaries. Further reductions in ductility can be expected as the neutron fluence is increased due to the increased concentration of voids and dislocations at low irradiation temperatures and the effects of increased helium concentrations at higher temperatures. Type 316 stainless steel irradiated in the 20% cold worked condition exhibited lower tensile ductility than when irradiated in the annealed condition. At temperatures below 550°C the postirradiation ductility was higher for the as-cold worked or cold worked and aged conditions, possibly due to enhanced recovery of the dislocation structure during irradiation.

Postirradiation tensile properties of Ti-modified type 316 stainless steel at 500 and 600°C are listed in Table 3.3. The yield stress is slightly lower than for standard type 316 stainless steel irradiated at the same temperatures and fluences. Compared with the standard alloy, the uniform strain and total elongation in Ti-modified type 316 stainless steel were slightly higher at 500°C (25.9% and 31.9% vs 24.0% and 27.5%) and higher by about a factor of 2 at 600°C (22.4% and 29.8% vs 12.0% and 14.7%).

Table 3.3. Postirradiation Tensile Properties of Titanium-Modified (0.23% Ti) Type 316 Stainless Steel

Irradiation Temperature oC	Neutron Fluence > 0.1 MeV × 10^{22}	Test Temperature oC	Yield Stress psi	Ultimate Tensile Stress psi	Uniform Strain %	Total Elongation %
510	1.5	500	35,100	78,300	25.9	31.9
630	1.2	600	31,200	56,600	22.4	29.8

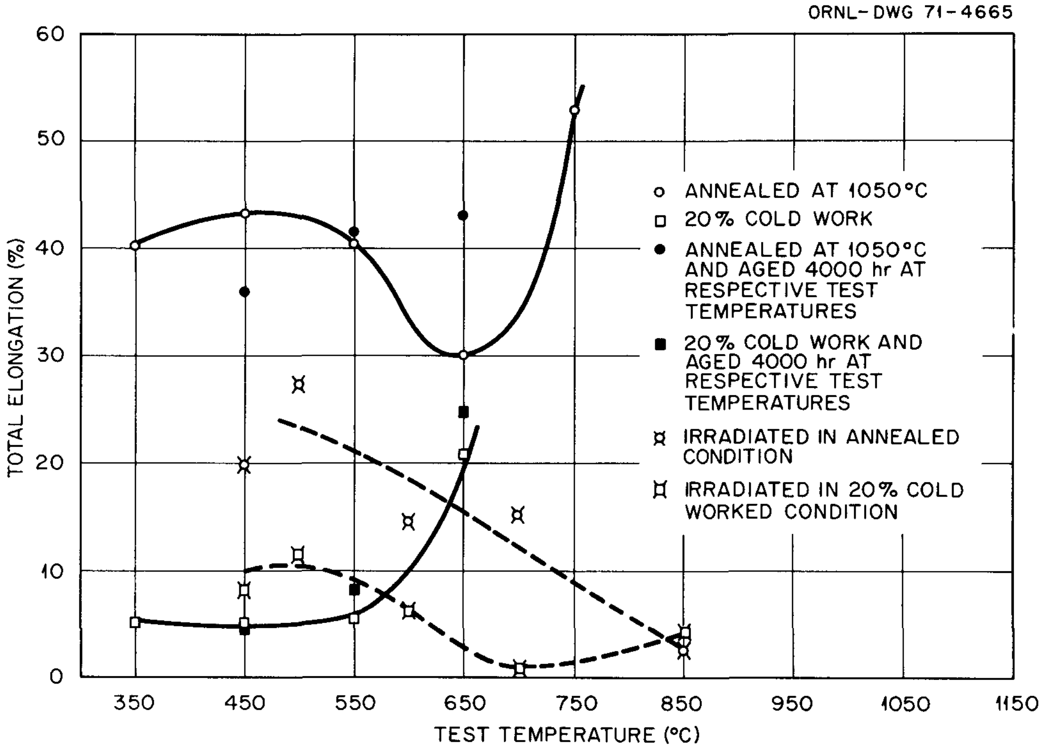

Fig. 3.6. Effect of Irradiation and Thermal Aging on the Elongation of Annealed and 20% Cold Worked Type 316 Stainless Steel. Specimens were irradiated at temperatures near the test temperature to fluences in in the range 1.2 to 2.3 X 10^{22} neutrons/cm^2 (> 0.1 MeV).

Swelling and Microstructural Studies on Standard Titanium-Modified Types 316 Stainless Steel (E. E. Bloom, J. O. Stiegler)

Specimens of standard and Ti-modified (0.23% Ti) types 316 stainless steel have been irradiated in the annealed and 10 and 20% cold worked conditions at temperatures between 450 and 800°C to peak fluences of 2.7×10^{22} neutrons/cm^2 (> 0.1 MeV) in EBR-II subassembly X034A. Postirradiation immersion density and transmission electron microscopy studies are in progress. Presently available immersion density results are listed in Table 3.4. These results may be adjusted as more information on density changes during thermal aging becomes available.

Annealed type 316 stainless steel irradiated at 450°C exhibited a density decrease considerably less than that observed for annealed type 304 stainless steel when irradiated at about 450°C, but approximately the same as expected for annealed type 304 stainless steel when irradiated at 580°C. In the 20% cold worked condition type 316 stainless steel exhibited small but consistent increases in density at all irradiation temperatures for which data are available. Titanium-modified type 316 stainless steel irradiated in either the annealed or 10% cold worked conditions did not undergo a detectable density change.

The microstructures of standard and Ti-modified types 316 stainless steel irradiated in the annealed condition at 580°C to fluences of 1.9×10^{22} and 2.3×10^{22} neutrons/cm^2 (> 0.1 MeV), respectively, are shown in Figs. 3.7 and 3.8. In the standard alloy the dislocation structure consists of Frank Sessile dislocation loops and a dislocation network apparently formed by the unfaulting of Frank loops. The void size distribution has not been measured, but appears to be bimodal with the largest voids being associated mainly with large precipitates and the smaller voids being associated primarily with the needle-like precipitates. The void concentration was 1.03×10^{13} voids/cm^3 in type 316 stainless steel, which is a factor of 4 to 10 less than would be found in standard type 304 stainless steel after a similar irradiation.

The void concentration was less than 1×10^{12} voids/cm^3 in the Ti-modified type 316 stainless steel irradiated to 2.3×10^{22} neutrons/cm^2 at 580°C, which is at least an order of magnitude less

Table 3.4. Irradiation Induced Density Change in Standard and Titanium-Modified (0.23% Titanium) Types 316 Stainless Steels

Irradiation Temperature,[a] °C	Neutron Fluence (> 0.1 MeV) $\times 10^{22}$	Density Change (%)				
		Type 316 Annealed[c]	Type 316, 10% Cold Worked[b,d]	Type 316, 20% Cold Worked[b,d]	Ti-Modified Type 316 Annealed[e]	Ti-Modified Type 316, 10% Cold Worked[b,e]
450	1.9	-0.13	-	-	-0.01	-
515	2.3	-	-	-	0.00	-0.04
480	1.9	-0.14	-	-	-	-
580	2.3	-0.16	-	+0.02	+0.04	-
580	2.7	-0.16	-	+0.07	-0.06	-
610	1.9	-	-0.04	-	-0.01	+0.01
360	2.3	-0.04	+0.07	+0.03	+0.02	-
725	2.3	-0.03	-	+0.06	-	-

[a] Calculated end-of-life irradiation temperature

[b] Specimens were annealed 1 hr at 1050°C and cold worked the indicated amount by swaging at room temperature

[c] Density change based on a control specimen annealed at 1050°C and aged 2000 hr at 550°C

[d] Density change based on a control specimen annealed at 1050°C, cold worked 20%, and aged 4000 hr at 550°C

[c] Density change based on a control specimen of annealed type 316 stainless steel

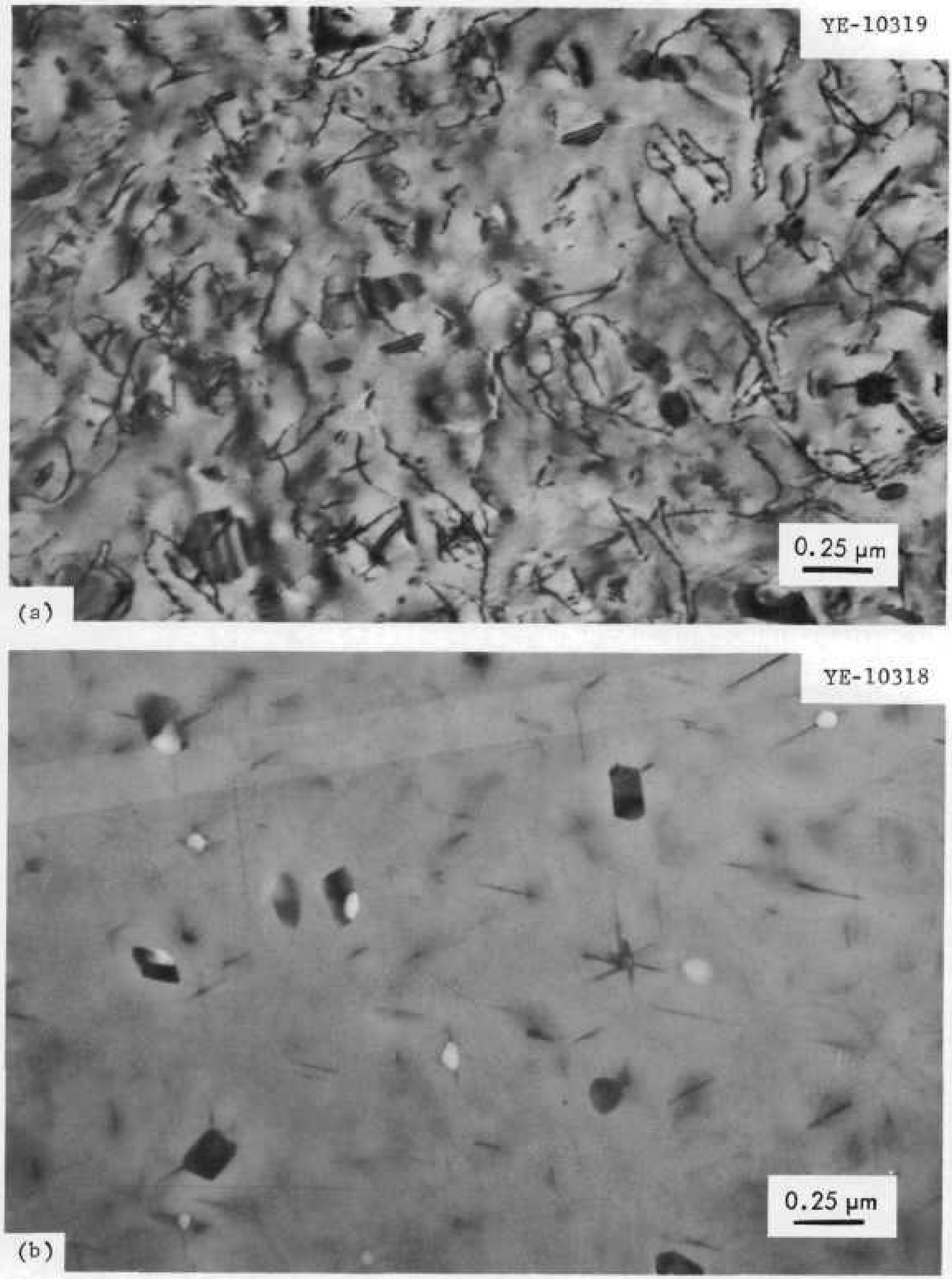

Fig. 3.7. Type 316 Stainless Steel Irradiated in the Annealed Condition to 1.9 × 10^{22} neutrons/cm^2 (> 0.1 MeV) at 580°C. a) dislocation structure, b) voids and precipitates.

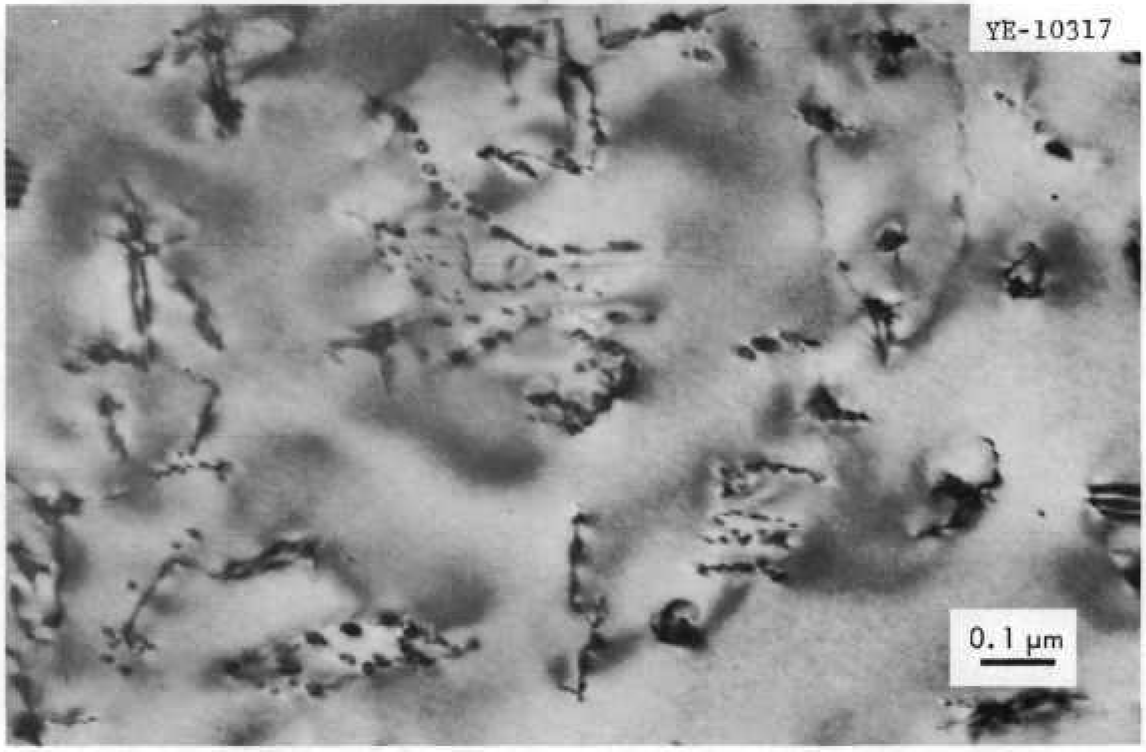

Fig. 3.8. Dislocation Structure in Titanium-Modified Type 316 (0.23% Ti) Stainless Steel Irradiated to 2.3 × 10^{22} neutrons/cm^2 (> 0.1 MeV). The void concentration was less than 1 × 10^{12} voids/cm^3. No change could be detected in the immersion density.

than that observed in standard type 316 stainless steel. The dislocation structure (Fig. 3.7) consists of a few large faulted dislocation loops and dislocation lines with smaller loops associated with them. This dislocation structure, with the exception of the faulted loops, is very similar to the structure found in irradiated nickel.[21] A major difference in the microstructure of these alloys appears to be the absence of both the blocky and needle precipitates in the Ti-modified type 316 stainless steel and their presence in standard type 316 stainless steel.

Analysis of End-of-Life Temperatures in EBR-II Subassembly X034A

(E. E. Bloom, A. F. Zulliger)

Cladding and structural materials irradiation experiments performed in EBR-II Mark B-7 subassemblies utilize a gas gap between the surface of the cylindrical specimen holder and the inside diameter of the Mark B-7 tube to obtain irradiation temperatures above the ambient sodium coolant temperature.[22] Differential swelling between the tube and the specimen holder during irradiation causes the width of the gas gap, and thus the irradiation temperature, to change.

The EBR-II subassembly X034A contained three elements that had received a peak fluence of 2.7×10^{22} neutrons/cm^2 (> 0.1 MeV) and four elements that had received a fluence of 6.1×10^{22} neutrons/cm^2. Following irradiation the outside diameters of the tubes were measured.[23] After removal from the tubes the diameter of each specimen holder was measured at three places (each end and middle). These measurements allowed us to determine the end-of-life gas gap.

The end-of-life irradiation temperature has been calculated for each specimen holder in the subassembly using the assumption of radial, steady state heat transfer.[24] Postirradiation measurements indicated that the tubes were elliptical rather than round in cross section (particularly the four high fluence tubes). Two-dimensional heat transfer calculations were performed on a specimen holder from a high fluence element to examine the effects of the elliptical tube shape on the temperature distribution in the holder. For the holder in question the element was filled with Ar and the minimum and maximum radial gas gaps were 0.0031 and 0.0057 in. This tube ovality produced specimen holder surface temperatures of 779 and 784°C at the minimum and maximum gas gaps, respectively. Using the average gas gap the calculated temperature was 781°C. Thus, an average gas gap and the assumptions of radial, steady state heat transfer can be used.

In the elements filled with Ar the initial gas gaps were much smaller than in an equivalent element filled with He due to the lower thermal conductivity of Ar. Swelling of the containment tubes did produce marked increases in temperature for those specimen holders located within the core. (About 100°C at the core midplane at 6.1×10^{22} neutrons/cm^2.) Specimen holders in elements filled with He experienced a much smaller temperature increase. (About 10°C at the core midplane at 2.7×10^{22} neutrons/cm^2.

Irradiation temperatures are being confirmed by the postirradiation annealing response of SiC. Figure 3.9 is a plot of length as a function of postirradiation annealing temperature for a silicon carbide sample irradiated in subassembly X034A to a fluence of 2.7×10^{22} neutrons/cm^2. The end-of-life irradiation temperature as determined by the temperature at which the irradiation induced volume increase began to recover was 580 or 590°C depending on whether or not a slope is allowed in the fit of the low temperature data. The 1000°C data point was not included in the analysis because it appeared that complete recovery may have occurred. This result is in good agreement with the calculated end-of-life temperature when a nuclear heating rate of 3.625 watts/gram is used.

Irradiation Damage to Refractory Metals

Hot Cell Preparation of High Activity Specimens for Transmission Electron Microscopy (C.K.H. DuBose, T. L. Chandler, C. Jones)

Since transmission electron microscopy specimens can be prepared from pieces of material weighing only a few milligrams, it has been possible to produce specimens from materials having high specific activities by using conventional techniques with only modest shielding for the operator. With a semiautomatic technique developed at Oak Ridge National Laboratory,[25-27] specimens have been prepared routinely from 0.125 × 0.125 × 0.020 in. pieces reading up to rad/hr. This

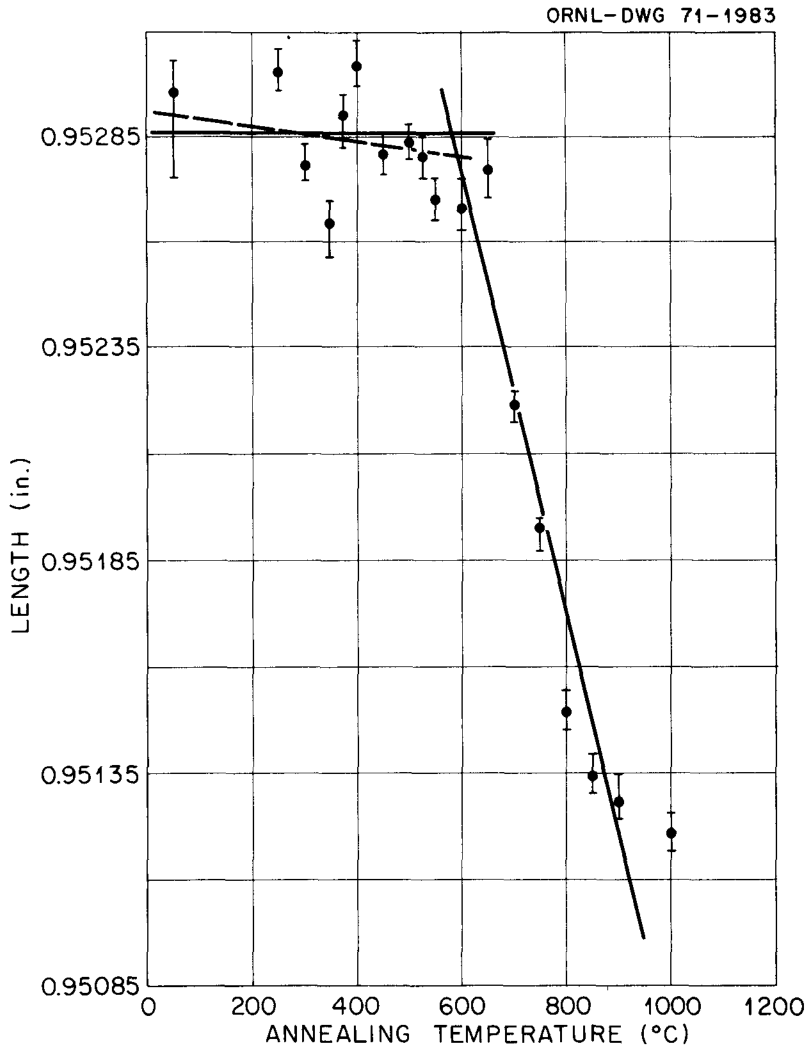

Fig. 3.9. Postirradiation Annealing Response of Silicon Carbide Irradiated in EBR-II Subassembly X034A, Position 12 of Element O-C-2. The calculated end-of-life temperature was 580°C using a nuclear heating rate of 3.625 watts/gram at reactor midplane.

technique involves first dimpling the specimen with an electrolytic jet and then polishing uniformly in a standard electrolytic cell until a hole forms in the dimpled region. The region adjacent to the hole is usually sufficiently transparent to electrons to provide a usable specimen. Better specimens are produced near smaller holes, and a light beam and photocell detector is used to halt the polishing automatically as soon as a hole first forms.

Tantalum from all irradiations and some stainless steels irradiated in HFIR have activities over an order of magnitude higher than the limit cited above for preparation of specimens in the laboratory. The need to examine such materials has led to the development of techniques for the complete preparation of specimens for transmission electron microscopy in a hot cell. While the previous ORNL technique produced excellent specimens, it is a two-step process that requires complicated handling procedures and precise manipulation and alignment of specimens. In the interest of simplicity, speed, and economy, we modified the commercial electropolishing unit produced by E. A. Fischione Instrument Manufacturing Company, Verona, Pennsylvania 15147, for hot-cell operation. This provides a one-step process in which the specimen is mounted in a special holder and immersed in an electrolyte that is agitated by a pair of submerged jets. A light source photocell system detects formation of a hole. The quality of specimens produced by this technique is not particularly high, especially if starting material is more than about 0.003 in. thick, but its simplicity recommends it for remote operation. Nevertheless, several modifications were required to improve the performance of the equipment and to make it compatible with hot-cell procedures. A flexible fiber-optics system was used so the photocell could be located outside the hot cell. This was necessary because sensitivity of the photocell was reduced in the intense radiation field near the specimen. For ease of maintenance, the light source and the electronic parts were also located outside the hot cell with fiber optics and appropriate wiring. Basically, the light source, electronic system, photo detector, and power supply from the ORNL system were substituted for those supplied with the commercial unit.

The specimen holder for electropolishing was also modified for loading in the hot cell. For ease of use by a manipulator, a new twist-on cap was designed to replace the original cap that had to be screwed into place (Fig. 3.10). Holders with specimen recess areas of 0.10, 0.17, and 0.20 in. in diameter were made to hold the variety of specimen sizes that can be accommodated in the microscope.

A jig was designed to support the specimen holder during loading and unloading of specimens. A light was built into the jig to allow confirmation that a hole had formed and to locate its position. The jig also allows different specimen holders to be aligned with the retaining ring that locates their position in the polishing unit (Fig. 3.11).

After polishing, the specimen is dropped into a wire basket that is dipped successively into two distilled water baths and into four alcohol baths to remove the polishing solution and dirt particles from the specimen. The specimen is dropped onto filter paper for drying. It then is picked up with tweezers and loaded into the microscope specimen holder which was modified with a pressure fitting slide cap to replace the conventional screw cap. The electropolisher, specimen holders, and remote-handling equipment are shown in Fig. 3.12.

The loaded specimen holders are transferred to the electron microscope in a shielded container. They are removed from the container and inserted in the microscope with special tongs which keep the operator at least three feet from the specimen. Once the specimen is in the microscope stage, the microscope itself provides adequate shielding for the operator.

Specimens of tantalum and stainless steel reading up to 100 rad/hr at 5 in. have been successfully prepared and examined by this technique. Electrolytes and polishing conditions are given in Table 3.5. Specimen quality is appreciably lower than for specimens prepared in the laboratory. However, usable areas are obtained in about 50% of the specimens and about 25% of the specimens are judged good. The low yield may occur because the technique is not well suited to the relatively thick (0.015 in.) starting material used in these studies. The speed and simplicity of the technique make this sacrifice worthwhile. Some surface dirt has been noted on the specimens, probably arising from difficulties in washing and drying

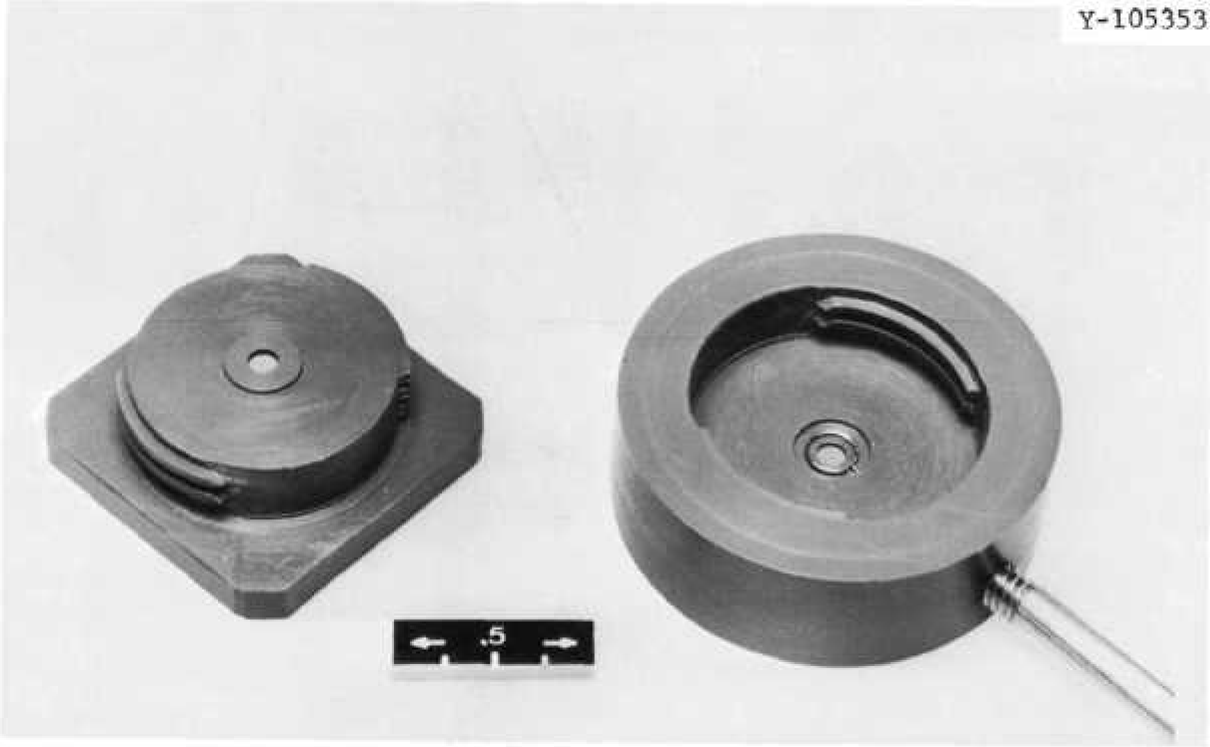

Fig. 3.10. Twist-lock Specimen Holder for Electropolishing. The specimen fits in the recessed area.

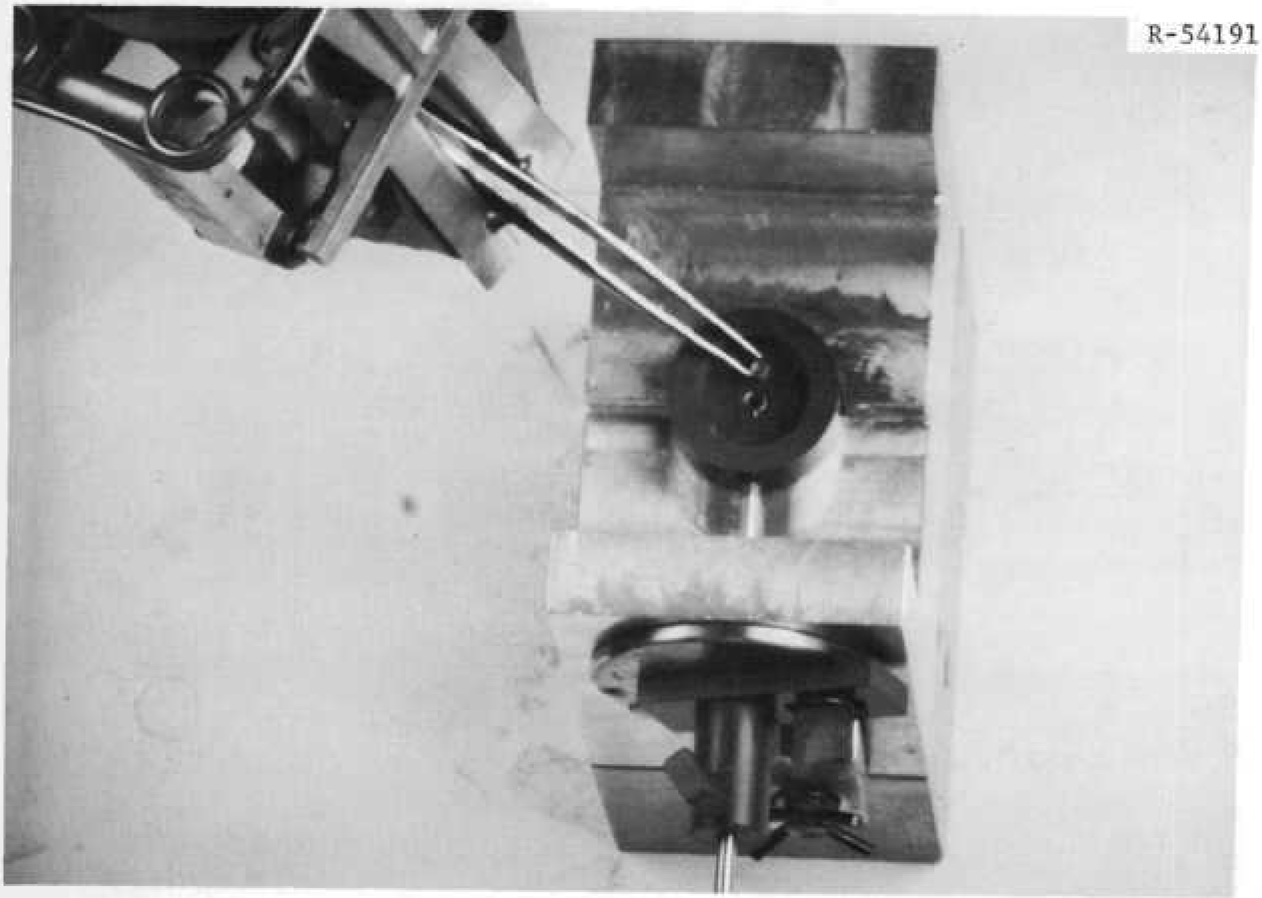

Fig. 3.11. Specimen Being Loaded Into Holder for Electropolishing. The retaining ring positions the specimen holder in the electropolishing unit.

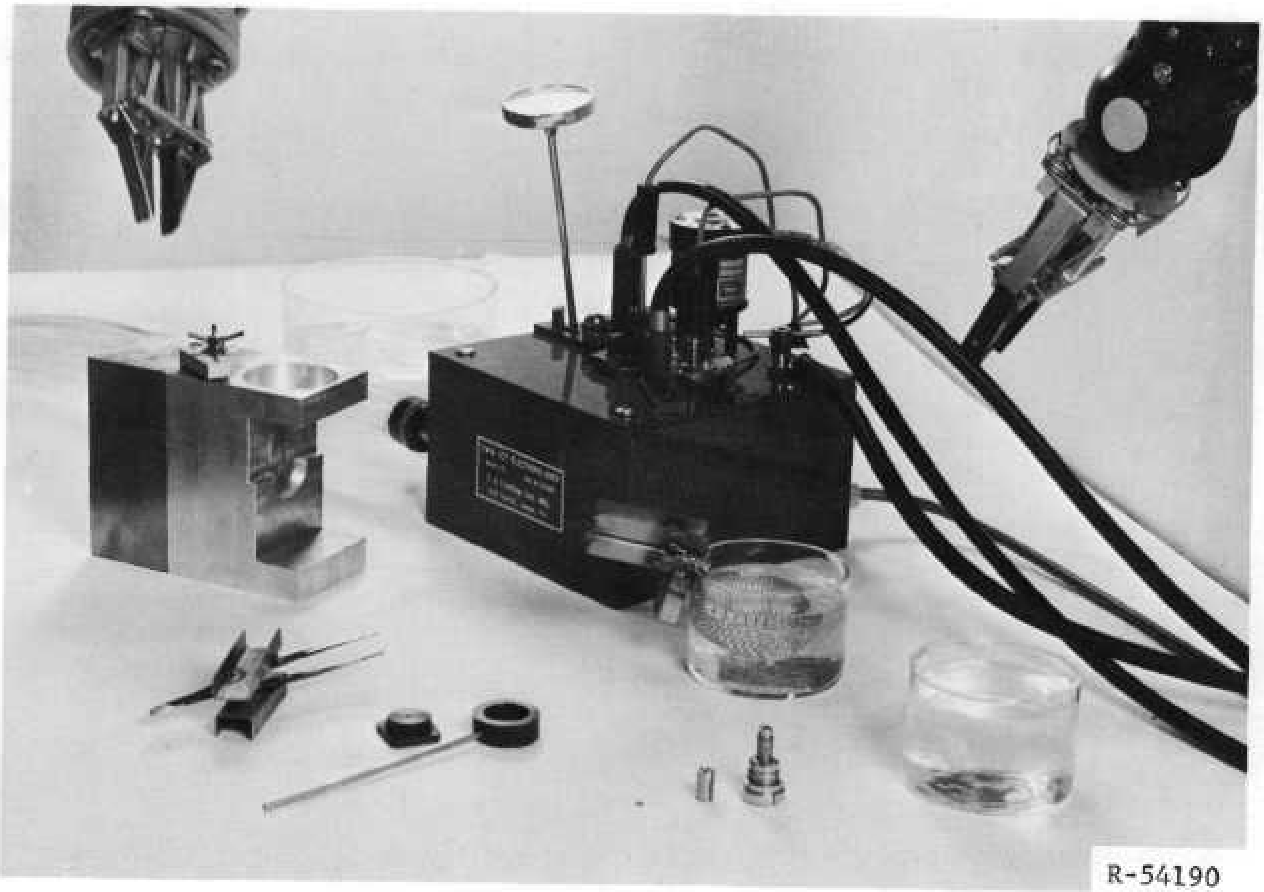

R-54190

Fig. 3.12. Overall View of Equipment for Remote Preparation of Specimens for Electron Microscopy.

the specimens remotely. Some bending of specimens in areas near the hole also occurs. This is probably a mechanical effect from the submerged jets. The equipment is now being modified to cut off the jets when the hole forms. Slight contamination of the microscope-specimen exchange mechanism has occurred, but the specimen stage and microscope column have been clean.

Table 3.5. Electrolytes and Polishing Conditions for Remote Preparation of Transmission Electron Microscopy Specimens

Material	Conditions
Tantalum	600 ml CH_3OH 10 ml H_2SO_4 5 ml HF 115 ma (~38 v)* 14–16°C
Stainless Steel	6% $HClO_4$ in C_2H_5OH 65 ma (~38 v)* 14–16°C

*Medium speed on jet pump.

Void Formation in Tantalum (F. W. Wiffen)

Specimens of tantalum and Ta–10% W were irradiated in row 2 of the EBR-II at temperatures of 425, 585, and 790°C to a fluence of 2.5×10^{22} neutrons/cm^2 (> 0.1 MeV) and at 1000°C to 4.4×10^{22} neutrons/cm^2. The specimens were in the form of 0.015 in. thick sheet and had been recrystallized before irradiation, the Ta at 1100°C and the Ta–10% W at 1450°C. The very high radioactivity of specimens cut to the size for microscopy use, greater than 100 rad/hr at contact, required that the specimens be cut, thinned, and loaded into electron microscope specimen holders in a hot cell. The hot cell techniques were described in the previous section.

The tantalum specimens have been examined by transmission electron microscopy. The microscopy confirmed that the material was fully recrystallized and most areas examined were found to be oriented with

{111} planes parallel to the surface of the specimen. The specimen irradiated to 2.5 X 10^{22} neutrons/cm^2 at 585°C has been characterized in detail. This irradiation condition produced a high density of small voids on a partially ordered void superlattice. The void density, using foil thicknesses determined by the stereographic technique, was 1.9 X 10^{17} voids/cm^3. Foil thickness determinations were difficult in this sample and we expect that the void density is the maximum possible and could be as much as 25% higher than the true void density. The void population had a maximum diameter of less than 100 A and an average diameter of 61 A. The swelling produced by the void population, calculated from the measured void density and void size distribution, is 2.4%. The void superlattice is identified in the {111} foils where the ⟨112⟩ traces of the three {110} superlattice planes normal to the foil surface can be seen. The measured spacingsof the {110} superlattice planes give a lattice parameter of 205 A for a bcc void superlattice parallel to the bcc metal lattice. The resulting density of 2.3 X 10^{17} superlattice points/cm^3 and the measured void density indicate a void occupancy of 80% of the superlattice sites. The measured spacing of {110} superlattice planes rules out the possibility that the superlattice is fcc or simple cubic, because neither of these superlattices would provide sufficient lattice points to accommodate the measured void density. The visible ordering is long range but can often be seen to break down locally.

Grain boundaries had little effect on the void population in this sample. The void denuded zone adjacent to the boundary was not over 200 A wide and there was no observable boundary effect outside this zone. The damage microstructure in diffraction contrast has been obscured by deformation produced in thinning and handling the foils. Some dislocation segments and loops are probably the result of irradiation, but these cannot be separated unequivocally from the dislocations introduced by specimen preparation.

Tantalum irradiated at 790 and 1000°C had fewer voids of larger size than the sample discussed above. The sample irradiated at 425°C contained a high density of small loops, but no voids could be detected. These samples will be characterized in a later report.

Irradiation Damage to Aluminum and Aluminum Alloys

Neutron Irradiation Damage to Aluminum Alloys at Elevated Temperatures[28] (R. T. King)

Two uninstrumented neutron irradiation experiments containing both uniaxial creep-rupture specimens and electron microscopy specimens of aluminum and aluminum alloys were irradiated in the High Flux Isotope Reactor. The intent of these experiments was to investigate the forms of irradiation damage which occur over the temperature range from 90°C to about 125°C, at fast neutron fluences ranging from about 0.4 to 1.6×10^{22} neutrons/cm^2 (> 0.82 MeV). After disassembling the sealed, helium-filled experiment cans and examining the electron microscopy specimens of high-purity aluminum, we concluded that the operating temperatures of specimens in these experiments were more than 50°C higher than the design temperatures. For the purpose of this discussion, we will arbitrarily add 50°C to all calculated irradiation temperatures.

Only electron microscopy specimens of the high-purity aluminum were irradiated in these experiments. The range of neutron fluences was the full range stated above, while the actual irradiation temperatures were between about 140°C and over 200°C. With increasing irradiation temperature, the void size passed through a maximum and then became zero, since voids were not observed at the highest irradiation temperature. The region immediately adjacent to grain boundaries was denuded of voids, but near the denuded zone the void size was considerably larger than in the grain interiors. Whenever voids were observed, they were associated with silicon precipitate particles; the size of these precipitates increased with increasing neutron fluence and increasing temperature. At the higher irradiation temperatures, the silicon precipitates tended to be elongated rather than equiaxed.

Electron microscopy specimens of annealed and 50% cold-worked 1100 grade and 8001 grade aluminum, and 6061 grade aluminum in the "O" temper (soft, overaged) and "T6" temper (fully age hardened) were also irradiated in the experiments. No voids were found in any of these materials under fluence and temperature conditions which led to void formation in the high-purity material. The maximum sizes of the silicon precipitate particles in the annealed solid solution alloys (1100 and 8001 aluminum) increased with increasing neutron fluence and temperature. A simple statement about the number density of silicon particles is not possible because at the higher temperatures Ostwald ripening occurred, depleting a region of precipitate, followed by further nucleation of silicon precipitates at a later time. No appreciable recovery of the cold-worked solid solution alloys occurred during irradiation. The silicon precipitates present in the cold-worked structures nucleated preferentially on dislocations, subboundaries, and grain boundaries; the particles located on grain boundaries and subboundaries were frequently about an order of magnitude larger than those which nucleated on individual dislocations. No observable change occurred in the Mg_2Si precipitates of the 6061 alloy during irradiation, but silicon precipitates formed as an additional phase. The immersion densities of each type of creep-rupture specimen were determined before and after irradiation, but no significant irradiation-induced changes occurred.

The trend of the creep-rupture results is typified by those shown in Fig. 3.13 for annealed 8001 aluminum tested at 100°C. Irradiation at 140 or 170°C increased the rupture time of the alloy, but there is very little effect of doubling the neutron fluence. Since there were no voids present in the electron microscopy specimens, it is unlikely that voids were present in the creep-rupture specimens. The increased strength must be due to silicon precipitates and any dislocation structure formed by irradiation-induced loops. The specimens irradiated at 140°C exhibited longer rupture times and lower minimum creep rates than those irradiated at 170°C which probably contained a coarser silicon particle distribution.

Irradiation-induced ductility losses occurred. Unirradiated specimens consistently deformed over 50% before failing, whereas the specimens irradiated at 170°C deformed from 10 to 20%, and specimens irradiated at 140°C deformed less than 10%. Much of this ductility loss must be associated with strengthening by the silicon and irradiation-induced dislocation structure, although gases may play some role in the fracture process.

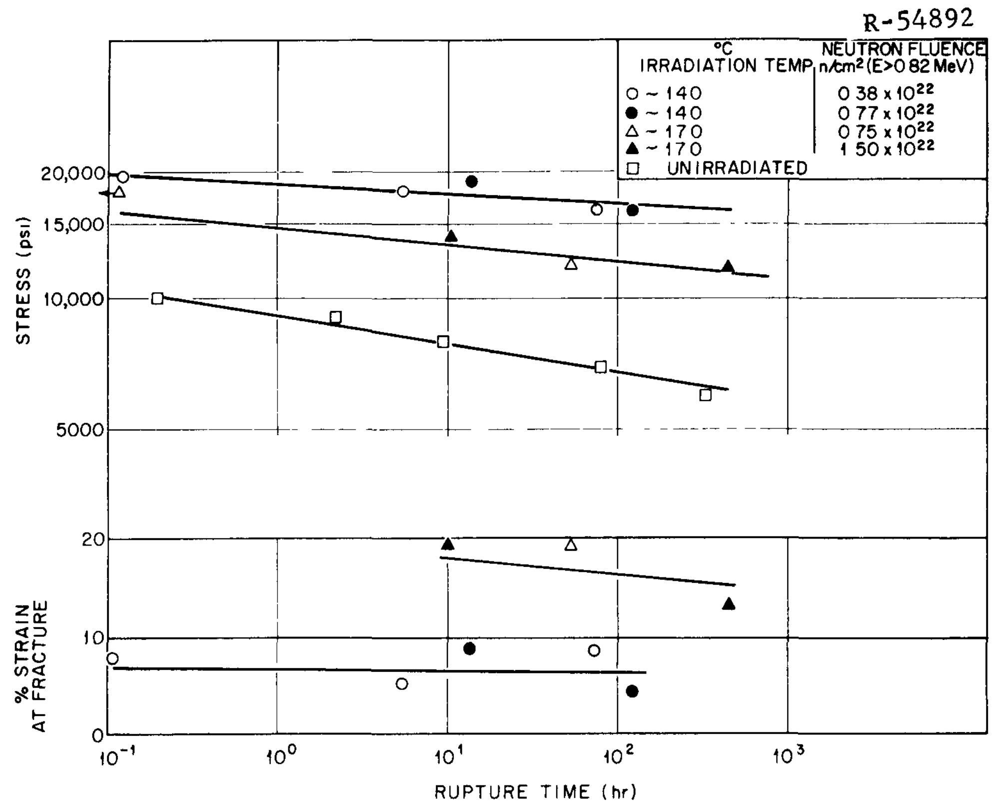

Fig. 3.13. Creep-Rupture Properties of Recrystallized 8001 Aluminum Alloy Tested at 100°C.

REFERENCES

1. E. E. Bloom and J. O. Stiegler, *Fuels and Materials Development Program Quart. Progr. Rept. Sept. 30, 1970*, ORNL-4630, pp. 73–78.

2. J. O. Stiegler, K. Farrell, C.K.H. DuBose and R. T. King, "High Fluence Neutron Irradiation Damage in Aluminum," p. 215 in *Radiation Damage in Reactor Materials, Vol. II*, International Atomic Energy Agency, Vienna, 1969.

3. J. J. Holmes,"Irradiation Induced Swelling in Nickel Alloys," *Trans. Am. Nucl. Soc.* **12** , 117 (1969).

4. J. O. Stiegler and E. E. Bloom, "Void-Formation in Irradiated Nickel 270," *Radiation Effects* (to be published).

5. T. Lauritzen, A. Withop and V. E. Wolff, "Swelling of Austenitic Stainless Steels Under Fast-Neutron Irradiation at Elevated Temperatures," *Nucl. Eng. Design* **9** 265 (1969).

6. E. E. Bloom and J. O. Stiegler, "A Comparison of Irradiation Induced Swelling and Void Formation in Two Austenitic Stainless Steels," *J. Nucl. Mater*. **35**, 244 (1970).

7. K. Farrell and J. Houston, "Non-Randomly Distributed Irradiation Voids in Iron," *J. Nucl. Mater*. **35**, 352 (1970).

8. R. Bullough, B. L. Eyre and R. C. Perrin, "The Growth and Stability of Voids in Irradiated Metals," *Nucl. Appl*. **9** 346 (1970).

9. H. R. Brager, J. L. Straalsund, J. J. Holmes and J. F. Bates, *Irradiation Produced Defects in Austenitic Stainless Steel*, WHAN-FR-16 (December 1970) (to be published in Metallurgical Transactions).

10. R. Bullough and R. C. Perrin, "Growth, Stability and Interactions of Voids and Gas Bubbles in Solids," p. 233 in *Radiation Damage in Reactor Materials, Vol. II*, International Atomic Energy Agency, Vienna (1969).

11. S. D. Harkness and Che-Yu Li, "A Model for Void Formation in Metals Irradiated in a Fast-Neutron Environment," p. 189 in *Radiation Damage in Reactor Materials, Vol. II*, International Atomic Energy Agency, Vienna (1969).

12. R. S. Nelson and D. J. Mazey, "Void Formation in Stainless Steel During Charged-Particle Irradiation at Elevated Temperatures," p. 157 in *Radiation Damage in Reactor Materials, Vol. II*, International Atomic Energy Agency, Vienna (1969).

13. E. E. Bloom and J. O. Stiegler, "The Effect of Helium on Void Formation in Irradiated Stainless Steel," J. Nucl. Mater. 36, 331 (1970).

14. K. Farrell, R. T. King and A. Wolfenden, "Effect of Preinjected Gases on Radiation Voids in Aluminum," Radiation Effects (to be published).

15. E. E. Bloom, An Investigation of Fast Neutron Radiation Damage in an Austenitic Stainless Steel, ORNL-4580 (August 1970).

16. D. Fahr, Fuels and Materials Development Program Quart. Progr. Rept. Dec. 31, 1970, ORNL-TM-3300.

17. J. J. Holmes, R. E. Robbins, J. L. Brimhall and B. Mastel, "Elevated Temperature Irradiation Hardening in Austenitic Stainless Steel," Acta Met. 16, 955–967 (1968).

18. E. E. Bloom and J. O. Stiegler, "Effects of Fast Neutron Irradiation on the Tensile Properties of Austenitic Stainless Steels," Proceedings of Second International Conference on the Strength of Metals and Alloys, Pacific Grove, California, 30 August–4 September 1970, Vol. II, P. 768.

19. E. E. Bloom, Fuels and Materials Development Program Quart. Progr. Rept. Sept. 30, 1968, ORNL-4350, p. 152.

20. E. E. Bloom and J. O. Stiegler, Fuels and Materials Development Program Quart. Progr. Rept. Sept. 30, 1970, ORNL-4630, p. 79.

21. J. O. Stiegler and E. E. Bloom, "Void Formation in Irradiated Nickel 270," Radiation Effects (to be published).

22. E. E. Bloom, J. W. Woods, and A. F. Zulliger, Description of EBR-II Subassembly X100, ORNL-TM-3389 (in press).

23. Postirradiation measurements of tubes performed by W. J. Larson and G. C. McClellan, ANL-Idaho.

24. D. A. Dylsin, Little MAMU — A Radial Steady State Heat Transfer Program, ORNL-TM (report in preparation).

25. C.K.H. DuBose and J. O. Stiegler, Semiautomatic Preparation of Specimens for Transmission Electron Microscopy, ORNL-4066 (Feb. 1967).

26. C.K.H. DuBose and C. Jones, Techniques for the Preparation of Transmission Electron Microscopy Specimens from Tubing, ORNL-TM-2408 (1969).

27. C.K.H. DuBose and C. Jones, "The Preparation of Transmission Electron Microscopy Specimens from Tubing," Metallography 2 (2-3), 31–39 (1969).

28. R. T. King, Neutron Irradiation Damage to Aluminum Alloys at Elevated Temperatures, ORNL-TM (in press).

4. FABRICATION DEVELOPMENT OF FBR CLADDING

G. M. Adamson, Jr.   W. R. Martin

This development effort involves evaluation of techniques for the fabrication of thin-walled tubing of high quality for fast reactor cladding. We are examining the relationship among processing variables, mechanical properties of elevated temperature, and the physical defects of the tubing.

Effect of Fabrication Variables During Mandrel-Plug Drawing on the Quality and Properties of Type 316 Stainless Steel Tubing

W. R. Martin

Studies of Artificial Defects (K. V. Cook, R. W. McClung)

The primary objective of the as-machined notch study is to establish the effect of flaws of various sizes (simulated by electro-discharge machined [EDM] notches) on the mechanical properties of 1/4-in. OD type 316 stainless steel tubing. Notches such as these are normally used to establish test sensitivity for both ultrasonic and eddy-current tests and are as narrow as we can machine them at the present time (0.0023 in.).

Three control sections were notched with OD notches to replace samples for mechanical properties tests which had prematurely failed at the welded end cap.

Studies of Altered Defects (K. V. Cook, R. W. McClung)

The primary objective of the altered notch study is to establish methods for fabricating artificially produced flaws in tubing to resemble natural defects. These simulated flaws are being used in studies involving the fabrication, inspection, and mechanical properties groups to evaluate and upgrade tubing fabrication and inspection methods as well as to establish the effect of the simulated flaws on mechanical properties.

A program outline has been established for producing tube burst specimens containing altered notches with lengths of 0.25 in., widths of 0.001 in., and depths of 0.0002, 0.0005, and 0.0015 in. The required tubing for this study is being drawn on a BA1-1 schedule, and the appropriate size notches will be introduced in the 0.537-in. OD × 0.043-in. wall size.

In addition we are studying the effect of tube fabrication on both transverse and longitudinal notches machined in a larger diameter tube (1 1/32-in. OD). A series of eight 1/8-in. long × 0.009-in. deep longitudinal and transverse notches were placed in one of a set of four tubes (1 1/32-in. × 0.125-in. wall). The inspection of these tubes was complicated because they were not straight enough to inspect in our tubing scanners. We developed special fixturing which rode on the tube maintaining the necessary ultrasonic alignment and allowing both a transverse and longitudinal inspection to be performed.

Effects of Artificially Induced Defects on the Mechanical Properties of Unirradiated Annealed Type 316 Stainless Steel Tubing (R. T. King, G. A. Reimann, and K. V. Cook)

A technical report on this subject has been written and is now in the process of being published. In summary, the effect of electrodischarged-machined longitudinal notches on the biaxial creep-rupture properties of 0.25 in. OD × 0.016 in. wall thickness, 20% cold-worked type 316 stainless steel tubing at 650°C was investigated. Notch dimensions were 0.030 in. length by 0.0025 in. width, while the depths were equal to about 10%, 33%, and 66% of the tube wall thickness. The presence of notches accelerated intergranular fracture, reducing rupture life and ductility; the effects of given size notches on either the inner or outer surface were not measurably different.

Effect of Planetary Swaging on the Structure and Creep Properties of Type 316 Stainless Steel

Drawing of Type 316 Stainless Steel Tubing by Planetary Swaging

(G. A. Reimann)

We have concluded our study of planetary swaging which intended to evaluate the process in terms of its applicability to the fabrication of high-quality type 316 stainless steel fuel cladding.

The most recent efforts concentrated on producing tubing of final size. To produce samples for room temperature and elevated temperature burst testing, redraw stock that was mandrel drawn in a conventional manner from Allegheny-Ludlum Steel Corporation heat No. 65808 into tubing measuring 0.267 in. OD by 0.230 in. ID. The diameter was increased by approximately 0.002 in. by reeling, which was necessary to remove the tubing from the mandrel. The tubing was annealed for 1/4 hr at 950°C and planetary swaged to the final size, 0.250 in. OD by 0.218 in. ID, producing a 20% reduction in area.

Previously we reported the results of planetary swaging to final size by using the same reduction schedule and swager head speed but varying the bench speed from 12 to 36 in./min (ref. 1). The most recent study involved maintaining constant swager speeds of 1000 rpm and bench speeds of 12 in./min but varying the reduction schedule so that final size was obtained by using from one to four passes.

Final size was achieved with minimal difficulty when three or four passes were employed, but serious problems with dimensional control developed when we attempted to achieve final size using less than three passes. The swager settings that produced final size on the third or fourth passes would not produce the final size tubing if a single pass was attempted at the same setting. The tubing emerged with outside and inside diameter considerably larger than anticipated, although wall thickness was reasonably close to predictions. Also, it was noticed that a ridge of metal developed around the circumference of the tube where the tube surface first contacted the swaging balls. The ridge was most pronounced during the first pass and became more prominent when greater reductions were obtained on the first pass.

Table 4.1 shows the results obtained when planetary swaging to final size using between one and four passes but maintaining a constant head speed of 1000 rpm, a bench speed of 12 in./min and a 0.217-in. mandrel. The ridge height was measured only after the first pass. A 0.217-in.-diam mandrel was employed throughout so tube deformation concentrated on ironing.

When using any schedule of less than four passes, the tubing seldom emerged with dimensions that would have been predicted from changes in the swager settings. Insufficient tubing was available for the numerous trial runs required to ensure that the size desired was the size actually obtained.

The tube produced by a single pass using 1/4-in. swaging balls exhibited a substantial number of surface defects which are believed to be directly related to the circumferential ridges formed. Also, substantial expansion of the tube results when a single 20% reduction is attempted. This causes an inordinate amount of flexing in the region of deformation and serves to propagate any surface flaws initiated by formation of the ridge just described.

Five samples were cut from the tubing produced by the several schedules which were subsequently pressurized to failure. The results are shown in Table 4.2. The conventionally drawn sample shown in Table 4.2 was produced by a single plug draw that resulted in a 18.6% reduction in area. This sample is included in the table for comparison; however, only the planetary swaged samples produced by four and two passes, and the single pass using 1/2-in. swager balls, approximated this level of area reduction. In all cases the ductility in the rupture region suffered as a result of planetary swaging. This has been attributed to the generation of surface flaws which was particularly troublesome when the single pass with 1/4-in. swaging balls was used. No samples could be found in this tube which were completely free of visible flaws, so the tube was examined under a microscope for selection of samples with the fewest small defects.

Samples produced by two, three, and four passes exhibited considerably greater strength than would be anticipated from a single 20% reduction in area, so the substantial amount of redundant work results from planetary

Table 4.1. Tube Dimensions Obtained During Planetary Swaging to Final Size Using From One to Four Passes

Experiment No.	Pass	Diameter Outside (in.)	Diameter Inside (in.)	Average Wall Thickness (in.)	Height of Ridge (in.)	Reduction Per Pass (%)	Total Reduction (%)
A	1	0.2567	0.2189	0.0189	0.0003	2.5	2.5
	2	0.2542	0.2184	0.0179		5.8	7.4
	3	0.2525	0.2185	0.0170		5.2	11.6
	4	0.2506	0.2186	0.0160		6.3	17.8
B	1	0.2565	0.2192	0.0186	0.0013	3.0	3.0
	2	0.2529	0.2190	0.0170		9.6	12.4
	3	0.2508	0.2187	0.0161		4.2	16.3
C	1	0.2568	0.2211	0.0177	0.0048	6.6	6.6
	2	0.2505	0.2189	0.0158		12.9	18.7
D	1	0.2559	0.2271	0.0144	0.0096	23.8	23.8
E	1[a]	0.2572	0.2262	0.0155	0.0021	18.0	18.0

[a] 1/2-in.-diam swaging ball.

Table 4.2. Results of Burst Testing Type 316 Stainless Steel Tubing Produced by Planetary Swaging

Sample Identification	Number of Passes	Swager Ball Diameter (in.)	Average Fiber Stress[a] (psi)	Average Elongation (%)
BA1-1	Conventionally drawn		158,700	3.1
BA1-4-4	4	1/4	183,700	1.3
BA1-4-3	3	1/4	183,600	1.4
BA1-4-2	2	1/4	180,400	1.8
BA1-4-1	1	1/4	150,000	0.9
BA1-4-1	1	1/2	151,500	2.8

[a] Fiber stress was based on failure at the thinnest measured wall thickness.

swaging does not permit equating reduction in area with percent cold work. The reduction of ductility observed with these samples stems partly from this cause.

The planetary swaged samples most closely resembling those produced by conventional drawing were obtained by a single pass using 1/2-in. swaging balls. This tubing was free of visible surface defects. We believe that the desired 0.250 in. OD by 0.218 in. ID could be obtained if a smaller diameter mandrel were used (i.e., 0.209 in.) to compensate for tube expansion during deformation.

The planetary swaging process is best suited for finishing passes if it is to be adapted for the production of fuel cladding. But the process is inherently slow and even had our machine been modified to permit higher output, it could not hope to approach the 20 to 30 ft/min output presently obtained by conventional drawing practice. This is especially significant considering projected near-term tubing requirements of 2×10^5 ft/year and even more so for the long term where 10^7 to 10^8 feet are anticipated.

In addition to an inclination toward developing surface flakes and longitudinal flaws, the nature of the process is such that an inordinately high level of cold work is obtained for a given change in cross section.

While the process cannot compete with conventional drawing in terms of output and quality level, it is capable of producing highly burnished surfaces, and it could be applied to specialized operations where conventional drawing techniques are not suitable, such as producing tubing with a variable outside diameter.

References

1. G. A. Reimann, *Fuels and Materials Development Program Quart. Progr. Rept. June 30, 1970*, ORNL-4600, p. 129.

5. WELDING DEVELOPMENT FOR FBR STAINLESS STEEL COMPONENTS

J. R. Weir, Jr.   G. M. Goodwin   G. M. Slaughter

We are evaluating the behavior of weldments in austenitic stainless steel at 370 to 750°C as a function of both welding process and the variables within a process for application to liquid-metal-cooled fast breeder reactor (LMFBR) vessels and components. The solidification substructure of the weld metal markedly influences the mechanical properties of a weldment at elevated temperature; since the size and type of substructure are significantly influenced by factors which the welder can control, our approach is to determine this link between welding variables, the solidification substructure which these variables produce, and the resultant mechanical properties. Also included in the studies are corrosion behavior, irradiation stability, and the effect of heat treatment on structure and properties.

Study of Submerged-Arc Process

<u>Investigations of Mechanical Properties</u> (R. G. Berggren, G. M. Goodwin)

Additional creep-rupture data have been obtained on 1-in.-thick submerged-arc weldments. We completed 14 creep-rupture tests with rupture times ranging from 9 to 5128 hr.

Six submerged-arc weldments are presently under test. These weldments are designated SA-2 through SA-7. Differences in welding procedures are shown in Table 5.1. The newly obtained results for as-welded specimens are presented in Table 5.2 and Fig. 5.1. Some previously reported results are included for comparison purposes. The stress-versus-rupture life plots in Fig. 5.1 show no marked differences in creep strength for these weldments. The somewhat lower rupture lives of weldments SA-2 and SA-7 may be due to the lower carbon contents of the plates in which these two weldments were made. The elongation-versus-rupture life plots show a general decrease in ductilities with increasing rupture life. The two possible exceptions to this general observation are weldments SA-2 and SA-7, which

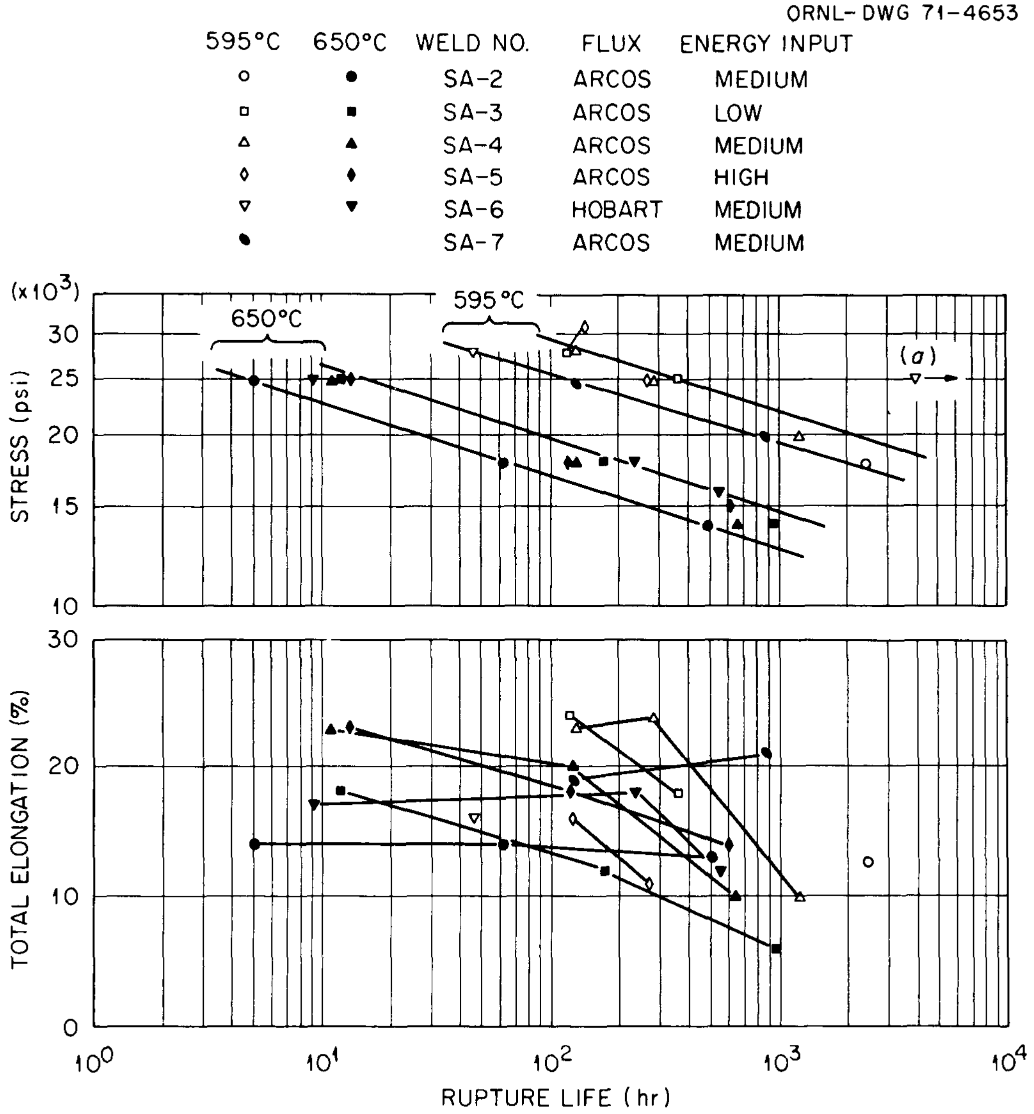

Fig. 5.1. Creep-Rupture Properties of Stainless Steel Submerged-Arc Welds. (a) Test still in progress.

Table 5.1. Description of Conditions for Submerged-Arc Weldments

Weld No.	Flux	Energy Input (kj/in.)	Restraint During Welding
SA-2	Arcos S-4	72 (medium)	None
SA-3	Arcos S-4	40.8 (low)	None
SA-4	Arcos S-4	68 (medium)	None
SA-5	Arcos S-4	272 (high)	None
SA-6	Hobart HS-300	70 (medium)	None
SA-7	Arcos S-4	68 (medium)	Full

were made in the plates of lower carbon content. However, these are rather meager data from which to draw definite conclusions. If we compare ductilities for the low-, medium-, and high-energy input welds (SA-3, -4, and -5, respectively), we find that, at a test temperature of 595°C, the high-energy input weld (SA-5) had lower total elongation than the other two, while at 650°C, the low-energy input weld (SA-3) had the lower total elongation. Again, we reach no obvious conclusion as to the best welding parameters. If we compare ductilities at the two test temperatures, we find that two weldments (SA-3 and SA-4) had greater elongations at 595°C than at 650°C, while one weldment (SA-5) had greater elongation at 650°C than at 595°C. There is insufficient data to make similar comparisons for the other weldments. One data point appears to be very different from the other results. This is the test of weldment SA-6 made with Hobart HS-300 flux and creep tested at 595°C and 25,000 psi stress. This test is still running at 4000 hr. This same weldment yielded rupture times in the scatter band for weld metal at tests at 595°C and 28,000 psi and three tests at 650°C (25,000, 18,000, and 16,000 psi). We have checked the test temperature, load, and stress calculations and found no error and have started another test at the same temperature (595°C) and stress (25,000 psi). At the present, this test is suspect for unknown reasons.

We also completed two long-term tests of heat-treated specimens of weldment SA-2. These results are presented in Table 5.3. The rupture lives at 595°C for the annealed and the annealed-and-aged specimens are a

Table 5.2. Creep-Rupture Properties of Submerged-Arc Welds in Stainless Steels[a]

Weld No.[a]	Energy Input[b]	Test Temperature (°C)	Stress (psi)	Rupture Time (hr)	Total Elongation (%)	Reduction of Area (%)	Minimum Creep Rate (%/hr)	Test No.
SA-2[c]	Medium	650	25,000	5	14	16	2.9	S-6
SA-3[c]	Low	650	25,000	12	18	54	0.98	S-38
SA-4[c]	Medium	650	25,000	11	23	47	1.4	S-35
SA-5[c]	High	650	25,000	13	23	36	0.75	S-39
SA-6	Medium	650	25,000	9	17	60	1.4	S-47
SA-2[c]	Medium	650	18,000	62	14	18	0.14	S-13
SA-3	Low	650	18,000	171	12	30	0.056	S-43
SA-4	Medium	650	18,000	126	20	38	0.12	S-44
SA-5	High	650	18,000	121	18	34	0.10	S-45
SA-6	Medium	650	18,000	236	18	21	0.061	S-50
SA-2[c]	Medium	650	14,000	493	13	8	0.017	S-19
SA-3	Low	650	14,000	949	5.9	12	0.0032	S-51
SA-4	Medium	650	14,000	663	10	17	0.011	S-49
SA-5	High	650	15,000	610	14	30	0.015	S-53
SA-6	Medium	650	16,000	556	12	19	0.017	S-54
SA-3[c]	Low	595	28,000	120	24	22	0.12	S-26
SA-4[c]	Medium	595	28,000	130	23	26	0.12	S-25
SA-5[c]	High	595	28,000	124	16	20	0.090	S-27
SA-6[c]	Medium	595	28.000	46	16	16	-----	S-31
SA-3[c]	Low	595	25,000	367	18	12	0.030	S-28
SA-4[c]	Medium	595	25,000	283	24	16	0.053	S-29
SA-5[c]	High	595	25,000	268	11	17	0.027	S-30
SA-6	Medium	595	25,000	> 4000[d]	--	--	0.0006	S-37
SA-7	Medium	595	25,000	128	19	46	0.096	S-48
SA-4[c]	Medium	595	20,000	1225	10	41	0.0051	S-36
SA-7	Medium	595	20,000	878	21	46	0.014	S-52

[a] Transverse, all-weld-metal specimens. One-inch type 304L stainless steel plate with AWS Class 308 filler wire. Welds SA-2, -3, -4, -5, and -7 were made with Arcos S-4 flux and SA-6 was made with Hobart HS-300 flux. Weld SA-7 was made with full mechanical restraint.

[b] Low energy input, 40.8 kj/in. Medium energy input, 68 to 72 kj/in. High energy input, 272 kj/in.

[c] Reported previously, repeated for comparison.

[d] Test still in progress.

Table 5.3. Effect of Heat Treatment on Creep-Rupture Properties of a Submerged-Arc Weld[a] at 595°C and 18,000 psi

Heat[b] Treatment	Rupture Time (hr)	Total Elongation (%)	Reduction of Area (%)	Minimum Creep Rate (%/hr)
0	2438	12.7	--	0.0032
0	> 1000[c]	----	--	0.003
1	4735	7.7	20	0.0005
2	5128	8.3	25	0.0006

[a] Transverse, all-weld-metal specimens from medium-energy input (68 kg/in.) weld SA-2.

[b] 0: As welded.
1: Annealed 30 min at 1065°C (1950°F).
2: Annealed 30 min at 1065°C (1950°F) and aged 10 hr at 800°C (1470°F).

[c] Discontinued test at 1000 hr. Up to this time, the creep curve was identical to that for the line above at the same conditions.

factor of two greater than for the as-welded specimens. This is greater than any observed effect of heat treatment in the same weldment tested at 650°C and opposite to the effects of heat treatment observed in the shielded metal-arc welds. The comparatively fast cooling rate from the solution treatment temperature for these specimens is probably responsible. We conducted a duplicate creep test on an as-welded specimen (Table 5.3) and the creep curve up to 1000 hr was identical to the previously obtained curve. The duplicate test was discontinued.

In summary, there are unexplainable differences in rupture strengths for the several submerged-arc welds being studied. There is considerable scatter in ductility results, and there is no obvious and consistent effect of energy input or test temperature on ductility. There is a general decrease in rupture elongation for longer rupture times.

Tensile Tests (N. C. Binkley)

Tensile testing of the 75 longitudinal, button head specimens of all weld metal described previously[1] has been completed. Observations were made of the percent elongation, tensile strength, and yield strength. The 75 specimens originally were randomly divided into three groups of 25 each. These three groups were prepared as follows: (1) as welded, (2) solution annealed for 2 hr at 1065°C (1950°F), and (3) solution annealed 2 hr at 1065°C followed by 10 hr at 800°C (1470°F) to agglomerate the carbides. Each group of 25 specimens was then subdivided into five equal subgroups, each of which received one of the following treatments: (1) no aging, (2) aging at testing temperature for 1000 hr, (3) aging at 540°C (1000°F) for 100 hr, (4) aging at 595°C (1100°F) for 100 hr, or (5) aging at 650°C (1200°F) for 100 hr.

The five specimens in each subgroup were tested at 0.02 in./min strain rate at different temperatures: 315, 425, 540, 595, and 650°C (600, 800, 1000, 1100, and 1200°F). All testing has been completed, and results of these tests are shown in Tables 5.4 through 5.8.

A basic statistical analysis of the tensile data has been completed and will appear in greater detail in a later report. Basic conclusions statistically derived which are available now include:

1. We cannot detect an effect due to aging time on yield strength and percent elongation. There is, however, a significant effect due to aging time on tensile strength.

2. In no case can we detect a difference between the solution-annealed and the solution-annealed-plus-carbide-agglomerated tensile specimens.

3. Aging temperature and test temperature combinations significantly affect the tensile strength.

4. The results of the as-welded versus the average of the results of the two solution-annealed treatments show significant differences in tensile strength, yield strength, and percent elongation.

5. Test temperature significantly affects tensile strength, yield strength, and percent elongation.

6. The differences between no age and aging for 100 hr has a significant effect on tensile strength.

Table 5.4. Results of Tensile Tests at 315°C (600°F) on Type 308 Submerged-Arc Weld Deposits

Specimen Condition	Aging Condition	Elongation in 1.125 in. (%)	Tensile Strength (psi)	Yield Strength (psi)
As welded	No age	22.04	64,855	36,625
	540°C, 100 hr	16.62	60,015	43,115
	595°C, 100 hr	19.73	63,785	32,510
	650°C, 100 hr	20.44	65,135	38.065
	315°C, 1000 hr	26.60	68,090	44,300
Solution annealed 1065°C - 2 hr	No age	24.70	62,245	29,020
	540°C, 100 hr	32.62	55,390	21,975
	595°C, 100 hr	22.75	53,655	27,035
	650°C, 100 hr	23.56	59,520	28,690
	315°C, 1000 hr	27.56	65,545	29,530
Solution annealed 1065°C - 2 hr followed with 800°C - 10 hr. Carbide agglomeration.	No age	22.20	55,975	23,665
	540°C, 100 hr	25.96	58,080	26,415
	595°C, 100 hr	22.66	51,860	22,130
	650°C, 100 hr	25.51	54,890	30,600
	315°C, 1000 hr	23.28	55,975	23,745

Table 5.5. Results of Tensile Tests at 425°C (800°F) on Type 308 Submerged-Arc Weld Deposits

Specimen Condition	Aging Condition	Elongation in 1.125 in. (%)	Tensile Strength (psi)	Yield Strength (psi)
As welded	No age	22.31	65,950	44,105
	540°C, 100 hr	19.02	54,090	28,075
	595°C, 100 hr	20.00	60,870	36,260
	650°C, 100 hr	16.80	60,725	36,645
	425°C, 1000 hr	25.50	47,425	30,660
Solution annealed 1065°C - 2 hr	No age	27.64	61,170	26,380
	540°C, 100 hr	23.46	55,135	22,595
	595°C, 100 hr	24.80	53,245	26,130
	650°C, 100 hr	21.10	53,000	25,310
	425°C, 1000 hr	22.22	53,820	24,815
Solution annealed 1065°C - 2 hr followed with 800°C - 10 hr. Carbide agglomeration.	No age	31.29	52,500	19,935
	540°C, 100 hr	24.71	57,450	24,525
	595°C, 100 hr	21.51	50,785	20,300
	650°C, 100 hr	25.42	53,675	25,105
	425°C, 1000 hr	31.90	53,820	20,130

Table 5.6. Results of Tensile Tests at 540°C (1000°F) on Type 308 Submerged-Arc Weld Deposits

Specimen Condition	Aging Condition	Elongation in 1.125 in. (%)	Tensile Strength (psi)	Yield Strength (psi)
As welded	No age	19.74	57,110	39,935
	540°C, 100 hr	17.51	50,250	28,510
	595°C, 100 hr	18.93	53,720	26,000
	650°C, 100 hr	19.02	53,675	27,830
	540°C, 1000 hr	18.22	48,905	26,950
Solution annealed 1065°C - 2 hr	No age	25.24	53,470	25,125
	540°C, 100 hr	27.90	53,180	23,945
	595°C, 100 hr	21.96	46,180	21,365
	650°C, 100 hr	23.56	49,710	22,870
	540°C, 1000 hr	19.11	44,880	20,720
Solution annealed 1065°C - 2 hr followed with 800°C - 10 hr. Carbide agglomeration.	No age	22.30	52,435	22,625
	540°C, 100 hr	22.13	46,835	18,490
	595°C, 100 hr	22.04	49,220	23,300
	650°C, 100 hr	21.60	47,905	19,230
	540°C, 1000 hr	22.93	46,825	22,425

Table 5.7. Results of Tensile Tests at 595°C (1100°F) on Type 308 Submerged-Arc Weld Deposits

Specimen Condition	Aging Condition	Elongation in. 1.125 in. (%)	Tensile Strength (psi)	Yield Strength (psi)
As welded	No age	32.44	44,925	27,455
	540°C, 100 hr	28.53	40,460	25,105
	595°C, 100 hr	22.22	48,480	26,950
	650°C, 100 hr	13.42	48,970	25,720
	595°C, 1000 hr	21.96	47,315	31,545
Solution annealed 1065°C - 2 hr	No age	23.64	47,245	20,955
	540°C, 100 hr	28.44	45,940	22,560
	595°C, 100 hr	20.18	45,105	23,375
	650°C, 100 hr	31.55	43,245	17,035
	595°C, 1000 hr	24.00	42,800	21,810
Solution annealed 1065°C - 2 hr followed with 800°C - 10 hr. Carbide agglomeration.	No age	27.83	47,660	24,650
	540°C, 100 hr	29.07	43,245	17,935
	595°C, 100 hr	26.13	44,300	17,885
	650°C, 100 hr	29.06	42,890	17,665
	595°C, 1000 hr	23.29	43,405	19,085

Table 5.8. Results of Tensile Tests at 650°C (1200°F) on Type 308 Submerged-Arc Weld Deposits

Specimen Condition	Aging Condition	Elongation in 1.125 in. (%)	Tensile Strength (psi)	Yield Strength (psi)
As welded	No age	30.13	34,710	25,040
	540°C, 100 hr	32.35	34,760	24,320
	595°C, 100 hr	20.80	41,495	31,225
	650°C, 100 hr	20.18	43,080	30,655
	650°C, 1000 hr	20.89	35,520	22,560
Solution annealed 1065°C - 2 hr	No age	24.89	40,675	22,185
	540°C, 100 hr	28.53	38,190	22,470
	595°C, 100 hr	27.55	40,130	21,785
	650°C, 100 hr	33.07	37,850	16,695
	650°C, 1000 hr	32.08	33,885	17,850
Solution annealed 1065°C - 2 hr followed with 800°C - 10 hr. Carbide agglomeration.	No age	31.20	38,645	21,885
	540°C, 100 hr	26.93	40,605	21,905
	595°C, 100 hr	26.40	42,985	24,290
	650°C, 100 hr	34.31	37,945	16,570
	650°C, 1000 hr	28.44	31,160	16,820

Study of Shielded Metal-Arc Process

Investigations of Mechanical Properties (R. G. Berggren, N. C. Binkley, G. M. Goodwin)

Of the 21 weld-metal compositions investigated in this program, the most promising have contained 0.002 to 0.009% B and up to 0.054% P. Three of these welds (F-17, F-18, and F-21) were selected for study of the effects of commercially feasible heat treatments on weldment properties. The compositions of deposited weld metal and welding parameters for these weldments are given in Table 5.9, and the heat treatments selected for study are shown in Fig. 5.2.

The creep-rupture test results that we have obtained for these weldments and heat treatments are presented in Table 5.10 and Figs. 5.3 and 5.4. A portion of the data for welds F-17 and F-18 was presented in the previous progress report[2] and the testing of weld F-21 is in progress with two tests completed. The rupture lives of as-welded specimens of weld F-17 are slightly better than for weld F-18, while the single result for weld F-21 is better than either weld F-17 or F-18. All of the heat treatments resulted in lowering the rupture lives about one order of magnitude, with the rupture lives for heat-treated specimens of welds F-17 and F-18 falling in a relatively narrow band. The total elongation results, Fig. 5.4, indicate that heat treatments 3, 7, and 8 did not improve ductility, but heat treatments 4 and 6 improved ductilities markedly. Heat treatments 4 and 6 involved both annealing at 1065°C (1950°F) and holding at 650°C (1200°F) for 100 hr. It is surprising that heat treatment 4 resulted in better ductility than for heat treatment 3, since the only difference between these two treatments was that heat treatment 4 included 100 hr at 650°C (1200°F), a treatment that might embrittle the weld by producing sigma phase. Total elongations for two tests of weld F-18 (as welded) are not plotted on Fig. 5.4 because the low elongations recorded probably were due to fracture at the specimen shoulder.

Heat-Treatment Studies (Nancy C. Cole, G. M. Goodwin, T. M. Kegley)

The welded specimens that were heat treated and reported last quarter[3] have been examined metallographically. By varying the temperature and concentrations of Murakami's etch, we were able to selectively

ORNL-DWG 71-2300R

HEAT TREATMENTS:

(1) AS WELDED
(2) 1200°F(100 hr), 100°F/hr → 850°F, WQ
(3) 1950°F(2 hr), 150°F/hr → 1472°F(10 hr), 400°F/hr → 850°F, WQ
(4) 1950°F(2 hr), 150°F/hr → 1472°F(10 hr), 400°F/hr → 850°F, WQ, 1200°F(100 hr), 100°F/hr → 850°F, WQ
(5) 1950°F(2 hr), 150°F/hr → 1472°F(10 hr), 100°F/hr → 850°F, WQ
(6) 1950°F(2 hr), 150°F/hr → 1472°F(10 hr), 100°F/hr → 850°F, WQ, 1200°F(100 hr), 100°F/hr → 850°F, WQ
(7) 1750°F(2 hr), 150°F/hr → 1472°F(10 hr), 400°F/hr → 850°F, WQ
(8) 1750°F(2 hr), 150°F/hr → 1472°F(10 hr), 400°F/hr → 850°F, WQ, 1200°F(100 hr), 100°F/hr → 850°F, WQ
(9) 1750°F(2 hr), 150°F/hr → 1472°F(10 hr), 100°F/hr → 850°F, WQ
(10) 1750°F(2 hr), 150°F/hr → 1472°F(10 hr), 100°F/hr → 850°F, WQ, 1200°F(100 hr), 100°F/hr → 850°F, WQ

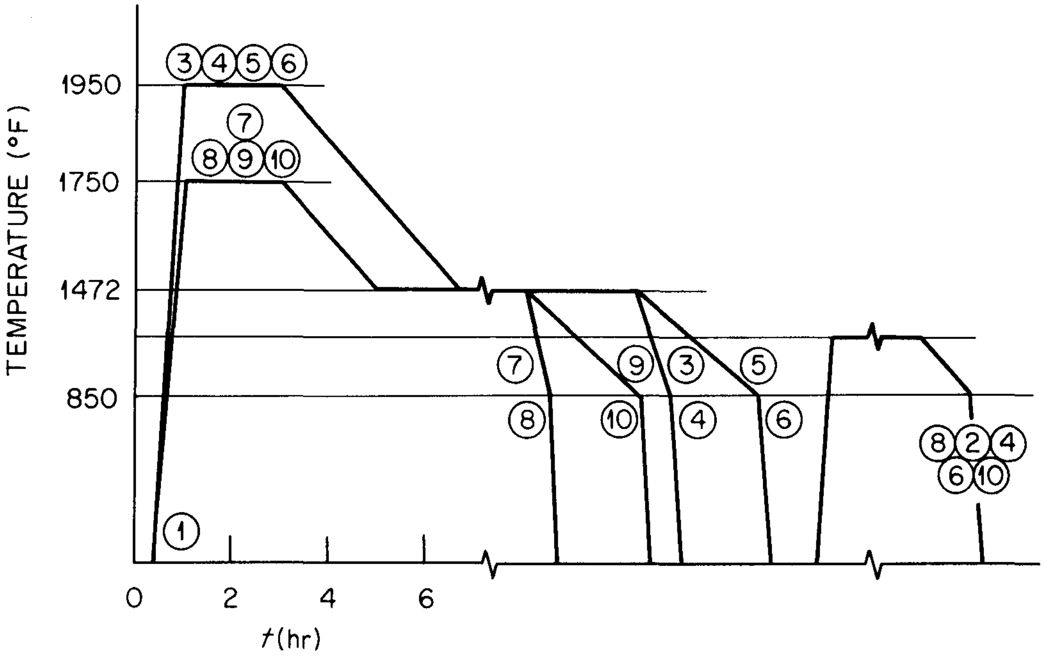

Fig. 5.2. Weldment Heat Treatment Schedule.

ORNL-DWG 71-2299R

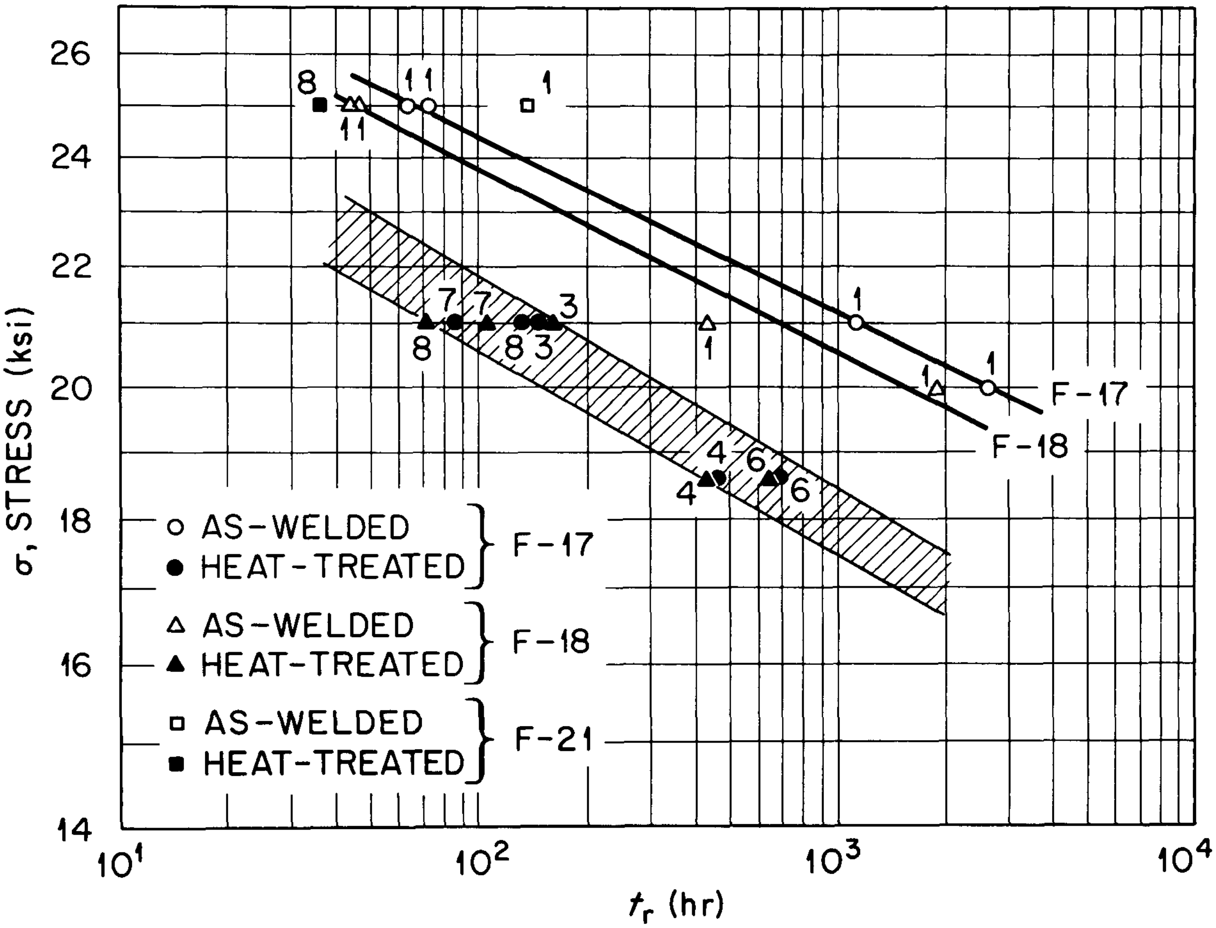

Fig. 5.3. Effect of Heat Treatment on Creep-Rupture Life of Boron-Containing Stainless Steel Weldments.

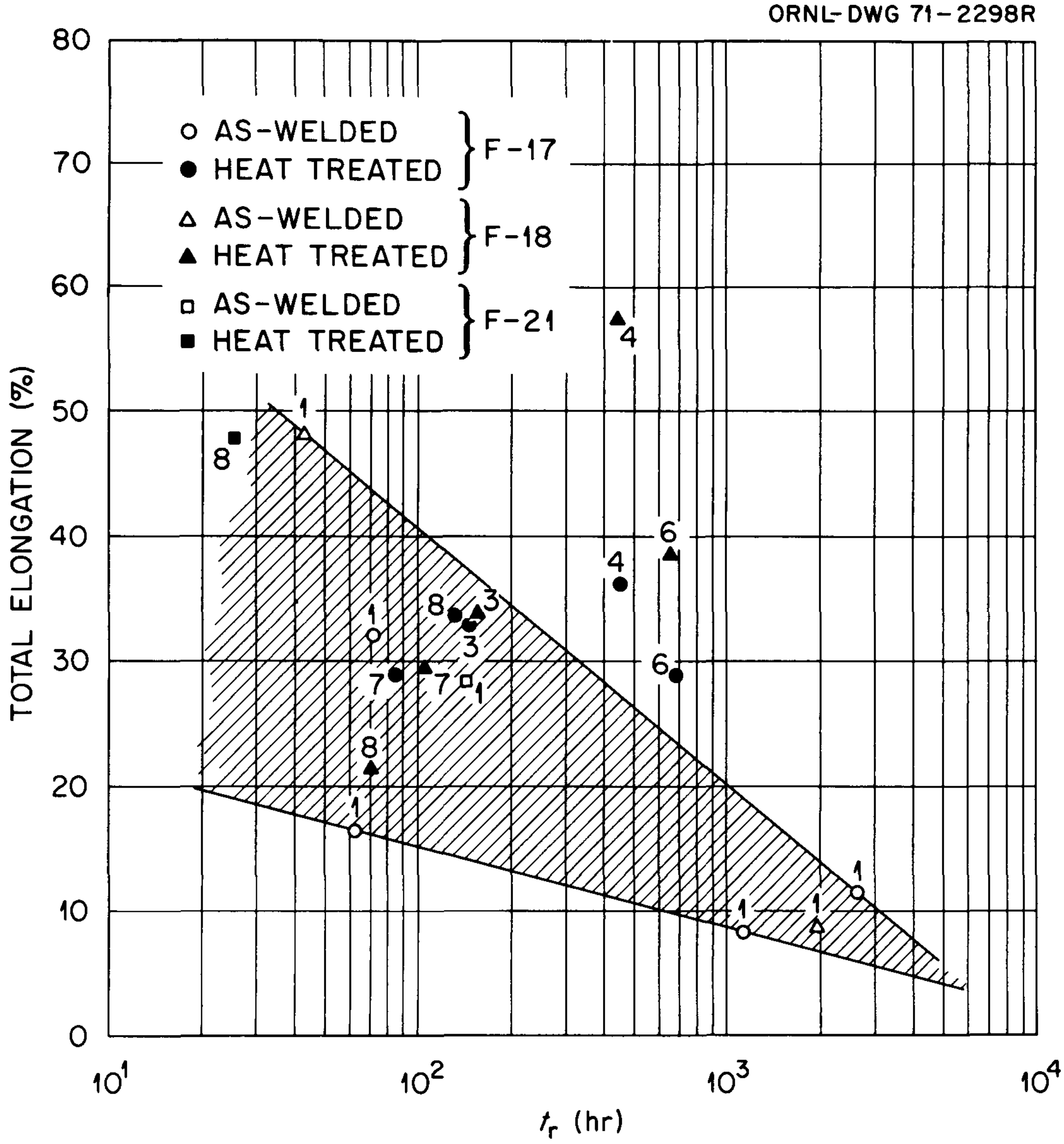

Fig. 5.4. Effect of Heat-Treatment on Creep-Rupture Elongation of Boron-Containing Stainless Steel Weldments.

Table 5.9. Composition of Deposited Weld Metal and Welding Parameters for Boron- and Phosphorus-Containing Stainless Steel Weldments

Weld	Composition, %												Current (amp)	Voltage (v)
	Si	S	P	Mn	C	Cr	Ni	Mo	Cu	Co	B	N		
F-17	0.42	0.017	0.037	1.78	0.050	19.86	10.13	0.04	0.06	0.02	0.005	0.042	140	20
F-18	0.50	0.013	0.033	1.73	0.041	19.93	9.82	0.02	0.02	0.038	0.0022	0.038	140	20
F-21	0.48	0.010	0.054	1.81	0.066	19.83	10.21	0.15	0.11	0.07	0.009	0.047	310	N.A.

Table 5.10. Effect of Heat Treatment on Creep-Rupture Properties of Boron-Containing Stainless Steel Weldments at 650°C

Weld	Heat Treatment	Specimen Type	Stress (ksi)	Rupture Life (hr)	Total Elongation (%)	Reduction in Area (%)	Minimum Creep Rate (%/hr)	Test No.	Remarks
F-17 (0.005% B, 0.037% P)	1	LW	25	72.3	32.0	61.5	0.026	W-56	
		LW	20	2631.7	11.7	58.1	0.00005	W-58	
		TW	25	62.7	16.4	65.6	0.028	W-62	
		TW	21	1112.9	8.4	56.1	0.00036	W-70	
	3	TW	21	148.5	33.1	65.6	0.14	W-63	
	4	TW	18.5	454.1	36.1	73.3	0.044	W-72	
	6	TW	18.5	695	28.8	45.4	0.023	W-73	
	7	TW	21	85.4	28.8	72.7	0.14	W-64	
	8	TW	21	132.5	33.8	68.9	0.10	W-66	
F-18 (0.0022% B, 0.033% P)	1	LW	25	43.2	48.0	59.9	0.062	W-57	
		LW	20	1940.0	8.9	33.7	0.0002	W-59	
		TW	25	45.8	5.3	2.4	0.032	W-65	Fractured at shoulder
		TW	21	436.0	3.4	1.6	0.0014	W-71	
	3	TW	21	155.2	33.5	67.3	0.14	W-67	
	4	TW	18.5	447.2	57.4	49.8	0.069	W-74	
	6	TW	18.5	651.9	38.4	49.4	0.036	W-75	
	7	TW	21	105.6	29.3	41.7	0.15	W-69	
	8	TW	21	70.5	21.4	51.3	0.16	W-68	
F-21 (0.009% B, 0.054% P)	1	LW	25	141.3	28.2	71.1		W-84	
	8	LW	25	27.4	47.0	74.5		W-85	

identify ferrite, sigma phase, and carbides. Boiling Murakami's etch brings out ferrite as well as sigma phase (very darkly) and carbides Room-temperature Murakami's etch for 20 sec shows carbides darkly, ferrite slightly, and sigma phase not at all. Room-temperature concentrated Murakami's etch [30 $K_3Fe(CN)_6$, 30 KOH, 60 H_2O] for 4 sec brings out sigma phase heavily, ferrite and carbides lightly. These etches are compared in Fig. 5.5. Figure 5.5(a) shows a large amount of sigma phase (dark etching) with ferrite lightly in the background. Figure 5.5(b) shows carbides outlining the substructure boundaries as well as in the austenitic matrix.

In addition to the submerged-arc (SA) and shielded metal-arc (SMA) welds reported previously,[3] for comparison a CF8 stainless steel casting which was electroslag welded by ESCO Corporation has been examined after selected heat treatments. Before heat treating, the base metal had 17% of very coarse ferrite in the substructure, as seen in Fig. 5.6(a). The weld metal had 6% of finer ferrite as seen in Fig. 5.6(c) in spite of the fact that the weld is composed primarily of filler wire fortified with ferrite-forming elements. This, presumably, is due to the gross differences in solidification rate between the massive casting and the electroslag weld.

Trends in the formation of sigma phase in these welds have been determined. Sigma phase does not form upon welding, nor after subsequent low-temperature heat treatment of 100 hr at 540°C (1000°F) or a high-temperature heat treatment of 930°C (1700°F) for 10 hr. It does form in varying amounts in the different welds in the temperature range of 595 to 870°C (1100 to 1600°F) after times of 10 to 1000 hr as seen in Fig. 5.7. This chart compares four shielded metal-arc welds, three submerged-arc welds, and the electroslag weld and its cast base metal described above.

As expected, sigma phase generally formed in greater amounts in the specimens with the most and coarsest ferrite. Longer times (1000 hr) at temperatures produced more sigma phase. At 870°C (1600°F), the SMA welds with finer ferrite substructure showed no sigma phase, whereas the coarser SA welds showed some sigma phase, and the much coarser electroslag weld and base metal shows much more sigma phase. After 1000 hr at 650°C (1200°F), the SA welds, the electroslag weld, and base metal had very large amounts of sigma phase, whereas the SMA welds had slight to moderate amounts. Apparently, sigma phase forms most rapidly between 705 and 816°C

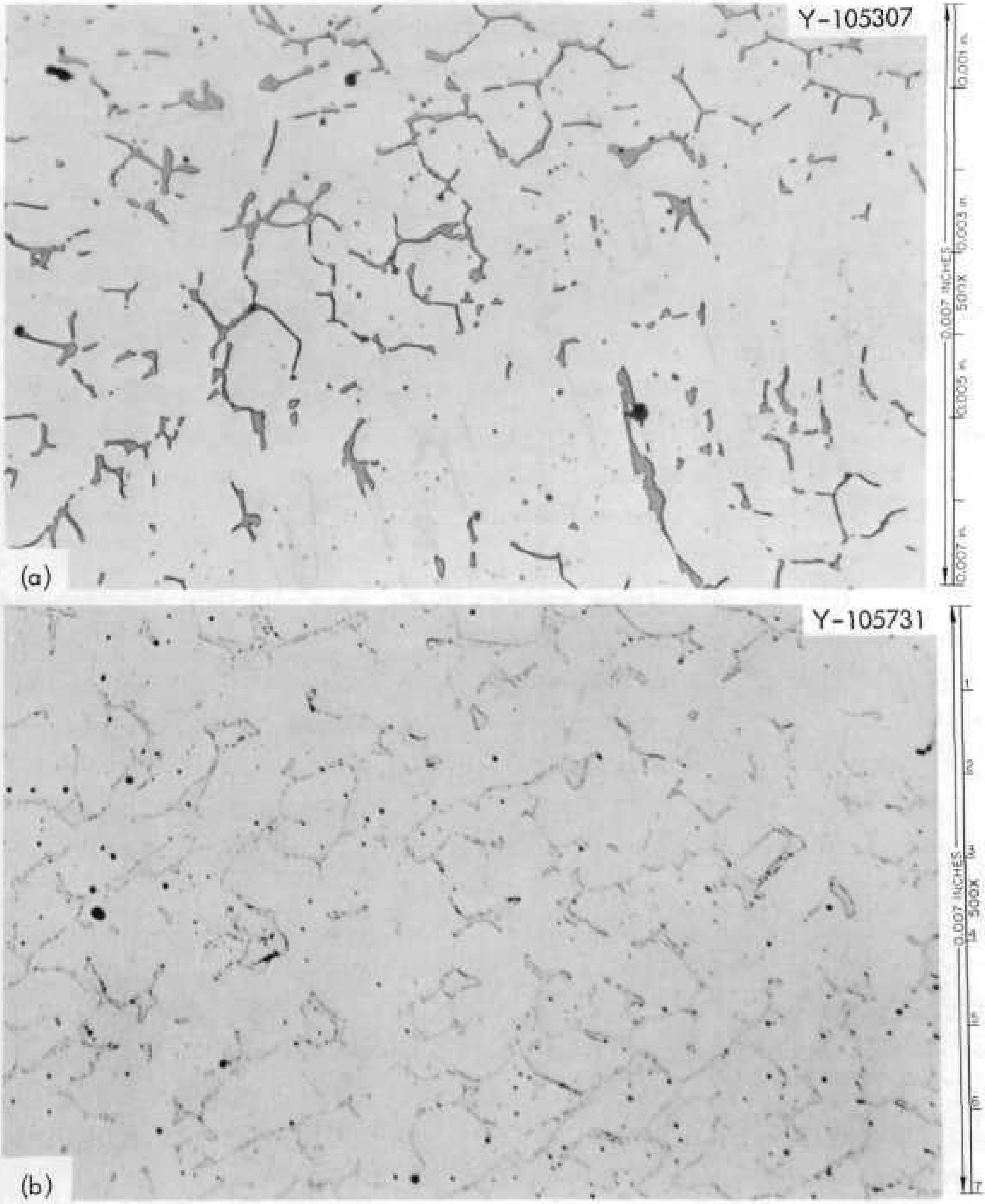

Fig. 5.5. Type 308 Stainless Steel Welds. (a) Etched with concentrated Murakami's reagent [30 $K_3Fe(CN)_6$, 30 KOH, 60 H_2O] for 4 sec at room temperature to show sigma phase darkly and ferrite and carbides lightly. (b) Etched with Murakami's reagent [10 $KFe(CN)_6$, 10 KOH, 100 H_2O] at room temperature for 20 sec to show carbides. 500X.

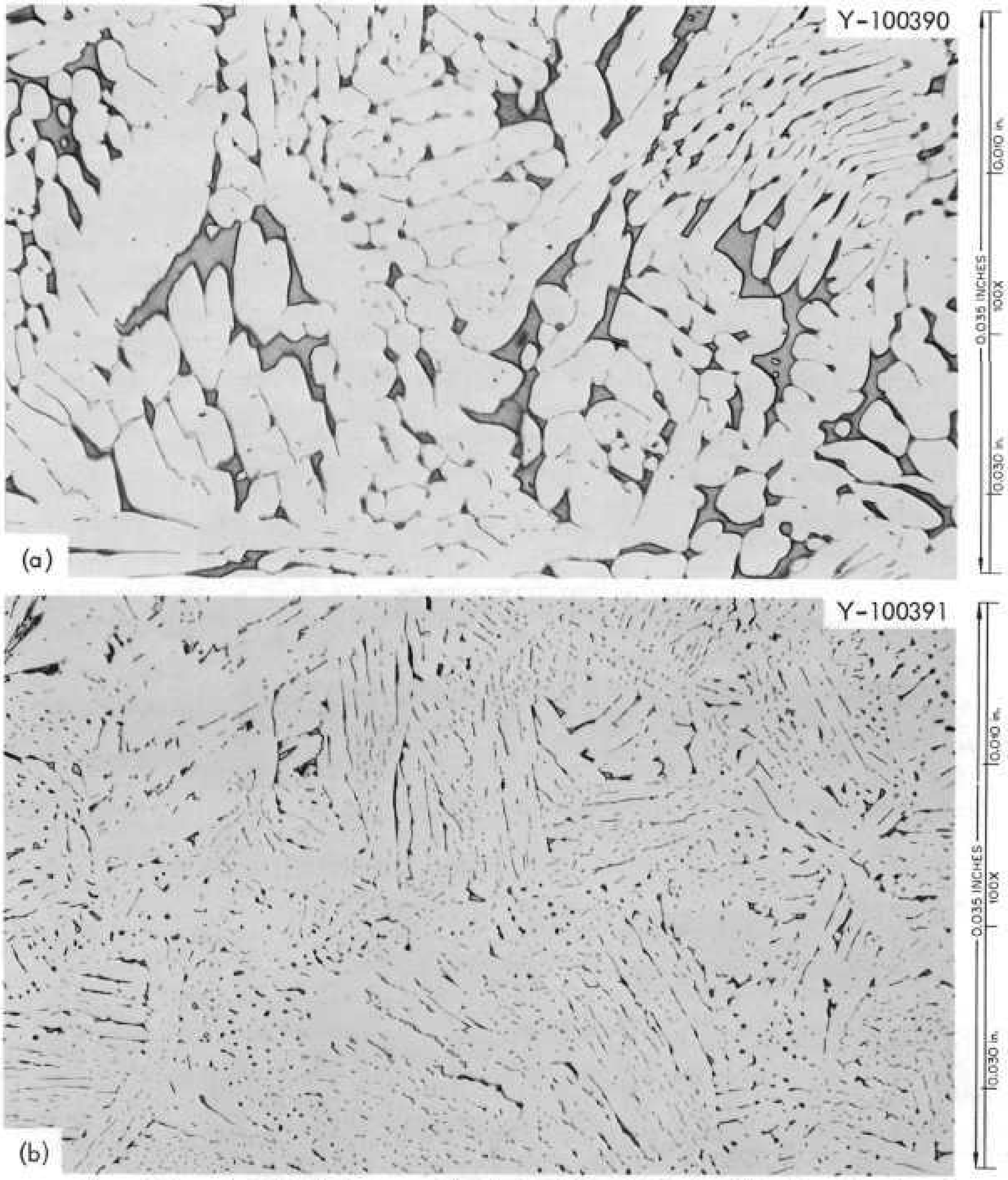

Fig. 5.6. A CF8 Stainless Steel Casting Welded with the Electroslag Process. (a) As-cast base metal containing 17% ferrite. (b) Electroslag weld in the above casting using type 308 filler metal. The weld contains only 6% ferrite. Etched with boiling Murakami's reagent. 100X.

ORNL-DWG 71-4683

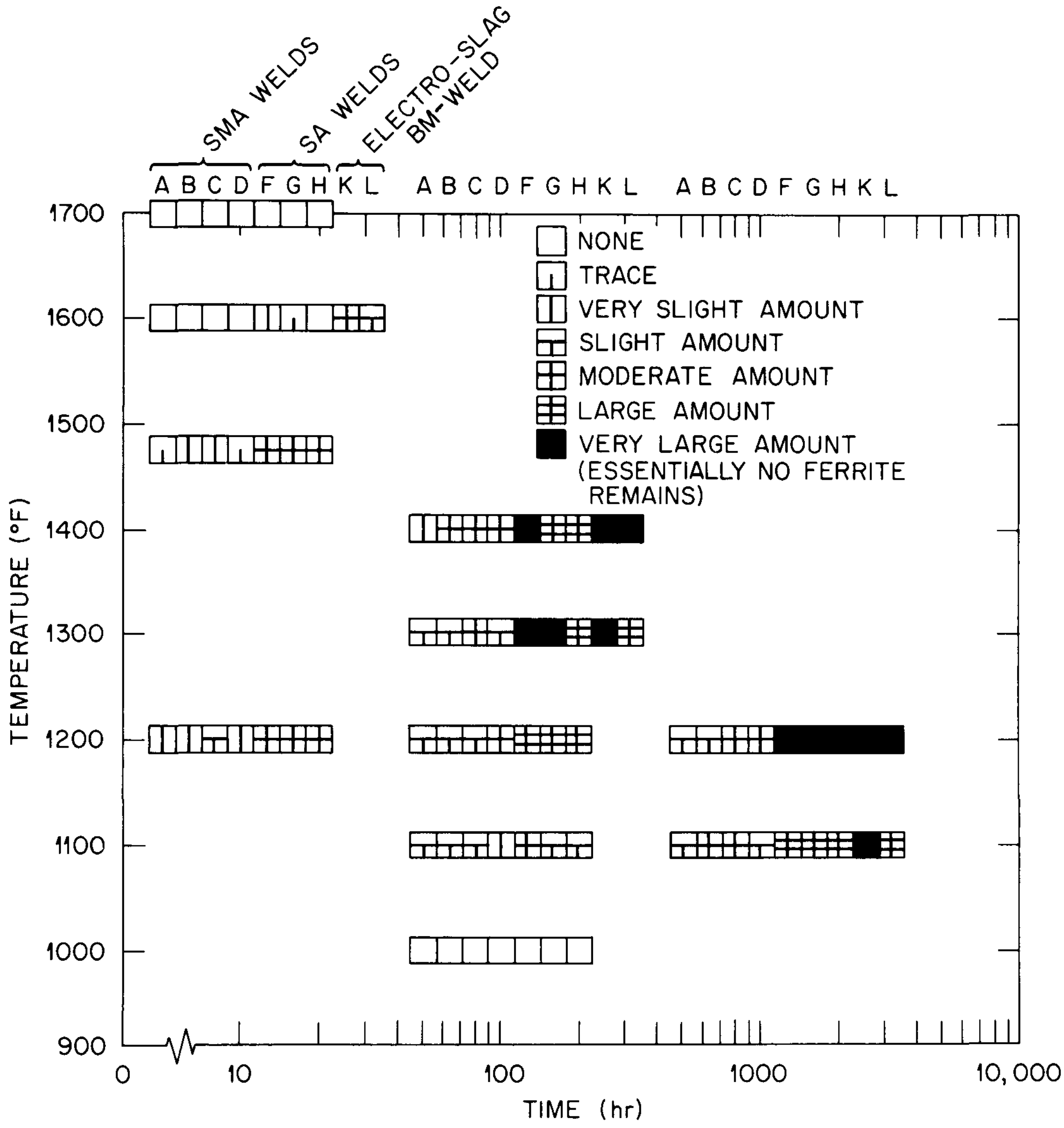

Fig. 5.7. Amount of Sigma Phase Formed from Ferrite in Austenitic Stainless Steel Welds During Heat Treatment.

(1300 and 1500°F), depending on the particular weld specimen. Figure 5.8 shows sigma phase in a SA weld after 100 hr at 540, 595, 705, and 760°C (1000, 1100, 1300, and 1400°F). Note that no sigma phase has formed at 540°C (1000°F).

Solution annealing at 1065°C (1950°F) for 1 hr appears to retard sigma phase formation as seen in Fig. 5.9. Both specimens were taken from the same SA weld. The one in Fig. 5.9(a) was annealed at 1065°C for 1 hr prior to holding at 800°C (1470°F) for 10 hr and the one in Fig. 5.9(b) was only held at 800°C for 10 hr without a solution anneal. Note that there is significantly less sigma phase in Fig. 5.9(a) which was exposed to 1065°C for 1 hr. Probably this is caused by the smaller amount of ferrite present after annealing at 1065°C. The smaller amount of sigma phase after the 1065°C anneal may be one reason why this anneal improves weld ductility in creep tests as discussed elsewhere in this report.[4]

Corrosion Studies (G. M. Goodwin, N. C. Cole)

The results of Strauss tests on specimens 15 through 56 are shown in Table 5.11. The heat treatment of these specimens was reported previously[5] and was based upon the results of tests 1 through 14, also reported earlier.[6] Note from the table that five different weldments are involved in this series of tests. It is significant to note that both the weld metal and base metal from each of the five weldments passed the Strauss test in the as-welded condition. Also, note that the nine heat treatments caused all base-metal specimens to fail, with two exceptions, tests 41 and 51. The base metal in each of these tests contained 0.028% C. Thus, since the heat treatments applied are typical of those being considered for the FFTF vessel and, considering the carbon effect noted in the first series of Strauss tests, it is highly likely that any reasonable heat treatment which may be applied to the FFTF vessel (approx 0.05–0.07% C) would cause it to fail the Strauss test.

Note also that weld F-21, which is most representative of the actual FFTF vessel welds, will pass the Strauss test in the weld metal if solution treated at 955°C, whereas it will fail if solution treated at 1065°C. It appears then that, based upon the Strauss test, lower solution treating temperatures are desirable.

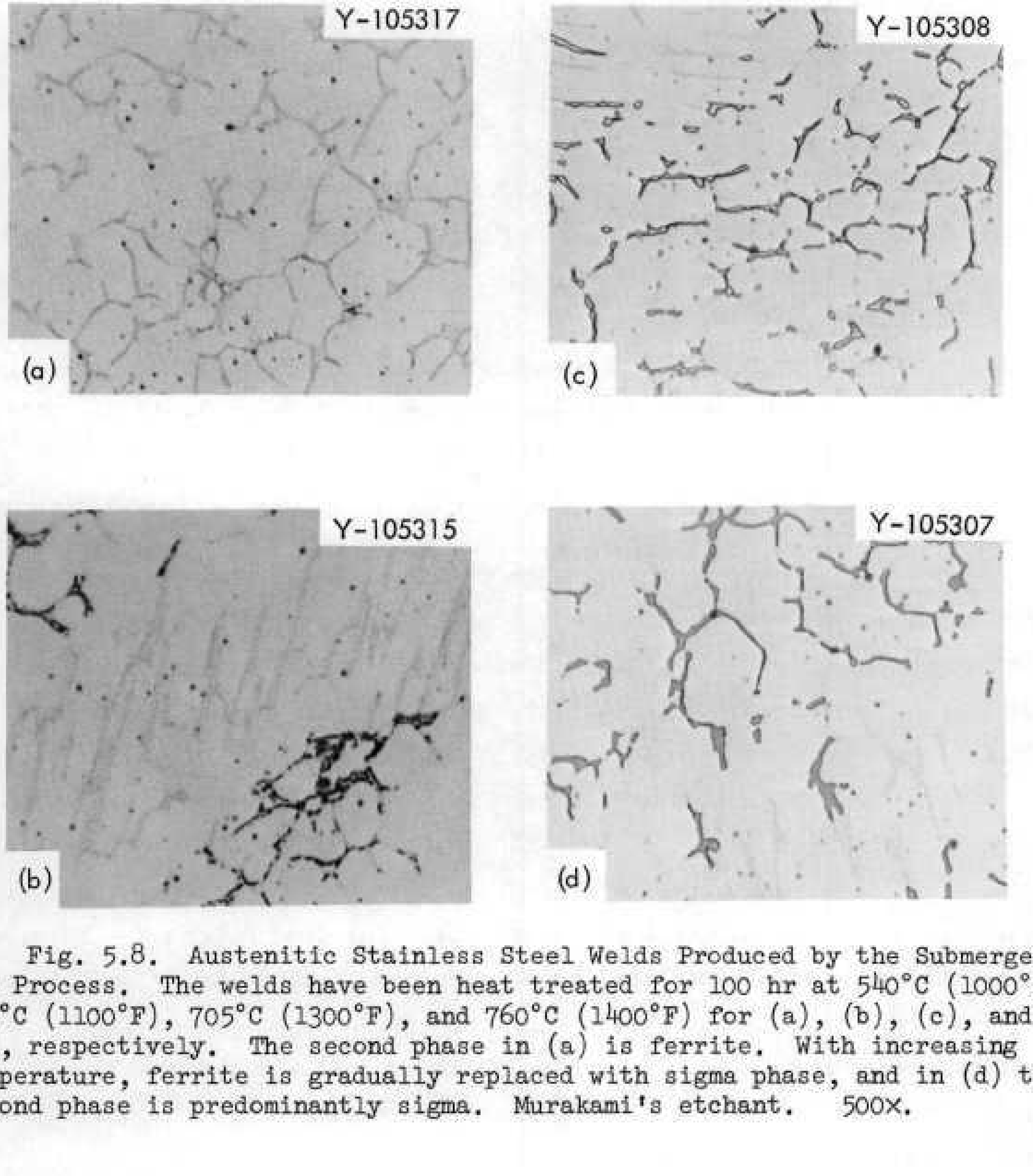

Fig. 5.8. Austenitic Stainless Steel Welds Produced by the Submerged-Arc Process. The welds have been heat treated for 100 hr at 540°C (1000°F), 595°C (1100°F), 705°C (1300°F), and 760°C (1400°F) for (a), (b), (c), and (d), respectively. The second phase in (a) is ferrite. With increasing temperature, ferrite is gradually replaced with sigma phase, and in (d) the second phase is predominantly sigma. Murakami's etchant. 500×.

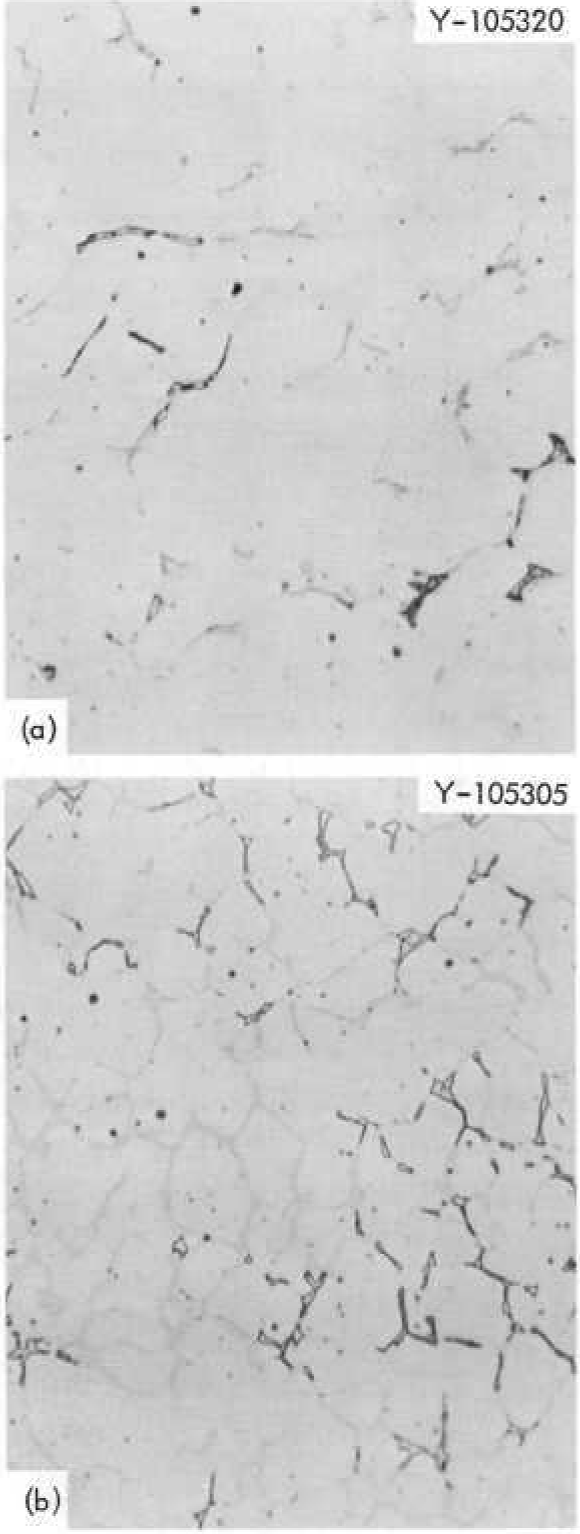

Fig. 5.9. Submerged Arc Stainless Steel Welds Heat Treated at (a) 1065°C (1950°F) for 1 hr, Furnace Cooled to 800°C and Held for 10 hr, and (b) 800°C (1472°F) for 10 hr After Welding. Murakami etchant. 500×.

Table 5.11. Summary of Results of Strauss Tests on Stainless Steel Weldment Wafers

Test No.	Weld No.[a]	Test Result[b]		Heat Treatment
		Weld Metal	Base Metal	
15	F17	P	P	As welded
16	F18	P	P	
17	F01	P	P	
18	F21	P	P	
19	SA8	P	P	
20	F17	P	F	650°C(100 hr), 55.5°C/hr → 455°C, WQ
21	F18	P	F	
22	F21	P	F	
23	F17	F	F	1065°C(2 hr), 83.3°C/hr → 800°C(10 hr), 222.2°C/hr → 455°C, WQ
24	F18	F	F	
25	F21	F	F	
26	SA8	P	F	
27	F17	F	F	1065°C(2 hr), 83.3°C/hr → 800°C(10 hr), 222.2°C/hr → 455°C, WQ, 650°C(100 hr), 55.5°C/hr → 455°C, WQ
28	F18	F	F	
29	F01	F	F	
30	F21	F	F	
31	SA8	P	F	
32	F17	F	F	1065°C(2 hr), 83.3°C/hr → 800°C(10 hr), 55.5°C/hr → 455°C, WQ
33	F18	F	F	
34	SA8	P	F	
35	F17	F	F	1065°C(2 hr), 83.3°C/hr → 800°C(10 hr), 55.5°C/hr → 455°C, WQ, 650°C(100 hr), 55.5°C/hr → 455°C, WQ
36	F18	F	F	
37	F01	F	F	
38	SA8	P	F	
39	F17	P	F	954°C(2 hr), 83.3°C/hr → 800°C(10 hr), 222.2°C/hr → 455°C, WQ
40	F18	P	F	
41	F01	P	P	
42	F21	P	F	
43	SA8	P	F	
44	F17	P	F	954°C(2 hr), 83.3°C/hr → 800°C(10 hr), 222.2°C/hr → 455°C, WQ, 650°C(100 hr), 55.5°C/hr → 455°C, WQ
45	F18	P	F	
46	F01	P	F	
47	F21	P	F	
48	SA8	P	F	

Table 5.11. (continued)

Test No.	Weld No.[a]	Test Result[b]		Heat Treatment
		Weld Metal	Base Metal	
49	F17	P	F	954°C(2 hr), 83.3°C/hr → 800°C(10 hr), 55.5°C/hr → 455°C, WQ
50	F18	P	F	
51	F01	P	P	
52	SA8	P	F	
53	F17	P	F	954°C(2 hr), 83.3°C/hr → 800°C(10 hr), 55.5°C/hr → 455°C, WQ, 650°C(100 hr), 55.5°C/hr → 455°C
54	F18	P	F	
55	F01	P	F	
56	SA8	P	F	

[a] F = shielded metal-arc process.
SA = submerged-arc process.
For additional details, refer to prior Fuels and Materials Quarterly Progress Reports.

[b] P = pass.
F = fail.

A more detailed analysis of the results of this series of tests will be presented after metallographic examination of the specimens.

References

1. N. C. Binkley, Fuels and Materials Development Program Quart. Progr. Rept. Dec. 31, 1970, ORNL-TM-3300.
2. R. G. Berggren, N. C. Binkley, and G. M. Goodwin, Fuels and Materials Development Program Quart. Progr. Rept. Dec. 31, 1970, ORNL-TM-3300.
3. N. C. Cole, G. M. Goodwin, and T. M. Kegley, Fuels and Materials Development Program Quart. Progr. Rept. Dec. 31, 1970, ORNL-TM-3300.
4. G. M. Goodwin and R. G. Berggren, Fuels and Materials Development Program Quart. Progr. Rept. Dec. 31, 1970, ORNL-TM-3300.
5. G. M. Goodwin and Nancy C. Cole, Fuels and Materials Development Program Quart. Progr. Rept. Dec. 31, 1970, ORNL-TM-3300.
6. G. M. Goodwin and Nancy C. Cole, Fuels and Materials Development Program Quart. Progr. Rept. Sept. 30, 1970, ORNL-4630, pp. 135,137.

6. ✓PROPERTIES OF FERRITIC STEEL WELDS

J. R. Weir, Jr.   G. M. Slaughter

The use of ferritic steels for tubing, piping, and headers in high-integrity steam generators requires that their overall weldability and the mechanical properties of weld metal and heat-affected zone at elevated temperatures (290 to 595°C or 555 to 1100°F) be assessed. The susceptibility of both the weld metal and the heat-affected zones to cracking is of particular interest.

This program deals with several classes of ferritic steel that are candidates for use in either liquid-metal-cooled or water-cooled reactors. The purpose of the program is to compare the weldabilities of these various steels and to determine the advantages and limitations of each. We emphasize determining susceptibility to cracking associated with the weld and the effects of welding on mechanical properties at the expected service temperatures.

Low-Carbon Low-Alloy Steels

<u>Preparation and Testing of Specimens</u> (D. A. Canonico, H. E. McCoy)

The low-carbon plate and tubing previously discussed[1] has been chemically analyzed and its composition is given in Table 6.1. It can be seen that there are pecularities in the steels. For instance, material identified as C is remelted 2 1/4 Cr—1 Mo steel. Its analysis matches that of nominal commercial material. The other two heats, A and B, were special heats; however, the Si in heat A is high. In fact, the Si in heat AT is above the allowable in ASTM A213-T22, and the P in heat B is high.

A weld joint preparation was selected that provided a 90° included angle, a 0.00- to 0.010-in. root face, and a 1/16-in. root opening. The plates were welded to 2-in.-thick strong-backs in order to simulate a fully restrained condition during welding. The welds were made using the gas tungsten-arc (GTA) process and cold wire feed. The welding parameters employed were: 180—200 amp, 1/8-in.-diam electrode, and 65—90°C (150—200°F)

Table 6.1. Chemical Analysis of Low-Carbon Low-Alloy Steels Used in This Program

Material Identification	Chemical Composition, wt %								
	C	Mn	Si	Cr	Mo	Ni	Nb	S	P
A[a]	0.003	0.33	0.41	2.6	1.14	< 0.02	< 0.05	0.008	0.002
AT[b]	0.008	0.50	0.58	2.5	0.98	< 0.05	< 0.05	0.008	0.006
B	0.035	0.30	0.20	2.4	1.17	< 0.02	< 0.05	0.016	0.022
BT	0.03	0.39	0.22	2.4	1.1	< 0.05	< 0.05	0.019	0.022
C	0.11	0.33	0.27	2.4	0.97	0.24	< 0.05	0.011	0.0095
CT	0.105	0.45	0.34	2.3	0.87	0.28	< 0.05	0.011	0.018

[a] Single letter is plate designation.

[b] T refers to tubular product.

interpass temperature. All weld-metal specimens were prepared and tested at room temperature and 565°C (1050°F). Transverse weldment metallographic specimens were also removed and microhardness traverses were made on these specimens.

The base material that remained after specimen removal was normalized at 925°C (1700°F) for 1 hr and tempered at 700°C (1300°F) for 1 hr.

The tensile specimens were tested in the as-welded condition and after a 700°C postweld heat treatment for 1 hr. The results of these tests are given in Table 6.2. There is a difference of more than a factor of two between the ultimate tensile strength of the low-carbon (A) and the nominal carbon (C) steels at 565°C (1050°F). This difference is not compensated for in ductility if total strain is the criterion for comparison. A difference, about 20%, does exist for the reduction-in-area (R.A.). Postweld heat treating has essentially no effect on the strength properties of the low-carbon (A) steel. It does, however, result in a large loss in strength in the high-carbon (C) steel. Further, at 565°C, the yield-to-tensile ratios of the heat-treated specimens are nearly unity (in all steels tested) with high R.A. values. If a postweld heat treatment is imposed on the

Table 6.2. Results of All-Weld-Metal Tensile Tests on Low-Carbon Low-Alloy Steel Welds

Specimen Designation	Test Temperature (°C)	Stress, ksi		Ductility, %	
		Yield	Ultimate	Total Strain	Reduction in Area
1A1-1	R.T.	88.5	101.4	14.35	79.5
1A1-2	565	53.8	56.7	12.05	80.5
1A1-3[a]	565	57.8	61.0	8.75	69.4
1A4-1A[b]	R.T.	60.2	74.0	20.1	88.7
1A4-2A[b]	565	46.3	50.1	15.9	86.3
1B1-1	R.T.	82.0	104.5	15.65	80.4
1B1-2	565	68.8	92.4	17.8	69.7
1B1-3[a]	565	74.6	90.7	12.55	52.5
1B6-1A[b]	R.T.	72.2	86.1	18.6	81.2
1B-2A[b]	565	55.0	57.5	13.1	87.5
1C1-1	R.T.	135.2	157.6	14.5	72.0
1C1-2	565	102.5	118.4	13.1	60.8
1C1-3[a]	565	101.5	116.9	7.7	13.1
1C7-1A[b]	R.T.	90.7	101.6	15.65	84.0
1C7-2A[b]	565	66.0	68.6	13.85	85.0

[a] Tests conducted at head speed of 0.002 in./min. All others at 0.05 in./min.

[b] Designation describes a postweld heat treatment of 700°C (1300°F) for 1 hr.

weldment, there does not appear to be any advantage to the medium-carbon (A) steel.

A deleterious effect of strain rate, particularly on the medium- and high-carbon (B and C) steels is suggested by these data. The R.A. values dropped rather precipitously, due to the 700°C (1300°F) treatment. These results strongly support the need for an extensive test program to generate long-time low-strain-rate data for welds in these steels.

Hardness traverses (diamond pyramid hardness test) were made across these weldments. Table 6.3 contains the results of this study. Both last weld pass and early weld pass (weld metal that has been exposed to thermal excursions due to the multipass weld technique employed) areas were investigated. The steel was used to provide the containment to provide all-weld-metal specimens with the correct amount of dilution from the base metal. It is significant to note the increased hardness in the heat-affected zone (HAZ) of the multipass region of the low-carbon (A) welds. Further, the low value of 129 DPH in the as-welded HAZ is extremely low and could result in a metallurgical notch in service. The HAZ of the medium- and high-carbon (B and C) steels do not reflect a significant hardness difference due to their thermal histories; however, it is certain that a hardness difference does exist. The high-carbon (C) weld metal underwent a large reduction in hardness due to the effect of the weld passes.

Table 6.3. Hardness Measurements in Low-Carbon Low-Alloy Steel Welds

Weld Designation	Carbon (%)	Diamond Pyramid Hardness Number			
		Heat-Affected Zone		Weld Metal	
		Last Pass	Early Pass	Last Pass	Early Pass
1A	0.003	129	161–171	224–257	162–210
1B	0.03	182	193	251–297	219–263
1C	0.11	245	251	339–401	276–305

Stabilized Low-Alloy Steels

Procurement of Material (D. A. Canonico)

One-inch-thick slabs of Nb-stabilized low-alloy steel from two heats have been received. This procurement has provided us with about 17 ft^2 of plate. Two slabs from each heat are being rolled, one to 1/4-in. thickness and one to 1/2-in. thickness. These plates will be used to make fully restrained welds similar to those made in the low-carbon low-alloy weldments.

References

1. D. A. Canonico and N. C. Binkley, Fuels and Materials Development Program Quart. Progr. Rept. Dec. 31, 1970, ORNL-TM-3300, p. 160.

7. NONDESTRUCTIVE TESTING TECHNIQUES FOR LMFBR

W. O. Harms   R. W. McClung

We are developing new methods, techniques, and equipment for nondestructively evaluating materials or components related to the liquid-metal fast breeder reactor (LMFBR). Among the methods studied are electromagnetic induction, ultrasonics, and penetrating radiation. Special emphasis is being given to developing techniques for measuring the degree of cold work in stainless steel tubing with a small diameter.

Development of Advanced Nondestructive Testing

Development of Eddy-Current Instrument (C. V. Dodd)

We are continuing the development of an eddy-current instrument to measure both the size of defects and their depth beneath the surface. We have completed construction of the dual-frequency oscillator and power amplifier module for the modular phase-sensitive eddy-current instrument. The modular instrument has been modified to work in a two-frequency mode. Eleven tuned amplifiers have been designed and constructed to operate at frequencies ranging from 1 KHz to 2 MHz in a 1, 2, 5 sequence.

Ultrasonic Schlieren Techniques for Evaluation of Welds (H. L. Whaley, K. V. Cook)

We are using the schlieren-imaging technique in conjunction with two established ultrasonic techniques for weld inspection to study the response of ultrasound to various types of weld defects. The samples were butt-welded from 1 in. thick aluminum and stainless steel plate and contain intentional defects such as porosity, inclusions, incomplete fusion and incomplete penetration.

Four stainless steel weld specimens were tested by the Delta technique, described in an earlier report.[1] Plan view recordings made at a variety of sensitivity levels indicate that the indications from the reference holes cannot be separated from other indications from the weld area. Whether the

---

"noisy" condition of the stainless steel welds is due to multiple flaws or grain boundary scattering will be determined by radiography and other ultrasonic tests to be conducted on the same specimens. If the "noisy" appearance of the stainless steel welds is due to scattering from grain boundaries, the Delta technique may loose some of its advantages relative to other techniques because of its inherent dependence on scattered energy.

Measurement of Cold Work in Stainless Steel Tubing

Studies in Coil Design (C. V. Dodd, W. A. Simpson)

We are investigating methods for nondestructively measuring the degree of cold work in stainless steel tubing that has a small diameter. We emphasize the use of electromagnetic induction for detecting the changes in magnetic permeability produced by cold work.

We are performing calculations on two new types of coil systems for measuring permeability changes, both of which have separate driver and detector coils. The first type consists of bifilar-wound coils, and the second type consists of separate driver and pick-up coils placed side-by-side. The bifilar-wound coils produce a voltage with a higher magnitude, and a slightly greater variation in voltage with change in permeability, but has a larger amount of drift. The side-by-side coils have approximately half the output voltage of the bifilar wound coils, but exhibit a smaller amount of drift. The side-by-side coils would also be easier to construct and would be easier to eliminate thermal expansion of these coils. Also, since the driver coil is slightly removed from the pick-up coil, thermal variations in the driver coil would be isolated from the pick-up coil. After we determine the optimum shape for the side-by-side configurations, we will construct and test it.

References

1. H. L. Whaley and K. V. Cook, Fuels and Materials Development Program Quart. Progr. Rept. June 30, 1970, ORNL-4600, p. 154.

8. /SODIUM CORROSION STUDIES

W. O. Harms J. H. DeVan

The purpose of this program is to investigate the chemical and metallurgical effects produced in refractory metals during exposure to molten Na. Of principal interest are the corrosion properties of V-base alloys, which have been under development as cladding materials for high-temperature fuels for LMFBR systems.

Comparative Corrosion Tests on Refractory Alloys

J. H. DeVan

Since refractory alloys strongly resist dissolution by Na, they have promise as advanced materials for cladding and control rods for Na-cooled reactor systems. However, the interactions of refractory alloys with impurities in Na must be understood before the feasibility of using these alloys for cladding can be decided. Accordingly, our studies of the compatibility of refractory metals with Na are aimed at effects associated with O supplied by the Na and with C and N supplied by stainless steel.

Effect of Oxygen on the Compatibility of Vanadium and Vanadium Alloys with Sodium (R. L. Klueh)

We previously discussed[1] how a specimen of unalloyed V can be combined with a V alloy in Na to determine the effect of Cr and Mo on the solubility and diffusion of O in V. We doped specimens of V, V–5% Cr, V–10% Cr, V–15% Cr, and V–20% Mo with approximately 5000 ppm O and exposed specimens of each alloy with a V specimen in type 304L stainless steel capsules in the following sequence: a doped alloy with undoped V, undoped alloy with doped V, and doped alloy with doped V. We also tested capsules with one doped and one undoped V specimen. Tests were run for 250 and 1000 hr at 600°C.

After test, the doped V specimens exposed with undoped alloys exhibited a uniform dark gray coating. Since there was little difference between the color of these specimens and the doped V specimen exposed to undoped V, the alloying elements do not appear responsible for the discoloration. The discoloration of the V–Cr alloys decreased in going from V–5% Cr to V–15% Cr; this was true for both the doped and undoped alloys, though the doped alloys were somewhat darker than the undoped alloys. None of the V–20% Mo specimens, doped or undoped, were discolored.

Table 1 compares the change in weight with changes in O concentration for each test. There is reasonable agreement between the weight change and change in O concentration for a given specimen, an indication that there was little or no interaction with the capsule. Also there appears to be a mass balance between the amount of oxygen transferred from the doped V and the amount picked up by the alloy to which it was exposed. All analytical chemistry techniques, including surface x-ray diffraction, wet chemistry, and neutron activation analysis of scrapings from V specimen surfaces showed no measurable pickup of Fe, Ni, Cr, C or N.

Based on the distribution coefficients for oxygen that were previously determined,[2] we did not achieve equilibrium between the specimen pairs even in the 1000 hr tests. Accordingly, the specimens from the 250 hr tests have been re-encapsulated and will be exposed another 2250 hr.

The most striking result in Tables 1 and 2 is the sluggishness of the O transfer from the doped V specimens. This is particularly apparent in the tests with two unalloyed V specimens. Considering the magnitude of the O diffusion coefficient in V, the sluggishness of the transfer must mean that the O transfer is limited by a surface reaction or by diffusion through a surface film. Specimens are being examined metallographically and their microhardness profiles are being measured to resolve this uncertainty.

Oxidation of Vanadium and Vanadium Alloys (R. L. Klueh)

We are conducting oxidation studies of V–20% Ti and V at 1000°C. V–20% Ti is being studied to determine if, by proper pre-treatment, a selective Ti oxide can be formed on the specimen surface such that it will be protective during further exposure to an oxidizing atmosphere.[3]

Table 1. Weight Change and Oxygen Redistribution for Vanadium and Vanadium Alloys Exposed 250 hr to Sodium at 600°C

Vanadium Alloy	Oxygen Concentration, ppm[a]						Weight Change, mg	
	Vanadium			Vanadium Alloy			Vanadium	Vanadium Alloy
	Before	After	Change	Before	After	Change		
V–5% Cr	90	590	+500	5690	5100	-600	+0.8	-0.6
	5530	5260	-300	60	350	+300	-0.1	+0.5
	5550	5700	+150	5710	5660	-50	+0.3	-0.1
V–10% Cr	60	540	+500	5540	5150	-400	+0.8	-0.8
	5440	5310	-150	110	340	+250	-0.1	+0.4
	5310	5380	+100	5720	5270	-450	+0.7	-0.8
V–15% Cr	60	1100	+1050	5530	4430	-1100	+1.7	-2.0
	5470	5250	-200	110	220	+100	-0.1	+0.3
	5570	6170	+600	5430	4580	-800	+1.3	-1.9
V–20% Mo	120	460	+450	5820	5290	-500	+0.8	-0.3
	5400	5180	-300	70	301	+250	+0.1	+0.4
Vanadium + Oxygen	60	230	+200	6300	5810	-500	+0.3	-0.2

[a] Determined by fast neutron activation analysis.

Table 2. Weight Change and Oxygen Redistribution for Vanadium and Vanadium Alloys Exposed 1000 hr to Sodium at 600°C

Vanadium Alloy	Oxygen Concentration, ppm[a]						Weight Change, mg	
	Vanadium			Vanadium Alloy			Vanadium	Vanadium Alloy
	Before	After	Change	Before	After	Change		
V–5% Cr	70	660	+600	5300	4750	-650	+1.4	-0.9
	5370	4930	-500	100	750	+650	-0.8	+1.1
	5260	5770	+500	5540	5230	-300	+1.1	-1.0
V–10% Cr	100	2340	+2200	5420	3720	-1700	+3.4	-3.5
	5600	4860	-800	100	640	+600	-0.6	+0.9
	5370	6780	+1400	5880	4430	-1350	+1.9	-5.0
V–15% Cr	80	2410	+2300	5560	3430	-2100	+3.8	-4.7
	5520	5300	-200	140	450	+300	-0.5	+0.6
	5490	7100	+1600	5520	3930	-1600	+2.4	-4.2
V–20% Mo	120	1500	+1400	5900	4540	-400	+2.1	-2.0
	5420	5070	-350	80	540	+450	-0.6	+0.8
	5560	6500	+950	5560	4500	-1100	+2.0	-1.9
Vanadium + Oxygen	90	520	+450	6180	5490	-700	+0.7	-0.7

[a] Determined by fast neutron activation analysis.

We tested V–20% Ti at 1000°C as a function of O_2 pressure (from 8×10^{-6} to 8×10^{-4} torr), surface area, and surface preparation. Under all conditions tested, oxidation occurred in two stages: an initial stage in which the weight increased at a constant rate with time and a subsequent stage in which the rate decreased with time. The initial stage is symptomatic of a reaction rate determined by the rate of O adsorption on the specimen surface. During the second stage a surface scale forms, and the reaction is probably controlled by diffusion through the scale; however, there is also a continuing dissolution of O in the metal matrix so that this stage is not completely parabolic.

The primary objective of this work is not to study the oxidation of V, but rather to determine ways that the oxidation of V and V alloys in Na can be retarded. We have previously suggested several ways this may be accomplished.[4] One suggestion was that a thin layer of Mo be deposited on the V surface. Because of the reactivity of V with O, we have been unsuccessful in our attempts to deposit Mo on V by conventional chemical vapor deposition techniques. With the system presently used for chemical vapor deposition at ORNL, it is not possible to heat the V to the coating temperature (900°C) in a high vacuum, so that the V is oxidized during the coating process. We are presently looking into the possibility of applying a thin coating of Ni on the V surface, then depositing the Mo on the less-reactive Ni.

References

1. R. L. Klueh, Fuels and Materials Development Program Quart. Progr. Rept. September 30, 1970, ORNL-4630, pp. 150-154.

2. R. L. Klueh, Fuels and Materials Development Program Quart. Progr. Rept. March 31, 1970, ORNL-4560, pp. 129–132.

3. R. L. Klueh and J. H. DeVan, J. of the Less-Common Metals 22, 389–398 (1970).

4. R. L. Klueh, Fuels and Materials Development Program Quart. Progr. Rept. December 31, 1970, ORNL-TM-3300, pp. 176–180.

9. ✓SODIUM REMOVAL AND CAUSTIC EFFECTS

W. O. Harms   J. H. DeVan

The purpose of this program is to evaluate the corrosion of structural components caused by the products of Na oxidation or hydrolysis. The program deals with the effects of leakage or spillage of Na on metal surfaces that are in contact with mixtures of N_2 and air. It is also concerned with corrosion effects that result from the cleaning and storage of materials after exposure to Na. Both tasks are in direct support of the FFTF.

Examination of ALCO/BLH Steam Generator

J. H. DeVan   G. M. Slaughter   R. H. Jones[1]

Status of Disassembly

Posttest examination of the LMEC ALCO/BLH steam generator is well underway.[2,3] This steam generator was removed from the Sodium Components Test Installation (SCTI) at LMEC after a major crack system was found in the bottom tubesheet. Water was observed leaking through the crack, and, in addition, deposits of Na_2O were visible on the outer surface of the tubesheet. Our examination is thus aimed at exploring several areas of interest, including the reason for failure and explanations for the relatively poor performance characteristics of the generator.

Liquid penetrant inspection of all tube-to-tubesheet welds revealed no evidence of cracking, and flow tests on open tubes (those not previously welded shut with plugs) revealed them to be essentially unblocked. In addition to the leaks in the lower tubesheet, leaks were found in two tubes that had been in service at the time of test termination.

Following the dye penetrant and leak tests, four small ports were cut in the shell and liner to permit attachment of strain gages on to the external (Na) surface of the heat exchanger tubes. Two of these ports were near the bottom of the unit and two were near the top. The strain gages will be used to determine the amount of residual stresses in typical tubes to assist in the overall failure analysis. Figure 9.1 shows the extensive amount of reaction products which were observed on the tubes and thermocouples from one of the top ports.

A portable orbiting saw was used to sever the 1 1/2 in. thick shell to permit band sawing of the tubes near the lower tubesheet. The cutting of the shell is shown in Fig. 9.2, and the appearance of the Na (shell) side of the tubesheet after removal from the rest of the generator is shown in Fig. 9.3. There was no visual evidence of corrosion in this location.

Nondestructive inspection of this lower tubesheet is underway to further define the size and nature of the crack pattern. The remainder of the shell is also being cut to expose the tube bundle.

Inspection of Cover Gas Region Above the Sodium

As noted above, we encountered a heavy concentration of non-metallic deposits near the upper tubesheet on the shell side of the steam generator (Fig. 9.1). These deposits covered the underside of the tubesheet, tube interslices, thermocouples, and the ID of the shell.

The affected region was approximately 5 ft above the sodium level in the generator and had been blanketed by argon while the generator was under test. The deposits were multicolored (white, grey, brown and green) and were strongly attracted to a magnet. They were deliquescent in room temperature air and dissolved in water to yield a black or brown finely divided precipitate.

From their external appearance, it was not obvious to what extent the deposits were composed of $Na\text{-}H_2O$ reaction products and to what extent they contained products of corrosion of the underlying base metal. However, inspection of thermocouples near the upper tubesheet confirmed that metal underneath the deposits had been corroded. The thermocouples had been protected by a 10-mil thick 316 stainless steel sheath and in many areas both the sheath and thermocouple wires had completely disappeared. Figure 9.4 shows the appearance of the thermocouple cladding after removing the thick, crusty deposits apparent in Fig. 9.1. Metallographic examination of the thermocouple sheathing revealed that the original 10-mil thickness had been uniformly reduced to < 1 mil in several places, and in addition, all surfaces had been attacked intergranularly to a depth of 1–2 mils.

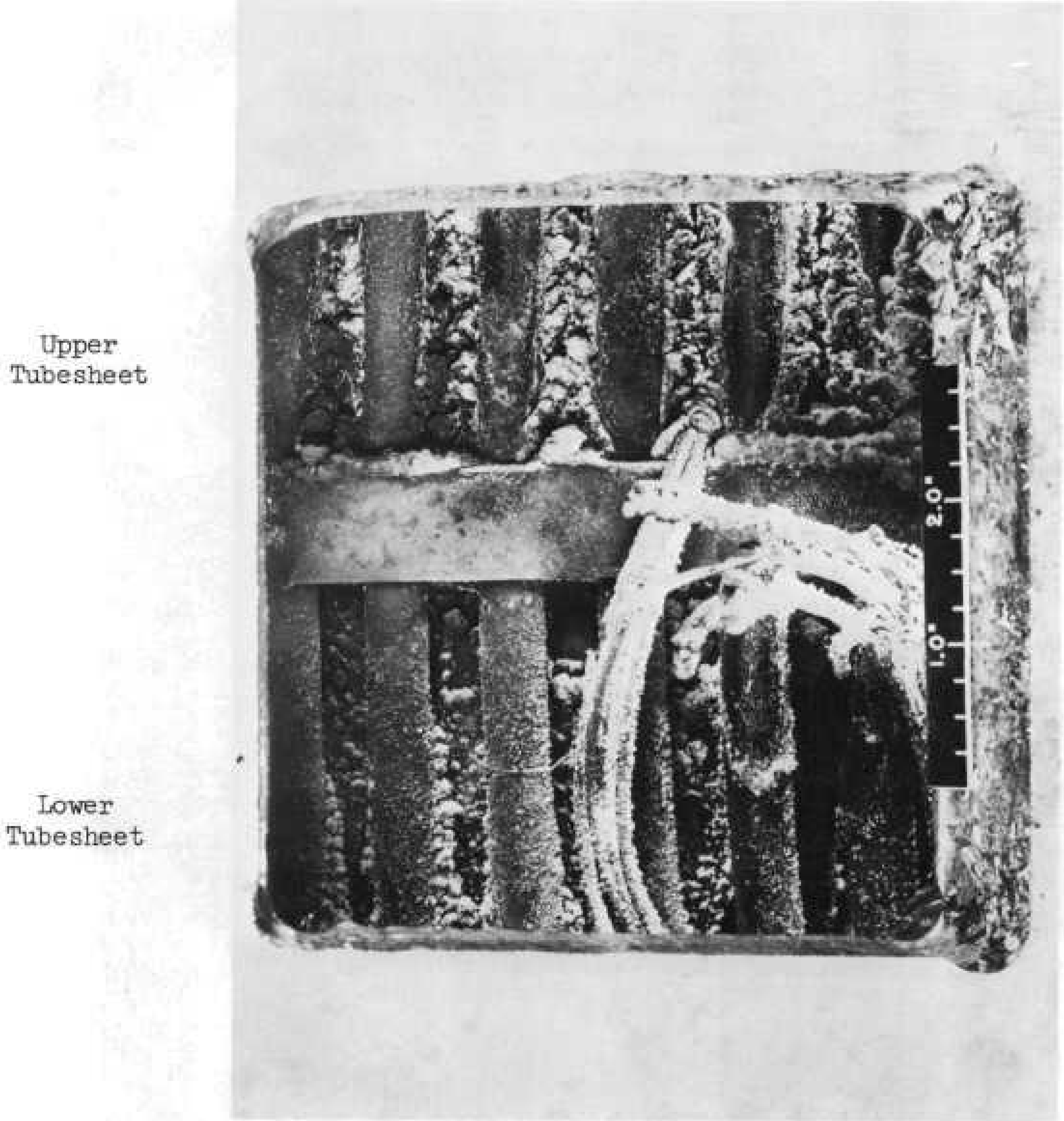

Fig. 9.1. Appearance of Heat Exchanger Tubes and Interslices as Viewed Through Cut-Out in Shell Near Upper Tube Sheet. Note damaged condition of thermocouples which originally connected to feedthrough in cut-out area.

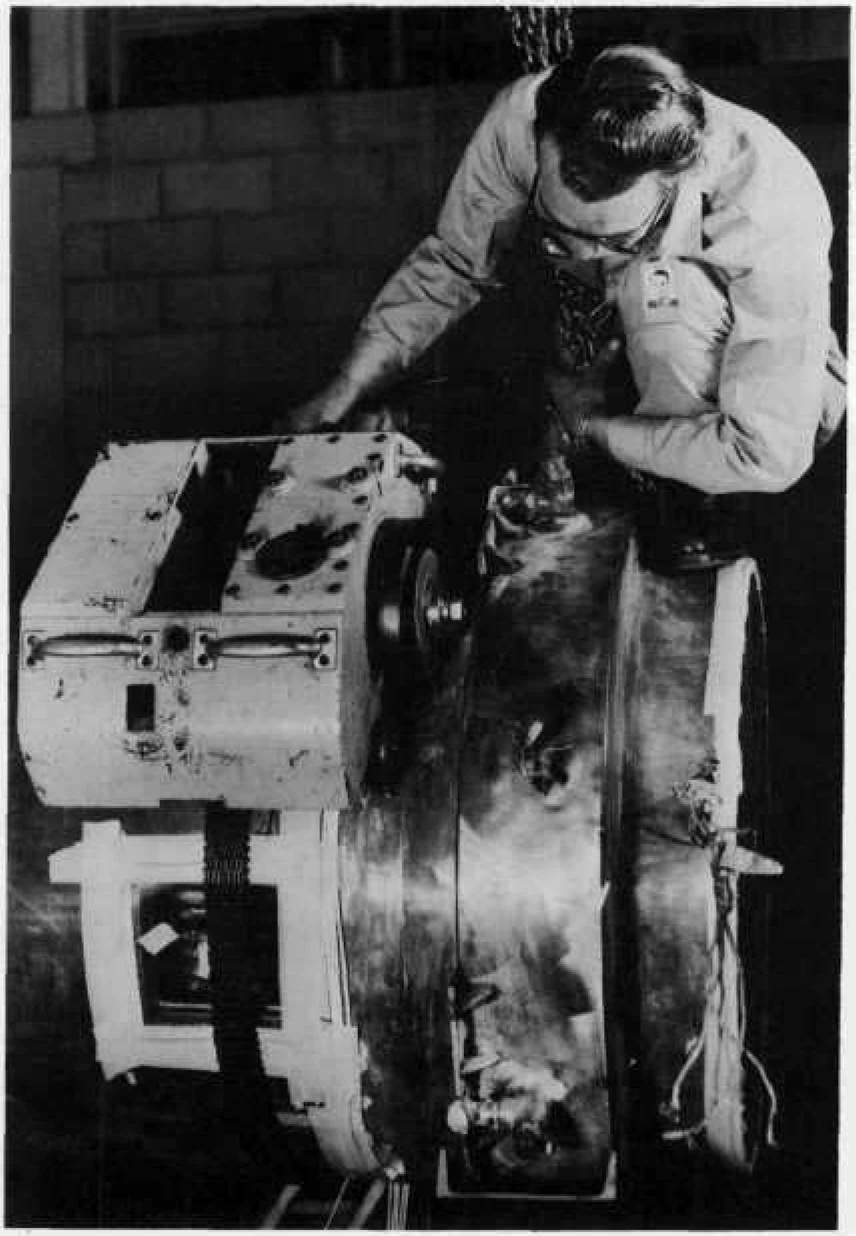

Fig. 9.2. Pneumatically-driven Orbital Saw Used for Cutting Through Steam Generator Shell. The cut is being made to remove the lower tubesheet.

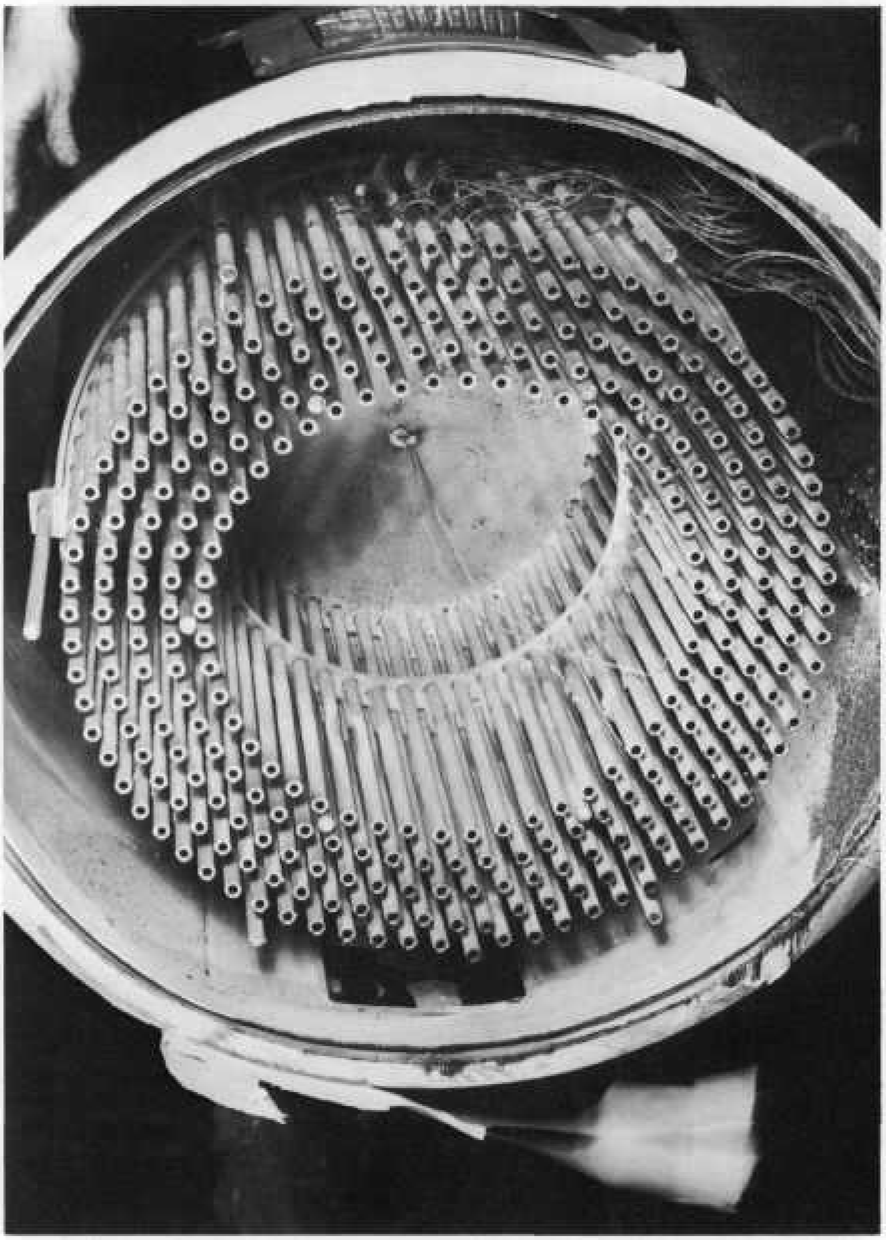

Fig. 9.3. Appearance of Lower Tubesheet as Viewed from Sodium Side. Surfaces were clean except for presence of metallic sodium.

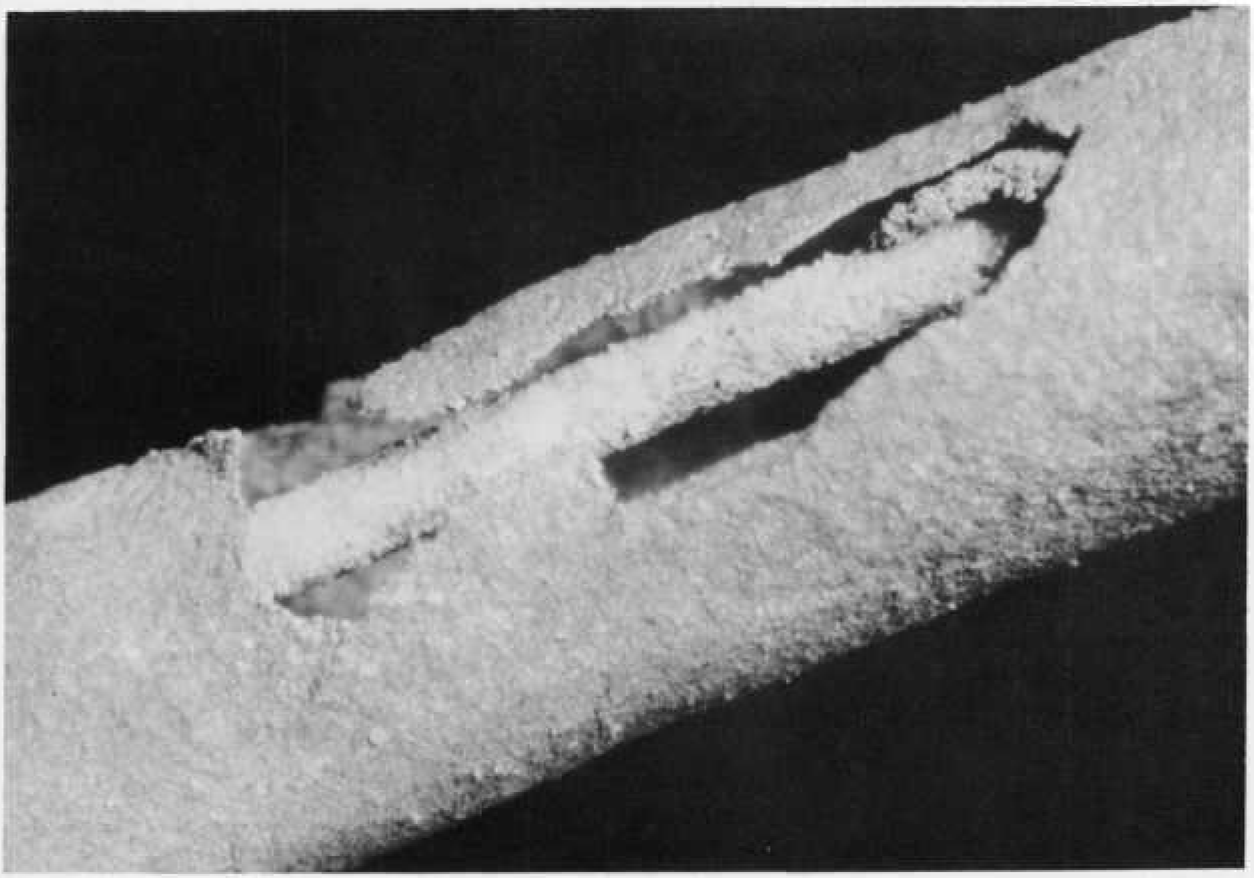

Fig. 9.4. Corroded Section of Type 316 Stainless Steel Thermocouple Sheath Located Near Upper Tubesheet. Sheath thickness = 0.010 in. Mag: ~ 45X.

Both the mode of corrosion and reaction products are symptomatic of attack by fused NaOH or anhydrous Na_2O. X-ray diffraction patterns which were obtained on crushed samples of the deposits gave evidence of three crystalline substances: Na_2CO_3, α-Fe, γ-Fe, $NaNiO_2$, Na_2CrO_3, and $NaFeO_2$. Metallographic examination of the inside surfaces of the 1 1/4 in. thick shell showed needles or wedges of a corrosion product penetrating into the base metal, in some cases as deep as 7 mils. The microstructures of these surfaces were strikingly similar to those of Inconel specimens exposed to fused sodium hydroxide in 600°C capsule tests conducted in 1956.[4] This similarity is illustrated in Fig. 9.5.

Corrosion Effects of Sodium Leaks or Spills in Gases Containing Oxygen

J. H. DeVan

Following the construction of the test apparatus described last quarter,[5] we began a series of tests to determine the effect of Na leaks on the oxidation behavior of stainless steel in nitrogen-oxygen mixtures. Four trial runs were conducted which established that our specimen design was suitable for evaluating Na leak rate in the range of 1–200 g/hr with specimen temperature controlled in the range 200 to 600°C. At this point the program was stopped; however, we will issue a design report covering the experimental apparatus.

Study of Methods for Cleaning Surfaces of Materials Exposed to Sodium

J. H. DeVan

Components removed from service in Na are conventionally cleaned by solvents such as water, steam, or alcohol, which oxidize and dissolve residual Na. Reactions of Na with these solvents give rise to alkaline reaction products and thus have the potential for inducing caustic attack and stress corrosion of structural materials. If not completely

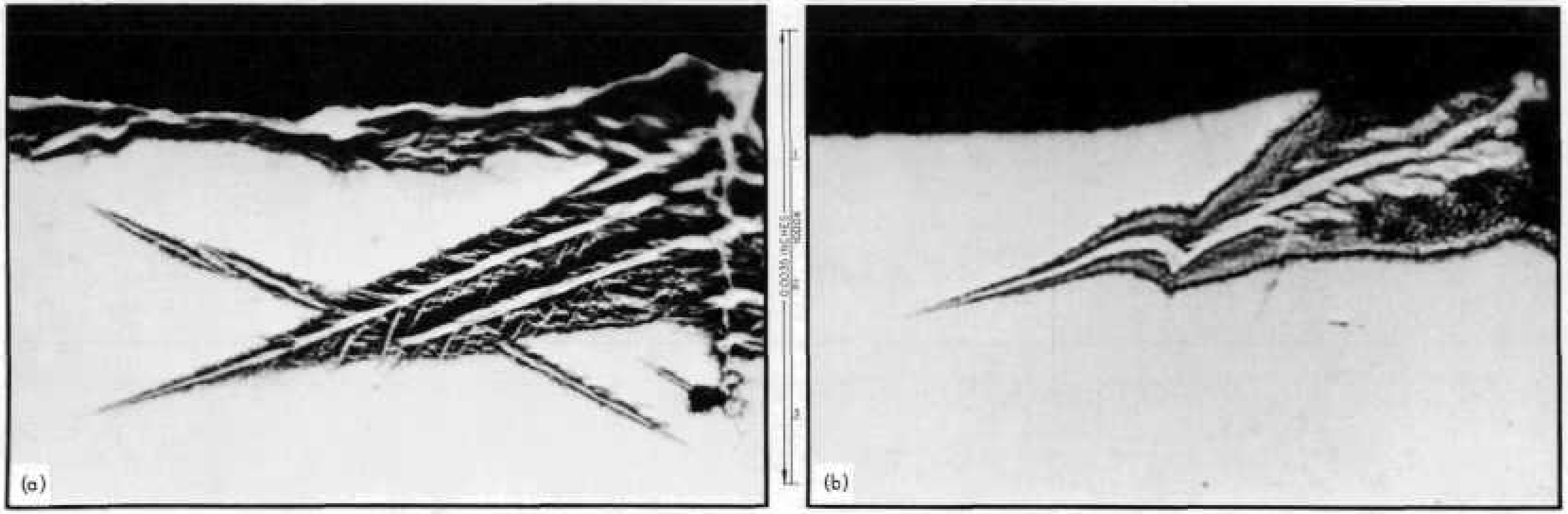

Fig. 9.5. Wedge-Shaped Structure of Corrosion Product Formed (a) on Inconel After 100-hr Exposure to NaOH at 600°C Under Helium and (b) on Shell of ALCO/BLH Steam Generator Near Upper Tubesheet.

removed, these reaction products, most of which contain O, can cause attack when the component is again used in Na. Accordingly, this program is concerned with corrosion effects resulting from the cleaning, storage, and re-use of materials after exposure to Na.

Crevice Effects (D. H. Jansen)

We have conducted a series of capsule tests to study the extent to which crevice attack may occur in LMFBR structural materials during Na stripping and during subsequent re-exposure to Na. As previously described,[6] we used two types of test specimens for these studies: overlapping sheet specimens and tube-in-socket joints. Alloys chosen for investigation were types 304-L and 321 stainless steel, 2 1/4 Cr—1 Mo steel, Incoloy 800, Inconel 625, and IN 102. Stripping techniques used to remove Na from the specimens included hydroxide-forming solvents (steam, water, and alcohol); anhydrous ammonia; and vacuum distillation. Also one set of specimens was simply drained and exposed to air with no attempt made to remove the residual Na prior to Na re-exposure.

Following cleaning, each specimen was weighed to determine the amount reaction product remaining on the specimen, and the specimens were then re-encapsulated for further exposure to Na. Specimens were grouped in capsules according to the cleaning method used, and each cleaning method was represented by four sets of specimens. Two sets were exposed to "pure" ($\leq$ 20 ppm O) Na and two sets to Na containing 100 ppm O. One set of every two was heated in Na for 100 hr at 370°C and then 900 hr at 590°C, and the other set was heated for 1000 hr at 1100°F.

Metallographic examinations of the specimens following these Na exposures showed significant corrosion in the case of all specimens except those cleaned by water or steam. Corrosion was the result of a residual coating of Na_2O which remained on the specimen surface following cleaning, and corrosion was no heavier in the built-in crevice than on other surfaces. There were no indications in these studies of caustic attack occurring during sodium removal, even in the crevices.

The stainless steels and nickel-base alloys exhibited equivalent attack, and the 2 1/4 Cr—1 Mo steel was attacked more than the other alloys. The extent of attack of type 321 stainless steel, from which Na was removed by vacuum distillation, is shown in Fig. 9.6.

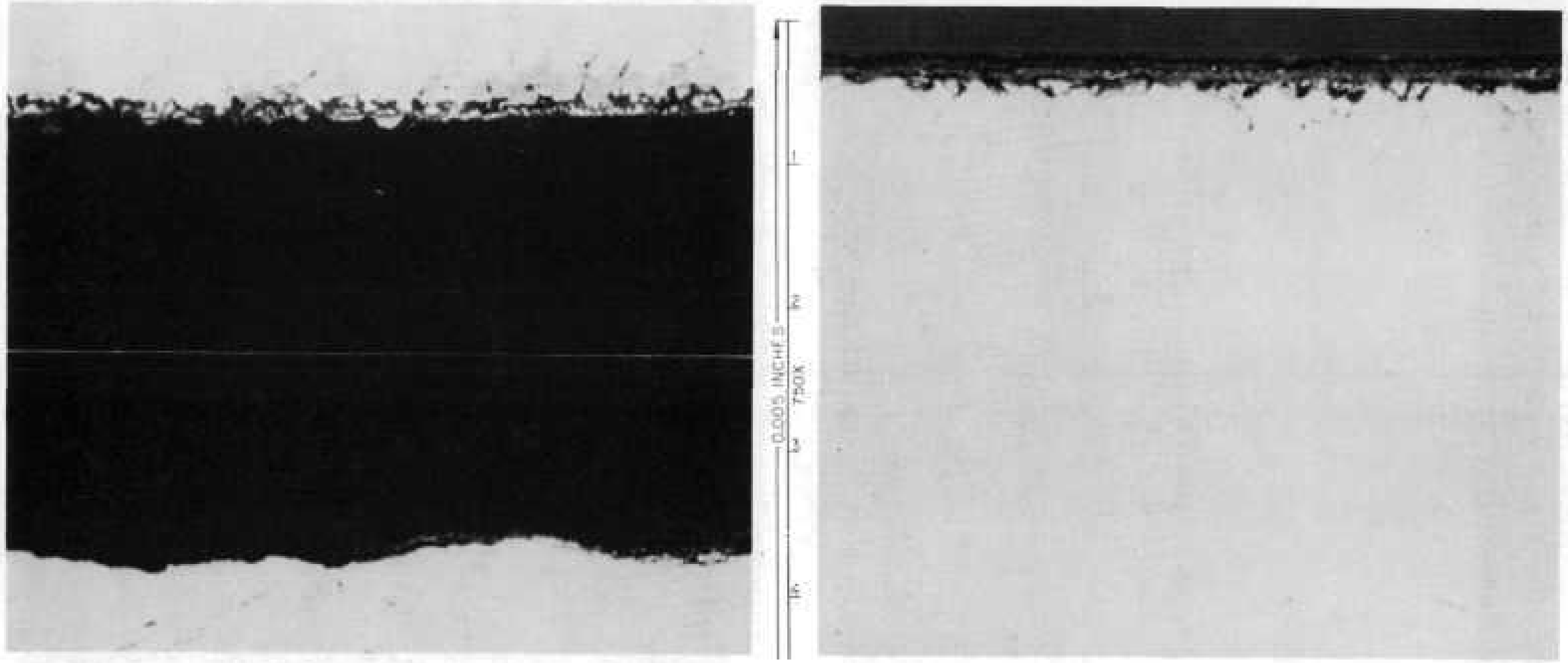

(a)

(b)

Fig. 9.6. Type 321 Stainless Steel Tube-to-Header Joint After Na Soak (700°C, 100 hr), Vacuum Distillation Cleaning Treatment, Na Test (1100°F, 1000 hr), and Final Distillation Na Removal. Field in (a) shows the crevice area (tube at top). In (b) on the edge of the tube outside of the crevice. Maximum attack is approximately 0.001 in. Specimen is in as-polished condition. (500X)

We saw no differences in attack as a function of the initial O concentration of the Na, which confirms that attack was due to the presence of a locally high concentration of caustic at the specimen surface. We also found the extent of attack to be the same at either of the two specimen heat-up rates which we evaluated.

In cases where components are to be re-used in Na, these tests show the necessity for careful mechanical cleaning or a water rinse of components to completely rid the surfaces of all traces of Na residues. This point is particularly important in the case of components cleaned by vacuum or inert gas distillation, since specimens cleaned by this technique showed the heaviest attack among all the cleaning techniques examined.

The above program has been terminated and a final report is being prepared. We feel the results of these tests warrant further study and strongly recommend that effects of cleaning residues be checked in flowing Na systems for comparison with these results in static Na.

References

1. Plant and Equipment Division.
2. J. H. DeVan and G. M. Slaughter, Fuels and Materials Development Program Quart. Progr. Rept. December 31, 1970, ORNL-TM-3300, pp. 182–184.
3. R. J. Gimera, "ALCO/BLH Steam Generator Operating Experience in the SCTI," paper IAEA-SM-130/65 of Proceedings of Sodium-Cooled Fast Reactor Engineering Conference, Monaco, March 23–27, 1970, pp. 595–627.
4. G. Pedro Smith, M. E. Steidlitz, and E. E. Hoffman, "Corrosion and Metal Transport in Fused Sodium Hydroxide," Corrosion **14**(1), 65–70 (Jan. 1958).
5. J. H. DeVan, Fuels and Materials Development Program Quart. Progr. Rept. December 31, 1970, ORNL-TM-3300, pp. 185–187.
6. D. H. Jansen, Fuels and Materials Development Program Quart. Progr. Rept. Sept. 30, 1970, ORNL-4630, pp. 159–160.

10. DEVELOPMENT OF FBR NEUTRON-ABSORBER MATERIALS

G. M. Adamson, Jr.   W. R. Martin

The prime candidate material for the safety and shim rods in the Fast-Flux Test Reactor (FTR) and liquid-metal-cooled fast breeder reactor (LMFBR) is boron carbide pellets in a stainless steel cladding. In spite of the widespread use of B_4C as a neutron absorber in thermal reactors, basic data have never been obtained. The material has never been fully characterized for structure, homogeneity range, effect of fabrication variables, and the effects of varying composition. The objective of our work is to characterize the material sufficiently to provide measurable control parameters to properly evaluate fabrication techniques and the effects of irradiation. The irradiation studies will emphasize basic effects of materials variables in both thermal- and fast-reactor environments. A secondary effort of this program will be the preliminary characterization of alternate materials that possess possible advantages over B_4C for use in fast reactors.

Boron Carbide

X-Ray Scattering from Neutron-Irradiated Boron Carbide Crystals (H. L. Yakel)

Two batches of selected crystals from a sample designated Norbide M-103 (B/C = 4.7) were included in a recently completed ORR irradiation experiment. The crystals represented a boron-rich boron carbide and were characterized by x-ray diffraction prior to irradiation. Integrated fluxes of 1.8×10^{20} neutrons/cm^2 (thermal) were estimated at irradiation temperatures of 350°C (capsule No. O-18) and 550°C (capsule No. O-19).

Crystals from both capsules were recovered and are being examined by x-ray diffraction methods. Data are more complete for O-19 material; rotation and Weissenberg photographs for O-18 crystals are just now being recorded.

Results to date show a significant variation from those reported in 1955 by Tucker and Senio[1] for boron carbide crystals irradiated to 3×10^{20} neutrons/cm^2 at an unspecified temperature. Like the earlier data, our patterns are a composite of sharp Bragg maxima (unbroadened relative to the unirradiated crystal reflections) and diffuse reflections located at or near these sharp maxima. Again like the earlier data, a highly anisotropic Debye-Waller factor diminishes the intensities of reflections with $\underline{l}$ large compared to $\underline{h}$ and $\underline{k}$ (hexagonal indices). But whereas Tucker and Senio reported an anisotropic lattice expansion ($\underline{a}$ increases, $\underline{c}$ decreases on irradiation), we have noted that, for 0-19 crystals, both $\underline{a}$ and $\underline{c}$ increase over their unirradiated values if the sharp maxima alone are considered. The lattice parameters estimated from the positions of the diffuse reflections correspond to an increase in $\underline{a}$ and a decrease in $\underline{c}$.

We suggest a tentative model of a damaged structure that might produce these observed x-ray diffraction effects. It imagines the crystal to be a composite of regions in which individual defects (displaced atoms, vacant icosohedral or chain sites) are located, and regions containing extended planar collections of defects. The former give rise to the sharp Bragg maxima; the latter produce the diffuse peaks.

Further refinements of this crude model must be made to interpret the anisotropic Debye-Waller factor and the variations in apparent lattice parameter. The model also obviously suffers from a lack of specification with respect to the detailed crystal structure of boron carbide. Variations of the observed x-ray diffraction effects with neutron dose and irradiation temperature must also be explored. To the latter end, 300 crystals (Norbide M-103) have been loaded into platinum tubes preparatory to a second ORR irradiation experiment.

Irradiation of Boron Carbide Powders in a Thermal Reactor (G. L. Copeland)

Further chemical analyses have been performed on the boron carbide powders used in capsules 0-7 through 0-12. The evaluation of these capsules was reported in the previous quarterly report.[2] Qualitative x-ray evidence indicated that the powders with higher gas release contained free boron. The boron and carbon contents and the "soluble boron" contents along with the gas release results are presented in

Table 10.1. The "soluble boron" refers to all boron in a crushed powder sample which dissolves in 1.6 M nitric acid at room temperature in two hours. This soluble boron includes both elemental boron and boron as B_2O_3. The soluble boron content appears to be the predominant factor in gas release from these powders. Powders with no soluble boron (Capsules O-1 through O-6) released from 2.5 to 5.8% of the gas generated independently of irradiation temperatures of 340°C to 625°C. As shown in Table 1, the gas release from Capsules O-7 through O-12 correlates well with the soluble boron content independently of temperature from 200°C to 575°C. This effect of the soluble boron may be accentuated in this test since the free boron or B_2O_3 would be predominantly on the surface of the powders where the burnup would be highest in the thermal flux.

The powders from two capsules from this series were analyzed for $^{10}B/^{11}B$ for comparison to the burnup as determined by lithium analysis. Two samples of powders from Capsule O-5 analyzed 16.49 and 14.59% burnup as compared to 5.1% as determined by lithium content. Two samples from Capsule O-12 analyzed 18.34 and 17.96% burnup as compared to 5.9% as determined by lithium content. If these samples are representative, this indicates that the burnups as indicated by lithium analyses are low and thus the reported gas releases based on lithium analysis are higher than the actual gas release. The $^{10}B/^{11}B$ ratio analysis is presently based on a very small sample (about two particles) and may not be representative of the average burnup.

The results of the gas release and burnup measurements of Capsules O-13 through O-16 are presented in Table 10.2. These capsules were irradiated three weeks in the isotope stringer of the ORR. The capsules were of essentially the same design as the previous ORR capsules; however, the powders were loaded so that they could be unloaded without copper contamination from the capsule. The powders were prepared by crushing with a hardened steel mortar and pestle from the -20 + 50 mesh fraction of a lot of Norbide 4F boron carbide. The chemical analysis before crushing indicated 19.1% carbon and 79.5% boron for a B/C ratio of 4.62. After crushing to -80 + 325 mesh (38 µm. Fisher average particle diameter) and -325 mesh(6.8 µm Fisher average particle diameter)

Table 10.1. Effect of Soluble Boron on Gas Release From Irradiated Boron Carbide Powders

Unirradiated Sample[a]	0-7-a	0-8-a	0-9-a
Annealing temperature, °C	1000	1500	2000
Chemical Analysis, wt %			
Carbon	18.94	19.63	20.00
Boron	79.40	78.15	79.10
Soluble boron[b]	11.6	2.2	0.60
B/C, atomic ratio			
Based on total carbon and total boron	4.65	4.42	4.39
Based on total carbon and combined boron	3.97	4.26	4.26
Irradiated Capsules	**0-7**	**0-8**	**0-9**
Temperature[c], °C	425	200	350
Burnup[d], % of ^{10}B	7.5	6.1	3.6
Burnup[d], 10^{20} $\frac{n,\alpha}{cm^3}$	16.4	13.4	7.85
Gas release, %	29.9	11.6	7.6
Irradiated Capsules	**0-10**	**0-11**	**0-12**
Temperature[c], °C	510	540	575
Burnup[d], % of ^{10}B	8.1	7.1	5.9
Burnup[d], 10^{20} $\frac{n,\alpha}{cm^3}$	17.7	15.5	13.0
Gas release, %	e	12.6	e

---

[a] Samples were prepared by blending boron powder with Norbide 325 F and annealing 1 hr at the indicated temperature.

[b] Boron soluble in 1.6 M nitric acid at room temperature for 2 hr.

[c] Determined by annealing irradiated SiC temperature monitors.

[d] Determined by analysis for lithium content.

[e] Not determined due to capsule leakage.

Table 10.2. Boron Carbide Powder Irradiations in the ORR

Capsule Number	0-13	0-14	0-15	0-16
Material	Norbide 4F[a]	Norbide 4F[a]	Norbide 4F[a]	Norbide 4F[a]
Particle size, U.S. mesh size	−80 + 325	−80 + 325	−325	−325
Fisher average particle diameter, μm	38	38	6.8	6.8
B/C atomic ratio (starting material)	4.62	4.62	4.62	4.62
Irradiation Temperature, °C				
Design	350	500	350	500
Actual[b]	400	450	~300	~600
Burnup[c]				
Depletion/cm^3 × 10^{-20}	4.25	3.67	2.41	8.03
% of B^{10}	1.87	1.62	1.06	3.53
Gas Release				
cm^3	d	0.1275±.01	0.1202±.01	0.1495±.01
% of He generated		14.0±4	23.4±1	8.56±24

[a] −20 + 50 mesh fraction crushed to the sizes indicated.

[b] Determined by SiC temperature monitors.

[c] Determined by $^{10}B/^{11}B$ isotopic analysis. Average of two runs of two particles each.

[d] Not determined due to capsule leakage.

the iron was removed by leaching in nitric acid. A chemical analysis at this stage indicated: 20.7% C and 76.5% B for a B/C of 4.10 for the −80 + 325 material, and 20.7% C and 75.7% B for a B/C of 4.06 for the −325 mesh material. This may represent variation in chemical analysis or loss of "soluble boron" in the nitric acid leach. We then rechecked the chemical analysis of the −20 + 50 mesh starting material. This analysis yielded 76.0% B and 23% C for a B/C of 3.67. The sample also analyzed 0.39% soluble boron and 1.7% free carbon. Thus, the −20 + 50 mesh starting material may be inhomogeneous leading to variations in the chemical analyses.

The purpose of Capsules 0-13 through 0-16 was to compare different particle size and determine gas release from a higher as-cast B/C ratio material. However, the results seem to be inconclusive due to the wide range and low values of analyzed burnups. Again, the $^{10}B/^{11}B$ ratio was determined by analyzing a very small sample of two particles. If we examine the absolute volume of gas released, the results indicate that smaller particle size and higher temperature increases gas release. However, when the burnups are considered and gas release as a percentage is considered, the results are just the opposite. We are now trying to obtain a more representative sample for burnup analysis.

Irradiation of Boron Carbide Pellets in the EBR-II (G. L. Copeland, R. G. Donnelly, and G. W. Keilholtz[3])

The experiment X099 is being irradiated in the 7F5 position of the EBR-II. We now plan to remove the experiment in October when the average burnup will be about 4.5% of ^{10}B. This will allow the evaluation to provide more timely data for the first core loading of the FTR. We have requested approval-in-principle for a second test to be inserted in the EBR-II when X099 is removed.

References

1. C. W. Tucker, Jr. and P. Senio, Acta Cryst. 8, 371 (1955).
2. G. L. Copeland, Fuels and Materials Development Program Quart. Progr. Rept. December 31, 1970, ORNL-TM-3300.
3. Reactor Chemistry Division.

PART II

SPACE POWER TECHNOLOGY

FUELS

11. DEVELOPMENT OF URANIUM MONONITRIDE FUELS

P. Patriarca J. L. Scott

Uranium mononitride (UN) is potentially attractive as fuel for space nuclear reactors because of its excellent stability at high temperatures, high thermal conductivity, and good irradiation stability up to 1000°C. The purpose of this program is to determine the basic mechanisms of fuel swelling and gas release at temperatures above 1000°C. Results will be used to develop a model for predicting the performance of UN as a function of temperature, burnup, and cladding restraint.

Irradiation Testing

T. N. Washburn

The basic objective of the ORNL program[1] for irradiation testing of UN is to investigate the performance capability of this fuel material at high temperatures and low heat ratings. Fuel temperatures of interest are 1000 to 1500°C, with temperatures of 900 to 1400°C at the outside surface of the cladding and linear heat ratings from 5 to 10 kW/ft. Fuel properties of most interest are swelling rate, release of fission gas, and compatibility with the cladding materials. The irradiation tests are conducted in the poolside facilities of the Oak Ridge Research Reactor (ORR). These facilities allow adjustment of the position of the test capsule relative to the reactor face and thereby make it possible to maintain a constant temperature at a selected reference point on the test specimen as the reactor flux profile changes or as the fissile content of the test fuel is diminished.

Fabrication (E. J. Manthos)

UN-4 and UN-5. — Fabrication of capsules UN-4 and UN-5 was completed and they were installed in the ORR. The Nb—1 Zr NaK containment vessel was successfully welded to the thermocouple bulkhead of capsule UN-4 without incident and returned to Y-12 where fabrication of the capsule was completed. The identical weld on capsule UN-5 was unsatisfactory because of contamination of the weld by braze metal. The weld and part of the Nb—1 Zr vessel wall were machined away and we fitted and unsuccessfully attempted to weld a Nb—1 Zr patch over the machined section. The assembly was returned to Y-12 and the patch was machined away and we fitted and brazed a Nb—1 Zr patch to the vessel. The patched region was vacuum He leak tested and x-ray radiographed and judged to be acceptable. Fabrication of the capsule was completed at Y-12.

UN-6. — The center fuel pin for capsule UN-6 and an identical thermal simulation fuel pin were assembled from T-111 and W components remaining from the fabrication of fuel pins for capsules UN-4 and UN-5. The two T-111 fuel pins were loaded with W liners and UO_2 pellets and were welded. Both pins were He leak tested, fluid penetrant inspected, and x-ray radiographed and judged to be acceptable.

Nb—1 Zr fuel pin tubing was fabricated from P and W-CANEL bar stock. Subsequent inspection of the tubing revealed surface flaws on the tubing OD. Metallographic examination of a typical defect showed that it was an 0.008-in.-deep crack. Because of the defects, the tubing was judged unacceptable and rejected.

Nb—1 Zr tubing, 3/8-in. OD × 0.065-in. wall and 42 in. long was procured from GE NSP. In addition, 34 in. of 3/8-in. OD × 0.050-in. wall tubing was obtained from NASA-Lewis. Both batches of tubing are being machined into 5- to 6-in. lengths and to 0.376 to 0.374-in. OD × 0.3180 to 0.3175-in. ID. After machining, both batches of tubing will be nondestructively tested and the better of the two batches will be used in the fabrication of the remaining two UN-6 and two thermal simulation fuel pins.

Components for the UN-6 Nb—1 Zr NaK vessel were fabricated, inspected, and accepted. The cap was welded to the bottom of the NaK vessel, inspected, and accepted. The six fuel pin thermocouples and He gas lines were successfully brazed to the Nb—1 Zr NaK vessel bulkhead and then the stainless steel primary containment vessel bulkhead.

Operation (B. Fleischer and K. R. Thoms)

UN-4. — The experimental assembly was installed in the ORR on February 4, 1971 and operation commenced on February 10. As of March 15, a total of 640 hr has been accumulated at operating temperatures above 800°C.

The approximate temperature-time history of operation since startup is portrayed in Fig. 11.1. Operation has been very stable except for short-lived perturbations that occurred during startup and early loss of one of the thermocouples on the lower pin cladding. Analysis of the perturbations indicates instantaneous shifts in the physical position of the NaK container. The sloping temperature profiles in Fig. 11.1 results from the continuous movement of reactor control rods. For control purposes we are attempting to hold the average temperature of the middle fuel pin cladding at 1000°C by periodic movement of the capsule location with respect to the reactor face. The middle fuel pin is currently being maintained at temperature by operating at about 10 kW/ft as compared to the intended design level of 8.6 kW/ft.

A preliminary analysis of the correlation between calculated cladding temperatures based on calorimeter thermocouples and measured cladding temperatures has been made as a function of heat rating. The location of the thermocouples involved in this correlation are shown in Fig. 11.2. The difference between the calculated and measured temperature for the middle pin is about 70°C at 10 kW/ft. The upper and lower pins show differences of about 100 and 130°C, respectively. In all cases the calculated values are higher than the values measured by the fuel pin thermocouples and deviate more as the heat rating increases. A portion of this discrepancy is attributable to off-center position of the NaK capsule with respect to the inner He containment vessel. This is based on correlations of specific calorimeter thermocouple pairs with specific cladding thermocouples and the nonuniform profile of heat flow around the calorimeter as indicated by these pairs.

UN-5. — This experimental assembly was inserted in the ORR during the week of March 1 and operation commenced on March 9. As of March 15, the capsule has accumulated 160 hr at operating temperatures above 800°C.

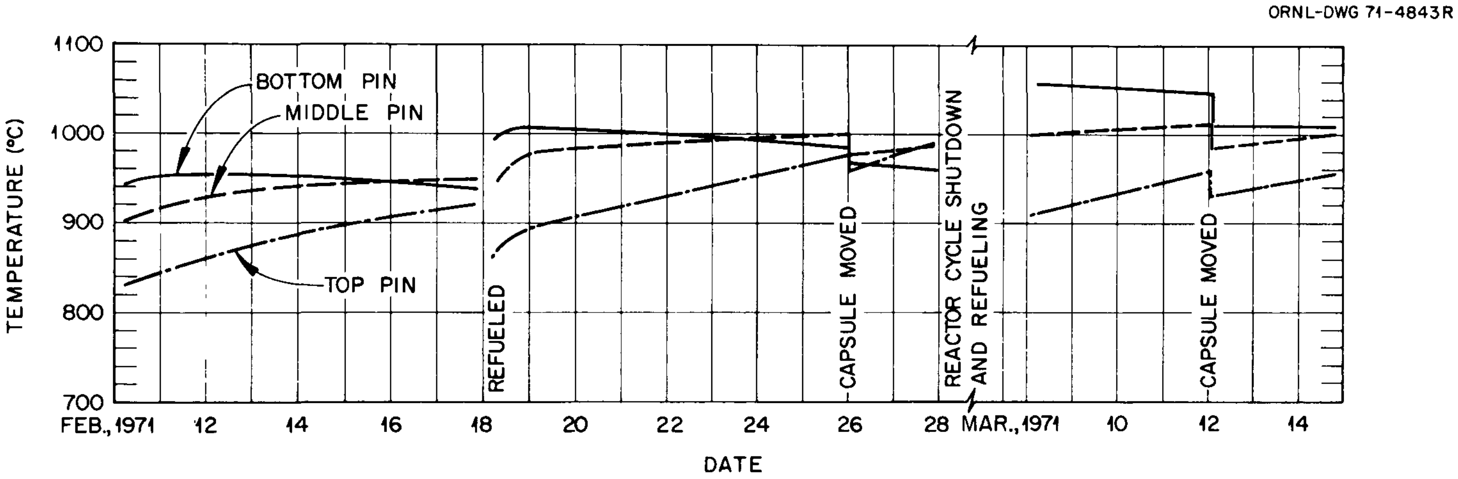

Fig. 11.1. History of the Average Cladding Temperature for the Top, Middle, and Bottom Elements of Capsule UN-4.

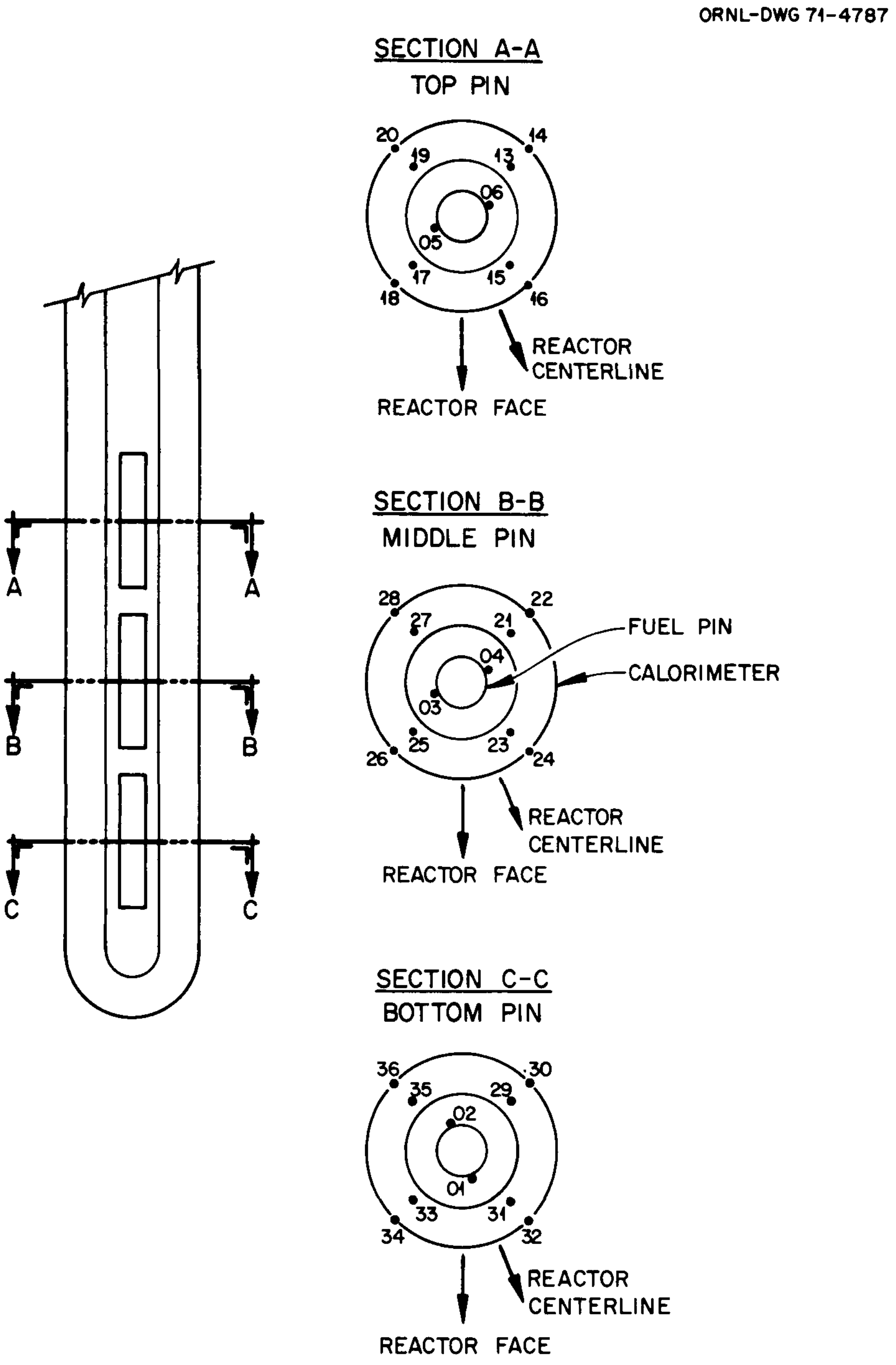

Fig. 11.2. Thermocouple Arrangement of ORR-UN Capsules 4, 5, and 6.

The approximate temperature-time history of operation is shown in Fig. 11.3. Startup operation showed the same type perturbations discussed earlier for UN-4. This capsule also lost one of the thermocouples on the lower pin cladding early in the operation. Except for these occurrences, operation has been stable.

As in UN-4, operation control is keyed to maintenance of 1000°C on the middle pin. However, the temperature spread between the middle and bottom pin may require somewhat lower operating temperature to remain below the maximum operating temperature limit of 1100°C for any one pin. The capsule is currently being maintained at temperature by operating the middle pin at about 10.4 kW/ft compared to the intended design level of 8.6 kW/ft. Part of disparity between the test conditions and designed conditions is believed to be the result of the inner He gap being slightly smaller than the design value.

Data Analysis (B. Fleischer and K. R. Thoms)

A study of the data collection and reduction techniques has been undertaken to determine how we can optimize usage of existing automatic data loggers and computer services for detailed description of system behavior. By proper management of these services we should be able to facilitate data analysis for both operational and reporting aids. As a result of these studies we plan to perform analysis of means and variances of each thermocouple and employ control limits derived from these analyses. Appropriate graphs reflecting the time behavior of these variables will be systematically obtained for observing and reporting general behavior patterns.

Proposed Irradiation Tests of UN/Refractory Metal Fuel Pins in EBR-II

B. Fleischer, T. N. Washburn, and M. K. Preston

The primary objective of the program is to determine the performance characteristics of UN-fueled refractory-metal-clad fuel pins in a fast flux test environment. The data is considered essential for future engineering development of fuel elements for space nuclear systems. The

ORNL-DWG 71-4844

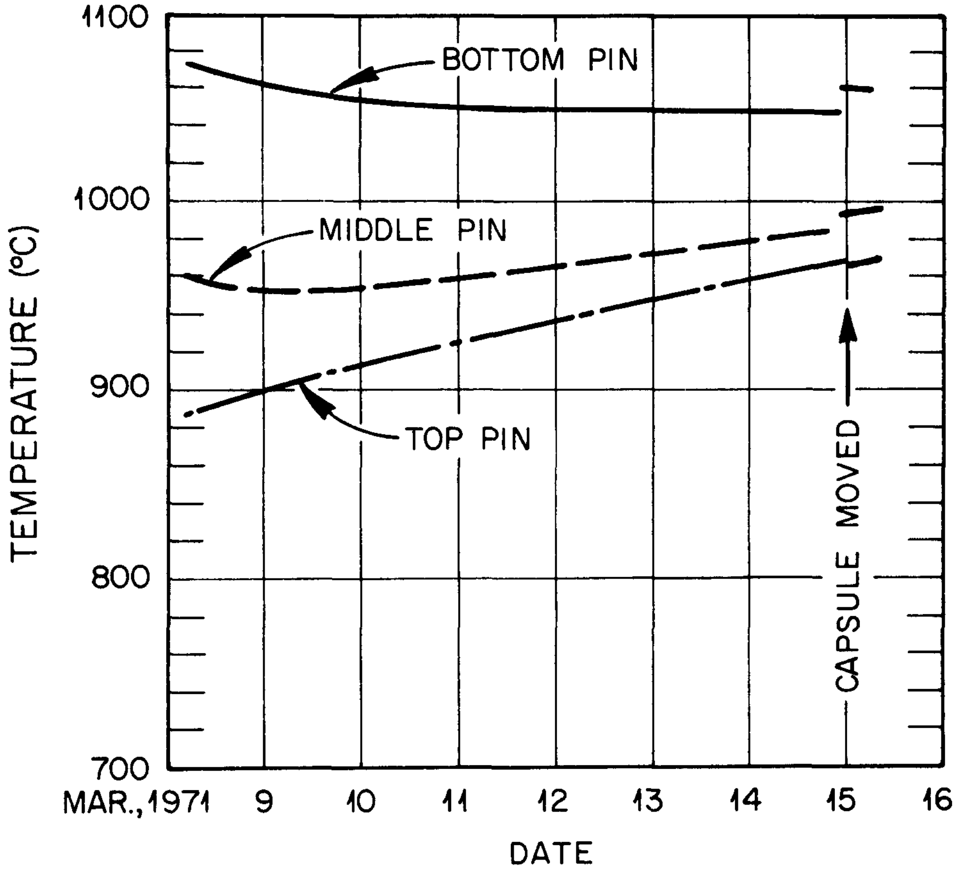

Fig. 11.3. History of the Average Cladding Temperature for the Top, Middle, and Bottom Elements of Capsule UN-5.

plans previously discussed[1] were further developed, culminating in the issuance of an informal 189a proposal.

In this test we would evaluate dimensional stability of the fuel and pin, compatibility of the fuel and cladding, ductility of irradiated cladding and capsule, and fission gas release of the fuel. These response variables would be studied as a function of linear heat rates from 4 to 11.5 kW/ft and burnup from 3/4 to 5 1/2% FIMA using 93% theoretically dense annular fuel pellets and a cladding temperature of 1000°C.

Two test plans reflecting different levels of emphasis of these candidate cladding materials, Nb-Zr, T-111, and W–25 Re, were proposed as presented in Figs. 11.4 (ORNL-Dwg 71-1226R) and 11.5 (ORNL-Dwg 71-1227R). Both plans entail testing 33 pins over a three-year irradiation period.

References

1. B. Fleischer, T. N. Washburn, and M. K. Preston, Fuels and Materials Development Program Quart. Progr. Rept. December 31, 1970, ORNL-TM-3300, pp. 220–222.

ORNL-DWG 71-1226R

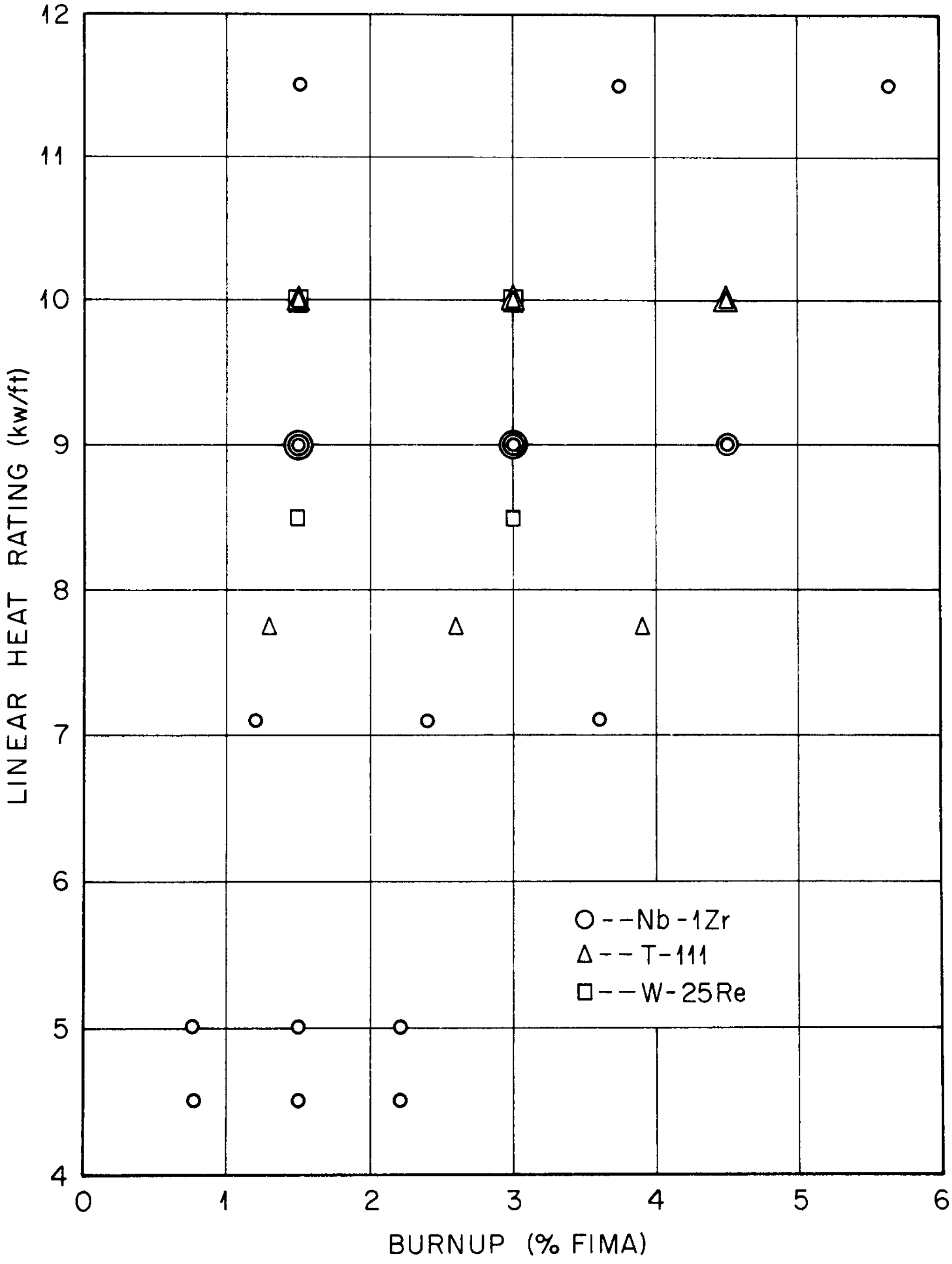

Fig. 11.4. Proposed Test Plan "A".

ORNL-DWG 71-1227R

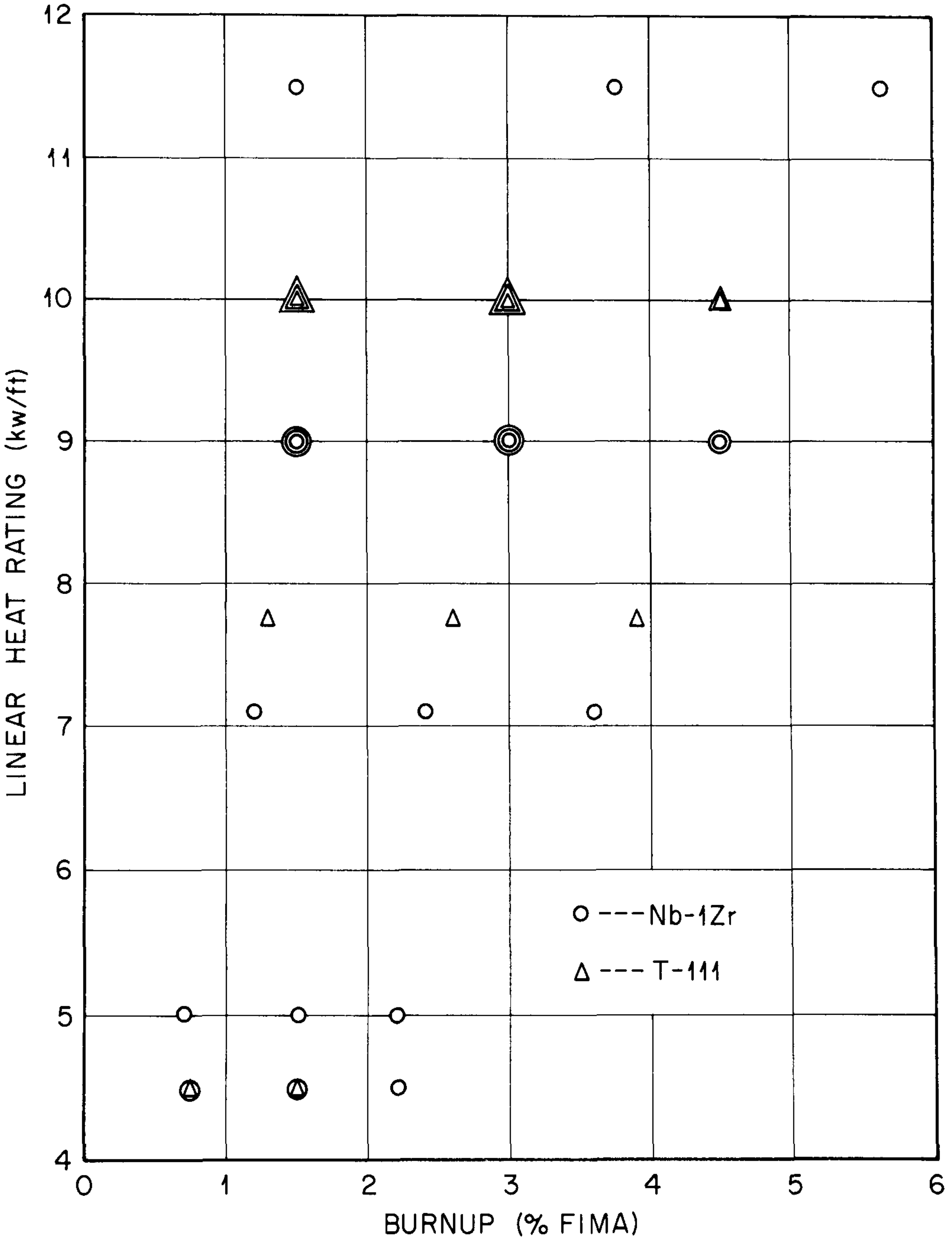

Fig. 11.5. Proposed Test Plan "B".

CLADDING AND OTHER STRUCTURAL MATERIALS

12. ✓CLADDING MATERIALS FOR SPACE ISOTOPIC HEAT SOURCES

R. G. Donnelly H. Inouye

Development of Improved Alloys

C. T. Liu

We are continuing to qualify the Pt-Rh-W alloys which have great potential to be used as cladding materials for space applications of isotopic power heat sources.

Fabrication

Sheet material of Pt-Rh-W alloys can be best fabricated by hot forging the as-cast button 30%, followed by hot rolling at about 1050°C. After a total of 60% reduction, the as-cast structure is broken and the alloy can be cold rolled satisfactorily. A 300 g button of the Pt–26% Rh–8% W alloy has been cold rolled to 0.020-in. sheet with several intermediate anneals at 1050°C. Also, bar stock has been prepared by electron beam drop casting followed by hot swaging at 1200°C.

Recrystallization and Grain Growth Behavior

To determine the recrystallization temperature, softening behavior, and bend ductility, the Pt–26% Rh–8% W alloy was cold rolled 35% and then aged one hour in the temperature range from 400 to 1600°C in vacuum. Table 12.1 summarizes the results. The hardness data in Fig. 12.1 shows that at temperatures above 400°C, the hardness decreases steadily with increasing temperature. A sharp drop in hardness is observed at temperatures above 1000°C. Fig. 12.2 shows the microstructures at various annealing temperatures. Recrystallization does not occur at 1000°C, but is complete at 1100°C. The recrystallized grains grow slowly with temperature until temperature reaches 1400°C.

Table 12.1. Effect of 1-hr Annealing Treatment on Hardness, Recrystallization, and Bend Ductility of Pt–26% Rh–8% W Alloy

Annealing Temperature (°C)	Microhardness (DPH)	Recrystallization Condition (%)	90° Bend Test
As-rolled	422	0	No crack
400	467	0	Cracked
600	439	0	Cracked
800	410	0	No crack
900	392	0	No crack
1000	366	0	No crack
1100	240	100	No crack
1200	234	100	No crack
1300	236	100	No crack
1400	207	100	No crack
1500	209	100	No crack
1600	196	100	No crack

The effect of annealing treatment on ductility has been determined by bending alloy strip to about 90°, followed by examining metallographically. All the annealed specimens were ductile with the exception that cracks were observed in two specimens annealed at 400 and 600°C (Table 12.1). As shown in Fig. 12.1, these cracked specimens have a hardness higher than the as-rolled one. The reason for this increase in hardness is not well understood, but may be related to the presence of impurities in the alloy.[1] An increase in hardness is also observed in many cold worked platinum-base alloys aged at low temperatures.[1,2]

Mechanical Properties

In order to determine the strength of Pt–26% Rh–8% W alloy in different structural states, two sets of tensile specimens were prepared; one set was stress-relieved at 1000°C, the other was recrystallized at

ORNL-DWG 71-4236

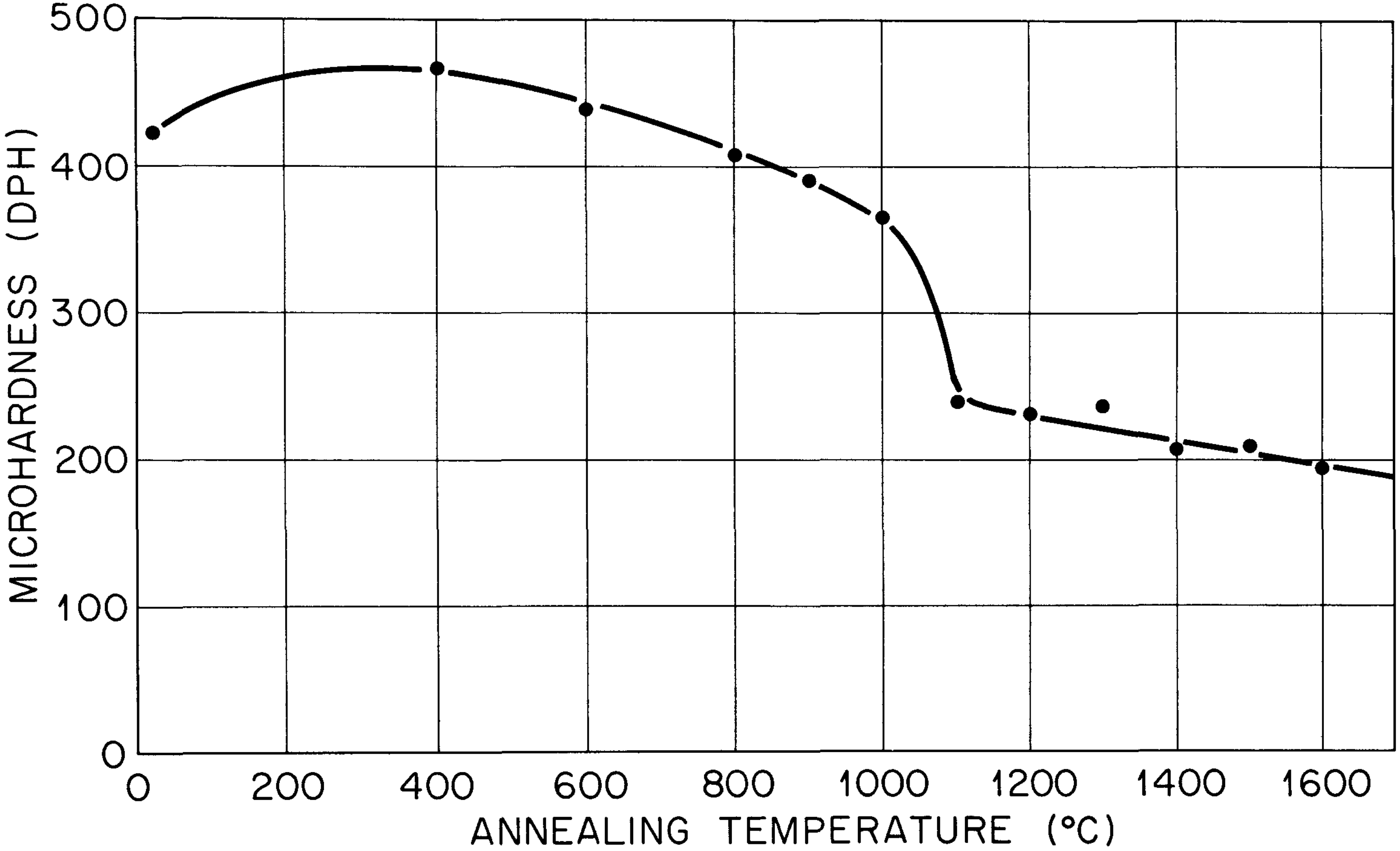

Fig. 12.1. Effect of Annealing Temperature on Hardness of Pt–26% Rh–8% W Alloy Cold-Rolled 35%.

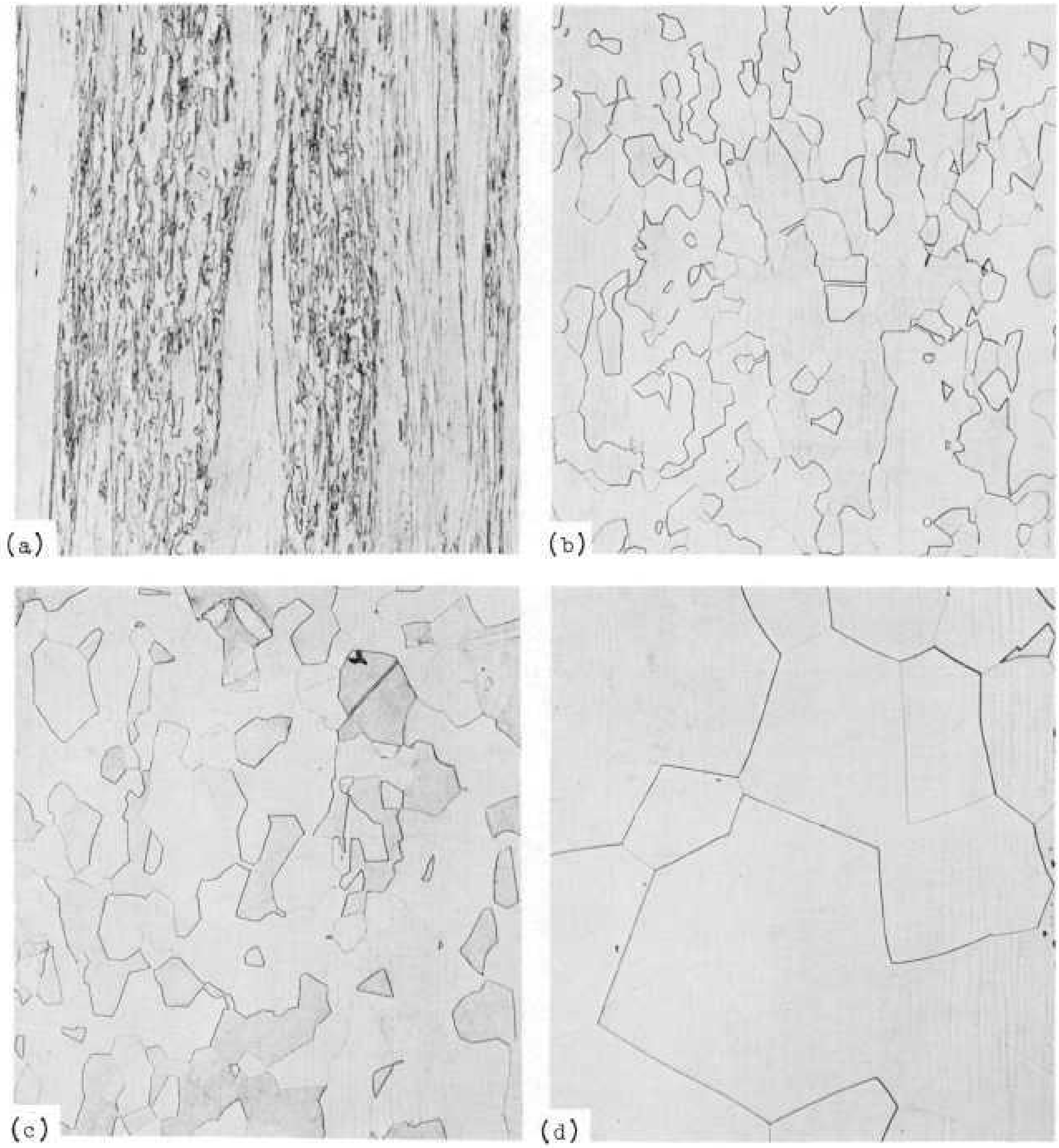

Fig. 12.2. Microstructures of Pt–26% Rh–8% W Alloy Cold Worked 35%, Followed by 1-hr Annealing at Different Temperatures. (a) 1000°C, (b) 1100°C, (c) 1300°C, and (d) 1400°C. 250X.

1200°C. Elevated-temperature tensile tests were done on an Instron testing machine in vacuum at temperatures up to 1316°C. The results for both Pt—26% Rh—8% W and Pt—30% Rh alloys are presented in Table 12.2. For comparison, data for TZM and T-111 are also included. The tensile strength of the Pt-Rh-W alloy is lower in the recrystallized state than in the stress-relieved state at temperatures up to 1093°C, but equal at 1316°C. This ternary alloy is much stronger than the Pt—30% Rh alloy at all temperatures. In fact, the ternary alloy is more than double the strength of the binary alloy at 1316°C. The Pt-Rh-W alloy is also stronger than TZM to 1093°C, and is comparable to TZM but weaker than T-111 at 1316°C.

The Pt-Rh-W alloy shows a minimum in the ductility at 760°C in the stress-relieved condition, but not in the recrystallized condition. However, the recrystallized heat treatment does not cause any increase in ductility at 1093°C. This alloy has excellent ductility at impact temperature (1316°C), that is, 44% elongation and 65% reduction of area, which is better than all the rest of the alloys shown in Table 12.2. Some earlier work on the Pt—6% W—1% Hf alloy indicated that the ductility at 1093°C can be increased from 2.6% to 36% by alloying with small amounts of titanium (e.g., less than 0.5%).

Air Oxidation

The determination of air oxidation behavior of Pt—30% Rh—9 to 10% W alloys at 649, 1000, and 1200°C has been completed and the results are summarized in Table 12.3. For comparison, literature data[1] for pure platinum is also included. No visible oxide layer was observed at 1000 and 1200°C, while a black oxide layer gradually appears on the surface of the specimen exposed to air at 649°C after 200 hr. Consequently, the specimen oxidized at 649°C first showed a decrease in weight followed by an increase. The oxidation rate of the alloys is higher than that of platinum by only a factor of 3. Therefore, we conclude that the oxidation resistance of these alloys is excellent at all the temperatures measured.

Table 12.2. Room-Temperature and Elevated-Temperature Tensile Properties of the Platinum-Base Alloys, T-111 and TZM

Alloy Composition (wt. %)	Ultimate Tensile Strength (psi)	Elongation (%)	Reduction in Area (%)
ROOM TEMPERATURE			
Pt-30 Rh	76,000	42	46
Pt-26 Rh-8 W[a]	171,000	15	20
Pt-26 Rh-8 W[b]	142,000	16	22
760°C (1400°F)			
Pt-30 Rh	52,000	23	33
Pt-26 Rh-8 W[a]	118,000	8	13
Pt-26 Rh-8 W[b]	95,000	16	19
TZM[c]	45,000	24	
T-111[c]	60,000	16	
1093°C (2000°F)			
Pt-30 Rh	24,000	27	30
Pt-26 Rh-8 W[a]	74,000	14	26
Pt-26 Rh-8 W[b]	56,000	12	22
TZM[c]	33,000	24	
T-111[c]	61,000	18	
1316°C (2400°F)			
Pt-30 Rh	10,000	26	29
Pt-26 Rh-8 W[a]	22,500	47	54
Pt-26 Rh-8 W[b]	21,000	44	65
TZM[c]	22,000	30	
T-111[c]	37,000	36	

[a] Initial Alloy State: Stress-relieved.

[b] Initial Alloy State: Recrystallized.

[c] Data collected from General Electric Company, Multi-Hundred Watt, Radioisotope Thermoelectric Generator Program, GESP-7034 (March 1970).

Table 12.3. Comparison of Air Oxidation Rate Between Pt–30% Rh–9 to 10% W Alloys and Platinum

Temperature (°C)	Oxidation Rate ($g/cm^2:hr$) Pt-Rh-W	Oxidation Rate ($g/cm^2:hr$) Pt[a]	Remarks
	($x\ 10^{-6}$)	($x\ 10^{-6}$)	
1200	−4.9	−2	No visible oxide layer
1000	−0.56	−0.2	No visible oxide layer
649	+0.042		Black oxide layer

[a] Data collected from Reference 1.

Compatibility with T-111

To simulate reentry heating conditions, the Pt–30% Rh–9 to 10% W and Pt–30% Rh alloys were heated in contact with T-111 in the temperature range of 2900 to 3100°F for 10 min. The results are summarized in Table 12.4. Two important points should be mentioned. First, the Pt–30% Rh shows interface melting when in contact with T-111 at 3000°F for 10 min, while the Pt–30% Rh–9% W alloy shows no such reaction until

Table 12.4. Compatibility of Pt–30% Rh and Pt-Rh-W Alloys with T-111

Alloy (wt %)	Temperature (°F)	Time (min)	Reaction Zone Thickness (micron)	Remarks
Pt–30 Rh	2900	10	25	No interface melting
Pt–30 Rh	3000	10	62	Interface melting
Pt–30 Rh–9 W	3000	10	5	No interface melting
Pt–30 Rh–9 W	3100	10	140	Interface melting
Pt–30 Rh–10 W	3100	10	90	Interface melting
Pt–30 Rh–9 W	1650	1000 hr	0	No interaction

3100°F. This observation suggests that a failure of Pt—30% Rh clad during reentry would not be due to exceeding the melting point, but would probably be due to the reaction between it and T-111. Secondly, as indicated in Table 12.4, when the tungsten content is increased from 9 to 10 wt %, the reaction zone observed at the interface is reduced in thickness from 140 to 90 microns. This indicates that tungsten is effective in slowing the reaction between the alloy and T-111.

For the benefit of the Isotope Brayton Program, we have conducted longtime Pt-Rh-W/T-111 compatibility tests at 900°C and 1200°C in vacuum. At present the 1000-hr test at 900°C (1650°F) has been completed, and metallographic examination shows no indication of a reaction (Table 12.4).

Compatibility with Tungsten

To determine the compatibility with tungsten, a piece of Pt—26% Rh—8% W alloy with dimensions of 2-in. × 0.25-in. × 0.030-in. was coated with a 9-mil thick layer of CVD tungsten at 600°C. The composite was then heated 17 hr at 1300°C and 10 min at 1600°C, and showed no indication of either cracking of the tungsten coating or apparent reaction with Pt-Rh-W. Several 1000-hr compatibility tests of this couple in vacuum at temperatures of 900, 1100, 1200, and 1300°C are in progress.

Weldability

Gas tungsten-arc welding was used to evaluate the weldability of the Pt—26% Rh—8% W alloy. Full penetration bead-on-plate welds were made on 20-mil sheet specimens in air and in an inert-gas chamber. The welded sheet showed no cracking "as welded" or after bending 90° when examined by dye penetrant and metallographic techniques.

References

1. R. W. Douglass, et al., High-Temperature Properties and Alloying Behavior of the Refractory Platinum-Group Metals, NP-10939 (1961).
2. C. T. Liu and H. Inouye, Fuels and Materials Development Program Quart. Progr. Rept. Sept. 30, 1970, ORNL-4630, pp. 186—189.

13. PHYSICAL AND MECHANICAL METALLURGY OF REFRACTORY ALLOYS

P. Patriarca   R. G. Donnelly

The purpose of this program is to provide a broad, base-technology evaluation of high-temperature alloys for use in high-performance nuclear reactors and isotopic heat sources for advanced space, terrestrial, and civilian power applications. Principal emphasis is placed on materials problems that involve Ta-, Nb-, and Mo-based alloys for systems that use alkali metals as thermodynamic working fluids and heat-transfer media.

Physical Metallurgy

H. Inouye

Solubility, Diffusivity, and Permeability of Interstitials in Refractory Alloys (H. Inouye)

An apparatus for measuring the solubility and diffusivity of nitrogen in T-111 was placed in operation during this period. The technique utilizes a pressure-drop technique in which the gases over T-111 are analyzed with an attached mass spectrometer. From calibration curves and ionization patterns of the gases, the nitrogen pressures over the specimen to as low as 10^{-9} torr is measured in the presence of other gases such as Ar, CO, CO_2, H_2O, and CH_4.

Presently the nitrogen solubility is being measured in the temperature range 1200–1600°C. The pressure-temperature-composition relationships in the N_2/T-111 system obtained to date are listed in Table 13.1. These measurements show that the nitrogen content of T-111 as expected. The results are about two orders of magnitude higher than data for unalloyed tantalum.[1]

Table 13.1. Equilibrium Nitrogen Pressure Over T-111

Temperature (°C)	Nitrogen Pressure (torr)	
	9 ppm Nitrogen	91 ppm Nitrogen
1200	(a)	1.2×10^{-8}
1300	(a)	4.1×10^{-8}
1400	4.0×10^{-8}	1.6×10^{-7}
1500	1.2×10^{-7}	9.8×10^{-7}
1600	7.5×10^{-7}	(a)

[a] Not measured.

Effect of Interstitials on Mechanical Properties of Refractory Alloys

Nitrogen in T-111 (H. Inouye). — The creep properties of T-111 are being measured in low-pressure nitrogen to determine the applicability of the creep data obtained in ultra-high vacuum to its performance as a cladding for UN.

The creep behavior of T-111 stressed to 4000 psi at 1400°C in nitrogen and in vacuum are compared in Table 13.2. These data show a moderate degree of strengthening of T-111 by nitrogen from the standpoint of both the time required for a given strain and the minimum creep rate.

Table 13.2. Effect of Nitrogen Partial Pressure on Creep Behavior of T-111 Stressed to 4000 psi at 1400°C

Pressure of Environment (torr)	Time (hr) to Strain of			Creep Rate
	0.5%	1.0%	2.0%	(in. in^{-1} hr^{-1})
4.7×10^{-8} (vacuum)	77	216	481	2.6×10^{-5}
4.7×10^{-6} (nitrogen)	90	258	719	2.1×10^{-5}

Measurements of the emissivity of T-111 concurrent with the creep tests showed no differences between tests run in vacuum or nitrogen. We infer from these results that a nitride film did not form at the test pressure and that the absorbed nitrogen was in solution. Based on the nitrogen solubility measurements above and the applicability of Sievert's Law, the nitrogen content of this T-111 specimen is estimated to be about 500 ppm.

Oxygen in T-111 (C. T. Liu). — The objective of this work is to determine the oxygen solubility in T-111 and to evaluate the effect of oxygen contamination on its mechanical properties. This study will provide the necessary information for the use of T-111 in high performance nuclear reactors and isotopic heat sources for space and civilian power applications.

The T-111 alloy with chemical composition listed in Table 13.3 was homogenized 1 hr at 1650°C and then cold rolled to 20 mil sheet. The 1-in. gage-length tensile specimens were stamped from the sheet stock.

Table 13.3. Chemical Composition of T-111 in Wt %

Element	As-Received	Heat Treated
Ta	Balance	
W	7.98	
Hf	2.02	
Nb	0.020	
Mo	0.040	
O	0.0026	0.0025
N	0.0002	0.0013
H		0.0001
C	0.0025	

After recrystallization (1 hr at 1450°C), the specimens were doped with controlled amounts of oxygen in a dynamic system at oxygen pressures of 1 to 2 $\times 10^{-5}$ torr at 1000°C. Interstitial analysis of a specimen prior to doping with oxygen is also shown in Table 13.3.

The reaction time was used to control the degree of oxygen contamination and the oxygen level was calculated from the weight gain. Although the weight of specimen can be very accurately measured, weight changes could also be produced by extraneous contamination, such as carbon and nitrogen; therefore, chemical analyses were required to verify the weight-gain measurement. An excellent correlation was obtained between weight gain and chemical analysis.

After oxygen doping, the specimens were tested in two different conditions. To homogenize and to simulate the reentry condition, one set of specimens were annealed 15 min at 1700°C. Subsequent weight measurements showed no apparent change due to this thermal treatment. Another set of specimens were tested in the as-doped condition. High-temperature tensile tests were performed on an Instron testing machine in a vacuum of 10^{-5} to 10^{-6} torr at temperatures to 1316°C. The results to date for the homogenized specimens are shown in Fig. 13.1 where the tensile strength and elongation are plotted as a function of oxygen content at three temperatures. With oxygen levels less than 200 ppm, a moderate reduction of ductility and increase of strength are observed at all temperatures. It is believed that the solubility limit of oxygen in T-111 is around 200 ppm. Beyond that level, surprisingly enough, both the strength and ductility were almost independent of oxygen content to a large extent. The data in Fig. 13.1 indicate that T-111 in the homogenized condition can tolerate oxygen contamination to 2800 ppm at temperatures above 760°C. Future work will determine the oxygen level (at a given temperature) which causes the ductile to brittle transition in T-111.

In contrast to the results shown in Fig. 13.1, we found that the T-111 alloy exhibits much less tolerance for contamination in the as-doped condition. The preliminary data show that the T-111 specimens with oxygen contamination at a level of 800 ppm, fractured in an extremely brittle manner; i.e., within the elastic limit, at temperatures as high as 1316°C. These results are certainly important, and indicate that the thermal history, by altering the form and distribution of the oxide precipitates, had a greater effect on the mechanical properties

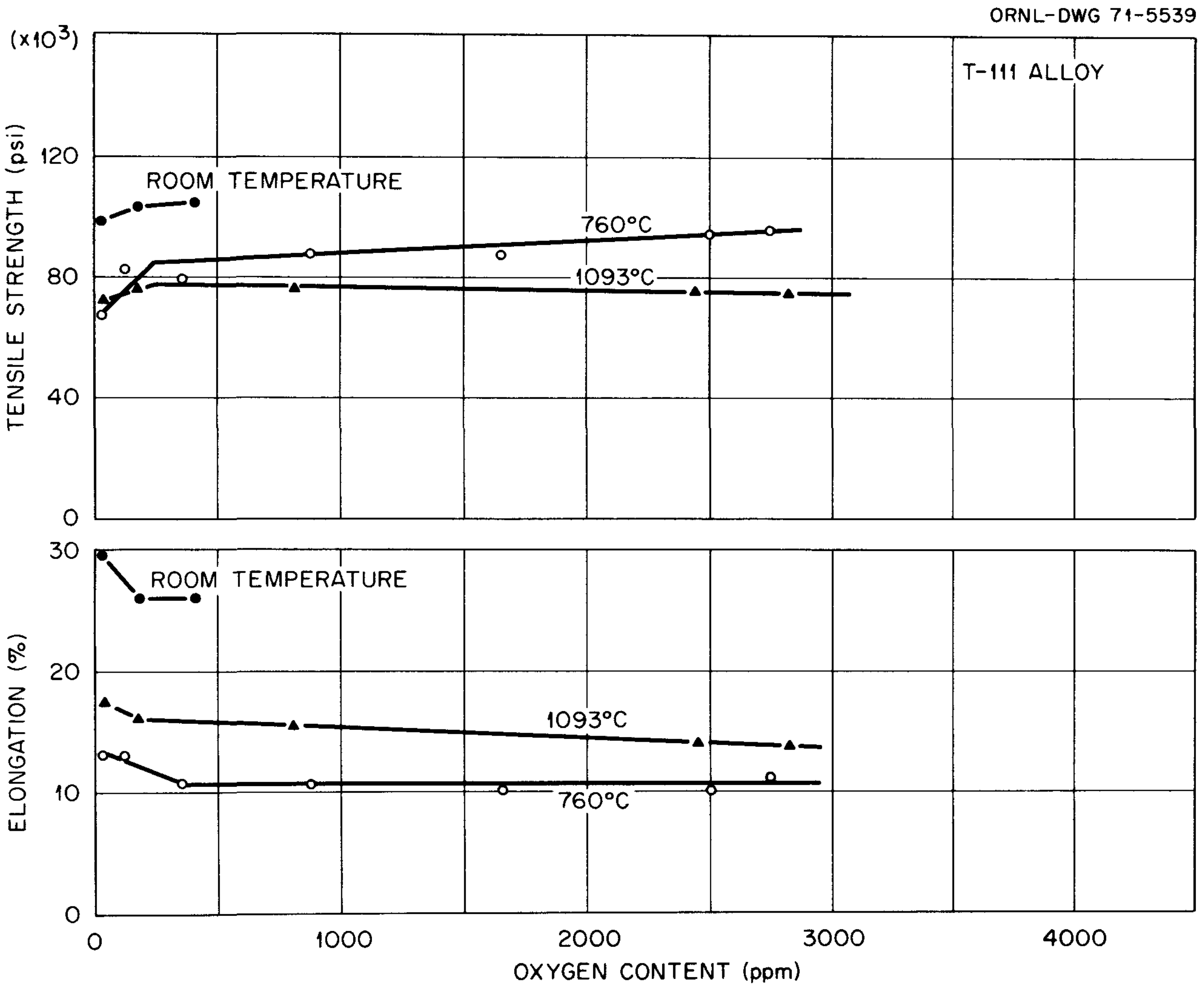

Fig. 13.1. Tensile Properties of T-111 as a Function of Oxygen Contamination.

of T-111 than the total oxygen content. Similar results have been reported in the literature.[2–4] A complete understanding of the mechanical properties of oxygen-contaminated T-111 has to rely on detailed study of microstructure and its correlation with heat treatment.

A general method for calculating the solubility limit of interstitials in refractory alloys from a single lattice parameter measurement is described in the previous report.[5] The calculation is based on thermodynamic considerations, and the results allow qualitative conclusions to be made about the randomness of the solute. The method was used to calculate oxygen solubility limits in Nb-Zr and Nb-Hf alloys, and to explain previously reported apparently quite different solubility limits in the two chemically similar alloys.[6] The solubility of oxygen in T-111 can be calculated by this method, if the lattice parameter of a specimen contaminated with a known level of oxygen is measured.

Mechanical Properties

H. E. McCoy, Jr.

Mechanical Properties of Welds (R. L. Stephenson)

Since most practical devices require joining, we consider the creep properties of welds to be of critical importance in evaluating materials for high temperature structural application. The stress-rupture properties of transverse welds in Ta–10% W were compared to those of control specimens in a previous report.[7] We are now testing longitudinal welds in this alloy. Figure 13.2 shows stress-rupture data at 1200, 1400, and 1650°C for unwelded control specimens, transverse GTA welds, transverse EB welds, and longitudinal GTA welds. At high stresses there is some tendency to fail at longer times but it is not conclusive.

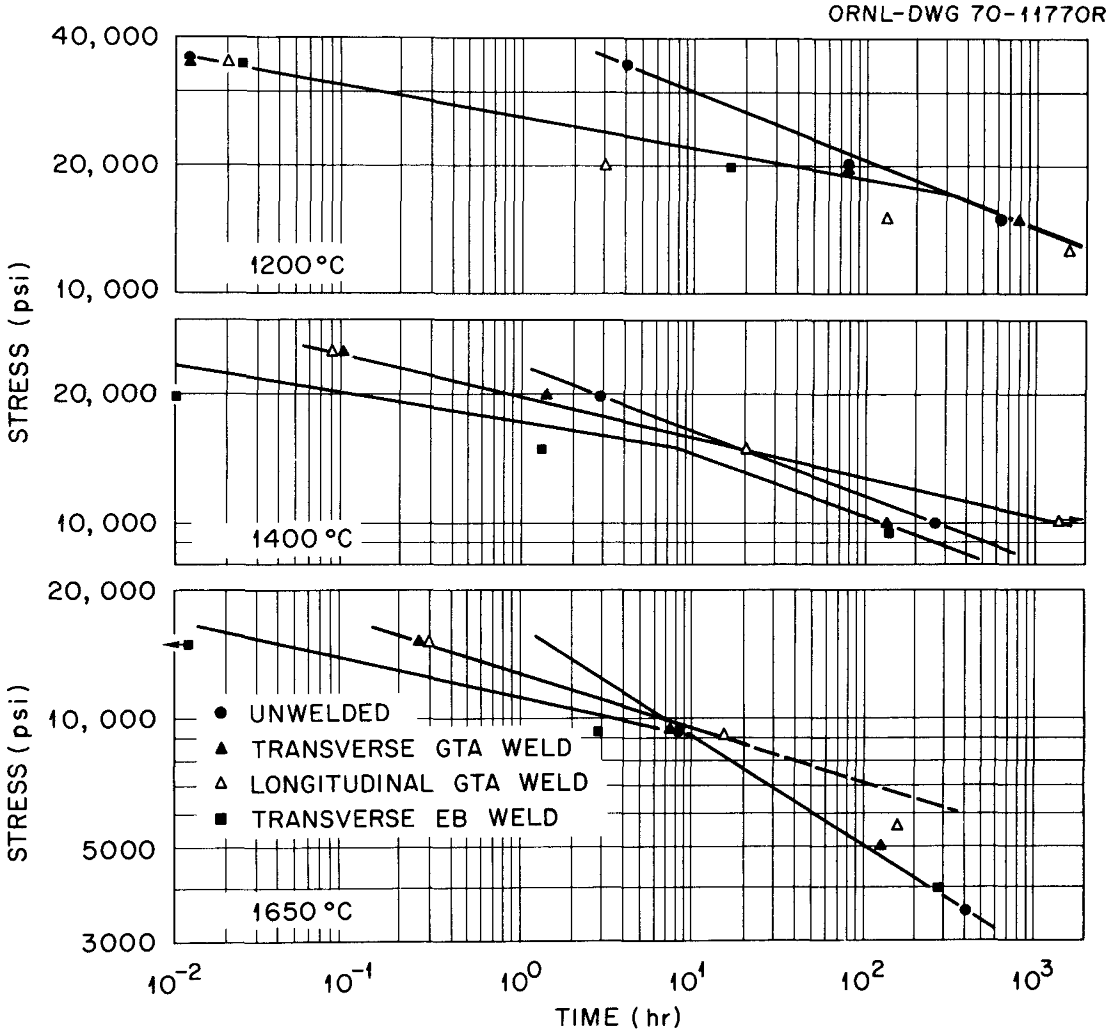

Fig. 13.2. Stress-Rupture Properties of Ta—10% Welds.

Long Time Creep Properties of Refractory Alloys (R. L. Stephenson)

We are continuing the creep testing of the niobium alloy SU-31 (Nb–17% W–3.5% Hf–0.12% C–0.03% Si). The secondary creep rate is shown as a function of stress in Fig. 13.3.

Joining

G. M. Slaughter

Cracking in TZM and Molybdenum Welds (C. D. Lundin)

Fracture morphology studies of welds in molybdenum and TZM have been continued. The fracture surfaces of TZM welds that have both hot cracks and cold cracks were carefully examined with the MAC 400 S scanning electron microprobe analyzer using the light element detection modifications. The results of this investigation are considered to be qualitatively significant. Modest amounts of oxygen were found in the hot-cracked areas, especially in the protuberances formed by liquid-metal necks during cracking.[8] No significant oxygen concentrations were found in the cold-cracked areas of the weld. Carbon was evident in small particles on the hot-cracked surfaces and in areas which produced a dark structure in the scanning micrographs. Thus, oxygen is seen to be important in the formation of hot cracks in TZM.

Stereographic analysis of the grain-boundary fractures in molybdenum revealed that the previously reported grain-boundary precipitate or porosity was in reality surface depressions caused during the fracture process.[9] The exact nature of these markings has not been determined, but they are strongly crystallographically dependent.

Fractured welds in molybdenum tubes were examined with the scanning microscope to reveal the nature of the solidification pattern. The favorable depth of field of the scanning electron microscope (SEM) permitted a semi-circular montage (Fig. 13.4) of the weld and weld fracture to be constructed. This type of microscopy permits the evaluation of the growth pattern during solidification and the influence of such a pattern on the cracking tendency and mechanical behavior of welds. Work in the area of factographic analysis of failures is continuing.

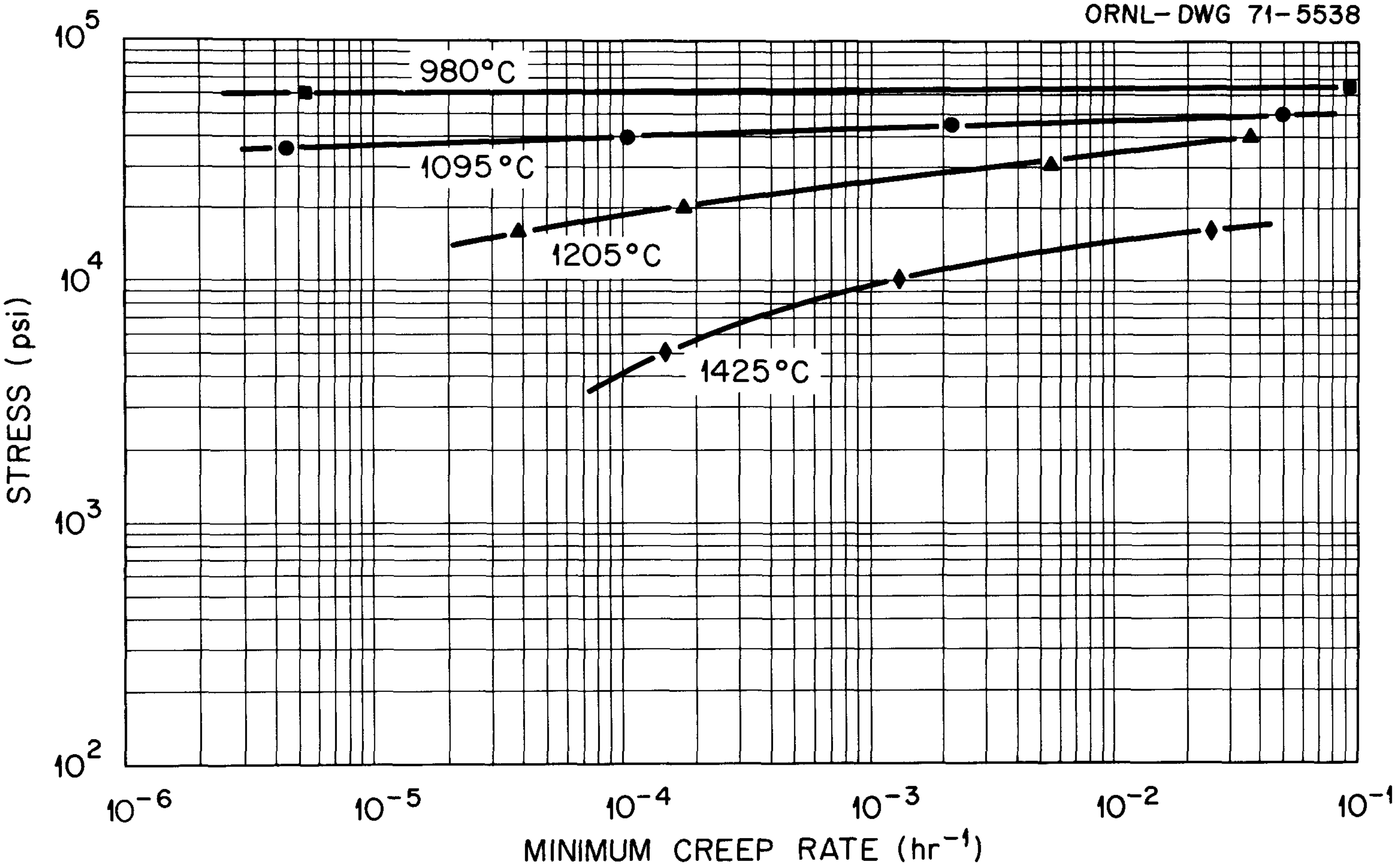

Fig. 13.3. Minimum Creep Rate Versus Stress for SU-31.

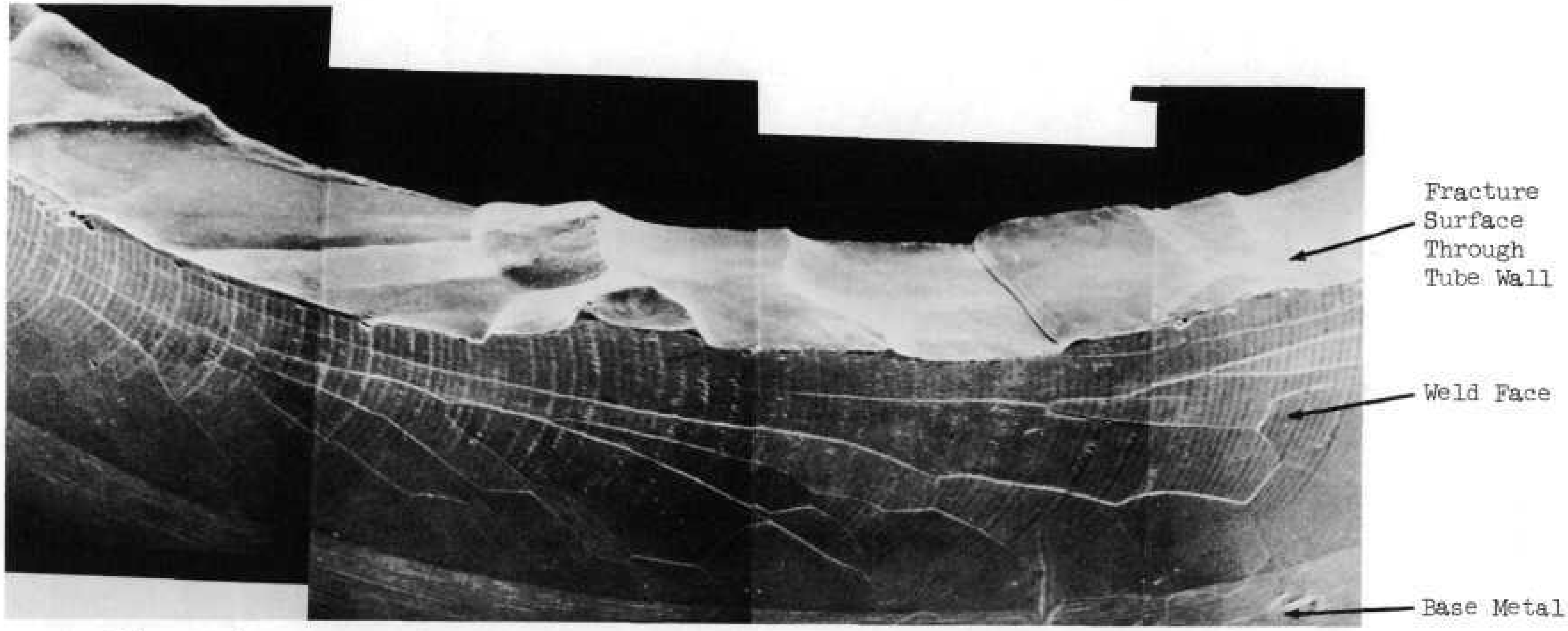

Fig. 13.4. Scanning Electron Microscope Photograph of Gas Tungsten-Arc Weld and Fracture Surface in a Low-Carbon Molybdenum Tube. 80X.

Fabrication of Refractory-Metal Components (A. J. Moorhead)

Two fractures in the molybdenum convection loop described earlier[10] have been repaired by gas tungsten-arc welding. The first failure occurred in one of the 1/4-in.-diam fill tubes during installation of the loop. It was decided to attempt to remedy this problem by replacing the molybdenum fill tubes and top of the feed pot with similar parts made of the more ductile alloy, T-111. The substitution of T-111 was permissible since these components would be in contact with the corrosive environment (bismuth) only during filling. Therefore, the reduced corrosion resistance of T-111 to bismuth would not be a problem. However, during the removal of the top of the pot, the hot leg of the loop was fractured just above the saddle weld joining the upper crossover line. The locations of the two failures are indicated in Fig. 13.5.

The first step in the repair of the loop was to reweld the hot leg. This was accomplished by machining off the fracture interface and then beveling the joint as shown in the drawing in Fig. 13.5. A simple jig was fabricated to hold the joint in alignment for welding. Precleaning only with acetone was used since we didn't want to risk contaminating the interior of the loop with the normal cleaning solutions. The tube-to-tube repair weld was made manually in an argon-filled glove box, using low-carbon molybdenum filler wire.

After welding the T-111 tubes to the new T-111 top, the top was welded to the molybdenum pot. Prior to welding this bimetallic joint, we made developmental welds using three filler metals (Mo, Mo—46% Re, and T-111) as shown in Fig. 13.6. Although all three welds were satisfactory visually, the weld bead made with T-111 filler metal was found to be cracked when inspected with fluorescent penetrant. At this time, we do not know whether the failure was due to hot cracking during welding or from handling. Metallographic specimens are being prepared to determine which factor was responsible for this fracture.

Based on our experience, it was decided to make the Mo to T-111 weld on the feed pot with Mo—46% Re filler. This filler metal has better ductility than the pure Mo and melts at a lower temperature than either Mo or T-111. A helium leak check of the entire loop after these repair operations did not reveal any leaks.

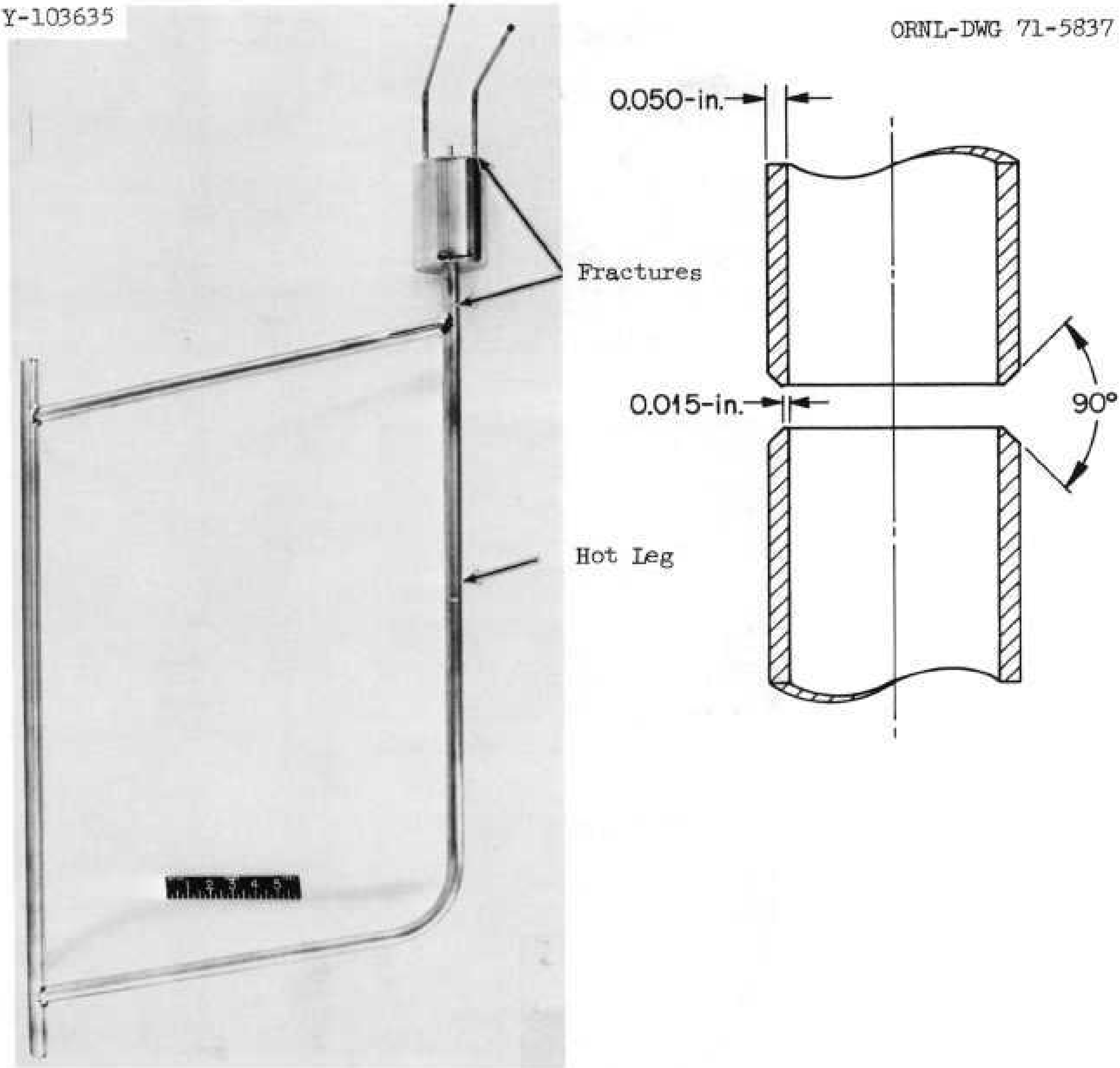

Fig. 13.5. Locations of Fractures in Molybdenum Convection Loop and Joint Design Used in the Repair of the Fracture in Hot Leg.

Y-106368

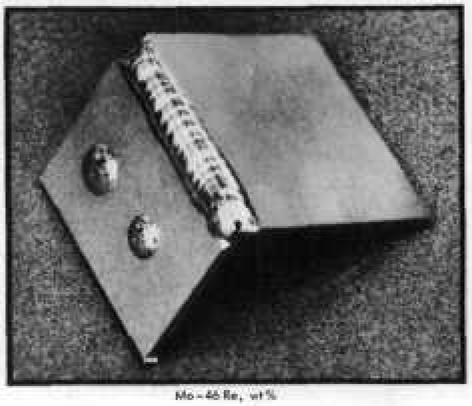

Mo-46 Re, wt %

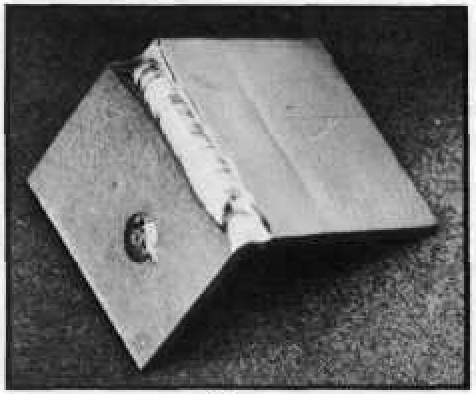

Mo

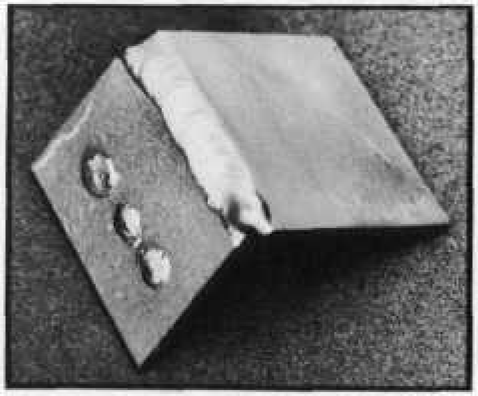

T-111

Fig. 13.6. Manual GTA Welds of Low-Carbon Molybdenum (Arc-Cast Stock) to T-111 (Ta-8 W-2 Hf, wt %) Using the Filler Metals Shown. The thickness of the coupon is 1/16 inch with the Mo on the left side.

Physical Properties

D. L. McElroy

Thermal Conductivity of Molybdenum Alloys (R. K. Williams, J. P. Moore)

To improve determinations of the electronic Lorenz function and the lattice thermal conductivity of molybdenum requires further improvements in the accuracy of our low temperature absolute linear heat flow apparatus. Consequently, we are constructing a modified apparatus which should be capable of determining thermal conductivity to about ±0.5% and electrical resistivity to ±0.1% in the range, 80 to 400K.

Samples of dilute Mo-Zr and Mo-Nb alloys have been obtained and characterized by density, electrical resistivity and chemical analysis for this study. For equal concentrations, the resistivity increment produced by Zr additions is about five times larger than the increment for Nb. Our estimates of the effect of impurities on the lattice thermal conductivity of Mo showed Nb to be an optimum element and Zr to induce larger lattice strains.

Room temperature electrical resistivity measurements were made on samples from two processes to produce 17.5% Mo-ThO_2 cermet fuel simulators. A sample with chemically vapor deposited Mo on ThO_2 proved to be a 40% better conductor than a blended Mo-ThO_2 powder sample. Tests on other blended Mo-ThO_2 powder samples show large variations in electrical resistivity. All of these samples are significantly poorer conductors than the Eucken mixture equation would predict. Estimates of the high temperature thermal conductivity of this class of cermets were made using our previous measurements of the thermal conductivity of molybdenum[11] and thoria.[12]

References

1. E. Gebhardt, H. D. Seghezzi, E. Fromm, Z Metalkunde, 52 (1961)
2. D. O. Hobson, High Temperature Materials II – publication of AIME Conference in April 1961, p. 325.

3. R. M. Bonsteel, et al., *Trans. Jap. Inst. Metals*, 9 (Suppl.) p. 597 (1968).

4. D. R. Stoner, WANL-PR-(P)-015, Westinghouse Astronuclear Laboratory (October 1969).

5. C. T. Liu, *Fuels and Materials Development Program Quart. Progr. Rept. December 3, 1970*, ORNL-TM-3300, pp. 227–230.

6. C. T. Liu, H. Inouye, and R. W. Carpenter, paper to be submitted to *J. Less Common Metals*.

7. R. L. Stephenson, *Fuels and Materials Development Program Quart. Progr. Rept. September 30, 1970*, ORNL-4630, pp. 193, 194.

8. C. D. Lundin, *Fuels and Materials Development Program Quart. Progr. Rept. September 30, 1970*, ORNL-4630, pp. 195–197.

9. C. D. Lundin, *Fuels and Materials Development Program Quart. Progr. Rept. December 31, 1970*, ORNL-TM-3300, pp. 235–236.

10. A. J. Moorhead, "Fabrication of Refractory Metal Components," *Fuels and Materials Development Program Quart. Progr. Rept., December 3, 1970*, ORNL-TM-3300.

11. R. K. Williams, J. P. Moore, and D. L. McElroy, "Physical Properties of Molybdenum," ORNL-4370, p. 66 (October 1968).

12. J. P. Moore, R. S. Graves, and D. L. McElroy, "Thermal Conductivity of ThO_2 and UO_2 From 77 to 1300°K," ORNL-4370, p. 37, (October 1968).

14. TUNGSTEN METALLURGY

P. Patriarca   A. C. Schaffhauser

The objective of this program is to provide the base technology on W alloys for advanced power applications in space and FBR high-temperature thermocouple components. We are developing fabrication processes for W alloys based on modification of conventional extrusion and warm-drawing techniques, direct dhemical vapor deposition (CVD), and welding. Since the primary criterion for the use of W alloys for fuel cladding is based on the creep-rupture properties, we are conducting extensive long-time tests at the temperatures of interest and determining the mechanisms that control the creep behavior and the effect of interactions with the vapor species from an isotope or reactor fuel. We are also determining the effect of high-temperature fast-neutron irradiation damage on the physical properties of W alloys.

Chemical Vapor Deposition

J. I. Federer

Deposition of Tungsten with a Dispersion of Fine Particles

We have continued efforts to introduce fine particles into tungsten deposits for the possible dispersion strengthening effect that the particles may produce. In these studies resistance-heated substrates measuring about five in. long by 0.5 in. wide were contained within a four-in. by 12-in.-long deposition chamber. The substrates were heated to 600°C and experiments were conducted in the pressure range of five torr to about one atm. We found that Al_2O_3 particles entrained in helium preferentially deposited on the chamber walls instead of the substrates although the deposition of particles on all surfaces appeared to increase with increasing pressure. Different methods, such as jets and deflectors, were used to disperse the particles in the chamber, but none were successful in causing the particles to coat the hot substrates.

We also investigated electrostatically attracting particles to the substrates by establishing a potential difference between the substrate and the chamber wall. The voltage was a function of pressure and varied from about 500 v at five torr to about 1500 v at one atm. However, voltages of these magnitudes did not effectively attract particles to the substrates. In a typical experiment we obtained 0.02 g/in.^{2} of Al_2O_3 particles on the substrate in five hr. If tungsten had been simultaneously deposited at a rate of 0.003 in./hr, the deposit would have contained only 0.05 wt % Al_2O_3. This amount would be substantially less than the desired one to four wt %. This method, then, does not appear to have potential for incorporating particles into tungsten deposits.

Deposition of Tungsten-Rhenium Alloys

We previously reported that nominal W–25% Re deposits with the fewest nodules and the finest grain structure were obtained with a near stoichiometric gas mixture.[1] We attempted to apply this knowledge to the deposition of small diam thermocouple sheath tubes. The objective of these experiments was to prepare 12-in.-long tubes of uniform wall thickness. A series of deposits was prepared on resistance-heated 0.040-in.-diam by 19-in.-long Mo substrates using the conditions shown in Table 1. Previous results showed that a minimum temperature of

Table 14.1. Conditions and Results of Nominal W–25% Re Deposits

H_2/MF_6(a)	Temperature[b] (°C)	Recovery (%)	Wall Thickness Range (mils)	Surface Texture
3	800	69	17 to 38	Numerous nodules.
3	750	49	16 to 27	Few nodules
3	700	36	23 to 27	Few nodules
5	675	43	23 to 28	Few nodules
3	600	2	2 to 4	Smooth

[a] Typical flowrates were 300 cm^3/min H_2, 75 cm^3/min WF_6, and 25 cm^3/min ReF_6.

[b] Measured at center of substrate, ends were cooler.

about 700°C was required for composition uniformity.^{2} Since the resistance-heated Mo wires were cooler on the ends, the center of the wire was heated to 800°C in the first experiment to ensure that the ends were above 700°C. Table 1 shows that the wall thickness varied by more than a factor of 2 over the length of the deposit due to gas depletion and the surface texture was rough and nodular. Decreasing the deposition temperature produced more uniform wall thicknesses and smoother surfaces. AAtemperature as low as 600°C would not be practical for these small diam tubes because of low deposition rates and metal recovery (2%). We believe that somewhat smoother deposits with fewer nodules would be obtained with a substoichiometric gas mixture but deposition rates and recoveries would be lower than were obtained in these deposits.

As previously discussed, the deposition of W-5% Re sheet on resistance-heated substrates is successful only if the thickness of the deposit is reasonably uniform along the length because thickness uniformity maintains temperature uniformity, which in turn maintains compositional uniformity. In previous attempts to prepare sheet-type deposits we have periodically reversed gas glows to minimize the effect of gas depletion and maintain thickness uniformity. In one experiment we used an internally heated substrate which does not depend at all on deposit thickness uniformity for temperature uniformity. The substrate was a 1 1/2-in. by 1 1/2-in. by 12-in.-long copper bar heated with an internal calrod heater. However, greater heat losses on the ends imposed a temperature gradient on the substrate and resulted in a deposit that contained about 8.7% Re on the ends and only 3.0% Re at the center. In addition, the thickness was greater at the gas inlet end than at the outlet end, as was expected since the gas flow was not periodically reversed. A substrate heated internally to a uniform temperature over the entire length could probably be designed and constructed, but no clear advantages over resistance-heated substrates are evident at this time.

Creep Behavior of Tungsten and Tungsten Alloys

H. E. McCoy H. Inouye

Creep Properties of Chemically Vapor Deposited Tungsten (R. L. Stephenson)

Our work on CVD-W is directed at filling two critical needs; 1) to provide preliminary design data for conceptual designs and 2) to provide an understanding of creep mechanisms. To provide preliminary design data we are extending the 1000 hr creep data of the strongest and weakest of five lots of materials to longer times.

It is becoming increasingly apparent that the growth of voids plays an important role in the creep of CVD tungsten. We are measuring the densities of all specimens before and after test in order to separate the contribution of voids to the total deformation.

Installation of New Equipment (R. L. Stephenson)

During this report period, a major effort has been devoted to the installation and checkout of six ultrahigh-vacuum creep machines. One of two new machines capable of testing to 3000°C is operational while the other is undergoing correction of a defect by the vendor. The remaining four creep machines have 1800°C capability and are currently undergoing vacuum testing. We are also in the process of placing an optical extensometer in operation for accurate measurements at low strains.

Effect of Low-Pressure CH_4 on the Creep Properties of Tungsten (H. Inouye)

The creep properties of 0.040-in. diam tungsten wire are being measured in low-pressure CH_4 to simulate the effect of its carburization by uranium carbide at thermionic temperatures.

Table 2 compares the creep behavior in vacuum and in 2.6×10^{-6} torr CH_4 at 1800°C and a stress of 2000 psi. The results of the single test indicate that the creep strength of tungsten is lowered during

Table 14.2. Comparison of Creep Properties of Tungsten in Vacuum and in CH_4 at 1800°C and 2000 psi

Pressure of Environment (torr)	Time (hr) for Strain of			Rupture		Creep Rate
	0.5%	1%	2%	(hr)	(% E)	(in. in^{-1} hr^{-1})
1.8×10^{-7} (vacuum)	23	53	117	327	7	1.5×10^{-4}
2.6×10^{-6} (CH_4)	16	30	62	278	6.5	2.0×10^{-4}

carburization with only a slight loss in ductility. Temperature measurements during the test show an increase in the 0.665 μ spectral emissivity of tungsten from 0.43 to about 0.6 after about a 30-hr exposure to CH_4. This increase is attributed to the formation of W_2C at the surface. Posttest evaluation of the specimen showed a silvery metallic surface and no change in the weight of the specimen.

Behavior of Tungsten Alloys Under Fast-Neutron Irradiation

H. E. McCoy D. L. McElroy A. C. Schaffhauser

Design of Experiment (F. W. Wiffen, D. A. Dyslin[3])

A single-pin experiment was designed to be irradiated in row 7 of the EBR-II. The experiment is designed to irradiate rod specimens at temperatures between 600 and 1500°C to a neutron fluence near 6.0×10^{21} neutrons/cm^2 (> 0.1 MeV). The experimental design used to achieve the elevated temperatures is basically the same as that used for ORNL experiments in EBR-II subassemblies X034, X035, X067, X099, and X100. The design balances the heat generated by gamma heating in the cylindrical specimen holder against the width of the Ar-filled conduction gap between the specimen holder and the containment tube. This temperature gradient across the gap gives the desired irradiation temperature.

This experiment was planned to evaluate the effect of irradiation temperature and material variables on the damage produced in W and W-Re alloys. Compositions of specimens range from unalloyed W to W-25% Re, and materials will be included that have been prepared by arc casting, powder metallurgy, and CVD processes. Postirradiation evaluation will include electron microscopy, density, and physical property measurements.

We are awaiting AEC concurrence on our Approval In Principal which was submitted in February.

High Temperature Physical Properties of Tungsten

(D. K. Williams, J. P. Moore)

Our high-temperature, ultrahigh-vacuum, electrical-resistivity/Seebeck coefficient apparatus is currently being used to obtain data on zone-refined tungsten. These experiments have demonstrated that uninsulated W-3% Re/W-25% Re thermocouples yield reliable temperature measurements. Thermocouple temperature measurements and those obtained from our automatically balancing optical pyrometer are in excellent (< 5 K) agreement to 1400 K, and the differences between the two measurements are within the combined uncertainties at the highest temperatures (2600 K). The inclusion of thermocouples in this test permits determination of the Seebeck coefficient of W-3% Re and W-25% Re relative to pure W.

Preliminary electrical resistivity ρ data on tungsten show a linear temperature dependence between 1800 and 2600 K in sharp contrast to the lower (300-1700 K) temperature results which are nonlinear. This work froms a useful basis for the study of the effects of irradiation-induced voids on the electrical resistivity of W and W-Re alloys.

We are redetermining the thermal conductivity, electrical resistivity, and Seebeck coefficient of zone-refined tungsten, W-2.8% Re, and W-5.4 Re from 80 to 400 K in a modified version of the existing low-temperature, aboslute-linear, heat-flow apparatus. These measurements were needed, since application of the alloying method of component separation using our original data indicated small inconsistencies near 400 K. Equipment alterations which were made since the original data were obtained suggested means to check this.

References

1. J. I. Federer, Fuels and Materials Development Program Quart. Progr. Rept. December 31, 1970, ORNL-TM-3300.
2. J. I. Federer, Fuels and Materials Development Program Quart. Progr. Rept. December 31, 1968, ORNL-4390, pp. 165–166.
3. General Engineering Division.

15. FAST-NEUTRON IRRADIATION EFFECTS ON ELECTRICAL INSULATORS

G. W. Keilholtz[1], G. M. Watson[1], R. E. Moore[1], H. E. Robertson[1]
and D. A. Dyslin[2]

The ORNL program to evaluate electrical insulators (primarily Al_2O_3) under irradiation has been completed with the exception of the 0-2 capsule in X090 subassembly now under test in position 7D5 in the EBR-II. In accordance with previous discussions between ORNL, LASL, and USAEC-SNS, the LASL group will assume responsibility for the completion of this work.

The following final topical report will be published June 1971 — "Effect of Fast Neutrons on Polycrystalline Alumina and Other Electrical Insulators at Temperatures from 60 to 1230°C," by G. W. Keilholtz, R. E. Moore, and H. E. Robertson.

The effects of fast neutrons on four commercial polycrystalline alumina products of high density were investigated. These materials have been considered for use as electrical insulators in nuclear-powered thermionic converters. Fast-neutron fluences up to 5.8×10^{21} neutrons/cm^2 (> 1 MeV) were achieved; irradiation temperatures ranged from 60 to 1230°C.

At temperatures below 100°C, there was very little damage, as is usually manifested by gross fracturing, volume increase, and separation at grain boundaries. Damage was much worse, however, at temperatures from 570 to 1070°C, which is the range of greatest interest for thermionic applications. At about 1100°C and above, in-reactor thermal annealing was rapid enough to reduce damage significantly, but at much higher temperatures ($\sim$ 1230°C), damage again increased.

Based on the irradiation results, the following conclusions and recommendations were made for the use of polycrystalline alumina in thermionic converters.

1. The alumina should be of high purity to minimize gross fracturing, and it should be of small grain size to minimize the effects due to separation at grain boundaries.

2. The thermionic device should be designed for continuous operation because thermal cycling apparently promotes separation at grain boundaries.

3. The design should allow for an increase in volume of the alumina insulators of about 3%.

4. Alumina of high purity and small grain size can withstand fast neutron fluences up to about 3×10^{21} neutrons/cm^2 in an ETR-type neutron spectrum and up to about 2×10^{21} neutrons/cm^2 in an EBR-II-type spectrum for those neutrons with energies greater than 1 MeV.

Four other electrical insulators were investigated in a preliminary manner as possible alternatives to polycrystalline alumina for thermionic applications. These are (1) single-crystal Al_2O_3, (2) single-crystal MgO of high purity, (3) transparent polycrystalline Y_2O_3, and (4) silicon oxynitride (Si_2ON_2). The preliminary results were very encouraging. More comprehensive investigations of these materials appear to be warranted.

References

1. Reactor Chemistry Division.
2. General Engineering Division.

PART III

GENERAL REACTOR TECHNOLOGY

FUELS

16. DEVELOPMENT OF FUEL ELEMENT FABRICATION

G. M. Adamson, Jr.   W. R. Martin

The purpose of this program is to advance the technology for fabricating fuel elements for research reactors by developing fuel elements with lower production cost and improved irradiation performance. Work on this program has been restricted to irradiation studies and evaluation of the ATR fuel element failures.

Irradiation Studies

R. G. Donnelly

Design and Fabrication of HFIR Irradiation Experiments (M. M. Martin)

Our objective is to determine these factors that influence the performance of Al-clad UAl_x and U_3O_8 dispersions in the ATR and HFIR at fission densities of up to 2.5×10^{21} fissions/cm^3. An experimental facility that would allow this maximum fission density to be achieved in five reactor cycles has been built for the reflector region of the HFIR. The experiment, designated PM Capsule No. 1, was inserted into the VXF-17 permanent beryllium position of HFIR on January 11, 1971.

The final assembly and testing of the experiment and its installation in HFIR were accomplished without difficulty. We cite our quality assurance plan and its enthusiastic implementation during all phases of the work for the smoothness of these final operations.

On March 26, 1971, the experiment completed three full HFIR cycles (Nos. 58, 59, and 60 — approximately 7020 MWd of reactor exposure) without any indications of failure. We anticipate achieving the designed exposure during the week of May 10, 1971. To date, our only difficulty has been a primary seal leak detector which gave spurious alarms during the second and third cycles. Spot resistance measurement showed that the signal from the detector fluctuated greatly over a period of days.

Since the system is designed to be self-protecting, the alarm was deactivated on March 19. A resistance indicator (microampere meter) has been connected to the leak sensor and should permit us to follow fluctuation in signal more closely than the on-off signal.

Technical Assistance to Others

W. R. Martin

Evaluation of UAl_3 (R. W. Knight)

Idaho Nuclear Corporation sent samples from two batches of UAl_3 to ORNL for analysis. Both samples are from a private vendor but the powders are behaving differently during fabrication. Sample I was defined as nonflowing; sample II was defined as flowing.

A sonic sifter analysis of each batch was made using a 2-g charge. Results of this analysis are shown in Table 16.1. The data in Table 16.1 indicates a substantial number of fines in sample I which were not apparent in the 50X microscope study. To further assess the material, a 5-g sample was examined using the Scanning Electron Microscope as shown in Fig. 26.1 and 16.2. At the lower magnifications for both samples I and II, there is a dramatic difference in the number of fines. But these photographs also show that these powders are not discrete particles but an agglomerate of platelets. At the higher magnifications, agglomerates from both batches look similar. For a final assessment of the material a simple friability test was run. A small amount of UAl_3 was put on a microscope slide in an oil vehicle and covered with a second slide. Each slide composite was then rotated between thumb and forefinger to create an abrasive action. Examination of the powder sizes before and after this simple friability test show clearly that the No. I sample is much more friable than the No. 2 sample. It appears that the powders produced by this vendor are agglomerates and not single particles. Some batches of these agglomerates are much more friable than other batches that would result in a different fabrication behavior.

Table 16.1. UAl_3 Sonic Sifter Analysis

Sample I			Sample II		
Nonflowing (charge 2 g)			Flowing (charge 2 g)		
Size Distribution	Weight (g)	(%)	Size Distribution	Weight (g)	(%)
+170	0.7058	35.29	+170	0.9933	49.66
−170 +230	0.4530	22.65	−170 +230	0.4550	22.75
−230 +400	0.3161)	15.81	−230 +400	0.3929	19.65
−400	0.2759	13.79	−400	0.0617	3.09
Total	1.7508	87.54		1.9029	95.15
Losses	0.2492	12.46		0.0971	4.85
Total −400 mesh	0.5251	26.25		0.1588	7.94

NOTE: Losses are fines by definition.

SM-17969

(a)

SM-17967

(b)

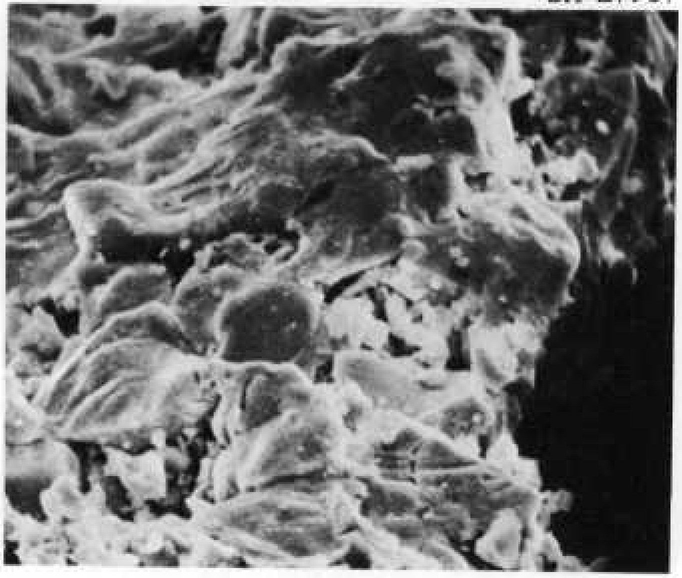

Fig. 16.1 Scanning Electron Micrograph of Non-Flowing UAl_3 Powder Showing Agglomerates and Fines. (a) 100X, (b) 1000X.

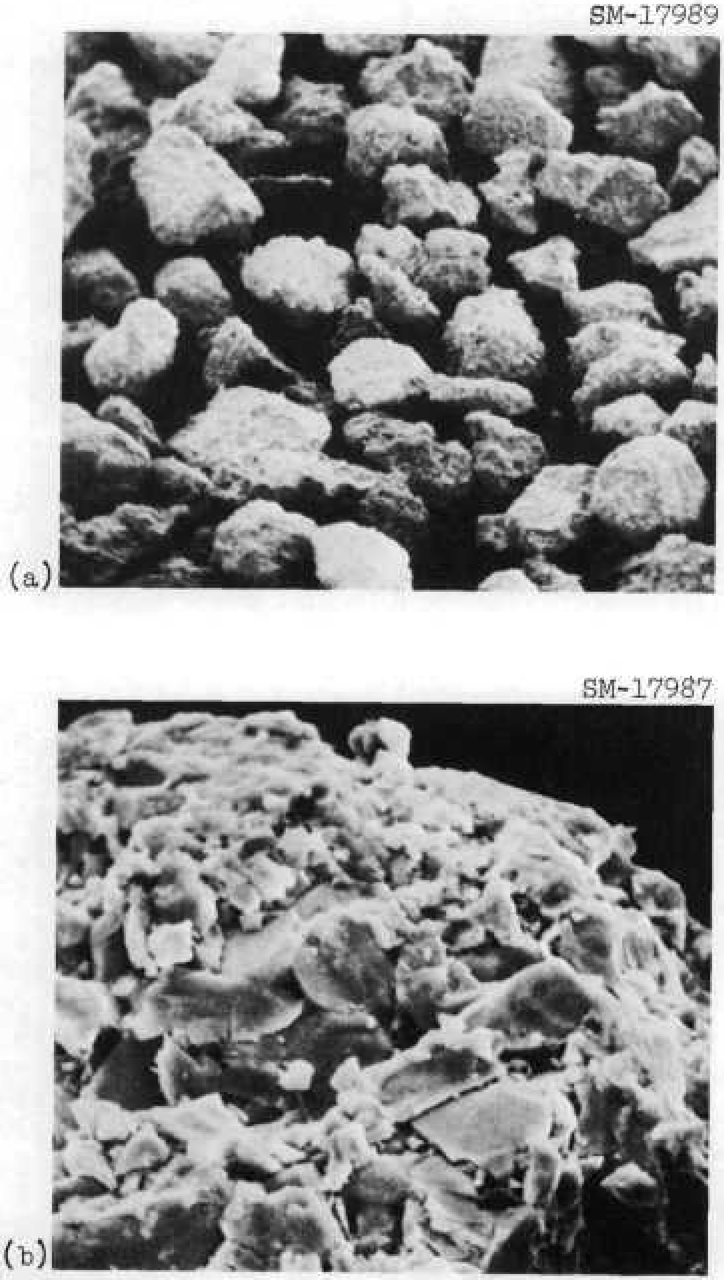

Fig. 16.2. Scanning Electron Micrograph of Flowing UAl_3 Powder Showing Agglomerates. (a) 100×, (b) 1000×.

CLADDING AND OTHER STRUCTURAL MATERIALS

17. IRRADIATION DAMAGE TO ALUMINUM AND ALUMINUM ALLOYS

J. R. Weir, Jr. R. T. King

Nothing to report for this period.

18. ✓ JOINING RESEARCH ON NUCLEAR MATERIALS

J. R. Weir, Jr.   G. M. Slaughter

The purpose of this program is to gather the fundamental and applied data needed to understand the weldability of materials that are either being considered or are currently used for nuclear applications. Fundamental studies are concerned with the effects of minor constituents on the behavior of weldments. We are especially interested in the austenitic stainless steels and the alloys that are rich in nickel, such as Incoloy 800 and Inconel 600.

As a result of this broad-based program, we plan to suggest modifications in both alloy composition and procedures needed to improve the quality of weldments used in the various activities of the USAEC.

The Effect of Minor Variations in Chemical Composition on Weldability

Our continuing investigation of the effect of minor variations in those elements usually present in structural material has included Inconel 600, Incoloy 800, and stainless steel.

Weldability of Incoloy 800 (D. A. Canonico)

Fully restrained welds made with our experimental filler metals in 1/2-in.-thick commercial Incoloy 800 plates have been tensile-tested at 650°C (1200°F). These results are presented in Table 18.1. In addition, we have included filler metals from electroslag remelted Incoloy 800, Inconel 82T (a commercial filler metal), and two candidate filler metals provided by the International Nickel Company (INCO). The latter two filler metals are being considered as alternatives for Inconel 82T. The Nb is replaced with Mo and the Ni content is considerably reduced. The analysis more closely approximates that of Incoloy 800. The analysis for the 82T and the candidate filler metals are given in Table 18.2.

The INCO submitted filler metals proved to be as strong and ductile as the commercially available 82T alloy. The elongation was in excess of

Table 18.1. Properties of Experimental and Commercially Obtained Incoloy 800 Filler Metals Tensile Tested at 650°C

Filler Metal Identification	Significant[a] Compositional Variation (%)	Strength, ksi		Elongation in 2 in. (%)
		Yield	Ultimate	
800-2	0.15 Al—0.15 Ti	27.6	39.9	9.4
800-3	None	29.15	46.1	16.0
800-4	0.60 Al—0.60 Ti	27.9	48	18.6
800-5	0.15 Ti	27.7	44.7	12.7
800-6	0.60 Ti	29.9	49.0	18.5
800-7	0.15 Al	29.4	45.5	13.0
800-8	0.60 Al	27.7	47.4	16.9
800-10	0.015 S	30.7	48.9	16.8
800-11	0.02 S	27.8	45.9	13.7
800-15	0.01 S—0.01 P	28.2	45.8	18.0
800-16[b]	0.015 S—0.015 P	29.2	48.1	16.0
800-18[c]	No Al	28.6	35.3	7.0
800-17	No Ti	27.8	45.3	17.6
800-23	No Al—No Ti—0.04 C	27.8	51.6	23.7
800-24[b]	No Al—No Ti—0.08 C	28.2	40.2	8.0
5409	See Table 18.2	30.2	57.5	25.5
Y32Al	See Table 18.2	25.5	55.0	25.0
ES remelted 800	None	29.1	54.9	22.2
Inconel 82T	See Table 18.1	29.2	56.6	25.4

[a] Deviation from nominal analysis which is Fe—31.5 Ni—21.5 Cr—0.38 Al—0.38 Ti.

[b] Failed bend test.

[c] Cracked during welding.

Table 18.2. Chemical Composition of Commercially Obtained Filler Metals

Filler Metal Designation	Form	Chemical Composition, wt %									
		C	Mn	Fe	S	Si	Cu	Ni	Cr	Mo	Others
82T[a]	Wire	0.02	3.00	1.00	0.007	0.20	0.04	Bal	20	----	Ti—0.55
Y32A1	Shielded	0.10	5.65	Bal	0.007	0.47	0.26	40.26	21.16	2.67	-------
5409	Wire	0.09	4.78	Bal	0.005	0.68	0.32	41.29	20.76	2.62	-------

25% and the ultimate tensile strengths are about 55,000 psi. The properties of the electroslag remelted commercial Incoloy 800 alloy were also quite impressive. Ductility and strength values approximated those of the commercially produced filler metals.

Most of the experimental alloys suffered from a lack of ductility. The tensile properties in most instances were within 10 to 15% of the Inconel 82T values. Nearly all had yield strengths within 5% of the commercial alloy. The experimental alloy that most closely matches the properties of the Inconel 82T alloy is No. 800-23, an alloy that contains a nominal 0.04% C. Other experimental alloys whose tensile strengths are noteworthy are 800-4, 800-6, 800-10, and 800-11. All of the alloys listed in Table 18.1 are currently being prepared for metallographic examination to assess their tendency toward microfissuring. No doubt some of the low-ductility values reported are due to microfissures which reduce the engineering ductility of the weldments.

An investigation of a commercially made tube-to-tubesheet weld which contained evidence of microfissures was conducted. The tubes are Inconel which has been autogeneously welded to 82T overlaid on carbon steel. The weld was made by the electron-beam (EB) process. Microfissures are evident in the as-deposited overlay (which is in the heat-affected zone of the EB weld) in a region which, due to the weld bead contour, is subjected to a concentration of stress. Figure 18.1(a) is a 50× photomicrograph showing the Inconel 600 tube, 82T overlay, EB weld, and microfissure in the 82T. A higher (500×) magnification photomicrograph of the fissure [Fig. 18.1(b)] shows evidence of a liquated phase in the heat-affected zone. We have chemically analyzed the crack region and found it to be associated with an enrichment of Nb. There is also some evidence of a slight enrichment of Mn associated with the intercellular regions of the overlay. The low melting phase may be associated with the eutectic that occurs at 52% Nb in the Nb–Ni system. Although definitive phase diagrams are not available, it appears that the Mn may also contribute to the liquation of the Nb-enriched areas in the HAZ.

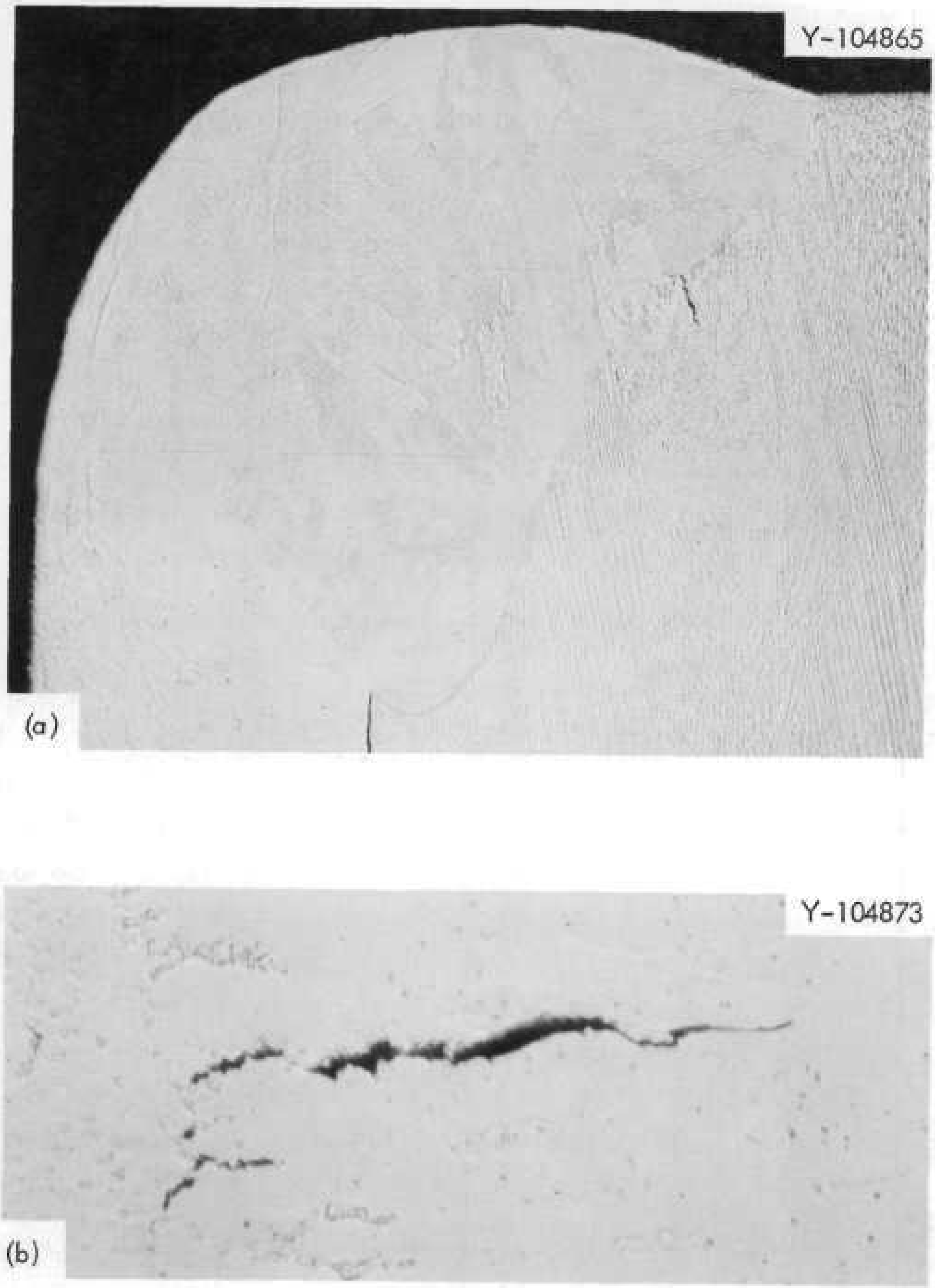

Fig. 18.1. Photomicrographs of a Microfissured Heat-Affected Zone in an Electron-Beam Tube-to-Tubesheet Weld. The tube is Inconel 600. The tubesheet is carbon steel overlaid with Inconel filler metal 82. The relationship between the tube, overlay, and weld is shown in (a). Note the microfissure is located at a region where the weld bead geometry has resulted in a stress concentration. 50×. A photomicrograph (b) of the microfissure shows the presence of a second phase which probably was melted during welding. 500×.

Weldability of Stainless Steels (A. J. Moorhead, D. A. Canonico)

We are presently measuring the ferrite content of autogeneous welds made on coupons from drop-cast heats No. 5408 through No. 5422. The procedures used in making these welds, by both the GTA and EB processes, were described earlier.[1] After etching cross sections with boiling Murakami's reagent, a series of measurements of ferrite content were taken along the weld centerline, using the Quantitative Television Microscope (QTM). At least 20 measurements were taken on each weld. The averages of these readings, along with the ferrite content predicted from the Schaeffler Diagram for stainless steel weld metal, are given in Table 18.3. Two important observations can be made from this table. First, although the Schaeffler Diagram predicts that the Mn-bearing heat (No. 5409) should be strongly austenitic, weld metal of this composition had from 3% (EB) to 8.5% (GTA) ferrite. This anomaly was indicated earlier when the drop-cast ingot had over 9% ferrite as measured with the Magne-Gage. A second Mn-bearing heat of similar composition (No. 5535) was found to have about 7% ferrite in the as-cast ingot. It is also interesting to note that a ternary alloy having the same Fe, Cr, and Ni contents of this alloy (i.e., 11.9 Ni—18.3 Cr—bal Fe, wt %) would be expected to contain about 2% ferrite in the weld metal. This indicates that, although small amounts of Mn may act as an austenitizer in greater amounts, this element may have no effect or, in fact, become a ferrite former.

The second noteworthy feature of this table is the effect of weld energy input on the ferrite content of the weld metal. The energy input of the EB weld was 1700 j/in. and of the GTA weld 4500 j/in. By comparing the ferrite content of the welds made on a single heat, the large effect of energy input can be seen. For example, welds having the composition of heat 5410 (which has Ni and Cr equivalents on the Schaeffler Diagram comparable to those of type 304) may or may not contain enough ferrite to prevent hot-cracking, depending on the process used. This effect is illustrated in Fig. 18.2.

References

1. A. J. Moorhead and D. A. Canonico, Fuels and Materials Development Program Quart. Progr. Rept. Dec. 31, 1970, ORNL-TM-3300, pp. 297–303.

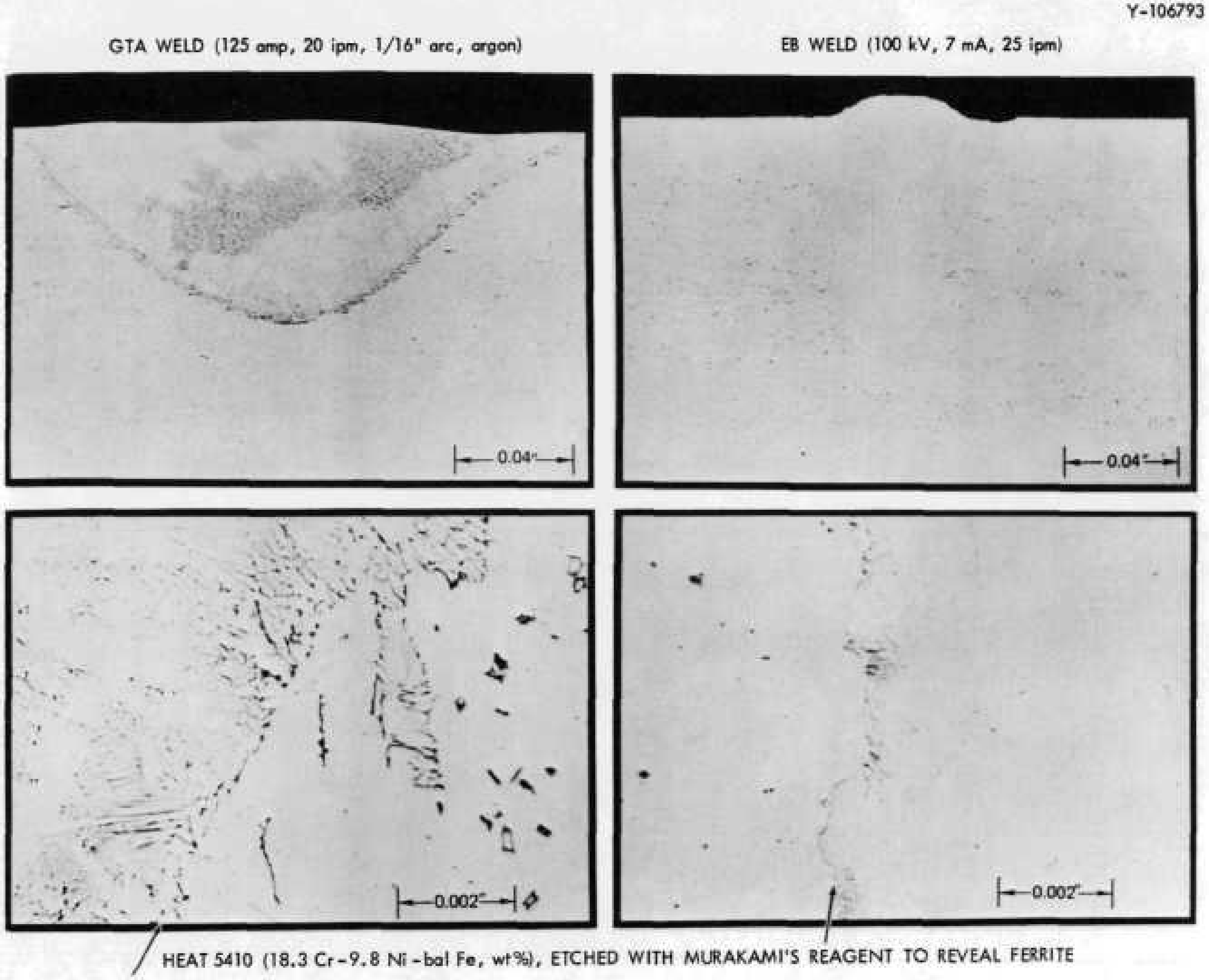

Fig. 18.2. Gas Tungsten-Arc (left) and Electron-Beam (right) Welds on Heat 5410 (18.3 Cr-9.8 Ni-bal Fe, wt %) Etched with Murakami's Reagent to Reveal Ferrite. The bottom photomicrographs show the fusion lines of the upper welds.

Table 18.3. Ferrite Content (Measured with the QTM) of Autogeneous Welds in Experimental Stainless Steel Alloys

Heat No.	Composition, wt % (bal Fe)			% Ferrite		
	Cr	Ni	Mn	Schaeffler Diagram	EB Weld	GTA Weld
5409	18.3	11.9	4.8	0	2.9	8.5
5410	18.3	9.8	---	7	0.25	3.3
5416	22.2	13.5	---	7	1.5	7.0
5422	24.1	18.8	---	0	0	0

19. NONDESTRUCTIVE TESTING

W. O. Harms   R. W. McClung

Our task is to develop new and improved methods of nondestructively testing reactor materials and components. We are studying various physical phenomena, developing instruments and other equipment, devising techniques, and designing and fabricating reference standards. Among the methods being studied for both normal and remote inspection are electromagnetics (with major emphasis on eddy currents), ultrasonics, and penetrating radiation.

Electromagnetic Inspection Methods (Eddy Currents)

Solutions for Electromagnetic Induction Problems (C. V. Dodd, W. A. Simpson, C. C. Lu and W. E. Deeds[1])

We continued research and development on both analytical and empirical bases. We have written a computer program to calculate the magnitude and phase of the impedance of a reflection type coil above an arbitrary number of planar conductors, each having an arbitrary conductivity and permeability. This versatile program allows the immediate analysis of a large number of problems without the need for performing a separate derivation and writing a separate program for each different layered problem.

We have also written a single program to calculate the magnitude and phase of a particular reflection type coil above a single conductor as the coil is connected in the actual circuit of the Phase-Sensitive Eddy-Current Instrument (formerly, we had to run three programs to calculate this).

Work is continuing on construction of accurate eddy-current conductivity standards. Scans for conductivity variations have been completed on all the different alloys, and they are now being machined into ac and dc standards. We are continuing our study of the variables affecting thickness and clad thickness measurements. Figure 19.1 shows the results of some of our calculations of cladding thickness for a reflection type coil. The solid line represents the phase shift for a 10% change in cladding thickness for various values of the parameter, $\bar{r}^2\omega\mu\sigma_1$. The dashed line represents the percent error in the measurement of thickness due to a lift-off variation of

---

ORNL-DWG 71-5373

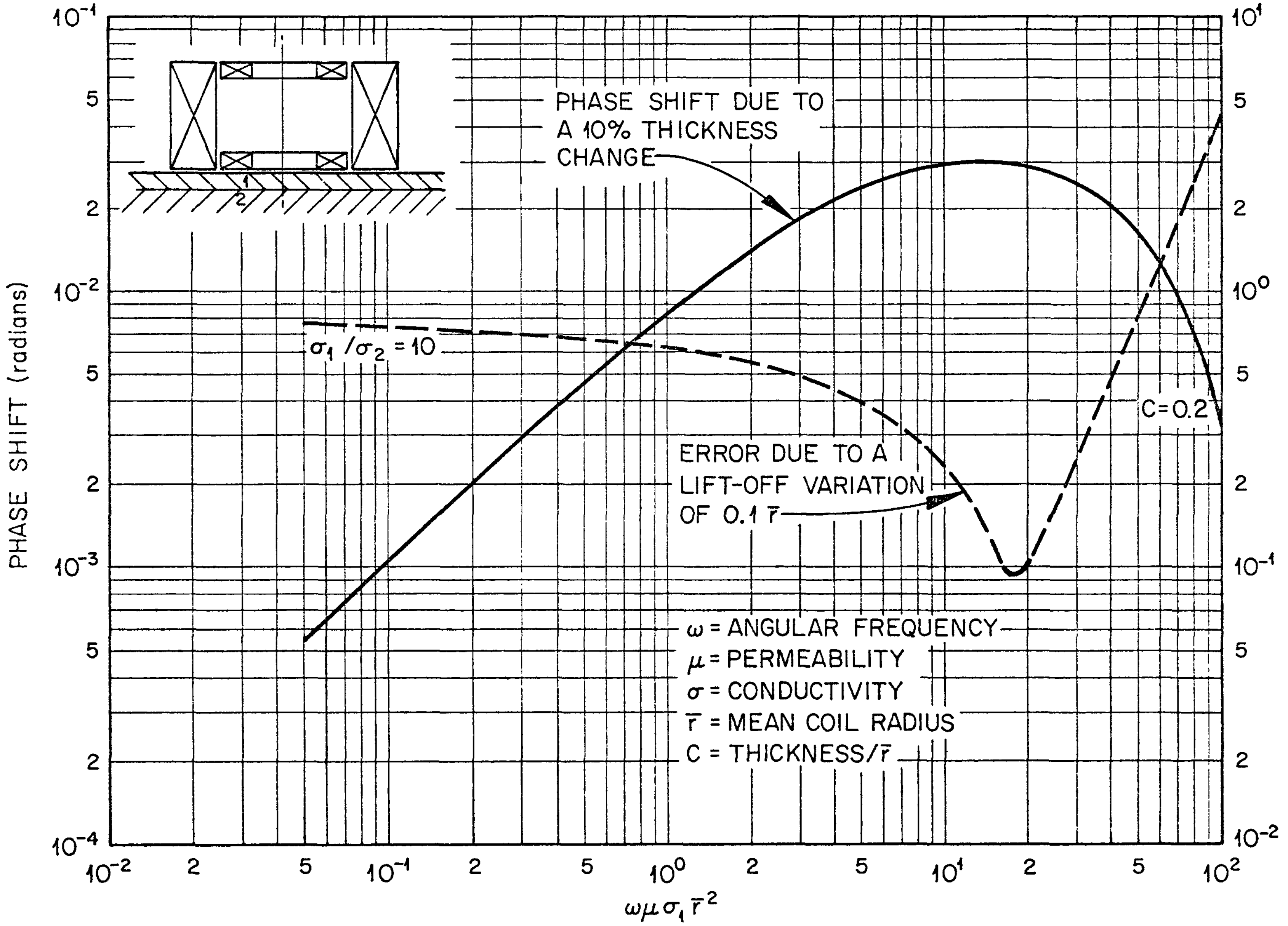

Fig. 19.1. Phase Shift for a 10% Change in Cladding Thickness and Error Due to Lift-Off vs $\bar{r}^2\omega\mu\sigma_1$.

0.1 $\bar{r}$ (mean coil radius). By varying the coil shape, we can generally make the point of minimum phase shift occur at the same value of $\bar{r}^2\omega\mu\sigma_1$ as the maximum phase shift due to a variation in thickness and therefore decrease the error due to lift off.

Ultrasonic Inspection Methods

Ultrasonic Frequency Analysis (H. L. Whaley, K. V. Cook, Laszlo Adler[2])

We continued our basic studies of frequency effects in ultrasonic testing by means of spectral analysis. We are employing a special electronic system developed for these studies to learn more about the effects of frequency on conventional ultrasonic techniques and potentially to develop new test techniques based upon principles derived from these studies.

We are studying the spectral variations in broad-banded ultrasonic pulses as a function of the acoustical discontinuity with which they have interacted. Such a study can lead to improvements in the characterization of hidden flaws in materials by ultrasonic inspection. Spectral analysis has been performed on ultrasonic pulses returned from reflection of various types and orientations, and systematic variations were observed as a function of the size, shape, orientation and position of the reflector. Analytical expressions which we have derived have been successful in accounting theoretically for these variations.

A method has been developed which allows various portions of the total ultrasonic signal to be selected for spectral analysis. This technique is in contrast to our usual method of analysis of the total signal pulse. The new method utilizes two separate electronic gates whose widths and relative spacing can be adjusted as desired so that any two selected portions of the reflected pulse may be fed to the spectrum analyzer. The ability to discriminate in analysis of the pulse becomes important in the case of flat, noncircular reflectors (elliptical, rectangular, etc. or irregular) or reflectors of any shape whose surfaces have varying contours. The integrated pulse from such a reflector may be very complex.

Earlier work with noncircular reflectors[3] was limited to observation of the spectral pattern as the reflector angle was changed in one plane. A study is now being made of the size determination of reflectors of various shapes having random orientation with respect to the transducer. These more nearly simulate the case of natural flaws in materials. It was determined that thin foils of brass would make adequate reflectors for this study. Thus samples of any desired shape or size can easily be prepared. The reflectors are not perfectly flat, but are not at the present time being intentionally bent to obtain various contours to the surface as this causes additional complications in analysis of the reflected ultrasonic signal.

Ultrasonic Imaging

Optical techniques (such as schlieren) for visualizing ultrasound have proved useful to gain an understanding of interactions difficult to analyze by conventional ultrasonic methods. Bragg diffraction and volume holography display the acoustical discontinuity with which the ultrasound field has interacted rather than forming an image of the sound field as with schlieren. The basic system we employ for imaging is a mirror schlieren system with continuous and pulsed light sources, a 6 in. diam working area and a television display. We have added a video tape system for data recording.

The equipment is currently being relocated in another laboratory space. We are redesigning the layout of the optical system to achieve an imaging system with more general capabilities. This will allow schlieren, Bragg diffraction, and volume holography to be done with only minor modification to change from one to another of the techniques. An improved mechanical system for sample positioning is being planned for a large portable tank which will be used with the imaging system in its new location.

Reference Notches (K. V. Cook)

Electrodischarge machined (EDM) notches were placed on the outer and inner surfaces of 0.155 in. OD tubing which was fabricated into a simulated thermocouple with an OD of 0.127 in. These notches were readily detected by ultrasonic techniques in the swaged finished product; thus, the test demonstrates that reference standards can be fabricated in a similar manner for thermocouple or fuel pin component tests. Early results indicate that reduced sensitivity for inspection may be necessary for swaged products because of the presence of a higher noise level; however, this would require investigation of samples in the actual products to be inspected.

Penetrating Radiation Inspection Methods

Radiation Scattering (B. E. Foster, S. D. Snyder)

Our studied have continued on the use of scattered and fluorescent radiation for measuring the thickness of coatings or claddings on reactor components. With the isotopic source presently being used the monitoring time required to accumulate a sufficient number of counts for a valid measurement is approx 25 minutes. This lengthy counting time is tolerable during initial development work. However, it would be quite troublesome as well as uneconomical for actual examinations. For the most practical applications, the technique should be capable of scanning the specimen with only a short dwell time on any given area. Of course, for measurements made at rapid scanning speeds, a very high intensity radiation source is necessary. This would frequently preclude the use of radioisotopes. We have begun studies using one of our mechanical scanning systems that incorporates a commercial x-ray unit as the radiation source. The energy of the x-ray beam is polychromatic as opposed to the near monochromatic beam from the isotope. Many of the available energies in the x-ray beam will be inefficient or unnecessary for a given evaluation, saturating the detector as well as creating extra shielding requirements for safety. We are taking steps to remove as much of the unwanted energies as possible before striking the specimen rather than depending upon only the pulse-height discrimination to electronically select the one energy of interest. Toward this end we have evaluated the use of several LiF crystals that were salvaged from a microprobe unit.

A lead shield with a narrow slit was fabricated and attached in the photomultiplier-crystal detector. We used a monochromatic source in an attempt to find the focal point of the crystals. However, the radius of the crystals and energy of the source proved to be a complete mismatch. The focal point was subsequently located using a light beam.

Through preliminary experiments with the versatile scanner and associated x-ray unit, we determined that a more intense beam of monochromatic radiation than the isotopic sources could be achieved. A further benefit is that the specific value of the energy can now be varied over a wide range. We will now conduct our studies of x-ray scattering and fluorescence in the dynamic mode.

Closed Circuit Television for Radiographic Evaluation (B. E. Foster, S. D. Snyder)

We are continuing the study on the use of a closed circuit television system as a rapid densitometer for reading radiographs.

We have completed the evaluation on the potential replacement of the Lumatron by a Biomation Transient Recorder sampling unit. The unit had several desirable features, however, the input frequency response was too low. Also, the number of available sample points was inadequate. At this time, the Tektronix 1S1 sampling unit will be used as the interface of the x-y recorder readout.

Some preliminary investigations indicate that we may be able to minimize the effects of the horizontal jitter of the video system by optical magnification of the radiographic image. We will make resolution studies using this approach.

Shield for ^{252}Cf Neutron Source (B. E. Foster, S. D. Snyder)

We completed the conceptual design of a facility to use 10 mg of ^{252}Cf as a neutron source for both attenuation studies and radiography. The facility is designed such that it could be safely located in the Nondestructive Testing Laboratory. Figure 19.2 is a simplified drawing of the facility. The collimator shields and beam catchers are not shown. A feature of this system is that the source will be retracted below the floor when not in use, reducing many problems of personnel safety.

References

1. Consultant from the University of Tennessee.

2. Consultant from the University of Tennessee.

3. H. L. Whaley, K. V. Cook, Laszlo Adler, Fuels and Materials Development Program Quart. Progr. Rept. December 31, 1969, ORNL-4520, pp. 311-312.

ORNL DWG. 71-6577

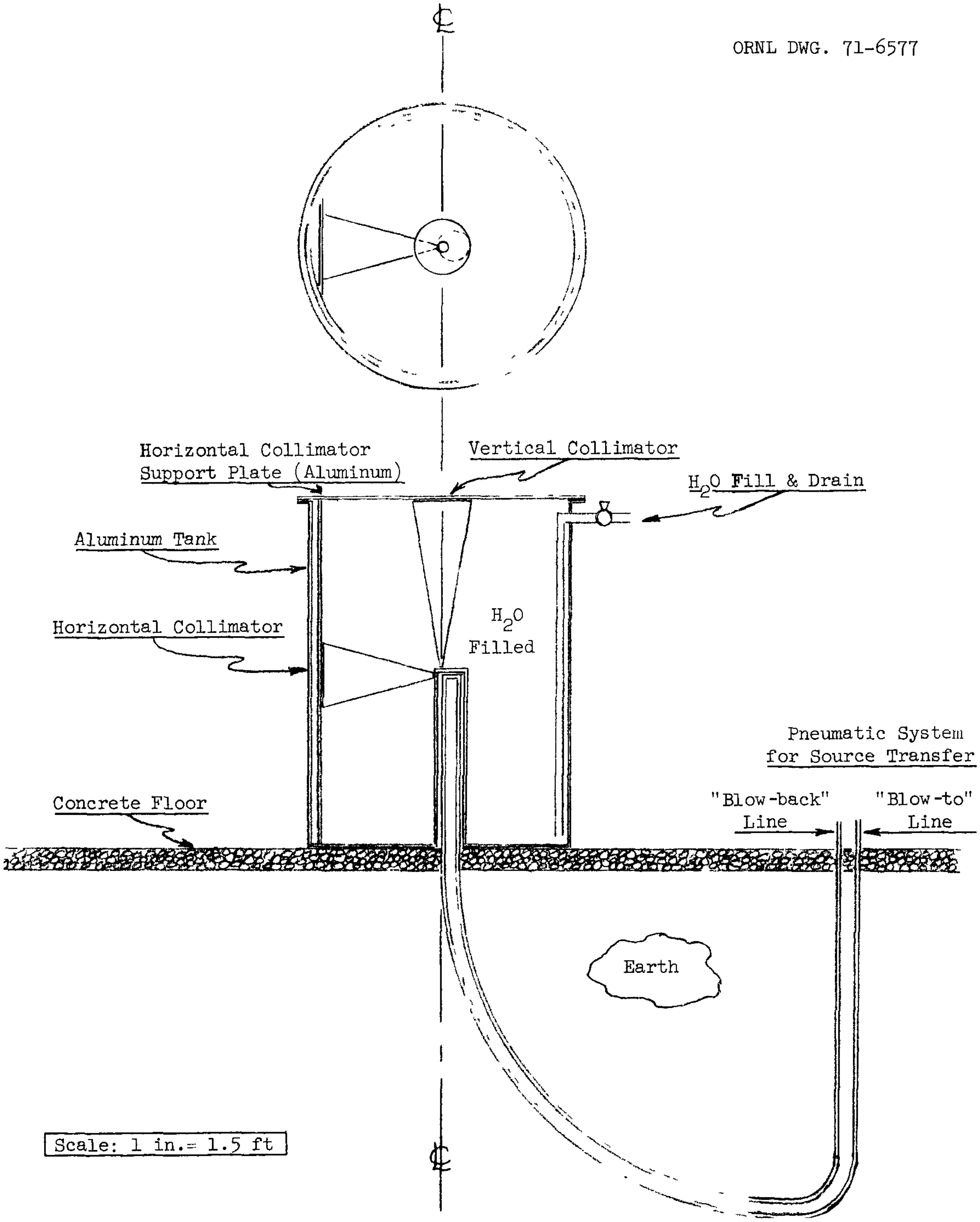

Fig. 19.2. Conceptual Design of Californium-252 Neutron Source Facility for Radiography and Attenuation Studies to be Located in the Nondestructive Test Development Laboratory.

20. ✓ADVANCED MATERIALS FOR STEAM GENERATORS

P. Patriarca G. M. Slaughter

The purpose of this program is to determine the corrosion resistance of welds in several high-temperature alloys being considered for use in steam generators for advanced high-temperature reactors. We need to know how well these weldments will resist both general and preferential corrosion in steam 480 to 650°C.

The program currently includes two areas of investigation: (1) general corrosion (uniform scale, including pitting and knife-edge attack at fusion lines) at 595 and 650°C together with an evaluation of the general weldability of various combinations of base and filler metals, and (2) stress-corrosion cracking (induced by chloride or caustic as contaminants) at 480°C and higher.

General Corrosion at 595 and 650°C

Studies of the Effects of Surface Finish on Corrosion of Steam Generator Alloy Weldments (J. P. Hammond)

In the last quarterly report,[1] results of general corrosion tests on steam generator alloy weldments in superheated steam at 595 and 650°C (1100 and 1200°F) was discussed. A total exposure of 16,000 hr had been accumulated. The calculated penetrations in 20 years for Inconel 625, Hastelloy X, and IN-102 similar-metal weldments (joined to themselves with themselves) were all below 0.0005 in. Based on weight gained in 14,000 hr of exposure, the amounts of corrosion incurred in dissimilar-metal weldments containing these base metals joined to Incoloy 800 both with themselves and with Inconel 82 as filler metals were also impressively low.

A comparison of our results on weldments with those of the General Electric Company (Vallecitos Laboratory) on wrought alloys show that our materials corroded only one-third to one-half as much as theirs.[2] Since a difference in surface treatment of the specimens could very well have been a factor in this discrepancy, we assessed the importance of surface finish as a corrosion variable. Identical studies were made with specimens ground on a 100-mesh-grit belt and with specimens electropolished to remove the effects of surface grinding (0.002 in. of metal removed). Dissimilar-metal weldments in the electropolished condition have received an exposure of 8000 hr and are presently being evaluated. To establish the effects of these finishes on the individual base metals involved, test specimens in duplicate were exposed for periods of 1000 and 2000 hr and at intervals of 2000 hr to a total exposure of 14,000 hr. The weight-gain results for electropolished specimens exposed at 650°C are compared with belt-ground specimens in Fig. 1. Figure 2 gives the same results on an expanded scale and includes curves for Incoloy 800 at 595°C as well.

Observe that the corrosion resistance of some of the alloys appears to improve with electropolishing, whereas that of others decreases substantially. Inconel 625 and Hastelloy X are included in the former category while Inconel 600 and Incoloy 800 are of the latter. The corrosion resistance of type 304 stainless steel also was greatly decreased by electropolishing, but results for it are not included in the graphs because of severe scale spallation. Whereas weight-gain data were not obtained for IN 102 in the electropolished condition, metallographic examinations on dissimilar-metal weldments involving it indicated that its corrosion resistance is only slightly reduced by electropolishing.

A mathematical analysis of the weight-gain curves of Fig. 2 indicates that the corrosion of Incoloy 800 in the electropolished condition is of a different form from that generally depicted for the steam corrosion of intermediate- and high-nickel alloys of this general class. Ordinarily, corrosion is considered to occur in two stages: rapid corrosion for a period of 1000 to 3000 hr that is of a parabolic form, followed by a second stage of corrosion that is linear with time.

Examination of the scaling of electropolished Incoloy 800 at 595 and 650°C shows that its second stage of corrosion is best described by an equation of the form

$$Y = A + (1/B + CT)\, T\ ,$$

where Y is the amount of weight gained, T is time, and A, B, and C are constants. Features prominent in the corrosion of electropolished Incoloy 800 are the unusually large amounts of corrosion during the first

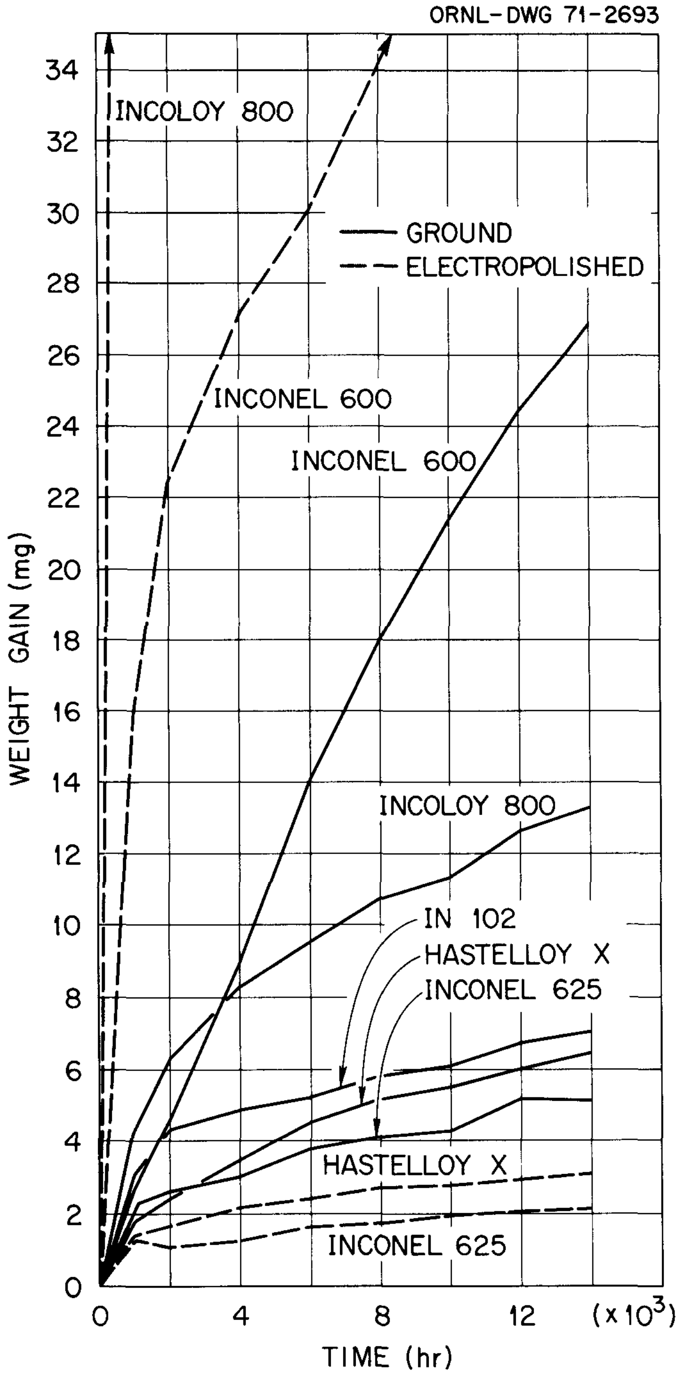

Fig. 20.1. Corrosion of Base Metal Alloys at 650°C, As-Ground and Electropolished (for specimens of 20 cm^2 area).

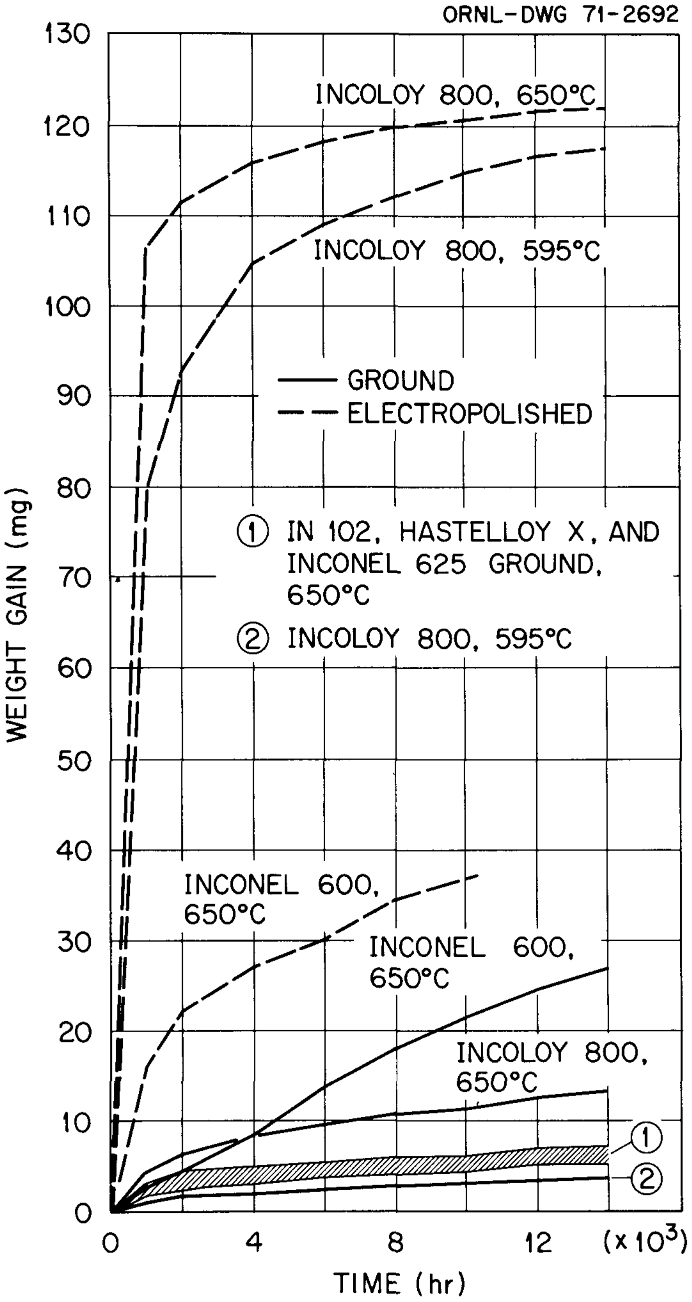

Fig. 20.2. Corrosion of Incoloy 800 As-Ground and Electropolished in Comparison with Other Base Metals (for specimens of 20 cm^2 area).

1000 hr of exposure and the fact that the rate of corrosion decreases significantly with time thereafter rather than remaining approximately constant. The latter feature, coupled with the fact that scale retention tests indicate that electropolished Incoloy 800 has high resistance to spallation and flaking, reflects encouragement for Incoloy 800 in high-temperature steam applications.

Stress Corrosion Cracking in Chloride Environment (J. P. Hammond)

During the last quarter, the fourth stress-corrosion cracking test discussed previously[3] was completed and the fifth run was initiated. The specimens included triplicate samples of the similar- and dissimilar-metal weldments tested earlier in general corrosion tests as well as numerous alloys in unwelded strips. Also, 36 different specimens of type 304 stainless steel welded with type 308 stainless steel filler metal were included. These incorporated welds of high and low carbon content; the ground, the ground-and-annealed, and the ground-and-annealed plus pickled conditions as surface finishes; and the as-welded, solution-annealed, and solution-annealed plus sensitized conditions as heat treatments.

The fourth stress-corrosion cracking run consisted of cycling for 4 weeks between 480°C (900°F) and the steam-saturation temperature (280°C or 540°F) with 1.5 ppm NaCl and 20 ppm O as contaminants. The specimens were cycled five times a week and held at the saturation temperature for 2 hr per cycle. Since there were no failures, the specimens were then exposed a fifth week with the NaCl and O concentrations raised to 10 ppm and 20 ppm, respectively, and the thermal cycling changed to three cycles per week with 24-hr sojourns at the steam-saturation temperature.

The results of this test were surprising in that two as-ground specimens of Hastelloy X welded to itself with itself completely failed. None of the other specimens failed(except for a small crack found in a third specimen) including the normally more susceptible stainless steel specimens. The specimen showing the small crack was a dissimilar-metal weldment of IN 102 joined to Incoloy 800 with Inconel 82.

The Hastelloy X U-bend specimens that failed are shown in Fig. 3 while the microstructural features of the crack are illustrated in Fig. 4. Note

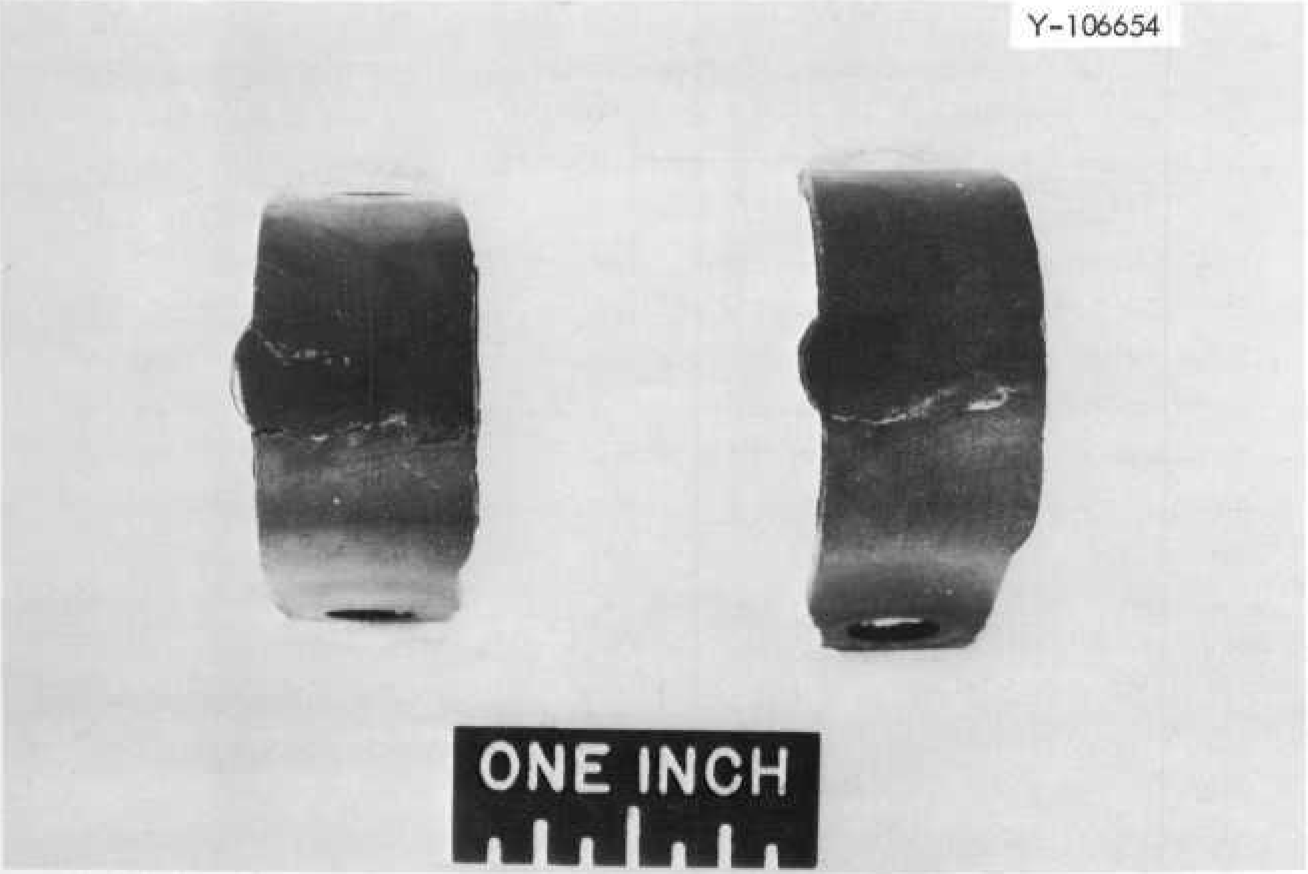

Fig. 20.3. As-Ground U-Bend Specimens of Hastelloy X Welded to Itself (Weld A5), Cracked by Stress Corrosion in NaCl-Contaminated Steam. Cracks initiate at surface adjacent to root pass and progress into base metal alongside fusion line before proceeding into the weld deposit.

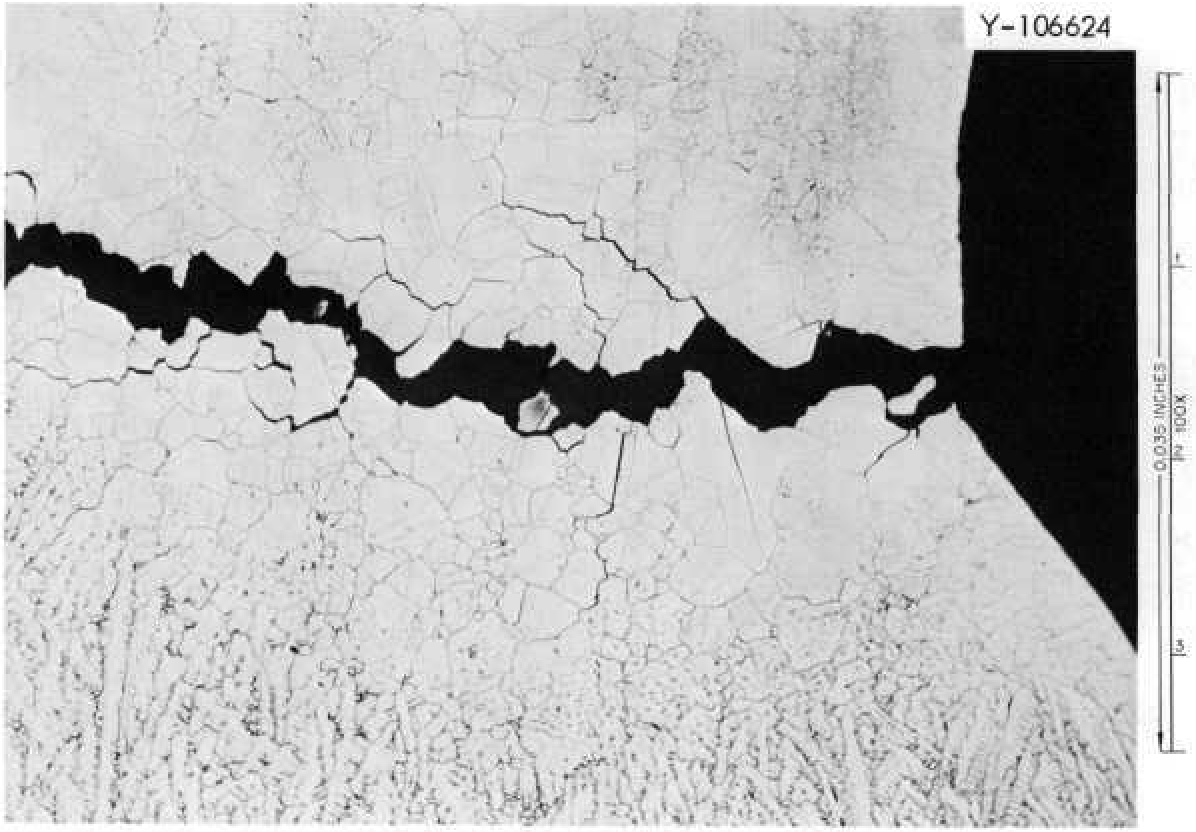

Fig. 20.4. Microstructural Characteristics of Stress-Corrosion Crack Formed in Weldment A5 Shown in Fig. 20.3. Crack is intergranular in nature and located in base metal immediately adjacent to fusion line. Etched with mixture of H_2O_2 and NCl. 100X.

that the cracks are intergranular in nature and are quite characteristic of stress corrosion.

The fifth stress-corrosion run is being thermally cycled under the same conditions as were used during the last week of the fourth run, that is, three cycles to the saturation temperature per week with 24-hr sojourns. However, the NaCl and O concentrations were increased to 25 ppm and 50 ppm, respectively, to increase the severity of the test. To increase data output, the unfailed specimens of run 4 were restressed and reinserted in run 5 along with fresh U-bend specimens of the various unwelded and welded materials.

References

1. J. P. Hammond, Fuels and Materials Development Program Quart. Progr. Rept. Dec. 31, 1970, ORNL-TM-3300.
2. G. P. Wozaldo and W. L. Pearl, "General Corrosion of Stainless Steels and Nickel Base Alloys Exposed Isothermally in Superheated Steam," Corrosion **21**, 355–369 (1965).
3. J. P. Hammond, Fuels and Materials Development Program Quart. Progr. Rept. Sept. 30, 1970, ORNL-4630.

Previous reports in this series:

ORNL-4330	Period Ending June 30, 1968
ORNL-4350	Period Ending September 30, 1968
ORNL-4390	Period Ending December 31, 1968
ORNL-4420	Period Ending March 31, 1969
ORNL-4440	Period Ending June 30, 1969
ORNL-4480	Period Ending September 30, 1969
ORNL-4520	Period Ending December 31, 1969
ORNL-4560	Period Ending March 31, 1970
ORNL-4600	Period Ending June 30, 1970
ORNL-4630	Period Ending September 30, 1970
ORNL-TM-3300	Period Ending December 31, 1970

INTERNAL DISTRIBUTION

1–3. Central Research Library
4. ORNL — Y-12 Technical Library
Document Reference Section
5–34. Laboratory Records Department
35. Laboratory Records, ORNL RC
36. ORNL Patent Office
37. G. M. Adamson, Jr.
38. S. E. Beall
39. J. A. Conlin
40. W. B. Cottrell
41–42. C. M. Cox
43. J. A. Cox
44. R. S. Crouse
45. F. L. Culler
46. J. E. Cunningham
47–48. J. H. DeVan
49. R. G. Donnelly
50. W. P. Eatherly
51. J. I. Federer
52. D. E. Ferguson
53. J. H Frye, Jr.
54. R. J. Gray
55. B. L. Greenstreet
56. W. R. Grimes
57. W. O. Harms
58–60. M. R. Hill
61. H. Inouye
62–94. P. R. Kasten
95. G. W. Keilholtz
96. J. M. Leitnaker
97. H. R. Livesey
98. E. L. Long, Jr.
99. A. L. Lotts
100. W. R. Martin
101. R. W. McClung
102–104. H. E. McCoy, Jr.
105. H. C. McCurdy
106. W. T. McDuffee
107. D. L. McElroy
108. J. R. McGuffey
109. C. J. McHargue
110. L. C. Oakes
111. R. E. Oakes
112. P. Patriarca
113. S. Peterson
114. P. L. Rittenhouse
115. M. W. Rosenthal
116. D. J. Rucker
117. A. W. Savolainen
118. A. C. Schaffhauser
119. J. L. Scott
120. J. D. Sease
121–122. G. M. Slaughter
123. J. O. Stiegler
124. D. A. Sundberg
125. V. J. Tennery
126. D. B. Trauger
127. J. E. Van Cleve
128. T. N. Washburn
129. J. R. Weir, Jr.
130. G. D. Whitman
131. R. G. Wymer
132. H. L. Yakel

EXTERNAL DISTRIBUTION

AEC-RDT SITE REPRESENTATIVES

133. R. H. Ball, Gulf General Atomic
134. D. F. Cope, Oak Ridge National Laboratory
135. Theodore Iltis, Westinghouse Advanced Reactor Division
136. M. E. Jackson, Argonne National Laboratory
137. C. L. Matthews, Oak Ridge National Laboratory
138. R. L. Morgan, Atomics International
139. D. A. Moss, Idaho
140. J. Sako, WADCO
141. Atomic Energy Commission Library, Washington

AIR FORCE MATERIALS LABORATORY, Wright-Patterson Air Force Base

142. C. H. Armbruster
143. H. M. Burte
144. I. Perlmutter

AMES LABORATORY, USAEC, Iowa State University, Ames, Iowa 50010

145. M. S. Wechsler

ARGONNE NATIONAL LABORATORY

146. B.R.T. Frost
147. J. H. Kittel
148. M. V. Nevitt
149. D. R. O'Boyle
150. P. G. Shewmon
151. R. C. Vogel

ATOMIC POWER DEVELOPMENT ASSOCIATES

152. A. A. Shoudy, Jr.

ATOMICS INTERNATIONAL

153. J. G. Asquith
154. T. A. Moss
155. H. Pearlman
156. S. Siegel

BABCOCK & WILCOX COMPANY, Beaver Falls, Pennsylvania 15010

157. William Buley

BABCOCK & WILCOX COMPANY, Lynchburg, Virginia 24505

158. C. J. Baroch
159. S. P. Grant
160. C. R. Johnson
161. L. R. Weissert

BATTELLE MEMORIAL INSTITUTE, Columbus, Ohio

162. D. Keller
163. S. J. Paprocki
164. Defense Materials Information Center

BROOKHAVEN NATIONAL LABORATORY

165. D. H. Gurinsky
166. C. Klamut

BUREAU OF MINES

167. Haruo Kato, Albany Metallurgy Research Center, P.O. Box 70, Albany, Oregon 97321
168. T. A. Sullivan, Bureau of Mines, Boulder City, Nevada 89005

COMBUSTION ENGINEERING

169. M. Andrews
170. W. P. Chernock

DIVISION OF NAVAL REACTORS, AEC, Washington

171. R. H. Steele

DIVISION OF REACTOR DEVELOPMENT AND TECHNOLOGY, AEC, Washington

172. J. C. Crawford, Jr.
173. G. W. Cunningham
174. R. P. Denise
175. K. E. Horton
176. J. R. Hunter
177. E. E. Kintner
178. W. H. Layman
179. W. H. McVey
180. J. J. Morabito
181. E. C. Norman
182. R. E. Pahler
183. A. J. Pressesky
184. M. A. Rosen
185. S. Rosen
186. J. M. Simmons
187. E. E. Sinclair
188. B. Singer

DIVISION OF REACTOR DEVELOPMENT AND TECHNOLOGY, AEC, Washington (contd)

189. A. Taboada
190. A. N. Tardiff
191. A. Van Echo
192. C. E. Weber
193. M. J. Whitman

DIVISION OF RESEARCH, AEC, Washington

194. L. C. Ianniello
195. P. W. McDaniel
196. D. K. Stevens

GENERAL ELECTRIC, Cincinnati

197. H. C. Brassfield

GENERAL ELECTRIC, Nuclear Systems Programs, Cincinnati

198. E. E. Hoffman

GENERAL ELECTRIC, Pleasanton

199. H. W. Alter

GENERAL ELECTRIC, San Jose

200. R. Duncan
201. J. L. Krankota

GENERAL ELECTRIC, Sunnyvale

202. R. E. Skavdahl
203. C. N. Spalaris
204. E. L. Zebroski
205. Technical Library

GEORGE C. MARSHALL SPACE FLIGHT CENTER, Huntsville, Alabama

206. R. J. Schwinghamer

GULF GENERAL ATOMIC

207. L. J. Colby
208. A. J. Goodjohn
209. J. P. Howe
210. J. N. Lindgren
211. J. F. Watson
212. L. Yang

IDAHO NUCLEAR CORPORATION

213. W. C. Francis
214. W. A. Yuill

KNOLLS ATOMIC POWER LABORATORY

215. R. F. Wojciescak

LMFBR PROGRAM OFFICE, Argonne National Laboratory

216. G. A. Bennet
217. P. F. Gast
218. J. M. McKee

LOS ALAMOS SCIENTIFIC LABORATORY

219. R. D. Baker

MOUND LABORATORY

220. W. T. Cave
221. R. E. Vallée

NASA HEADQUARTERS

222. J. J. Lynch

NASA, LEWIS RESEARCH CENTER

223. G. M. Ault
224. J.W.R. Creagh
225. J. J. Lombardo
226. F. E. Rom
227. L. Rosenblum
228. N. T. Saunders
229. C. M. Scheuermann

NAVAL RESEARCH LABORATORY

230. J. R. Hawthorne

NUCLEAR MATERIALS AND EQUIPMENT CORPORATION

231. K. H. Puechl

OAK RIDGE OPERATIONS OFFICE

232. Laboratory and University Division

OHIO STATE UNIVERSITY, Columbus, Onio 43212

233. R. W. Staehle

RENSSELAER POLYTECHNIC INSTITUTE

234. D. W. Dickinson
235. W. F. Savage

SANDIA CORPORATION

236. J. R. Holland
237. P. D. O'Brian

SPACE NUCLEAR SYSTEMS OFFICE, AEC, Washington

238. R. E. Anderson
239. D. Beard
240. J. F. Griffo
241. H. Jaffe
242. C. E. Johnson
243. A. P. Litman
244. J. A. Powers
245. F. C. Schwenk

UNION CARBIDE CORPORATION, New York

246. J. A. Swartout

UNION CARBIDE CORPORATION, Carbon Products Division, Cleveland, Ohio 44101

247. C. F. Leitten, Jr.

UNITED NUCLEAR CORPORATION

248. A. A. Strasser

UNIVERSITY OF CALIFORNIA, Lawrence Radiation Laboratory, Livermore

249. W. R. Holman
250. L. W. Roberts
251. A. J. Rothman

U.S. NAVAL AIR SYSTEM COMMAND :AIR-52031B;

252. I. Machlin

USAEC Scientific Representative, American Embassy, Box 40, FPO, N.Y. 09510

253. W.L.R. Rice

WADCO, P.O. Box 1970, Richland, Washington 99352

254. T. T. Claudson
255. D. L. Condotta
256. E. A. Evans
257. J. W. Finnigan
258. J. E. Hanson
259. B. R. Hayward
260. B. M. Johnson
261. H. N. Pederson
262. W. E. Roake
263. W. F. Sheely
264. J. C. Tobin

WESTINGHOUSE, Advanced Reactor Division, Waltz Mill Site

265. E. C. Bishop
266. A. Boltax
267. P. J. Levine
268. P. Murray
269. W. E. Ray
270. J. J. Taylor
271. G. A. Whitlow

WESTINGHOUSE, Astronuclear Laboratory

272. R. T. Begley
273. D. C. Goldberg

WESTINGHOUSE, Atomic Power Division

274. Library

WESTINGHOUSE, Bettis

275. R. H. Fillnow
276. P. N. Gustafson
277. Westinghouse Bettis Laboratory Library

WESTINGHOUSE, Nuclear Energy Systems, Tampa Division

278. M. E. Eilbeck

279–280. Division of Technical Information Extension
281–283. Director, Division of Reactor Licensing, AEC, Washington, D.C. 20545
284–285. Director, Division of Reactor Standards, AEC, Washington, D.C. 20545